ISSN 2074-272X

науково-практичний журнал 2024/4

Електротехніка і Електромеханіка

Electrical Engineering & Electromechanics

Електричні машини та апарати
Електротехнічні комплекси та системи
Промислова електроніка
Інженерна електрофізика.
Техніка сильних електричних та магнітних полів
Електричні станції, мережі і системи

Журнал включено до найвищої категорії «А»
Переліку фахових видань України

З 2019 р. журнал індексується у Scopus

З 2015 р. журнал індексується
у Web of Science Core Collection:
Emerging Sources Citation Index

Electrical Engineering & Electromechanics

Scientific Journal was founded in 2002
Founder – National Technical University «Kharkiv Polytechnic Institute» (Kharkiv, Ukraine)

EDITORIAL BOARD

Sokol Ye.I.	**Editor-in-Chief**, Professor, Corresponding member of NAS of Ukraine, Rector of National Technical University «Kharkiv Polytechnic Institute» (NTU «KhPI»), **Ukraine**
Korytchenko K.V.	**Deputy Editor,** Professor, NTU «KhPI», **Ukraine**
Rozov V.Yu.	**Deputy Editor,** Professor, Corresponding member of NAS of Ukraine, Anatolii Pidhornyi Institute of Mechanical Engineering Problems of NAS of Ukraine, Kharkiv, **Ukraine**
Bolyukh V.F.	**Deputy Editor,** Professor, NTU «KhPI», **Ukraine**
Abu-Siada A.	Professor, Curtin University, Perth, **Australia**
Aman M.M.	Professor, NED University of Engineering & Technology, Karachi, **Pakistan**
Babak V.P.	Professor, Corresponding member of NAS of Ukraine, General Energy Institute of NAS of Ukraine, Kyiv, **Ukraine**
Baltag O.	Professor, Grigore T. Popa University Medicine and Pharmacy, **Romania**
Baranov M.I.	Professor, Research and Design Institute «Molniya» of NTU «KhPI», **Ukraine**
Batygin Yu.V.	Professor, Kharkiv National Automobile and Highway University, **Ukraine**
Bíró O.	Professor, Institute for Fundamentals and Theory in Electrical Engineering, Graz, **Austria**
Bouktir T.	Professor, Ferhat Abbas University, Setif 1, **Algeria**
Buriakovskyi S.G.	Professor, NTU «KhPI», **Ukraine**
Butkevych O.F.	Professor, Institute of Electrodynamics of NAS of Ukraine (IED of NASU), Kyiv, **Ukraine**
Colak I.	Professor, Nisantasi University, Istanbul, **Turkey**
Cruz S.	Professor, University of Coimbra, **Portugal**
Doležel I.	Professor, University of West Bohemia, Pilsen, **Czech Republic**
Féliachi M.	Professor, Technological Institute of Saint-Nazaire, University of Nantes, **France**
Guerrero J.M.	Professor, Aalborg University, **Denmark**
Gurevich V.I.	PhD, Honorable Professor, Central Electrical Laboratory of Israel Electric Corporation, Haifa, **Israel**
Hajjar A.A.	Professor, Tishreen University, Latakia, **Syrian Arab Republic**
Hammarström T.	Professor, Chalmers University of Technology, **Sweden**
Ida N.	Professor, The University of Akron, Ohio, **USA**
Izykowski J.	Professor, Wroclaw University of Science and Technology, **Poland**
Kildishev A.V.	Associate Research Professor, Purdue University, **USA**
Klepikov V.B.	Professor, NTU «KhPI», **Ukraine**
Korzeniewska E.	Professor, Lodz University of Technology, **Poland**
Ktena A.	Professor, National and Kapodistrian University of Athens, **Greece**
Kuznetsov B.I.	Professor, Anatolii Pidhornyi Institute of Mechanical Engineering Problems of NAS of Ukraine, Kharkiv, **Ukraine**
Kyrylenko O.V.	Professor, Academician of NAS of Ukraine, IED of NASU, Kyiv, **Ukraine**
Malik O.P.	Professor, University Of Calgary, **Canada**
Maslov V.I.	Professor, National Science Center «Kharkiv Institute of Physics and Technology», **Ukraine**
Mikhaylov V.M.	Professor, NTU «KhPI», **Ukraine**
Miljavec D.	Professor, University of Ljubljana, **Slovenia**
Milykh V.I.	Professor, NTU «KhPI», **Ukraine**
Nacke B.	Professor, Gottfried Wilhelm Leibniz Universitat, Institute of Electrotechnology, Hannover, **Germany**
Oleschuk V.	Professor, Institute of Power Engineering of Technical University of Moldova, **Republic of Moldova**
Petrushin V.S.	Professor, Odessa National Polytechnic University, **Ukraine**
Podoltsev A.D.	Professor, IED of NASU, Kyiv, **Ukraine**
Reutskiy S.Yu.	PhD, Anatolii Pidhornyi Institute of Mechanical Engineering Problems of NAS of Ukraine, Kharkiv, **Ukraine**
Rezinkin O.L.	Professor, NTU «KhPI», **Ukraine**
Rezinkina M.M.	Professor, NTU «KhPI», **Ukraine**
Shcherbak Ya.V.	Professor, NTU «KhPI», **Ukraine**
Sikorski W.	Professor, Poznan University of Technology, **Poland**
Strzelecki R.	Professor, Gdansk University of Technology, **Poland**
Suemitsu W.	Professor, Universidade Federal Do Rio de Janeiro, **Brazil**
Trichet D.	Professor, Institut de Recherche en Energie Electrique de Nantes Atlantique, **France**
Vaskovskyi Yu.M.	Professor, National Technical University of Ukraine «Igor Sikorsky Kyiv Polytechnic Institute», Kyiv, **Ukraine**
Vazquez N.	Professor, Tecnológico Nacional de México en Celaya, **Mexico**
Vinnikov D.	Professor, Tallinn University of Technology, **Estonia**
Yagup V.G.	Professor, O.M. Beketov National University of Urban Economy in Kharkiv, **Ukraine**
Yatchev I.	Professor, Technical University of Sofia, **Bulgaria**
Zagirnyak M.V.	Professor, Member of NAES of Ukraine, Kremenchuk M.Ostrohradskyi National University, **Ukraine**
Zgraja J.	Professor, Lodz University of Technology, **Poland**
Grechko O.M.	**Executive Managing Editor,** PhD, NTU «KhPI», **Ukraine**

From no. 1 2019 Journal «Electrical Engineering & Electromechanics» is indexing in **Scopus** and from no. 1 2015 Journal is indexing in **Web of Science Core Collection: Emerging Sources Citation Index (ESCI)**

Also included in DOAJ (Directory of Open Access Journals), in EBSCO's database, in ProQuest's databases – Advanced Technologies & Aerospace Database and Materials Science & Engineering Database, in Gale/Cengage Learning databases.

Editorial office address:
National Technical University «Kharkiv Polytechnic Institute», Kyrpychova Str., 2, Kharkiv, 61002, Ukraine
phones: +380 57 7076281, +380 67 3594696, **e-mail:** a.m.grechko@gmail.com (**Grechko O.M.)**

ISSN (print) 2074-272X
ISSN (online) 2309-3404

© National Technical University «Kharkiv Polytechnic Institute», 2024

Printed 21 June 2024. Format 60 × 90 ⅛. Paper – offset. Laser printing. Edition 50 copies.
Printed by Printing house «Madrid Ltd» (18, Gudanova Str., Kharkiv, 61024, Ukraine)

Electrical Engineering & Electromechanics
Scientific Journal

no. 4, 2024

Table of Contents

Electrical Machines and Apparatus

Electrotechnical Complexes and Systems

Industrial Electronics

Engineering Electrophysics. High Electric and Magnetic Fields Engineering

Power Stations, Grids and Systems

UDC 621.313 https://doi.org/10.20998/2074-272X.2024.4.01

A. Kimouche, M.R. Mekideche, M. Chebout, H. Allag

Influence of permanent magnet parameters on the performances of claw pole machines used in hybrid vehicles

Introduction. *Claw pole machines (CPM) are commonly used in the automotive industry. Recently, importance has focused on the use and introduction of permanent magnets (PM) in this type of machine to increase the power density. This paper studies the performance of permanent magnet claw pole machines (PM-CPM) used in hybrid electric vehicle applications. The structure considers that the PMs are placed between the claws of the rotor.* ***Purpose****. The influence of the PM magnetization effect on the performance of synchronous PM-CPM is analyzed. Radial and tangential magnetizations are applied to obtain the best possible sinusoidal shape of the electromotive force and an acceptable cogging torque. Then, the electromagnetic performance of the PM-CPM is analyzed and evaluated. Furthermore, due to the complexity of the rotor armature, it seems difficult to give a direct relationship between the PM parameters and the machine torque. This led us to study the effects of magnets geometrical dimensions variations on the torque and its ripple.* ***Method.*** *3D nonlinear model of the machine is analyzed using the finite element method and comparisons between some electromagnetic performances are processed.* ***Results****. It was found that the tangential magnetization of PMs makes it possible to obtain a better distribution of the flux density and a minimum of cogging torque mainly responsible for vibrations and acoustic noise. Also, we observed a non-linear variation between the torque and its ripples depending on the dimensions of the PM. In fact, electromagnetic torque increases linearly with PM size but this is not the case for torque ripples.* References 22, tables 2, figures 16.
Key words: **claw pole machine, permanent magnet dimension, hybrid electric vehicles, finite element method, torque ripple.**

Вступ*. Машини з нігтьовим полюсом (CPM) зазвичай використовуються в автомобільній промисловості. Останнім часом велика увага приділяється використанню та впровадженню постійних магнітів (PM) у машинах цього типу для збільшення питомої потужності. У цій статті вивчаються характеристики машин з нігтьовим полюсом із постійними магнітами (PM-CPM), що використовуються у гібридних електромобілях. У конструкції передбачено, що PM розміщуються між кулачками ротора.* ***Мета****. Проаналізовано вплив ефекту намагнічування PM на продуктивність синхронного PM-CPM. Радіальна та тангенціальна намагніченість застосовуються для отримання максимально можливої синусоїдальної форми електрорушійної сили та прийнятного зубчастого моменту. Потім аналізуються та оцінюються електромагнітні характеристики PM-CPM. Крім того, через складність якоря ротора здається скрутним встановити пряму залежність між параметрами PM і крутним моментом машини. Це спонукало вивчити вплив змін геометричних розмірів магнітів на крутний момент і його пульсації.* ***Метод****. Тривимірна нелінійна модель машини аналізується з використанням методу скінченних елементів та виконується порівняння деяких електромагнітних характеристик.* ***Результати****. Встановлено, що тангенціальне намагнічування PM дозволяє отримати кращий розподіл магнітної індукції та мінімуму зубчастого моменту, відповідального головним чином за вібрації та акустичний шум. Також ми спостерігали нелінійну зміну крутного моменту та його пульсацій залежно від розмірів PM. Фактично, електромагнітний крутний момент збільшується лінійно з розміром PM, але це не відноситься до пульсацій крутного моменту.* Бібл. 22, табл. 2, рис. 16.
Ключові слова: **машина з нігтьовим полюсом, розмір постійного магніту, гібридні електромобілі, метод скінченних елементів, пульсація крутного моменту.**

Introduction. Claw pole machines (CPMs) are widely used in automotive applications; they are considered the energy of many electrical consumers of a vehicle. However, the mild hybrid vehicles technology allows energy transfer in both modes of operation. The system consists of recharging the battery and powering the electrical equipment in generator mode, and starting the vehicle in engine mode [1, 2]. In this case and unlike conventional vehicles, the diode bridge associated with the classic alternator is replaced by a voltage inverter transistor [1, 3].

A peculiarity of the CPMs is the structure of its rotor, the poles of which have the shape of a claw, hence its name. This particular structure makes claw alternators exceptionally competitive from an economic point of view, because they can be manufactured easily and quickly while having very good mechanical strength for operation at high rotational speed.

Traditionally, conventional CPMs use a single excitation winding which creates the rotor magnetic field. However, the high demand for electricity from automotive equipment such as security systems comfort and the use of starter-generator system leads to the consideration and introduction of permanent magnets (PMs).

Different rotor topologies containing PMs are used. The study presented in [4] concerning hybrid excitation CPMs for vehicles with 3D-FEM leads to increasing the air gap flux density. Thus, the electromagnetic torque of the CPM is increased and the torque ripples are reduced. In [5] the addition of PMs between the rotor claws allows a significant increase of more than 22 % in the output power of the CPM, but there is a non-linear relationship between the weight of the PMs and the torque when the PMs weight is considerable.

The equivalent magnetic circuit proposed and presented in [6] aims to visualize the influence of the type and volume of the PM (NdFeB) on the characteristics of a CPM, the proposed analytical method makes it possible to calculate the dimensions a PM which will create the desired electrical voltage. Therefore, in [7], a brushless PM claw pole motor with a soft magnetic composite is proposed. PMs are positioned on the claw pole surface and consequently, the optimal method applied gives an improvement of power density and torque density.

In order to eliminate the slip-ring and brush arrangement, a brushless electrically excited claw pole generator was proposed in [8, 9]; it had strong excitation magnetic performance, reduced excitation copper loss, and increased energy conversion efficiency. In [10], the ring PM structure is inserted in the stator yoke, and the stator and rotor are both claw-pole structures. Its power

© A. Kimouche, M.R. Mekideche, M. Chebout, H. Allag

density has significantly increased. Another topology with skewed and non-skewed PMs in the claw-pole rotor fingers is presented in [10]. Results show that the CPM performances such as back-EMF value augments and the cogging torque vary when the skew angle increases.

Several techniques are used to introduce and place the PMs in the machine for hybrid excitation [11-15], however, the PMs placed between the claws destroy the excitation leakage flux in the rotor and, thus, improve the main flux for all speeds [1, 3, 4].

In this article, we examine how the PMs placed between the rotor claws affect the performance of the permanent magnet claw pole machine (PM-CPM) (Fig. 1) by taking into account the appropriate magnetization orientation and the PM's geometrical dimensions. An alternating arrangement of PMs between the claws of the rotor (Fig. 2) is required to have a possible sinusoidal waveform of the EMF. The magnetization of the PMs is chosen by carrying out a nonlinear 3D electromagnetic simulation of PM-CPM with consideration of the tangential and radial directions of magnetization.

Finally, in order to improve its power density, torque, and ripple torque, the impacts of PMs dimensions such as length and thickness on PM-CPM output torque are studied.

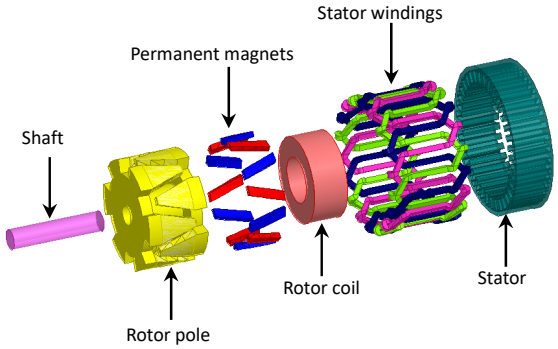

Fig. 1. Exploded view of the study machine

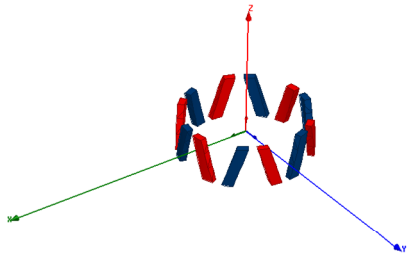

Fig. 2. PMs placement in the rotor and its arrangements

Electromagnetic model of PM-CPM. The claw pole rotor has an asymmetric structure relative to the length of the machine and produces 3D flux distributions. The model must take into account the components of the radial, tangential and axial field, the study therefore consists of a 3D model. PM-CPM analysis can take into account periodicity conditions to enable 3D simulation of a single pole pair. This pole pair structure is complex due to the shape of its two claws and its hybrid excitation. Thus, for electromagnetic design and analysis, a transient nonlinear 3D FEM model is used.

The mathematical model of the machine with hybrid excitation is described in reference *d*-*q*. The *d*-axis flux φ_d and the *q*-axis flux φ_q equations can be written as:

$$\varphi_d = L_d \cdot i_d + \varphi_r ; \quad (1)$$

$$\varphi_q = L_q \cdot i_q , \quad (2)$$

where i_d, i_q are the *d*-axis and *q*-axis stator current components; L_d, L_q are the *d*-axis and *q*-axis inductance respectively.

The rotor flux linkage φ_r is given as:

$$\varphi_r = L_{df} \cdot i_r + \varphi_{PM} , \quad (3)$$

where i_r is the rotor excitation coil current; φ_{PM} is the flux due to the PMs; L_{df} is the *d*-axis mutual inductance between the field winding and the armature winding.

The voltage equation of *d*-axis voltage component V_d and *q*-axis voltage component V_q are expressed as:

$$V_d = R_a \cdot i_d + \frac{\mathrm{d}\varphi_d}{\mathrm{d}t} - \omega \cdot \varphi_q ; \quad (4)$$

$$V_q = R_a \cdot i_q + \frac{\mathrm{d}\varphi_q}{\mathrm{d}t} - \omega \cdot \varphi_d , \quad (5)$$

where R_a is the stator winding phase resistance; ω is the angular velocity.

The torque T_e is given as:

$$T_e = \frac{3}{2} p\left(\varphi_d \cdot i_d + \varphi_q \cdot i_q\right), \quad (6)$$

where p is the number of pole pairs.

The above equation becomes:

$$T_e = \frac{3}{2} \cdot p \cdot \left[\left(L_d - L_q\right) \cdot i_d \cdot i_q + L_{df} \cdot i_r \cdot i_q + \varphi_{PM} \cdot i_q\right]. \quad (7)$$

Therefore, in the case for L_d close to L_q, the torque equation becomes:

$$T_e = \frac{3}{2} \cdot p \cdot i_q \cdot \varphi_r . \quad (8)$$

Equation (8) shows that the rotor flux is mainly responsible to create the electromagnetic torque. In this study, the parameters of the claw pole model used are shown in Table 1.

Table 1

The parameters of the machine

Rotor excitation current I_{ext}	4.5 A
Rotor coil number of conductor	400
Stator number conductor	12
Stator core length	32.5 mm
Stator number slots	36
External stator diameter	125.1 mm
Air gap length	0.8 mm
Rotor core diameter	93 mm
Number of poles	12
Rotor core length	52.4 mm

The PM's dimensions introduced between claws are shown in Table 2.

Table 2

PMs dimensions

Magnet length *l*	28.94 mm
Magnet width *d*	7.68 mm
Magnet thickness *th*	4.6 mm

Magnetization effect of PMs on PM-CPM. PMs magnetization orientation has an effect on PM-CPM performance at high or low speeds. However, different magnetization directions of PM and arrangements can generate different magnetic field distributions in the system as well as different motor performances [16]. These directly influence the quality of the air gap flux

density distribution and affect the FEM induced, the producing torque, and the ripple torque [17, 18].

Furthermore, in electric motors with PMs, the waveform of the back EMF depends on the excitation and arrangement of the PMs and windings, the structure of the motor, and the pole/slot combinations. Thus, the designers want to get a purely sinusoidal or trapezoidal back-EMF waveform based on motor types and control [16]. The model proposed in this study can take into account two different directions of magnetization of the PMs [19], the application contents tangential magnetization and radial magnetization (Fig. 3).

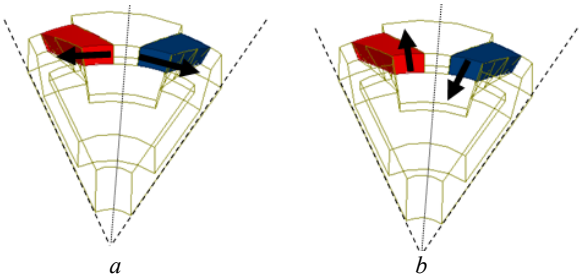

Fig. 3. The orientation of PMs placed between the claws of a pole pair of the machine: *a* – tangential; *b* – radial

Electromagnetic field computation at 3000 rpm is carried out with the FEM. In order to analyze the effect of the magnetization orientation on the performance of the PM-CPM and to visualize only the impact of the excitation of the PMs, we consider the excitations of the rotor coils and those of the stator as zero. The PM-CPM magnets are oriented as shown in Fig. 3.

Figure 4 shows the magnetic flux distribution; we observe the difference repartitions of flux density between the tangential and radial magnetization. Furthermore, it can be seen that in the case of tangential magnetization the lines of flux pass directly into the adjacent claw and are channeled more into the magnetic circuit, which gives less leakage flux (Fig. 4,*a*). Whereas for the case of radial magnetization, the lines of flux pass in the vacuum existing between the claw and the rotor coil (Fig. 4,*b*), which does not help the principal flux and creates more leakage flux, and there will be a reduction in main flux, so the impact of radial magnetization is not significant.

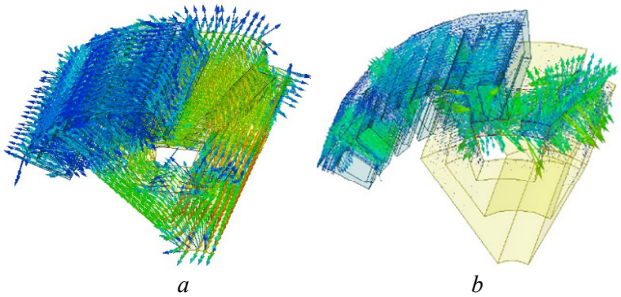

Fig. 4. Magnetic field distribution:
a – tangential magnetization; *b* – radial magnetization

EMF considering only the magnetic excitation is shown in Fig. 5, the flux distributions in the tangential magnetization give induced three-phase voltage waveforms close to the sinusoid compared to that given by the radial magnetization.

One of the particular problems of electric machines with PMs is the shape of the cogging torque resulting from the interaction of the PMs and the teeth of the stator without even the stator winding being excited [20]. Also, a strong cogging torque can cause acoustic vibrations and noise.

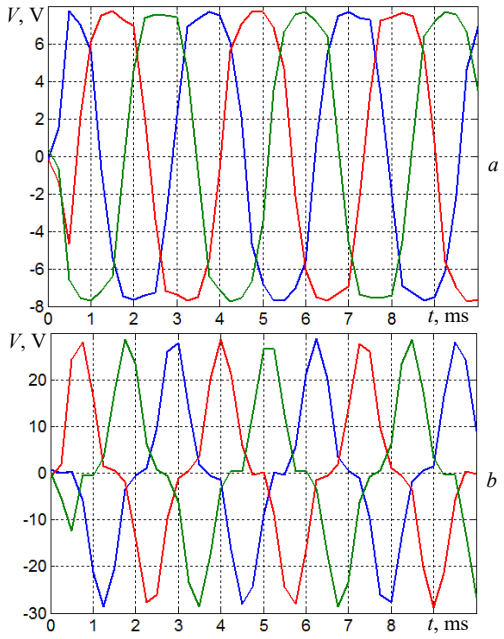

Fig. 5. Induced voltage for no-load and I_{ext} = 0:
a – tangential magnetization; *b* – radial magnetization

Figure 6 shows a comparison of the cogging torque between the two directions of magnetization in the case where the rotor excitation current is zero. We can see that the tangential magnetization gives a low cogging torque compared to that given by the radial magnetization. Then the tangential direction is strongly solicited.

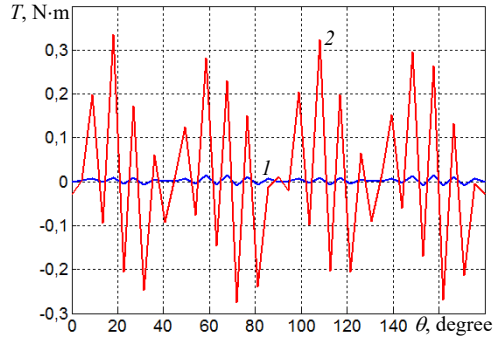

Fig. 6. Comparison cogging torque vs. rotational angle θ:
1 – tangential magnetization; *2* – radial magnetization

Hybrid excitation CPM performance. The rotor coil is preserved in case the regulator needs to change the battery voltage. For a hybrid excitation with a value I_{ext} = 4.5 A of the excitation rotor current and with PMs excitation, the calculation of the induced no-load voltage is illustrated in Fig. 7. The rates correspond to the 2 cases of magnetization tangential and radial magnetization. We can see that the RMS value of induced voltage in the case of tangential magnetization which is 32.3 V is greater than that in the case of radial magnetization which is 22.8 V. This comes down to the fact that in the case of the tangential direction the flux created by the PM is added to the flux created by the rotor coil and follows the same path. In addition, the use of inter-claw PMs with tangential magnetization makes it possible to reduce the leakage flux between claws.

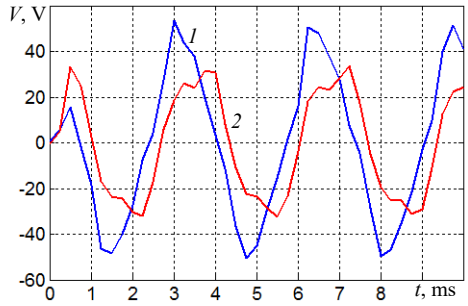

Fig. 7. Induced voltage of one phase comparison for I_{ext} = 4.5 A: *1* – tangential magnetization; *2* – radial magnetization

To better show the positive effect of tangential magnetization, Fig. 8 illustrates the induced voltage in the case of the presence of the PM with tangential orientation and in the case of the absence of the PM. We can see that the maximum value of the voltage increases almost twice.

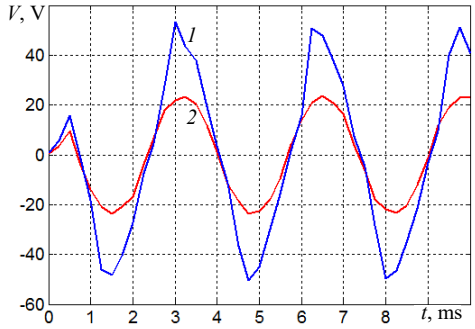

Fig. 8. Induced voltage comparison for I_{ext} = 4.5 A: *1* – with PMs tangential magnetization; *2* – without PMs

For load operation, the three-phase stator windings are fed by three-phase AC currents, the simulations with PM tangential magnetization and without PM of torque vs. rotor position at a nominal point such that stator current RMS value is 176.7 A and excitation current rotor is 4.5 A are given in Fig. 9. The structure without PMs gives an average torque of 21.2 N·m, after the introduction of PMs placed in inter-claws means that the torque increases because of the magnetic strength, and its average value is around 24.8 N·m. The result shows that the rotor design with PMs generates about 17 % more torque than the rotor design without PMs. We can see also that there are a lot of ripples, the ratio between the torque and its ripples is almost 16 % and 20 % for PMs rotor design and without PMs rotor design respectively.

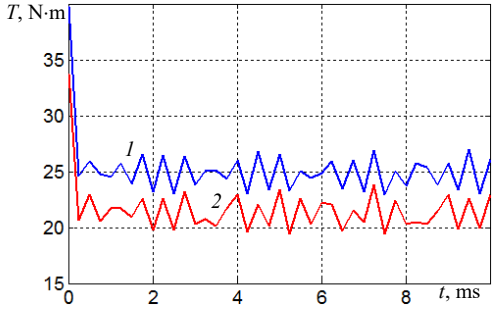

Fig. 9. Torque for I_{ext} = 4.5 A: *1* – with PM tangential magnetization; *2* – without PM

The torque as a function of the different values of the rotor current is presented in Fig. 10. We note the average torque value of 13.18 N·m at zero current excitation and we can be seen that the average torque increases linearly with the increase in excitation current due to the unsaturated claw rotor core. This variation becomes non-linear from 7 A of the excitation current due to rotor claws saturation. The electromagnetic torque depends mainly on the rotor flux, which verifies (8).

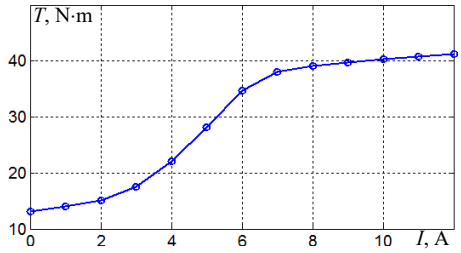

Fig. 10. Average torque vs. rotor current

To highlight the operation under load in steady state, the load angle is used as the parameter in this analysis of PM-CPM [21]. We assume that the instantaneous values of phase current and the load angle are known to investigate the electromagnetic torques.

The calculated values of the average torque with respect to load charge are shown in Fig. 11. In this case, we used a rotor excitation current I_{ext} = 7 A, in order to reach the magnetic saturation state of the machine. We can see the maximum value of 37.5 N·m of the electromagnetic torque corresponding to a load angle $\theta = 90°$.

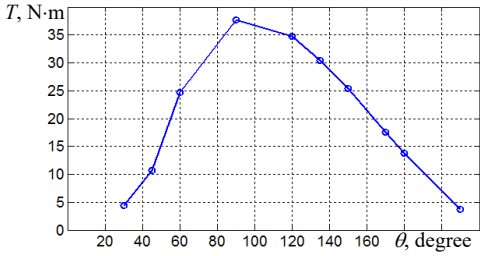

Fig. 11. Average torque vs load torque with for I_{ext} = 7 A

Parametric studies. In this study, the PMs placed between claws are applied with tangential magnetization to investigate the torque characteristics such as torque and ripple torque. The three-phase stator windings are fed by three-phase AC currents. As the PMs placed on the rotating part of the PM-CPM are responsible for the flux field, then a consideration of the dimensions of the PMs is taken into account. In particular, it takes into account the geometric length and the thickness of the PM (Fig. 12).

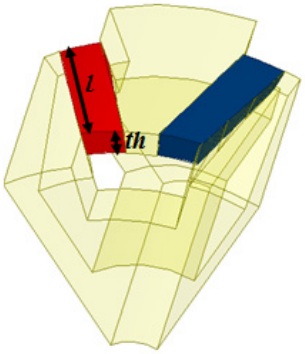

Fig. 12. PM dimensions variation

Varying magnet thickness. In this case, we vary the dimension of the magnet thickness *th* from 1.5 mm to 4.6 mm, when magnet length *l* keeps constant 30 mm.

Considering an optimal charging regime and for non-linear study state with rotor excitation current I_{ext} = 7 A, we notice that the torque increases with the increase of the PM thickness (Fig. 13).

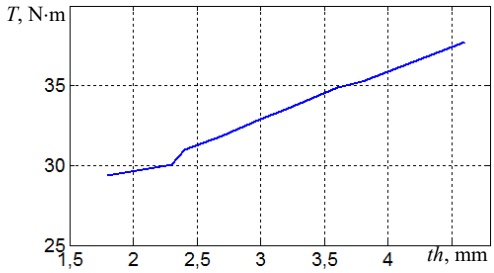

Fig. 13. Average torque vs. PM thickness with l = 30 mm

The ripple torque T_{ripp} can be defined as the rapport of the difference between the maximum torque and his minimum and the average value of torque [22], it is expressed as:

$$T_{ripp} = \frac{\max(T_e) - \min(T_e)}{\text{avg}(T_e)}. \quad (9)$$

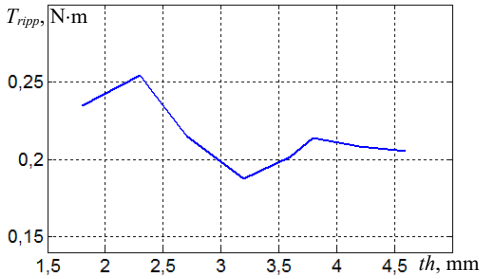

Fig. 14. Ripple torque vs. PM thickness

Varying magnet length *l*. For the same optimal conditions, we change l from 14 mm to 30 mm when the PM thickness th keeps constant 4.6 mm. We can see that when PM length increases the torque also increases (Fig. 15, 16).

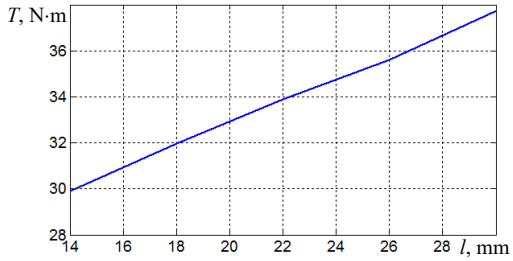

Fig. 15. Average torque vs. PM length with th = 4.6 mm

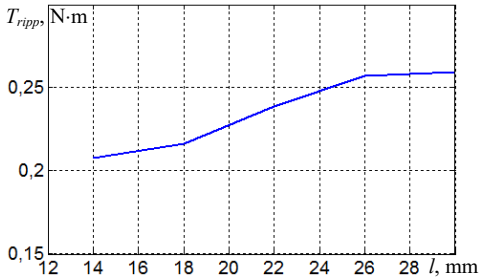

Fig. 16. Ripple torque vs. PM length

According to Fig. 13 – 16, we can see that the average torque increases with the increase in the size of the PMs. However, the impact on the torque ripples is not consistent; in fact, the torque ripples are minimal when the length of the PMs l is between 14 mm and 18 mm. Also, these ripples are minimal when the thickness th is between 2.9 mm and 3.6 mm. Then the torque ripples have a non-linear variation depending on the dimensions of the PMs.

Conclusions. In this paper, our first intention was to investigate the magnetization direction of PMs introduced between rotor claws. Two different PMs orientations were applied and presented different flux distributions, which in turn several motor performances.

As a result, the tangential magnetization direction shows the best performances of the permanent magnet claw pole machine (PM-CPM) such as a sinusoidal induced voltage and a best cogging torque. Furthermore, under optimal loading conditions, the CP-CPM with PMs tangential magnetization gives a higher average torque and a lower ripple torque compared to that given by the structure without magnets.

Finally, to know the impact of the size of the PMs of the CP-CPM on the torque characteristics, a parametric analysis of the variations in length and thickness of the PM showed evidence of an increase in magnetic force and torque. However, the torque ripples have a non-linear variation depending on the study parameters.

Conflict of interest. The authors declare that they have no conflicts of interest.

REFERENCES

1. Boldea I. Automotive Claw-Pole-Rotor Generator Systems. *Variable Speed Generators, Second Edition*, CRC Press, 2015, pp. 195-244 doi: https://doi.org/10.1201/b19293-7.

2. Ibrar A., Ahmad S., Safdar A., Haroon N. Efficiency enhancement strategy implementation in hybrid electric vehicles using sliding mode control. *Electrical Engineering & Electromechanics*, 2023, no. 1, pp. 10-19. doi: https://doi.org/10.20998/2074-272X.2023.1.02.

3. Bruyere A., Semail E., Bouscayrol A., Locment F., Dubus J.M., Mipo J.C. Modeling and control of a seven-phase claw-pole integrated starter alternator for micro-hybrid automotive applications. *2008 IEEE Vehicle Power and Propulsion Conference*, 2008, pp. 1-6. doi: https://doi.org/10.1109/VPPC.2008.4677668.

4. Li Y., Yu Z., Meng H., Wang J., Jing Y. Design and Optimization of Hybrid-Excited Claw-Pole Machine for Vehicle. *IEEE Transactions on Applied Superconductivity*, 2021, vol. 31, no. 8, pp. 1-4. doi: https://doi.org/10.1109/TASC.2021.3094433.

5. Upadhayay P., Kedous-Lebouc A., Garbuio L., Mipo J.-C., Dubus J.-M. Design & comparison of a conventional and permanent magnet based claw-pole machine for automotive application. *2017 15th International Conference on Electrical Machines, Drives and Power Systems (ELMA)*, 2017, pp. 1-5. doi: https://doi.org/10.1109/ELMA.2017.7955390.

6. Bachev I., Lazarov V., Zarkov Z. Analysis of the Influence of NdFeB Permanent Magnet's Type and Volume on the Characteristics of a PM Claw-pole Alternator. *2021 17th Conference on Electrical Machines, Drives and Power Systems (ELMA)*, 2021, pp. 1-6. doi: https://doi.org/10.1109/ELMA52514.2021.9502990.

7. Zhang Z., Liu H., Song T. Optimization Design and Performance Analysis of a PM Brushless Rotor Claw Pole Motor with FEM. *Machines*, 2016, vol. 4, no. 3, art. no. 15. doi: https://doi.org/10.3390/machines4030015.

8. Zhao X., Niu S., Ching T.W. Design and Analysis of a New Brushless Electrically Excited Claw-Pole Generator for Hybrid Electric Vehicle. *IEEE Transactions on Magnetics*, 2018, vol. 54, no. 11, pp. 1-5. doi: https://doi.org/10.1109/TMAG.2018.2823743.

9. Popa G.N., Maria Dinis C., Baciu I., Deaconu S.I. Automotive PM Surface Alternator, Analyse with Experiments. *2021 International Conference on Applied and Theoretical*

Electricity (ICATE), 2021, pp. 1-6. doi: https://doi.org/10.1109/ICATE49685.2021.9465009.
10. Zhao J., Hu C., Zhao Z., Tang M., Tang X. Suitable claw shape design for improving the magnetic properties of forged claw pole parts in generator. *IET Electric Power Applications*, 2021, vol. 15, no. 10, pp. 1331-1342. doi: https://doi.org/10.1049/elp2.12102.
11. Wardach M. Hybrid excited claw pole generator with skewed and non-skewed permanent magnets. *Open Physics*, 2017, vol. 15, no. 1, pp. 902-906. doi: https://doi.org/10.1515/phys-2017-0108.
12. Tong C., Zheng P., Wu Q., Bai J., Zhao Q. A Brushless Claw-Pole Double-Rotor Machine for Power-Split Hybrid Electric Vehicles. *IEEE Transactions on Industrial Electronics*, 2014, vol. 61, no. 8, pp. 4295-4305. doi: https://doi.org/10.1109/TIE.2013.2281169.
13. Geng H., Zhang X., Zhang Y., Hu W., Lei Y., Xu X., Wang A., Wang S., Shi L. Development of Brushless Claw Pole Electrical Excitation and Combined Permanent Magnet Hybrid Excitation Generator for Vehicles. *Energies*, 2020, vol. 13, no. 18, art. no. 4723. doi: https://doi.org/10.3390/en13184723.
14. Cao Y., Zhu S., Yu J., Liu C. Optimization Design and Performance Evaluation of a Hybrid Excitation Claw Pole Machine. *Processes*, 2022, vol. 10, no. 3, art. no. 541. doi: https://doi.org/10.3390/pr10030541.
15. Fujikura S., Hidaka Y. A Novel Rotor Structure of Claw-pole Motor Designed by Magnetomotive Force-based Simulation Method. *IEEJ Journal of Industry Applications*, 2020, vol. 9, no. 6, pp. 685-690. doi: https://doi.org/10.1541/ieejjia.20002397.
16. Bouakacha R., Ouili M., Allag H., Mehasni R., Chebout M., Bouchekara H.R.A. Measurement and three-dimensional calculation of induced electromotive force in permanent magnets heater cylinders. *Metrology and Measurement Systems*, 2022, vol. 29, no. 2, pp. 315-331. doi: https://doi.org/10.24425/mms.2022.140029.
17. Phyu H.N., Chao B. Effect of magnetization on high-speed permanent magnet synchronous motor design. *2012 15th International Conference on Electrical Machines and Systems (ICEMS)*, Sapporo, Japan, 2012, pp. 1-6.
18. Krishnan R. *Permanent Magnet Synchronous and Brushless DC Motor drives*. CRC Press, Taylor & Francis Group, 2017. 611 p. doi: https://doi.org/10.1201/9781420014235.
19. Boutora Y., Takorabet N., Ibtiouen R. Analytical model on real geometries of magnet bars of surface permanent magnet slotless machine. *Progress In Electromagnetics Research B*, 2016, vol. 66, pp. 31-47. doi: https://doi.org/10.2528/PIERB15121503.
20. Panchal T.H., Patel A.N., Patel R.M. Reduction of cogging torque of radial flux permanent magnet brushless DC motor by magnet shifting technique. *Electrical Engineering & Electromechanics*, 2022, no. 3, pp. 15-20. doi: https://doi.org/10.20998/2074-272X.2022.3.03.
21. Kurihara K., Wakui G., Kubota T. Steady-state performance analysis of permanent magnet synchronous motors including space harmonics. *IEEE Transactions on Magnetics*, 1994, vol. 30, no. 3, pp. 1306-1315. doi: https://doi.org/10.1109/20.297769.
22. Cao Y., Zhu S., Yu J., Liu C. Optimization Design and Performance Evaluation of a Hybrid Excitation Claw Pole Machine. *Processes*, 2022, vol. 10, no. 3, art. no. 541. doi: https://doi.org/10.3390/pr10030541.

Received 17.01.2024
Accepted 27.03.2024
Published 20.06.2024

A. Kimouche[1], *Assistant Lecturer,*
M.R. Mekideche[1], *Professor,*
M. Chebout[2], *Associate Professor,*
H. Allag[1], *Professor,*
[1] L2EI Laboratory, Department of Electrical Engineering, Jijel University, Algeria,
e-mail: abdelghani.kimouche@univ-jijel.dz (Corresponding Author); mohamed.mekideche@univ-jijel.dz; allag.hicham@univ-jijel.dz
[2] L2ADI Laboratory, Department of Electrical Engineering, Djelfa University, Algeria,
e-mail: m.chebout@univ-djelfa.dz

How to cite this article:
Kimouche A., Mekideche M.R., Chebout M., Allag H. Influence of permanent magnet parameters on the performances of claw pole machines used in hybrid vehicles. *Electrical Engineering & Electromechanics*, 2024, no. 4, pp. 3-8. doi: https://doi.org/10.20998/2074-272X.2024.4.01

UDC 621.313.39 https://doi.org/10.20998/2074-272X.2024.4.02

M.I. Kotsur

Development of methods for adapting the parameters of spatial end winding sections in 2D circuit-field models of induction-synchronous electric machines

Introduction. *Recently, the theory of a special class of cascade slow-speed non-contact induction-synchronous electrical machines (ISEM) has been developed. This allowed to obtain a combination of positive properties from conventional induction and synchronous electric machines.* ***Problem.*** *The lack of circuit and field models of ISEM imposes restrictions on further research of electromagnetic, mechanical and energy processes, in transient and quasi-steady modes of its operation.* ***Goal.*** *Development of 3D and adapted 2D circuit-field models of ISEM, decomposition methods, and dynamic synthesis with adaptation of electromagnetic parameter coupling conditions at the boundaries of calculated subdomains of ISEM.* ***Methodology.*** *Spatial elements of ISEM design are represented by separate spatial calculation subareas. The conditions of compliance with electromagnetic processes, which are formed by a complete calculation area and separate spatial calculation subareas of ISEM, are accepted. The influence of end effects and the parameters of the frontal parts of ISEM windings are determined by the inequality of the magnetic field energy of separate calculation subareas. These parameters, including end effects, are displayed as circuit elements in the 2D circuit-field model.* ***Results.*** *The obtained combination of 3D area decomposition methods and dynamic synthesis with adaptation of electromagnetic parameters coupling conditions at the boundaries of its calculated ISEM's subdomains. The proposed technique for determining the resistance and inductive resistances of the frontal parts of the ISEM windings, taking into account edge effects. The accuracy and effectiveness of the proposed methods is confirmed by the results of an experimental study.* ***Originality.*** *An adapted dynamic 2D circuit-field model of transient processes of ISEM has been developed, which allows taking into account parameters of the frontal parts of its windings.* ***Practical value.*** *The proposed methods can be used for various types of electrical machines.* References 27, tables 3, figures 12.

Key words: **electromagnetic field, end effects, methods of decomposition and dynamic synthesis, circuit-field modeling, electric machine.**

Вступ. *За останній час набули розвитку теорія спеціального класу каскадних тихохідних безконтактних асинхронно-синхронних електричних машин (АСЕМ) та отримана принципова нова її конструкція, за допомогою якої одержано поєднання позитивних властивостей від звичайних асинхронних та синхронних електричних машин.* ***Проблема.*** *Відсутність колових та польових моделей АСЕМ накладає обмеження щодо подальшого дослідження електромагнітних, механічних та енергетичних процесів, в перехідних та квазіусталеному режимах її роботи.* ***Мета.*** *Розробка 3D та адаптованої 2D коло-польових моделей АСЕМ, методів декомпозиції і динамічного синтезу з адаптацією умов сполучення електромагнітних параметрів на границях розрахованих підобластей АСЕМ.* ***Методологія.*** *Просторові елементи конструкції АСЕМ представляються просторовими окремими розрахунковими підобластями. Для кожній із цих підобластей ставиться у відповідність протікання електромагнітних процесів, які утворені цілісною розрахунковою областю. За нев'язкою енергії магнітного поля окремих підобластей з цілісною розрахунковою зоною визначаються дія крайових ефектів в торцевих зонах та параметри лобових частин обмоток АСЕМ. Ці параметри з врахуванням крайових ефектів відображаються як елементи кола для 2D коло-польової моделі АСЕМ.* ***Результати.*** *Отримана комбінація методів декомпозиції 3D області АСЕМ і динамічного синтезу з адаптацією умов сполучення електромагнітних параметрів на границях його розрахованих підобластей, яка дозволяє забезпечити чисельну реалізацію 3D коло-польового моделювання електромагнітних полів в окремих електричних та магнітних контурах складної просторової конструкції АСЕМ, а також визначити вплив крайових ефектів в торцевих зонах лобових частин АСЕМ за нев'язкою енергії магнітного поля. Запропонована методика щодо визначення активних та індуктивних опорів лобових частин обмоток АСЕМ з врахуванням дії крайових ефектів. Точність та ефективність запропонованих методів підтверджується результатами експериментального дослідження.* ***Наукова новизна.*** *Розроблена адаптована динамічна 2D коло-польова модель нестаціонарних взаємопов'язаних електромагнітних та електромеханічних процесів АСЕМ, яка дозволяє врахувати в перехідних режимах роботи параметри лобових частин його обмоток через її схемну реалізацію, нелінійність магнітних та електрофізичних властивостей активних матеріалів, поверхневі і крайові ефекти торцевих зон його активної частини.* ***Практична цінність.*** *Запропоновані методи можуть бути використані для різних типів електричних машин.* Бібл. 27, табл. 3, рис. 12.

Ключові слова: **електромагнітне поле, крайові ефекти, методи декомпозиції та динамічного синтезу, коло-польове моделювання, електрична машина.**

Introduction. Further improvement of designs and development of the theory of electric machines (EM) is directly related to the search for new technical solutions and technologies. This will enable the creation of devices with improved technical characteristics and high energy efficiency indicators of regulated electric drives, autonomous power supply systems for a number of consumers in industry, energy, agriculture, and special purpose devices.

Recently, the theory of a special class of cascade low-speed contactless induction-synchronous electric machines (ISEM) has been developed and a fundamentally new and improved design of it has been obtained [1]. This class of EM is a combination of two EMs, namely an induction motor (IM) and an inverted synchronous generator (SG) in a single magnetic core [2]. Here, the stator winding of the first EM is a three-phase $2p_1$-pole winding, and the stator winding of the second EM is a single-phase $2p_2$-pole excitation winding. The three-phase $2p_1$ winding and the single-phase $2p_2$ winding are electrically connected to each other and form a single conductive system on the stator (armature) side of the ISEM. The rotor combined winding is short-circuited with the number of mutually independent phase coils $n_2=p_1+p_2$ [3]. For this class of EM, various configurations of the combined stator winding with different variants of the ratio of the number of pairs of poles $2p_1/2p_2$ have been developed in [4], which makes it possible to obtain different values of the cascade synchronous speed of ISEM from 125 to 1000 rpm.

© M.I. Kotsur

The latest improvement in the ISEM design puts this class of EM in terms of ease of manufacture and weight and size indicators in full compliance with classic induction EMs with a short-circuited rotor, with a control channel from the side of the fixed part of the ISEM armature. The simplicity of the design, the availability of control only from the side of the armature, the combination of IM and SG properties make this class of low-speed EM promising for further development. However, at present, for this class of EM, there is still no mathematical description and relevant research on electromagnetic and mechanical processes in the transient and quasi-steady modes of its operation, the control properties and characteristics of ISEM have not been determined. Therefore, in addition to conducting research on a physical sample of ISEM, there is a need to develop a mathematical model of ISEM, which will allow taking into account the design features and schematic implementation of the armature and rotor windings, as well as the nonlinearity of the magnetic and electrophysical properties of active materials, the skin and edge effects of the end zones of its active part, to obtain high accuracy and efficiency of the numerical implementation of electromagnetic parameters with a moderate use of computing resources, time consumption and stability of the computation process, with the reproduction of electromagnetic and mechanical processes as close as possible to the results of experimental research.

Analysis of research and publications. Modern methods of EM research are associated with the use of stationary and transient mathematical models of the transformation of electric, magnetic and mechanical energies [5]. Existing mathematical models of EM are divided into circuit and field models.

Circuit models are based on the theory of circuits and are based on the EM substitution circuits utilization. The interdependence between electric, magnetic, and design parameters of the EM is carried out between the inductive and active parameters of the EM substitution circuits [6]. Such models are described either by a system of algebraic equations or by a system of nonlinear differential equations of the first order. There are methods for designing and calculating the parameters of EM substitution circuits, which are based on empirical calculations and calculations based on catalog or experimental data [7]. In [8], the author states that in order to obtain a satisfactory accuracy of the numerical calculation of the parameters, the substitution circuits must be refined using field simulation. In [9], the methods of mathematical, structural and physical modeling in MATLAB of a DC motor with independent excitation and an induction motor with a short-circuited rotor were analyzed. The simulation results were compared with real experimental data. It was established that the disadvantage of this modeling method is the presence of a high calculation error, which is associated with the impossibility of fully taking into account all the features of the EM configuration, the nonlinearity of the electrophysical and magnetic properties of active materials.

The development of computer technology and specialized software complexes, such as ANSYS, COMSOL Multiphysics, OpenFEM, Impact, SALOME, Elmer, etc., has expanded the possibilities of practical use of 3D and 2D field modeling, which is based on the solution of a system of partial differential equations by the Finite Element Method [10]. In contrast to 2D field modeling, the application of 3D field modeling of electromagnetic processes can ensure the fulfillment of requirements for the accuracy of numerical calculations of electromagnetic parameters. For example, in [11] during the three-dimensional analysis of the magnetic field of a special spherical motor with permanent magnet with double stator, in [12] of a two-phase induction motor, in [13] of electromagnetic processes in the end zones of the rotor of a turbogenerator in its asymmetric modes of operation, the authors note an increase in the accuracy of the calculation in comparison with two-dimensional field modeling, which is confirmed by the results of an experimental study. However, depending on the problem to be solved, the authors use an assumption about the absence of frontal parts of the windings of their geometric EM models to reduce in the dimensionality of the problem itself. In [14], the analysis of the electromagnetic field in IM with short-circuited rotor is considered in the frequency and step-by-step time formulation of the problem for various 2D and 3D models of the rotor core destruction process and, at the end of this process, the core damage. The authors note the difficulty in implementing the 3D field modeling, reduce the convergence of numerical calculations at the boundary of two media with different magnetic and electrophysical properties, especially for complex nonlinear structural elements, significantly increase the calculation time and RAM requirements compared to 2D field modeling. Therefore, authors are proposed cases when the option of using a 2D model instead of a 3D model is accepted. In [15], the authors conducted an analysis of the distribution of the electromagnetic field along the EM, taking into account the complete design of the EM, that is, taking into account the frontal parts of its windings. It was established that in the end zones of the EM, the magnetic field energy increases in comparison with the value of the magnetic field energy in the active part, a comparative assessment of the calculation accuracy was carried out, depending on the choice of the degree of the Lagrange shape function when constructing the mesh of finite elements, the regularities of the increase in the calculation time were established, as well as RAM requirements. In [16], the authors performed an analysis of the numerical calculations of the EM based on its complete construction, an approach was proposed that would increase the finite elements using Lagrange shape functions of the first order within the boundaries of the calculation subdomains with different physical properties of the medium, which made it possible to increase the convergence of numerical calculations.

In most works related to the application of numerical field analysis, it is not necessary to take into account the frontal parts of the windings in the geometric model, which allows using 2D field modeling with sufficient accuracy. For example, in [17] the authors developed a method that allows, on the basis of a single approach, to calculate the geometric parameters of the frontal parts of the concentric and loop winding of the EM, taking into account their detailed structure and the sizes of all constituent elements, which gives much more accurate

results compared to classical methods of EM design. Also, in [18], a numerical field calculation and analysis of active and reactive resistances of IM windings in the entire range of changes in its slip was performed, with further calculation of its mechanical characteristics. However, taking into account the parameters of the frontal parts of EM windings using the methodology based on empirical equations is sufficient, provided that the system of phase currents is used as the initial conditions, taking into account the geometric direction of their flow. However, for cases when the distribution of currents in the conductive parts of the EM is unknown, especially when studying ISEM, both for 2D and for 3D field models of the EM, it is necessary to add circuit models to take into account the peculiarities of the circuit implementation of the connection of its windings.

In [19], the feasibility of using the circuit-field model of the EM, which is based on the combination of the 2D field model of the slot part of the EM with the circuit model of the stator winding of the EM, taking into account the schematic implementation of the connection of the coil groups of the phases of the stator windings of the EM, which makes it possible to additionally take into account parameters of their frontal parts is proved. As initial conditions, phase voltages are used when powered from a sinusoidal or non-sinusoidal source, which ensures the determination of currents in the process of numerical calculation. At the same time, it is possible to take into account the real-life distortion of the stator winding currents, which occurs even with a sinusoidal supply voltage.

Thus, taking into account the fact that the constant use of complex dynamic 3D circuit-field models, taking into account the schematic implementation of ISEM windings in the study of electromagnetic and mechanical processes in transient and quasi-steady modes of its operation, will lead to significant costs of computing resources, time and stability of the computational process, therefore there is a need to develop methods and approaches that will ensure the conditions of a qualitative transition from spatial to plane-parallel distribution of the electromagnetic field in the active part of ISEM while reducing the time spent on its numerical implementation and maintaining high accuracy of numerical calculation.

The goal of the work is the development of 3D and adapted 2D circuit-field models of ISEM, methods of decomposition and dynamic synthesis with adaptation of the conditions of coupling of electromagnetic parameters at the boundaries of the calculated subdomains of ISEM.

Object of study. Based on the MTF-111-6 crane motor (2.6 kW at duration of operation 100 %), an experimental sample of ISEM with cascade synchronous speed of rotation of the rotor n=500 rpm, U_n=127 V was made. The main dimensions of the experimental sample correspond to the MTF-111-6. The armature core has z_2=36 slots. The combined armature winding is three-phase-single-phase, two-layer with $2p_1$=4 and $2p_2$=8. The rotor core has z_2=30 slots, which are concentrated in 5 slots in a group. The number of slot groups is 6. Between the groups of ordinary slots, a massive toothed zone is formed, the number of which is equal to the number of slot groups. According to this, the groups of slots are placed at an angle of 60°, and the slots in the groups are respectively at an angle γ=6.66° (Fig. 1,*b*). The rotor winding has 6 phase short-circuited independent coils, 3 sections in each coil, which are placed around a massive tooth (Fig. 1,*b*).

3D circuit-field model of ISEM. The calculation 3D geometric model of ISEM accurately and in detail reflects the features of its design structure (Fig. 1), which includes the calculation subdomains of the components of its active part: armature core 1; three-phase-single-phase $2p_1$=4 and $2p_2$=8 armature winding 2; insulation system in the slot zone of the armature core 3; rotor core 4; independent short-circuited rotor winding 5; insulation system in the slot zone of the rotor core 6 (Fig. 1,*b*). The coil sections of the armature winding consist of frontal and slot parts, which are connected geometrically and form 12 coils, 2 coils in each coil group (two coil groups per phase). The coils of the armature and rotor windings have complete geometric symmetry between them. Each coil of the armature winding has input 7 and output 8 (Fig. 1,*a*). The rotor winding consists of 6 independent phase coils A, B, C, D, E, F (Fig. 1,*b*). Each phase coil contains 3 sections – 1, 2, 3 (Fig. 1,*b*), which are connected together in a short circuit.

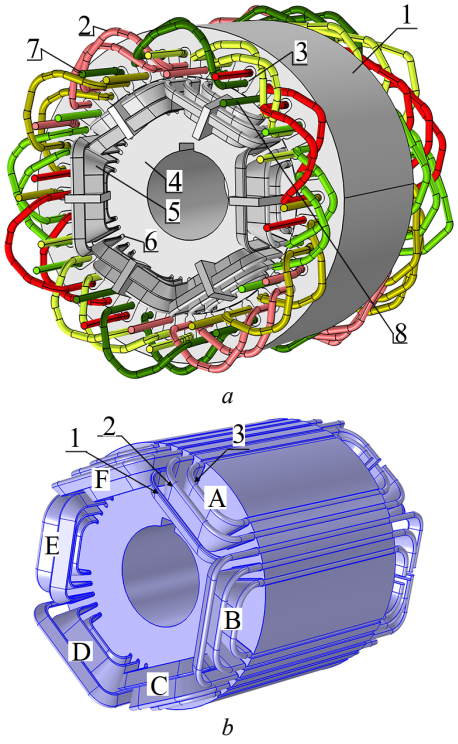

Fig. 1. Complete 3D geometric model of ISEM (*a*); calculation 3D geometric model of ISEM rotor (*b*)

The mathematical description of electromagnetic processes assumes the isotropic nature of the electrophysical and electromagnetic properties of materials, the absence of displacement currents and free charges [20]. In this case, the transient electromagnetic processes in ISEM in the short-circuit mode can be described by a coupled system of nonlinear partial differential equations [21]:

$$\begin{cases} \sigma_j \partial \boldsymbol{A}_j / \partial t + \sigma_j(\theta_j)\nabla V_j + \nabla \times \left[\left(\mu_0 \mu_j(B) \right)^{-1} \nabla \times \boldsymbol{A}_j \right] = \boldsymbol{J}_{ej}; \\ -\nabla \cdot \partial\left(\varepsilon_0 \varepsilon_r \nabla V_j \right) / \partial t - \nabla \cdot \left(\sigma_j(\theta_j) \cdot \nabla V_j - \boldsymbol{J}_{ej} \right) = 0, \end{cases} \quad (1)$$

where $\boldsymbol{A}$ is the magnetic vector potential; V is the electric scalar potential; $\boldsymbol{B}$ is the magnetic flux density; μ, ε_r, $\sigma(\theta)$ ate, respectively, the relative magnetic and dielectric permeability, specific electrical conductivity (for each calculation domain it is specified separately according to the magnetic, electrophysical and dielectric properties of materials); θ is the temperature; ω is the angular frequency; $\boldsymbol{J}_e$ is the density of the external current source; subscripts j correspond to subdomains of the geometric calculation domain. In accordance with [20, 21], the system of equations (1) is supplemented by the Coulomb gauge condition div($\boldsymbol{A}$)=0.

Uniform boundary conditions are set on the outer boundaries of the 3D domain of the generalized ISEM geometric model [21]:

$$\begin{cases} \boldsymbol{A}_j = 0\big|_{\forall j\in(1,6)},\ A_j = \overline{k}\cdot A_y(x,z)\big|_{j=1}, \\ V_j = \varphi_j\big|_{\forall j\in(2,6)}, \\ \boldsymbol{n}_j\cdot\left(\boldsymbol{J}_j\right)=0\big|_{j=1} \end{cases} \tag{2}$$

and coupling conditions for magnetic and electric fields:

$$\begin{cases} \boldsymbol{n}_{i,k}\times\left(\boldsymbol{H}_i-\boldsymbol{H}_k\right)=0\big|_{\forall i,k\in(1,6),i\neq k}, \\ \boldsymbol{H}=\left(\mu_0\mu\right)^{-1}\nabla\times\boldsymbol{A}, \\ \boldsymbol{n}_{i,k}\cdot\left(\boldsymbol{J}_i-\boldsymbol{J}_k\right)=0\big|_{\forall i,k\in(1,6),i\neq k}, \\ \boldsymbol{J}=\sigma(\theta)\cdot\boldsymbol{E},\ \boldsymbol{E}=-\nabla V-\partial\boldsymbol{A}/\partial t, \end{cases} \tag{3}$$

where $\boldsymbol{H}$ is the magnetic field strength; $\boldsymbol{E}$ is the electric field strength.

The design of the two-layer three-phase-single-phase combined winding of the ISEM armature contains 2 coil groups (2 coils in each coil group) per phase. The first and third, second and fourth coils are connected in series. The second and fourth coils are connected in parallel with the first and third coils. The outputs of the coil groups of all phases are connected in two independent «stars» – zero points «0+» and «0–» (Fig. 2). Regarding the inputs of phases A, B, C, to which the alternating voltage is supplied, the combined armature winding of ISEM is a conventional three-phase winding with the number of pole pairs $2p_1$=4. Relative to the zero points «0+» and «0–», to which the constant voltage is supplied, it is single-phase, with the number of pairs of poles $2p_2$=8.

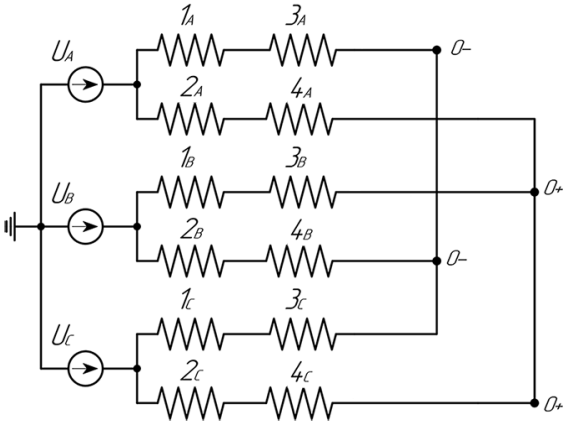

Fig. 2. Electrical diagram of the model implementation of power supply of coil groups of phase windings of the ISEM armature

When studying the processes of electromagnetic energy conversion in ISEM, it is assumed that it is connected to a network with unlimited power and a symmetrical system of phase voltages [21]. Therefore, the initial conditions correspond to the first commutation law [21]:

$$\begin{cases} i_A\big|_{0-}=i_A\big|_{0+}=0; \\ i_B\big|_{0-}=i_B\big|_{0+}=0; \\ i_C\big|_{0-}=i_C\big|_{0+}=0, \\ u_A(t)=\sqrt{2}\cdot U_{fase}\cdot\sin(\omega\cdot t); \\ u_B(t)=\sqrt{2}\cdot U_{fase}\cdot\sin(\omega\cdot t+2\pi/3); \\ u_C(t)=\sqrt{2}\cdot U_{fase}\cdot\sin(\omega\cdot t-2\pi/3). \end{cases} \tag{4}$$

The geometric model of the ISEM armature winding coil (Fig. 1) is implemented in the form of one effective conductor. The number of turns of the ISEM armature winding coils is taken into account according to the equation [21]:

$$\boldsymbol{J}_e=\frac{n\cdot I_{cir}}{S_{cir}}\boldsymbol{e}_{coil}, \tag{5}$$

where n is the number of winding turns; I_{cir} is the phase current; S_{cir} is the cross section of the effective conductor; $\boldsymbol{e}_{coil}$ is the vector variable representing the local density of effective conductors in the coil, length and cross section.

The schematic implementation of the armature winding (Fig. 2) together with the equations of the mathematical model of the electromagnetic field can be performed, for example, with the help of COMSOL Multiphysics using the multiphysics structure when combining the «Rotating Machinery, Magnetic» and «Electrical Circuit» interfaces. The connection and agreement of the parameters of the armature winding, which are elements of both the field model and the elements of the electric circuit, is performed with the help of «External I vs. U» terminals. A schematic implementation for the ISEM rotor winding is not required, since the connection of sections to each other for each of the phase coils of the rotor winding is implemented geometrically.

Decomposition and dynamic synthesis methods for modeling complex spatial elements of the active part of ISEM. The application of 3D field modeling of transient electromagnetic processes in ISEM, taking into account the multi-component spatial structure, as well as the nonlinearity of the electrophysical and magnetic properties of active materials, allows to reproduce with high accuracy and efficiency the peculiarities of the flow of transient electromagnetic processes. However, when taking into account the rotation of the moving part of the active part of the ISEM, that is, the rotor itself, difficulties arise in the numerical implementation of the problem of calculating the 3D transient electromagnetic field, which is associated with an increase in the degree of freedom of the electromechanical system, namely, an increase in the number of independent variables in the general system of equations, which requires significant increase in computing resources. Therefore, it is expedient to switch to the plane-parallel formulation of the ISEM electromagnetic field with the implementation of rotor

rotation. This requires the development of special approaches for 3D modeling of electromagnetic fields, which will allow for the coordination of field and circuit models of ISEM.

The mathematical procedure of decomposition of a complex electrotechnical system of ISEM consists in the representation of the spatial calculation domain by several separate subdomains – calculation zones. Each of these zones should be matched with the flow of electromagnetic processes, which are formed by a complete calculation domain. The purpose of the decomposition of a complex ISEM electrotechnical system is to separate the frontal parts of the armature and rotor windings from the spatial model of the ISEM and display them in the schematic model while preserving the connections of electromagnetic processes between them, which will allow us to obtain grounds for an adaptive transition to plane-parallel circuit-field modeling.

The ISEM spatial calculation domain (Fig. 1) can be divided into 6 separate calculation subdomains (Fig. 3): *a* – core and slot part of the ISEM armature winding (*j*=1), *b* – respectively, left (*j*=2) and right (*j* =3) front parts of the armature winding; *c* – core and slot part of the rotor winding (*j*=4); *d* – respectively, left (*j*=5) and right (*j*=6) front parts of the phase coils of the rotor winding.

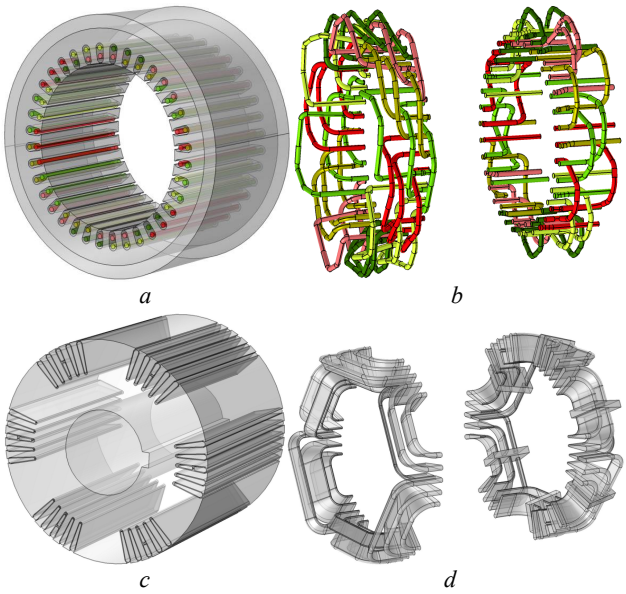

Fig. 3. Decomposition 3D ISEM calculation zones:
the core and slot part of the armature winding (*a*);
left and right front parts of the armature winding (*b*);
core and slot part of the rotor winding (*c*);
left and right front parts of the phase coils of the rotor winding (*d*)

Then, in integral relations, the volume of the area of electromagnetic energy conversion of alternating and direct currents for ISEM can be represented as the sum of the volumes of the above-mentioned six subdomains:

$$\iiint_{V} \mathrm{d}x\mathrm{d}y\mathrm{d}z = \sum_{i=1}^{6} \iiint_{V_i} \mathrm{d}x\mathrm{d}y\mathrm{d}z \,. \tag{6}$$

In this case, electrical losses and magnetic energy in the domain of the active part of the ISEM are defined as the sum of their values for the corresponding subdomains in the form:

$$P_{\Sigma} = \sum_{i=1}^{6} P_i = \sum_{i=1}^{6} \iiint_{V_i} \sigma_{i,j}(\theta)^{-1} \left|\dot{\boldsymbol{J}}_i\right|^2 \mathrm{d}x\mathrm{d}y\mathrm{d}z, \tag{7}$$

$$W_{\Sigma} = \sum_{i=1}^{6} W_i = \sum_{i=1}^{6} \iiint_{V_{i,j}} \mu_i \mu_0 \left(\dot{\boldsymbol{H}}_i, \dot{\boldsymbol{H}}_i\right) \mathrm{d}x\mathrm{d}y\mathrm{d}z. \tag{8}$$

When decomposing the three-dimensional domain of the active part of ISEM in the zones that form it, electromagnetic processes are described by differential equations (1) with conditions (2), (3), but they can be considered separately from each other. At the same time, appropriate conditions must be set at the boundaries of their connection.

For the slot zone of the armature core and the rotor, the plane-parallel field conditions are set:

$$\left\{ n \times \boldsymbol{H} = 0 \right|_{\Omega_{i,i+1}} . \tag{9}$$

At the junction of the surfaces of the frontal and slot parts of the armature and rotor windings, the following conditions are accepted:

$$A_{z,i} = A_{z,i+1}\big|_{\Omega_{i,i+1}} , \tag{10}$$

$$A_{x,i} = A_{y,i} = 0\big|_{\Omega_{i,i+1}} . \tag{11}$$

Also, the condition of equality of electric potentials is assumed at the junction of the surfaces of the frontal and slot parts of the armature winding:

$$\left\{U_i = U_{i+1}\right\}\big|_{\Omega_{i,i+1}} = \mathrm{const}_j , \tag{12}$$

as well as the condition of equality of currents for the sections of the phase short-circuited coils of the rotor winding:

$$\left\{I_{rm} = I_{rm+1}\right\}\big|_{\Omega_{m,m+1}} = \mathrm{const}_n . \tag{13}$$

The currents in the coil groups of the armature winding are determined for the given values of the short-circuit voltage U_{sc}:

$$\Delta\dot{\boldsymbol{U}}_{sc} = \sum_{i} \left\{\Delta\dot{\boldsymbol{U}}_{i,j}\right\}, \tag{14}$$

where $\left\{\Delta\dot{\boldsymbol{U}}_{i,j}\right\}$ is the voltage drop; *i*, *j* are the number of series and parallel branches of the armature winding.

In conjunction conditions (14), const_i values are «free». Therefore, the potential at the outer boundaries of the conjugation of the subdomains of the frontal and slot parts of the armature winding, as well as the values of the currents at the boundaries of the conjugation of the slot and frontal parts of the sections of the phase coils of the rotor winding cannot be specified in advance. They are determined from the solution of the optimization problem.

Therefore, when synthesizing calculation zones in the 3D domain of the contour, the synthesis accuracy criterion and the corresponding objective function are determined by the sum of the squares of residuals of the current amplitudes in the armature and ISEM rotor windings:

$$\min\left\{ M(\boldsymbol{D},\boldsymbol{R}) = \sum_{j} \Delta\dot{\boldsymbol{I}}^2_{\Sigma j} = \sum_{j} \left(\sum_{i} \dot{\boldsymbol{I}}_i - \dot{\boldsymbol{I}}_{sc} \right)^2_j \right\}. \tag{15}$$

In the general case, the objective function $M(\boldsymbol{D},\boldsymbol{R})$ is a function of vectors of independently varied $\boldsymbol{D}$ and

dependent $\boldsymbol{R}$ parameters. The voltage drops on the sections of the armature winding contours are considered as projections of the vector of independently varied parameters $\boldsymbol{D}$. This makes it possible to transform the objective function $M(\boldsymbol{D},\boldsymbol{R})$ into the function $\tilde{M}(\boldsymbol{D})$ and bring the optimality condition (15) to the form:

$$\min \tilde{M}(\boldsymbol{D}) = \sum_j \left(\sum_i \dot{\boldsymbol{I}}_i(\boldsymbol{D}) - \dot{\boldsymbol{I}}_{sc} \right)_j^2 . \qquad (16)$$

To implement task (16), it is advisable to apply the well-proven method of dynamic programming [22] for a similar class of tasks.

When constructing a recurrent system of Bellman equations the vector of optimization parameters with components $\Delta\dot{\boldsymbol{U}}_{i,j}$ should be represented as a sum of initial approximation vectors [22]:

$$\left\{\Delta\dot{\boldsymbol{U}}_{i,j}\right\} = \left\{\Delta\dot{\boldsymbol{U}}_{i,j}\right\}_0 + \left\{\delta\Delta\dot{\boldsymbol{U}}_{i,j}\right\}_1 . \qquad (17)$$

This will allow representing the objective function as:

$$\tilde{M}\left(\left\{\Delta\dot{\boldsymbol{U}}_{i,j}\right\}\right) = \tilde{M}\left(\left\{\Delta\dot{\boldsymbol{U}}_{i,j}\right\}_0 + \left\{\delta\Delta\dot{\boldsymbol{U}}_{i,j}\right\}_1\right) = \\ = \tilde{M}_0 + \Delta\tilde{M}\left(\boldsymbol{D}_0, \boldsymbol{\delta D}_1\right) = \tilde{M}_0 + \Delta\tilde{M}_1. \qquad (18)$$

Let us represent the optimality condition (16) as a system of recurrent Bellman equations [22]:

$$\min \Delta\tilde{M}_\Sigma = \Phi(\boldsymbol{D}_0) = \min_{\boldsymbol{\delta D}_1} \ldots \min_{\boldsymbol{\delta D}_k} \left[\left(\Delta\tilde{M}_1(\boldsymbol{D}_0, \boldsymbol{\delta D}_1) + \ldots \right. \right. \\ \left. \left. \ldots + \Delta\tilde{M}_k(\boldsymbol{D}_{k-1}, \boldsymbol{\delta D}_k) \right) \right] \qquad (19)$$

Relationships (16) and (19) determine the dynamic adaptation of electromagnetic field coupling conditions (9) – (14) between the frontal part of the calculation zone and the active part of the slot of 3D calculation zone of the ISEM armature and rotor. The iterative computation process is implemented by means of dynamic programming [22] with specified accuracy of current amplitude modulus $\varepsilon_I \le 0.1$ % and phases $\varepsilon_\varphi \le 0.5$ %. For direct current, accuracy is specified only in absolute value.

Figures 4, 5 show the results of field modeling of the decomposed calculation zones of the active part of ISEM in the form of the distribution of the z-component of the magnetic vector potential A_z and the magnetic field energy E using the method of dynamic adaptation according to the criterion of current errors. The results of the numerical calculation were compared with the results obtained for a complete calculation zone, both for the ISEM field model (Fig. 1,*a*) and with separate field model of the active part of the ISEM armature [21]. Table 1 shows the errors of calculations by the method of dynamic adaptation of field models during the synthesis of the electromagnetic circuit of the decomposed zones of the active part of ISEM. Here, discrepancy for active losses power is 0.042 – 0.109 % for alternating current, and 0.015 – 0.0184 % for direct current, depending on the calculated subdomain of the structural elements of the active part of the ISEM.

Discrepancy by voltage drop in the frontal and slot parts of the armature winding is 0.74 – 0.98 % (for alternating current) and 0.0211 – 0.091 % (for direct current), respectively.

Based on the results of the numerical calculation, the components of the magnetic field energy of the decomposed zones of the active part of the ISEM armature were determined, and the discrepancy between the total value of the magnetic field energy and the value of the magnetic field energy in the numerical calculation of the integral calculation zone of the active part of the armature was calculated (Table 1). Since the energy of the magnetic field is a dependent parameter during the optimization of individual calculation zones when applying (15), the significant discrepancy in the value of the magnetic field energy for alternating current $\delta E_a|_{AC}$ = 14.841 % and for direct current $\delta E_a|_{DC}$ = 4.587 % is caused by not taken into account the action of edge effects, which leads to magnetization by the frontal parts of the winding in the end zone of the armature core. To take into account the effect of edge effects for numerical calculation problems with separate 3D zones for the optimization equation (15), the magnetic field energy parameter must be assigned to the group of varied parameters $\boldsymbol{D}$. At the same time, the error in the magnetic field energy will be reduced by alternating current to $\delta E_a|_{AC}$ = 0.274 % and by direct current up to $\delta E_a|_{DC}$ = 0.0831 %.

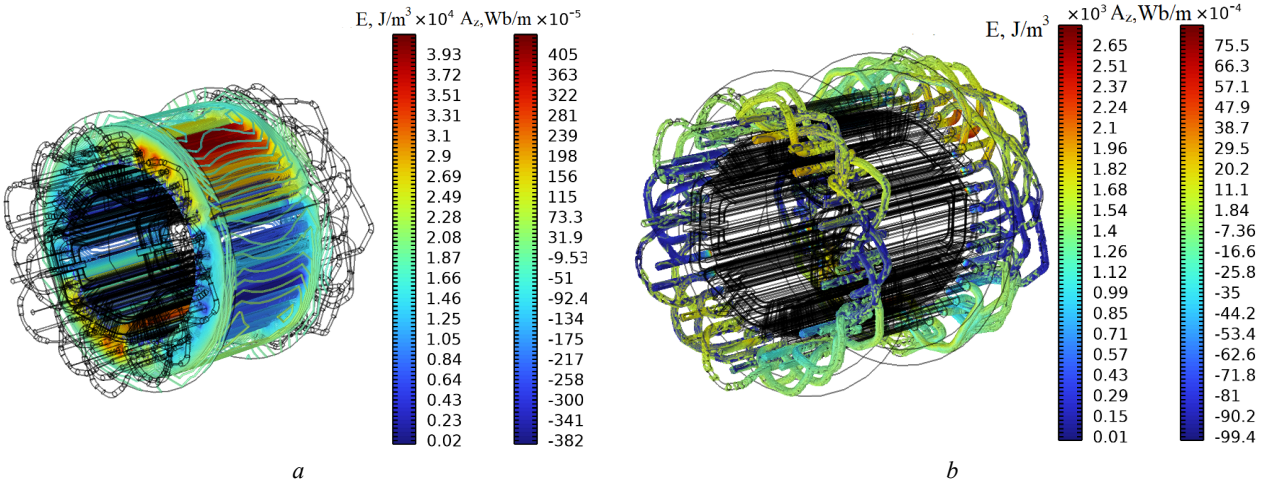

a *b*

Fig. 4. z-component of the magnetic vector potential A_z and the energy of the magnetic field E in the active part of the ISEM armature: *a* – slot zone of the active part of the armature (j = 1); *b* – the frontal zone of the active part of the armature (j = 2,3)

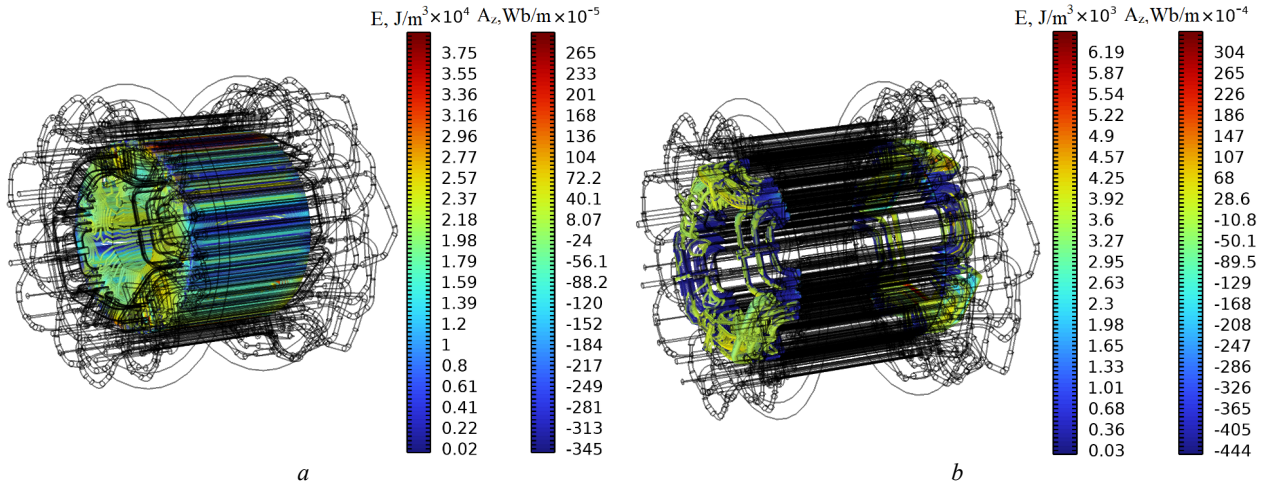

a *b*

Fig. 5. *z*-component of the magnetic potential vector A_z and the magnetic field energy E in the active part of the ISEM rotor: *a* – slot zone of the active part of the rotor (j = 4); *b* – the frontal zone of the active part of the rotor (j = 5,6)

Table 1

Calculation errors by the method of dynamic adaptation of field models in the synthesis of an electromagnetic circuit of decomposed zones of the active part of ISEM

Calculation subdomains (zones)	slot zone of the active part of the armature (j=1)	frontal zone of the active part of the armature (j=2,3)	slot zone of the active part of the rotor (j=4)	frontal zone of the active part of the rotor (j=5,6)
Losses of active power (from alternating / direct currents)	0,042 % / 0,015 %	0,064 % / 0,0168 %	0,096 % / 0,019 %	0,109 % / 0,0184 %
Voltage drop (module / phase)	0,74 % / 0,091 %	0,98 % / 0,0211 %	–	–
DC voltage drop	0,184 %	0,156 %	–	–
Energy of the magnetic field of the active part of the armature	when modeling the active part of the armature (when separating the active part of the rotor) (from AC/DC currents)			
	$\delta E_a\|_{AC/DC}$ = 14,841 % / 4,587 %			
Energy of the magnetic field of the active part of the rotor	when modeling the active part of ISEM (when separating the active part of the rotor) (from AC/DC currents)			
	$\delta E_r\|_{AC/DC}$ = 6,33 % / 1,71 %			

In another case, for the tasks of replacing the spatial elements of the front parts of the armature winding with elements of an electric circuit (in the tasks of adapting 3D to 2D numerical calculations), the effect of edge effects, in relation to magnetization by the front parts, can be taken into account through the addition of mutual inductance between the slot and front zones of the armature winding, which can be determined using the following expression, according to [21]:

$$L_j\Big| = 2 \cdot W_j \Big/ I_j{}^2 . \qquad (20)$$

At the same time, the energy of the magnetic field, which reflects the manifestation of the edge effect, can be defined as:

$$E\big|_{end.a} = E_{res}\big|_a - \left(\sum_{j=1}^{3} E_j \right), \qquad (21)$$

where E_j is the energy of the magnetic field of the j-th calculation subdomain; $E_{res}|_a$ is the energy of the magnetic field when modeling the active part of the armature (when separating the active part of the rotor).

By the same method, it is possible to determine the mutual inductance between the slot and frontal zones of the sections of the phase coils of the rotor winding. At the same time, the energy of the magnetic field, which reflects the effect of magnetization of the frontal zone in the end region of the rotor core, can be defined as:

$$E\big|_{end.r} = E_{res}\big|_{em} - E_{res}\big|_a - \left(\sum_{j=4}^{6} E_j \right), \qquad (22)$$

where $E_{res}|_{em}$ is the energy of the magnetic field when simulating the active part of ISEM.

Thus, the reliability and accuracy of modeling results using methods of decomposition of 3D active part zone of the ISEM and dynamic synthesis of electrical parameters in its circuit can be ensured provided that the distribution of electric potentials on the boundaries of the connection of zones is close to uniform, and the distribution of the magnetic field corresponds to a plane-parallel field. In this case, the sum of active losses and energy of the magnetic field, taking into account edge effects in the area of conjugation of slot and frontal parts in the calculation zones, will correspond with high accuracy to active losses and magnetic energy losses for the 3D domain of the entire active part of ISEM.

Determination of active resistances and inductances of end parts of windings when modeling complex spatial elements of the active part of ISEM. In the case when the speed of rotation of the rotor $n > 0$, the active resistance and total inductance of the rotor winding will depend on the rotor slip s of ISEM. Therefore, for the adaptive transition from 3D to plane-parallel circuit-field modeling, it is necessary to additionally take into account the change in active resistance and inductance of the frontal parts of the sections of the phase coils of the rotor

winding in the form of dependencies $R^{end}{}_r=f(s)$ and $L^{end}{}_r=f(s)$. To do this, for the calculation domain of the frontal parts of the armature windings and the ISEM rotor, we will use the variational formulation of the electromagnetic field equations (1) [23], which allows us to set the equation of rotation of the electromagnetic field in the calculation domain of the frontal part of the rotor winding coils relative to the stationary magnetic field of the calculation domain of the frontal part of the armature winding. In this case, when solving the boundary value problem for the first equation of the system of equations (1), it is necessary to multiply the left and right parts by the trial vector function $\boldsymbol{\psi}$ from the space of trial functions H^{rot} on the boundaries of the inner S_0 and outer S_1 surfaces Ω of the frontal part of the rotor winding (upon fulfillment of the condition $\boldsymbol{n}\times\boldsymbol{\psi}=0$) and must be integrated over the volume of the calculation domain Ω:

$$\begin{aligned}&\iiint_V \boldsymbol{\psi}\cdot\left[\nabla\times\left(\mu_0^{-1}\mu_r^{-1}\nabla\times\boldsymbol{A}\right)\right]\mathrm{d}x\mathrm{d}y\mathrm{d}z+\ldots\\&\ldots+\iiint_V \boldsymbol{\psi}\cdot\left(j\sigma\omega\boldsymbol{A}+\sigma\nabla V\right)\mathrm{d}x\mathrm{d}y\mathrm{d}z=\iiint_V \boldsymbol{\psi}\cdot\boldsymbol{J}_e\mathrm{d}x\mathrm{d}y\mathrm{d}z.\end{aligned}\tag{23}$$

To reduce the order of differentiation in the integrand expression of the first volume integral, it is necessary to use the relation for the *curl* operator

$$\boldsymbol{v}\cdot\nabla\times\boldsymbol{u}-\boldsymbol{u}\cdot\nabla\times\boldsymbol{v}=\nabla\cdot\left(\boldsymbol{u}\times\boldsymbol{v}\right).$$

Let's accept that

$$\boldsymbol{v}=\boldsymbol{\psi},\quad \boldsymbol{u}=\mu\nabla\times\boldsymbol{A},\ \text{and}\ \ \mu=\mu_0^{-1}\mu_r^{-1},$$

then the relation (23) will have the form:

$$\begin{aligned}&\iiint_V \mu\cdot\left(\nabla\times\boldsymbol{A}\right)\left(\nabla\times\boldsymbol{\psi}\right)\mathrm{d}x\mathrm{d}y\mathrm{d}z+\ldots\\&\ldots+\iiint_V \nabla\cdot\left[\left(\mu\nabla\times\boldsymbol{A}\right)\times\boldsymbol{\psi}\right]\mathrm{d}x\mathrm{d}y\mathrm{d}z+\ldots\\&\ldots+\iiint_V \boldsymbol{\psi}\cdot\left(j\sigma\omega\boldsymbol{A}+\sigma\nabla V-\boldsymbol{J}_e\right)\mathrm{d}x\mathrm{d}y\mathrm{d}z=0.\end{aligned}\tag{24}$$

Next, we convert the second volume integral into a surface integral using the Gauss–Ostrogradsky formula [24]:

$$\iiint_V \nabla\cdot\left(\boldsymbol{u}\right)\mathrm{d}x\mathrm{d}y\mathrm{d}z=\iint_S \boldsymbol{u}\cdot\boldsymbol{n}\mathrm{d}S\ ,$$

taking into account that

$$\boldsymbol{u}=\left(\mu\nabla\times\boldsymbol{A}\right)\times\boldsymbol{\psi}\ ,$$

and

$$\left(\boldsymbol{u}\times\boldsymbol{v}\right)\cdot\boldsymbol{w}=-\left(\boldsymbol{w}\times\boldsymbol{v}\right)\cdot\boldsymbol{u}\ .$$

Then equation (24) can be represented as:

$$\begin{aligned}&\iiint_V \mu\cdot\left(\nabla\times\boldsymbol{A}\right)\left(\nabla\times\boldsymbol{\psi}\right)\mathrm{d}x\mathrm{d}y\mathrm{d}z-\iint_S\left(\boldsymbol{n}\times\boldsymbol{\psi}\right)\left(\mu\nabla\times\boldsymbol{A}\right)\mathrm{d}S+\ldots\\&\ldots+\iiint_V \boldsymbol{\psi}\cdot\left(j\sigma\omega\boldsymbol{A}+\sigma\nabla V-\boldsymbol{J}_e\right)\mathrm{d}x\mathrm{d}y\mathrm{d}z=0.\end{aligned}\tag{25}$$

Since only the boundary condition of the first kind, for which $\boldsymbol{n}\times\boldsymbol{\psi}=0$, is set on the surfaces S_0 and S_1, which limit the calculated domain of the frontal parts of the phase coils of the rotor winding Ω, then for equation (25) in its final form it can be represented as:

$$\begin{aligned}&\iiint_V \mu\cdot\left(\nabla\times\boldsymbol{A}\right)\left(\nabla\times\boldsymbol{\psi}\right)\mathrm{d}x\mathrm{d}y\mathrm{d}z+\ldots\\&\ldots+\iiint_V \boldsymbol{\psi}\cdot\left(j\sigma\omega\boldsymbol{A}+\sigma\nabla V-\boldsymbol{J}_e\right)\mathrm{d}x\mathrm{d}y\mathrm{d}z=0.\end{aligned}\tag{26}$$

We multiply the second equation from the system of equations (1) by the function N from the space of trial scalar functions Φ with simultaneous integration over the volume V [24]:

$$-\iiint_V N\cdot\left[\nabla\cdot\left(j\sigma\omega\boldsymbol{A}+\sigma\nabla V-\boldsymbol{J}_e\right)\right]\mathrm{d}x\mathrm{d}y\mathrm{d}z=0\ .\tag{27}$$

To reduce the order of differentiation, we will use the relation for the divergence operator

$$\nabla\cdot\left(f\boldsymbol{u}\right)=f\,\nabla\cdot\boldsymbol{u}+\boldsymbol{u}\nabla f\ .$$

If we make the assumption that

$$f=N\ ,\quad \boldsymbol{u}=\boldsymbol{J}\ ,$$

where the total current can be defined as [26]:

$$\boldsymbol{J}=\sigma\nabla V+j\sigma\omega\boldsymbol{A}-\boldsymbol{J}_e\ ,\tag{28}$$

then according to (27) we get that

$$\iiint_V\left(\boldsymbol{J}\cdot\nabla N\right)\mathrm{d}x\mathrm{d}y\mathrm{d}z-\iiint_V\nabla\cdot\left(N\boldsymbol{J}\right)\mathrm{d}x\mathrm{d}y\mathrm{d}z=0\ .\tag{29}$$

Let's transform the second volume integral into a surface integral, and make the assumption that

$$\boldsymbol{u}=N\cdot\boldsymbol{J}\ ,$$

then:

$$\iiint_V\left(\boldsymbol{J}\cdot\nabla N\right)\mathrm{d}x\mathrm{d}y\mathrm{d}z-\iint_S\left(N\boldsymbol{J}\cdot\boldsymbol{n}\right)\mathrm{d}x\mathrm{d}y=0\ .\tag{30}$$

In its final form, the equivalent variation formulation for equations (1) will have the form:

$$\begin{cases}\iiint_V \mu\left(\nabla\times\boldsymbol{A}\right)\left(\nabla\times\boldsymbol{\Psi}\right)\mathrm{d}x\mathrm{d}y\mathrm{d}z+\iiint_V\left(\boldsymbol{J}\cdot\boldsymbol{\Psi}\right)\mathrm{d}x\mathrm{d}y\mathrm{d}z=0;\\ \iiint_V\left(\boldsymbol{J}\cdot\nabla N\right)\mathrm{d}x\mathrm{d}y\mathrm{d}z-\iint_{S_1}\left(NJ_n\right)\mathrm{d}x\mathrm{d}y=0.\end{cases}\tag{31}$$

To solve the variational equation (31), the sought scalar potential V is represented in the form of expansion by quadratic Lagrangian basis functions, and the magnetic vector potential by second-order basis vector functions. Figure 6 shows the results of the numerical calculation in the form of lines of force of the magnetic vector potential, as well as x-, y-, z-components of the magnetic vector potential A_x, A_y, A_z for the calculation domain of the frontal parts of the armature windings and the ISEM rotor.

Based on the found distribution of potential $\boldsymbol{A}$, full current $\boldsymbol{J}$ and electric field strength $\boldsymbol{E}$, it is possible to find the active resistance and inductance of the frontal parts of the sections of the phase coils of the rotor winding, taking into account the speed of rotation of the electromagnetic field relative to the frontal parts of the ISEM armature winding [25]:

$$\begin{cases}R=\dfrac{\iiint_V \mathrm{Re}\left(\boldsymbol{J}\cdot\boldsymbol{E}^*\right)\mathrm{d}x\mathrm{d}y\mathrm{d}z}{\left|I_i\right|^2};\\ L=\dfrac{1}{I_i{}^2}\iiint_V\left(\boldsymbol{A}\cdot\boldsymbol{J}^*\right)\mathrm{d}x\mathrm{d}y\mathrm{d}z,\end{cases}\tag{32}$$

where I_i is the current in the i-th circuit of the calculation domain; E^*, J^* are the complex-conjugate quantities of electric field strength and full current, respectively.

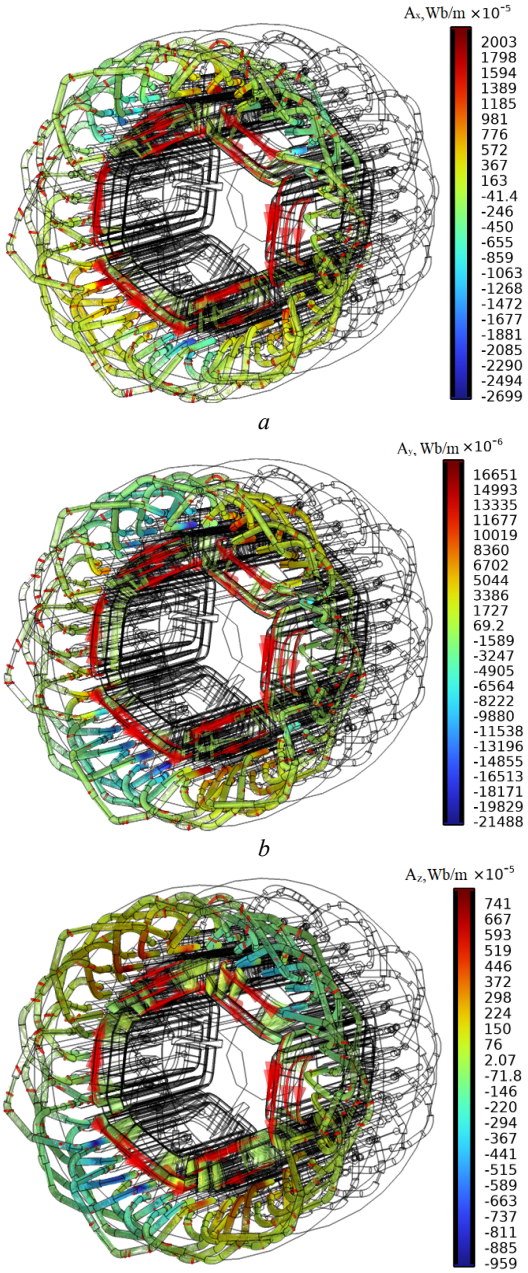

Fig. 6. Components A_x (*a*), A_y (*b*), A_z (*c*) of the magnetic vector potential in the domain of the front parts of the armature windings and ISEM rotor

Inductance and mutual inductance of the front parts of the armature winding:

$$L_{ii} \vee L_{jj} = \frac{1}{I^2_{i\vee j}} \left(\iiint_V (\boldsymbol{A} \cdot \boldsymbol{J}) \mathrm{d}x\mathrm{d}y\mathrm{d}z \right) \Bigg|_{I_{i\vee j}=0}, \quad (33)$$

$$M_{ij} = \frac{1}{I_i \cdot I_j} \left(\iiint_V (\boldsymbol{A} \cdot \boldsymbol{J}) \mathrm{d}x\mathrm{d}y\mathrm{d}z - L_{ii} \cdot I_i^2 \right) \Bigg|_{I_{i\wedge j\neq 0}}, \quad (34)$$

where I_i, I_j are the currents in i and j phases of the armature winding.

If during the rotation of the front parts of the rotor windings, the total inductance of the front parts of the armature winding L_i does not change, that is, its value corresponds to the value when the front parts of the rotor winding are statically placed relative to the armature, then the total inductance and active resistance of the front parts of the rotor winding will depend on the sliding of the ISEM rotor (Fig. 7).

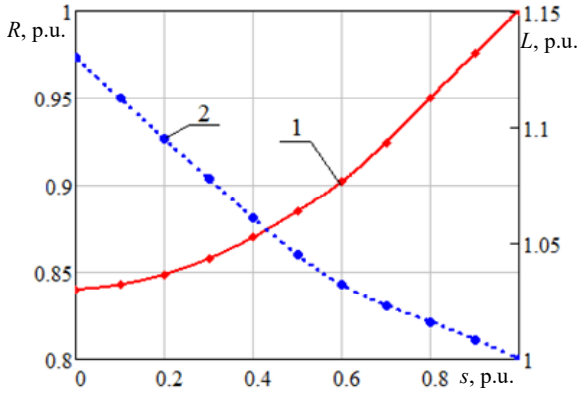

Fig. 7. Results of the numerical calculation regarding the dependence of the active resistance (1) and total inductance (2) of the front parts of the sections of the phase coils of the rotor winding on the sliding of the ISEM experimental sample

Taking into account the conditions of dynamic adaptation of the parameters of the spatial elements of the active part of the ISEM during the transition from 3D to 2D field modeling. The three-dimensional domain of the frontal parts of the armature windings and ISEM rotor can be represented as active and inductive elements of an electric circuit. Figure 8 shows the principle of the structure of the circuit-field model, where the slot parts of the armature and rotor windings, which are elements of the geometric calculation domain of the active part of the ISEM field model ($\Omega 1$ – subdomain of the armature core; $\Omega 2$ – subdomain of the upper and lower layers of the slot part of the armature winding; $\Omega 3$ – subdomain of the rotor core; $\Omega 4$ – subdomain of the slot part of the rotor winding), connected respectively to the frontal parts of the armature and rotor windings, which are represented by elements of electric circuits: mutual inductance between the frontal and slot parts of the armature winding section M^s_{nm}, which takes into account the edge effect regarding the magnetization of the end zone of the armature core by the frontal parts of the winding; the active resistance of the frontal part of the section R_{ls}; the total inductance of the front part of the winding section L_{ls}. For rotor winding sections – M^r_{nm}, R_{lr}, L_{lr}, respectively. The active resistance R_{lr} and the total inductance L_{lr} are presented as a function of the slip s.

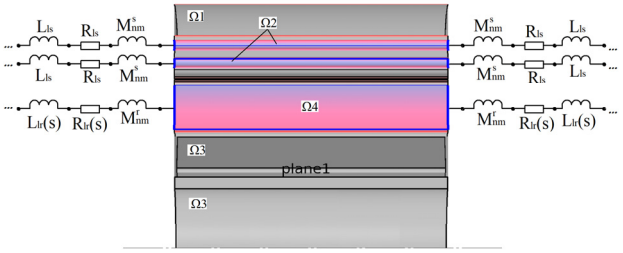

Fig. 8. *yz* cross-sectional plane of the active part of ISEM showing the frontal parts of the sections of the armature windings and rotor as elements of an electric circuit

The combination of the frontal and slot parts of the section of the armature windings and the rotor (i.e., the electric circuit with the spatial subdomain of the

geometric model) can also be performed, for example, with the help of «External I vs. U» terminals when combining «Rotating Machinery, Magnetic» and «Electrical Circuit» interfaces in the structure of COMSOL Multiphysics tools.

After the edge effects were taken into account, as well as the change in the active resistance and inductance of the front parts of the rotor winding due to ISEM sliding, it is reasonable to switch from the spatial to the plane-parallel formulation of the electromagnetic field distribution. At the same time, the spatial slot active part of ISEM can be represented as its projection in the *xy*-plane at a given equivalent depth L_z of the calculation area [10, 12, 14]:

$$\begin{cases} \boldsymbol{A}_{i,j} = L_z \cdot A_{z\,i,j}; \quad \boldsymbol{B}_{i,j} = \boldsymbol{i} \cdot B_{x\,i,j} + \boldsymbol{j} \cdot B_{y\,i,j}; \\ \boldsymbol{H}_{i,j} = \boldsymbol{i} \cdot H_{x\,i,j} + \boldsymbol{j} \cdot H_{y\,i,j}; \overline{B}_{x\,i,j} = -\dfrac{\partial \overline{A}_{i,j}}{\partial x}; \\ \overline{B}_{y\,i,j} = -\dfrac{\partial \overline{A}_{i,j}}{\partial y}; \overline{H}_{x\,i,j} = \dfrac{\overline{B}_{x\,i,j}}{\mu_{i,j}}; \overline{H}_{y\,i,j} = \dfrac{\overline{B}_{y\,i,j}}{\mu_{i,j}}. \end{cases} \tag{35}$$

This reduction of the geometric dimension allows us to use flat triangular elements of the calculation mesh and significantly increase the efficiency of the numerical implementation. In this case, the electromagnetic field description model for transient operating modes will correspond to (1), and the gauge condition is automatically fulfilled.

Thus, the adapted 2D circuit-field model of an induction-synchronous electromechanical converter can be represented as shown in Fig. 9, where the solid lines show the electrical connection of the ISEM armature winding inputs to the power cells, and the dashed lines show the electrical connection of the armature winding terminals, which form two independent «stars», which are connected according to the anode and cathode groups of the rectifier (the connection of the front and slot parts of the sections, as well as the coils in the coil groups of the armature winding is not shown in Fig. 9).

In order to carry out an ISEM study in the modes of non-operation and under load, the equations of the transient electromagnetic field must be supplemented with a system of equations of the angular speed of the rotor and the electromagnetic torque [26, 27]:

$$\begin{cases} \dfrac{\mathrm{d}\omega_m}{\mathrm{d}t} = \dfrac{M_e - M_c}{J}; \\ \dfrac{\mathrm{d}\phi}{\mathrm{d}t} = \omega_m; \\ M_e^{\,ave} = \dfrac{1}{R_o - R_i} \cdot \dfrac{L_z}{\mu_0} \int\limits_{S_{ag}} B_r B_\varphi r \mathrm{d}S_{ag}, \end{cases} \tag{36}$$

where M_e is the electromagnetic torque, N·m; M_c is the load moment, N·m; J is the moment of inertia of the rotor, kg·m^2; ω_m is the rotor angular speed, rad/s; φ is the rotor position angle, rad; r is the outer radius of the rotor core, m; L_z is the length of the armature and rotor package, m; B_r, B_φ are the radial and azimuthal components of magnetic flux density, T; R_o is the outer radius of the air gap, m; R_i is the inner radius of the air gap, m; S_{ag} is the cross-sectional area of the air gap, m^2.

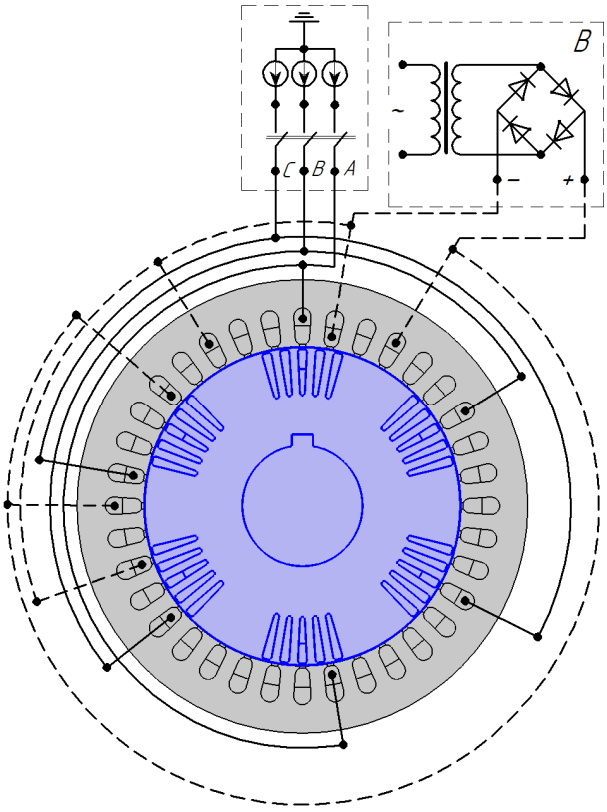

Fig. 9. Schematic-geometric interpretation of the adapted 2D circuit-field model of ISEM

Thus, an adapted dynamic 2D circuit-field model of ISEM was developed, which with high accuracy and efficiency of numerical implementation allows for transient modes of operation to take into account interconnected electromagnetic and mechanical processes, taking into account both design features and schematic implementation of the winding system, nonlinearity of magnetic and electrophysical properties of active materials, skin and edge effects of the end zones of the active part, as well as changes in the active resistance and inductance of the front parts of the rotor windings depending on its sliding in the transient and quasi-transient modes of its operation.

Experimental study of the ISEM test sample. In order to confirm the adequacy of the studied electromagnetic and mechanical processes and the accuracy of numerical calculations based on the proposed adapted 2D circuit-field model, physical tests of the ISEM experimental sample (Fig. 10) in the short-circuit and non-operation modes were carried out in the laboratory conditions of National University «Zaporizhzhia Polytechnic». The experimental ISEM sample itself is shown in Fig. 11. Currents in the phases of the armature winding, as well as in its parallel branches, were measured using an oscilloscope type OWON XDS3202E.

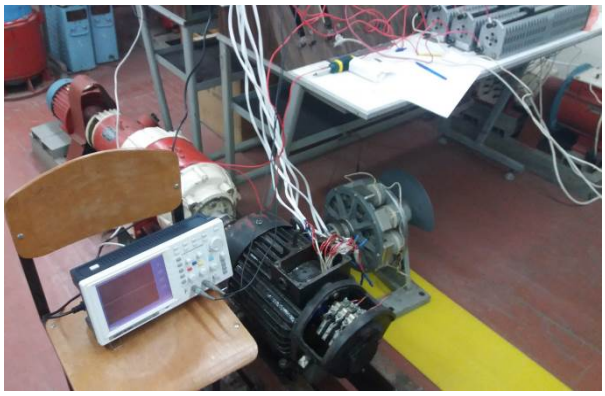

Fig. 10. Experimental stand of the ISEM test sample

a *b*

Fig. 11. Active part of the armature (*a*) and rotor (*b*) of the ISEM experimental sample

Table 2 shows the results of data validation of 3D and 2D circuit-field modeling and physical testing according to phase currents with simultaneous supply of the phases of the armature winding *A*, *B*, *C*, and ISEM excitation current in the short-circuit mode. When measuring the excitation current, the phase inputs of the armature winding were disconnected from the network. DC voltage from the excitation system was applied alternately to each phase *A*, *B*, *C* with the terminals of the winding phases open, forming two separate «stars» (points «0–» and «0+»), and immediately behind all phases of the armature winding at connecting the winding terminals into separate «stars». As the analysis of experimental data (Table 2) shows, the current discrepancy for the 3D circuit-field model does not exceed 3.45 %, and for the 2D adapted circuit-field model – 4.34 %, which confirms the high efficiency of the proposed methods of dynamic adaptation of complex spatial elements of the active part of ISEM, as well as the high accuracy of the numerical calculation of the 3D circuit-field model itself. The most difficult task in the development of a 3D spatial geometric model (not only ISEM, but also any EM) is the implementation of a symmetrical arrangement of the coils of the armature winding (rotor) among themselves, as well as the movement of their frontal parts. This is further complicated when the armature winding is two-layered, that is, the left part of the section is placed in the lower layer of the slot, and the right part of the section is placed in the upper one. To confirm the condition of symmetrical placement of the armature winding coils of the ISEM 3D geometric model, there is a measurement of the ohmic resistance in each phase. At the same time, the resistance of each phase coil group must be the same. Thus, the validation of ohmic resistance data in each of the phases was carried out using 3D numerical modeling and an adapted 2D circuit-field model as well as the results of measuring the ohmic resistance of the phases of the armature winding of the ISEM experimental sample. According to the results of numerical calculation and actual measurement, the discrepancy by ohmic resistance of phases *A*, *B*, *C* of the ISEM armature winding does not exceed $\delta R_a \leq 0.00694$ %.

Table 3 shows the results of the validation of 2D circle-field modeling and physical testing based on the available spectra of harmonics (k = 1,2,3,6,7) of the phase currents of the armature *A*, *B*, *C*, in the non-operation mode at the excitation current $I_f = 0$. Experimental oscillograms of ISEM phase currents are shown in Fig. 12.

As the data analysis (Table 3) shows, the discrepancy of the fundamental harmonic current in numerical calculations based on the adapted 2D circuit-field model and the results of the experimental study of the experimental ISEM does not exceed 8.61 %. At the same time, the current spectra of the digital current signals of the experimental ISEM during the test fully correspond to the harmonic composition of the phase currents according to the adapted 2D circuit-field model, and also have a negligible value of discrepancy in the amplitude values of the current spectra of higher harmonics (2.06 % – 4.33 %).

Table 2

Validation of 3D and 2D circuit-field modeling and physical testing by phase currents and ISEM excitation current in the short-circuit mode

ISEM armature winding power suuply options	Discrepancy by current $\delta I_{a,i}\|_{A,B,C}$ and $\delta I_{f,i}\|_{A,B,C}$, %	
	by 3D circuit-field model	by 2D adapted circuit-field model
With simultaneous power supply of phases *A*, *B*, *C* without excitation current	3,18 – 3,45	3,96 – 4,34
Power supply with rectified current of phases *A*, *B*, *C* of the armature winding when opening zero points «0–» and «0+»	2,58 – 2,62	3,03 – 3,24
Power supply with excitation current of phases *A*, *B*, *C* of the armature winding at connecting the winding terminals into separate «stars» («0–» and «0+» points)	2,39 – 2,78	3,11 – 3,31

Table 3

Validation of data based on the spectra of phase currents of 2D circuit-field modeling and physical testing of the experimental ISEM in the non-operation mode without the presence of excitation current

	Discrepancy by amplitude values of phase current harmonics $\delta I_{a,i}\|_{A,B,C}$, $\delta I_{a,i}\|_{A1,B1,C1}$, $\delta I_{a,i}\|_{A2,B2,C2}$, %				
	k = 1	k = 2	k = 3	k = 6	k = 7
Armature current (phases *A*, *B*, *C*)	7,96 – 8,61	2,06 – 2,12	4,11 – 4,33	2,8 – 3,09	3,66 – 3,96
Armature current in the first parallel branch (phases *A*1, *B*1, *C*1)	7,38 – 7,98	2,54 – 2,62	4,18 – 4,27	2,18 – 2,25	3,22 – 3,81
Armature current in the second parallel branch (phases *A*2, *B*2, *C*2)	7,89 – 8,26	2,42 – 2,5	3,96 – 4,05	2,89 – 3,13	3,9 – 4,21

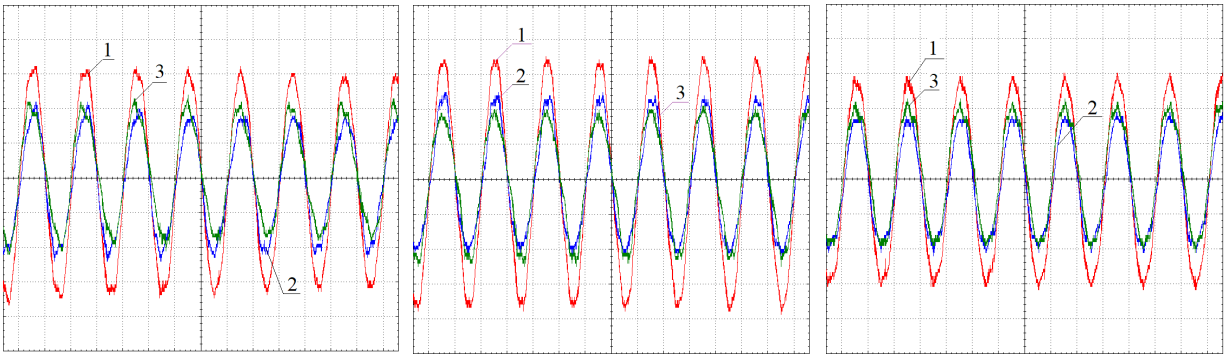

a *b* *c*

Fig. 12. Oscillograms of ISEM armature currents in the non-operation mode in the absence of excitation current:
a) 1 – armature current of phase *A*, 2 – phase *A*1 current (branch 1), 3 – phase *A*2 current (branch 2);
b) 1 – armature current of phase *B*, 2 – phase *B*1 current (branch 1), 3 – phase *B*1 current (branch 2);
c) 1 – armature current of phase *C*, 2 – phase *C*1 current (branch 1), 3 – phase *C2* current (branch 2)

Thus, the high efficiency and accuracy of the numerical implementation of the mathematical adapted 2D circuit-field model of ISEM in the non-operation mode are confirmed, as well as the convergence of the reproduction of the armature phase current curves. In addition, according to the obtained data of current discrepancies of the experimental ISEM, the high accuracy and efficiency of the proposed methods of decomposition and dynamic synthesis are confirmed, as well as the methodology for determining the active resistances and inductance of the end parts of the windings depending on the ISEM rotor slip, which provides the conditions for dynamic adaptation of 3D-2D circuit-field model of ISEM

Conclusions.

1. Based on the developed 3D circuit-field model of transient electromagnetic processes of the ISEM experimental sample, a decomposition method is proposed, which consists in separating its multi-component spatial structure into several separate subdomains (calculation zones): the core and the slot part of the armature winding; the left and right front parts of the armature winding; core and slot part of the rotor winding; respectively, the left and right front parts of the phase coils of the rotor winding.

2. A method of dynamic synthesis is proposed with adaptation of the conditions for combining electromagnetic parameters at the boundaries of the calculation subdomains of the frontal and slot parts of the armature and rotor windings of ISEM, which allows to match the flow of electromagnetic processes in the decomposed subdomains of ISEM to the electromagnetic processes in its integral calculation domain.

3. On the basis of the proposed methods, the share of the magnetic field energy determined by the action of edge effects in the end zones of the ISEM is determined. For problems of adaptation of 3D to 2D numerical calculations, it is proposed to take it into account through mutual inductance when replacing the spatial elements of the frontal parts of the armature winding with elements of the electric circuit.

4. For separate calculation subdomains of the frontal parts of the armature and ISEM rotor windings, when applying the variational formulation of the electromagnetic field equations taking into account the movement of the frontal parts of the ISEM rotor winding, the dependence of the active resistance and inductance of the frontal parts of the armature and rotor on the ISEM rotor slip has been determined.

5. Based on the developed methods, a new principle of the structure of the 2D circuit-field ISEM model is proposed, which consists in the fact that the slot parts of the armature and rotor windings are elements of the geometric calculation domain of the active part of the ISEM field model, and the frontal parts of the armature and rotor windings are represented by elements of electric circuit.

6. Due to the validation of the results of the numerical calculation with the data of the experimental study of the ISEM test sample, the high efficiency of the proposed methods of decomposition and dynamic synthesis and the accuracy of the numerical implementation of 3D and 2D circuit-field models of the ISEM have been confirmed. In the short-circuit mode, the discrepancy by armature current for the 3D circuit-field model does not exceed 3.45 %. For the adapted 2D circuit-field model – 4.34 %. In the non-operation mode, the discrepancy by the armature current of the main harmonic in numerical calculations based on the adapted 2D circuit-field model and the results of the ISEM experimental study does not exceed 8.61 %.

7. The proposed methods can be used for different types of electric machines.

Conflict of interest. The author declares no conflict of interest.

REFERENCES

1. Lushchyk V.D., Ivanenko V.S. Multipole cascade synchronous machines. *Electromechanical and Energy Saving Systems*, 2011, no. 2, pp. 121-123. (Ukr).

2. Luschik V.D., Ivanenko V.S., Borzik V.L. Synchronous cascade engine with combined winding. *Electrical Engineering & Electromechanics*, 2011, no. 1, pp. 31-32. (Ukr).

3. Lushchyk V.D., Semenov V.V. A new type of low-speed asynchronous-synchronous motor. *Coal of Ukraine*, 2008, no. 9, pp. 39-41. (Ukr).

4. Lushchyk V. D. *Prospective Directions for Improving Electric Machines*. Kyiv, Myronivska drukarnia Publ., 2015 264 p. (Ukr).

5. Kopylov Y.P. *Mathematical Modeling of Electrical Machines*. Moscow, Vysshaia Shkola Publ., 2001. 327 p. (Rus).

6. Lozynskyi A.O., Moroz V.I., *Paranchuk Ya.S. Solving Electromechanics Problems in MathCAD and MATLAB Environments*. Lviv, Mahnoliia Publ., 2007. 215 p. (Ukr).

7. Rohozyn H.H. *Determination of Electromagnetic Parameters of AC Machines. New Experimental Methods*. Kyiv, Tekhnika Publ., 1992. 168 p. (Ukr).

8. Amiri E. Circuit modeling of double-armature rotary-linear induction motor. *IECON 2014 - 40th Annual Conference of the IEEE Industrial Electronics Society*, 2014, pp. 431-436. doi: https://doi.org/10.1109/IECON.2014.7048536.
9. Semenova M.N., Yakushev I.A., Vasilyeva A.V., Sabychikova A.A., Monastyrev A.K., Kazazaeva D.V. Computer Modeling of DC and AC Motor Systems by Different Methods and Determination of Errors them. *2022 4th International Conference on Control Systems, Mathematical Modeling, Automation and Energy Efficiency (SUMMA)*, 2022, pp. 711-715. doi: https://doi.org/10.1109/SUMMA57301.2022.9973896.
10. Andrzej D. Finite element modeling of magnetic field in electrical machines: Scalar or vector potential formulation part I: Comparative description of methods. *2016 13th Selected Issues of Electrical Engineering and Electronics (WZEE)*, 2016, pp. 1-6. doi: https://doi.org/10.1109/WZEE.2016.7800208.
11. Zhang B., Wu F., Zhang Z., Wei Z., Xi J. 3D Magnetic Field Finite Element Analysis of Dual-Stator PM Spherical Motor. *2019 Chinese Control And Decision Conference (CCDC)*, 2019, pp. 5616-5620. doi: https://doi.org/10.1109/CCDC.2019.8832404.
12. Ferkova Z. Comparison of two-phase induction motor modeling in ANSYS Maxwell 2D and 3D program. *2014 ELEKTRO*, 2014, pp. 279-284. doi: https://doi.org/10.1109/ELEKTRO.2014.6848902.
13. Vaskovskyi Y.M., Tsivinskiy S.S. Three dimensional mathematical model of electromagnetic processes in the end zone of the turbogenerator rotor. *Technical Electrodynamics*, 2016, no. 1, pp. 34-39. (Ukr). doi: https://doi.org/10.15407/techned2016.01.034.
14. Fireteanu V., Constantin A.-I., Zorig A. Finite Element 2D and 3D Models of a Rotor Bar Breakage in a Squirrel-Cage Induction Motor. *2019 IEEE Workshop on Electrical Machines Design, Control and Diagnosis (WEMDCD)*, 2019, pp. 157-162. doi: https://doi.org/10.1109/WEMDCD.2019.8887801.
15. Yarymbash D., Kotsur M., Subbotin S., Oliinyk A. A new simulation approach of the electromagnetic fields in electrical machines. *2017 International Conference on Information and Digital Technologies (IDT)*, 2017, pp. 429-434. doi: https://doi.org/10.1109/DT.2017.8024332.
16. Kotsur M., Yarymbash D., Yarymbash S., Kotsur I. A new approach of the induction motor parameters determination in short-circuit mode by 3D electromagnetic field simulation. *2017 IEEE International Young Scientists Forum on Applied Physics and Engineering (YSF)*, 2017, pp. 207-210. doi: https://doi.org/10.1109/YSF.2017.8126620.
17. Milykh V.I., Tymin M.G. A comparative analysis of the parameters of a rotating magnetic field inductor when using concentric and loop windings. *Electrical Engineering & Electromechanics*, 2021, no. 4, pp. 12-18. doi: https://doi.org/10.20998/2074-272X.2021.4.02.
18. Milykh V.I. Numerical-field analysis of active and reactive winding parameters and mechanical characteristics of a squirrel-cage induction motor. *Electrical Engineering & Electromechanics*, 2023, no. 4, pp. 3-13. doi: https://doi.org/10.20998/2074-272X.2023.4.01.
19. Vaskovskyi J.M., Haydenko J.A. Research of electromagnetic processes in permanent magnet synchronous motors based on a «electric circuit - magnetic field» mathematical model. *Technical Electrodynamics*, 2018, no. 2, pp. 47-54. doi: https://doi.org/10.15407/techned2018.02.047.
20. Yarymbash D., Yarymbash S., Kotsur M., Divchuk T. Enhancing the effectiveness of calculation of parameters for short circuit of three-phase transformers using field simulation methods. *Eastern-European Journal of Enterprise Technologies*, 2018, vol. 4, no. 5(94), pp. 22-28. doi: https://doi.org/10.15587/1729-4061.2018.140236.
21. Kotsur M., Yarymbash D., Kotsur I., Yarymbash S. Improving efficiency in determining the inductance for the active part of an electric machine's armature by methods of field modeling. *Eastern-European Journal of Enterprise Technologies*, 2019, vol. 6, no. 5(102), pp. 39-47. doi: https://doi.org/10.15587/1729-4061.2019.185136.
22. Bellman R., Dreyfus S. *Applied Dynamic Programming*. Princeton University Press, New Jersey, 1962. 363 p.
23. Raviart P.A. Pseudo-viscosity methods and nonlinear hyperbolic equations. *Proceedings of the Royal Society of London. A. Mathematical and Physical Sciences*, 1971, vol. 323, no. 1553, pp. 277-283. doi: https://doi.org/10.1098/rspa.1971.0104.
24. Landau L.D., Lifshyts E.M. *Theoretical physics. Vol. 2. Field Theory*. Moscow, Nauka Publ., 1988. 59 p. (Rus).
25. Silvester P.P., Ferrari R. L. *Finite Elements for Electrical Engineers*. Cambridge University Press, 1990. 425 p.
26. Sadowski N., Lefevre Y., Lajoie-Mazenc M., Cros J. Finite element torque calculation in electrical machines while considering the movement. *IEEE Transactions on Magnetics*, 1992, vol. 28, no. 2, pp. 1410-1413. doi: https://doi.org/10.1109/20.123957.
27. Skalka M., Ondrusek C., Schreier L., Michailidis P. Torque components identification of induction machine by FEM. *International Aegean Conference on Electrical Machines and Power Electronics and Electromotion, Joint Conference*, 2011, pp. 185-189. doi: https://doi.org/10.1109/ACEMP.2011.6490592.

Received 27.01.2024
Accepted 09.03.2024
Published 20.06.2024

M.I. Kotsur[1]*, PhD, Assistant Professor,*
[1] National University «Zaporizhzhia Polytechnic»,
64, Zhykovskii Str., Zaporizhzhia, 69063, Ukraine,
e-mail: kotsur_m@ukr.net (Corresponding Author)

How to cite this article:
Kotsur M.I. Development of methods for adapting the parameters of spatial end winding sections in 2D circuit-field models of induction-synchronous electric machines. *Electrical Engineering & Electromechanics*, 2024, no. 4, pp. 9-21. doi: https://doi.org/10.20998/2074-272X.2024.4.02

UDC 621.3.013 https://doi.org/10.20998/2074-272X.2024.4.03

B.I. Kuznetsov, T.B. Nikitina, I.V. Bovdui, K.V. Chunikhin, V.V. Kolomiets, B.B. Kobylianskyi

The method for design of electromagnetic hybrid active-passive shielding by overhead power lines magnetic field

Aim. *Development of the method for designing electromagnetic hybrid active-passive shield, consisting from active and multy-circuit passive parts, which is characterized by increased effectiveness of reducing the industrial frequency magnetic field created by two-circuit overhead power lines in residential buildings.* ***Methodology****. The designing problem of electromagnetic hybrid active-passive shield including robust system of active shielding and multy-circuit passive shield of initial magnetic field comes down to a solution of the multy-criteria two-player zero-sum antagonistic game. The game payoff vector calculated based on the finite element calculations system COMSOL Muliphysics. The game solution calculated based on the particles multyswarm optimization algorithms.* ***Results.*** *During the design of the electromagnetic hybrid active-passive shield the coordinates of the spatial arrangement of 11 circuits passive shield and the coordinates of the spatial location of one compensation winding, as well as the current and phase in this winding of the active shielding system are calculated. The results of theoretical and experimental studies of hybrid active and multy-circuit passive shield by magnetic field in residential building from two-circuit power transmission line with a «Barrel» type arrangement of wires presented.* ***Originality****. For the first time the method for designing hybrid active and multy-circuit passive shield, consisting from active and multy-circuit passive parts, which is characterized by increased effectiveness of reducing the magnetic field of industrial frequency created by two-circuit overhead power lines in residential buildings is developed.* ***Practical value****. Based on results of calculated study the shielding efficiency of the initial magnetic field what is confirmed by experimental studies determined that shielding factors whith only multy-circuit passive shield is more 1.2 units, whith only active shield is more 4 units and with electromagnetic hybrid active-passive shield is more 6.2 units. It is shown the possibility to reduce the level of magnetic field induction in residential building from two-circuit power transmission line with a «Barrel» type arrangement of wires by means of electromagnetic hybrid active shielding with single compensating winding and multy-circuit passive shielding with 11 circuit passive shield to 0.5 μT level safe for the population.* References 51, figures 17.

Key words: **overhead power line, magnetic field, electromagnetic hybrid active-passive shield, computer simulation, experimental research.**

Мета*. Розробка методу проектування електромагнітного гібридного активно-пасивного екрану, який складається з активної та багатоконтурної пасивної частин, та характеризується підвищеною ефективністю зниження магнітного поля промислової частоти, що генерується дволанцюговими повітряними лініями електропередачі в житлових будинках.* ***Методологія.*** *Задача проектування електромагнітного гібридного активно-пасивного екрану, яка включає розробку робастної системи активного екранування та багатоконтурного пасивного екрану вихідного магнітного поля, зводиться до вирішення багатокритеріальної антагоністичної гри двох гравців з нульовою сумою. Вектор виграшів гри розраховується з використанням кінцево-елементної системи обчислень COMSOL Muliphysics. Рішення гри розраховується на основі алгоритмів оптимізації мультироїв частинок.* ***Результати.*** *При проектуванні електромагнітного гібридного активно-пасивного екрану були розраховані координати просторового розташування 11 контурів пасивного екрану і координати просторового розташування однієї компенсаційної обмотки, а також струм і фаза в цій обмотці системи активного екранування. Наведено результати теоретичних та експериментальних досліджень електромагнітного гібридного активно-пасивного екрану магнітного поля в житловому будинку від дволанцюгової лінії електропередач із розташуванням проводів типу «бочка».* ***Оригінальність.*** *Вперше розроблено метод проектування електромагнітного гібридного активно-пасивного екрану, який складається з активної та багатоконтурної пасивної частин, та характеризується підвищеною ефективністю зниження рівня магнітного поля промислової частоти, яке генерується дволанцюговими повітряними лініями електропередачі в житлових будинках.* ***Практична цінність****. За результатами розрахункових досліджень ефективності екранування вихідного магнітного поля, які підтверджені експериментальними дослідженнями, встановлено, що коефіцієнт екранування тільки багатоконтурним пасивним екраном становить більше 1,2 одиниць, а тільки з активним екраном становить більше 4 одиниць, і при використанні електромагнітного гібридного активно-пасивного екрану становить більше 6,2 одиниці. Показана можливість зниження рівня індукції магнітного поля в житловому будинку від дволанцюгової лінії електропередачі з розташуванням проводів типу «бочка» за допомогою гібридного активного екрану з однією компенсуючою обмоткою та багатоконтурного пасивного екрану з 11 контурами до безпечного для населення рівня в 0,5 μТ.* Бібл. 51, рис. 17.

Ключові слова: **повітряна лінія електропередачі, магнітне поле, електромагнітний гібридний активно-пасивний екран, комп'ютерне моделювання, експериментальні дослідження.**

Introduction. Overhead power lines are the main source of power frequency magnetic field (MF). The effect of prolonged exposure of people to a power frequency MF increase in the likelihood of cancer [1–3]. The standards for the power frequency MF being tightened for long-term safe residence of the population in residential buildings located near power lines. Decrease in the initial MF by a factor of 2–4 is required [4–7]. Active and passive shielding of the initial MF usually used for reduction of power frequency MF [4–10].

Active shielding requires the use of external power supplies to supply currents appropriate magnitude and phase to the reduction system opposite to the original MF to provide the desired reduction effect, and as such, is capable of providing a high reduction in the original MF [11–15]. However, this requires a complex suppression system; since in addition to the MF sensors, it is necessary to install expensive equipment, such as power supplies, and a monitoring system to continuously adjust the supplied current to achieve the required suppression. All this makes this solution much more expensive than passive methods.

With passive shielding, MF weakening is achieved, since the mitigation system acts in response to the initial MF generated by the source according to Faraday's law

© B.I. Kuznetsov, T.B. Nikitina, I.V. Bovdui, K.V. Chunikhin, V.V. Kolomiets, B.B. Kobylianskyi

and induces currents that generate a new MF that compensates for the original one [16–20]. To increase the shielding efficiency of the initial MF, multy-circuit passive shields are often used [21, 22]. Passive shield have a significantly lower shielding factor, so passive screens are often used as a complement to active screens [23–25].

The aim of the work is to develop the method for designing electromagnetic hybrid active-passive shield, consisting from active and multy-circuit passive parts, to improve the effectiveness of reduction of industrial frequency MF created by two-circuit overhead power lines in residential buildings.

Problem statement. First, consider the design of the mathematical model of the initial MF generated by the power transmission line. We set the currents amplitude $\boldsymbol{A_i}$ and phases $\boldsymbol{\varphi_i}$ of power frequency ω of wires currents power lines. Then we set wires currents in power lines in a complex form

$$\boldsymbol{I_i}(t) = \boldsymbol{A_i} \exp j(\omega t + \boldsymbol{\varphi_i}). \quad (1)$$

To assess the impact of the MF of power lines on the environment, most calculations were performed based on the Biot-Savart-Laplace law [6] for elementary current

$$\mathrm{d}\,\boldsymbol{B_l}(Q_i,t) = \frac{\mu\mu_0 i_l(t)}{4\pi R^3}(\mathrm{d}\,\boldsymbol{l}_l \times \boldsymbol{R}_l), \quad (2)$$

where the vector $\boldsymbol{R}_l$ is directed from an elementary segment $\mathrm{d}\boldsymbol{l}_l$ with a total current $\boldsymbol{i_l}(t)$ to the observation point Q_i, μ_0 is the vacuum magnetic permeability.

Then the total MF vector is equal to:

$$\boldsymbol{B_l}(Q_i,t) = \frac{\mu\mu_0 \boldsymbol{i_l}(t)}{4\pi}\int_L \frac{(\mathrm{d}\boldsymbol{l}_l \times \boldsymbol{R}_l)}{R^3}. \quad (3)$$

This formula is widely used to calculate the MF of air power transmission lines instead of Maxwell's system of equations.

Let us introduce the vector $\boldsymbol{\delta}$ of the uncertainty parameters of the problem of designing a combined shield, the components of which are inaccurate knowledge of the currents and phases in the wires of the power transmission line, as well as other parameters of the electromagnetic hybrid active-passive shield, which, firstly, are initially known inaccurately and, secondly, may change during the operation of the system [26–28].

Then the vector $\boldsymbol{B_L}(Q_i,\boldsymbol{\delta},t)$ of the initial MF generated by all power lines wires $\boldsymbol{B_{Li}}(Q_i,\boldsymbol{\delta},t)$ in point Q_i of the shielding space calculated based Biot-Savart's law [6]

$$\boldsymbol{B_L}(Q_i,\boldsymbol{\delta},t) = \sum \boldsymbol{B_l}(Q_i,\boldsymbol{\delta},t). \quad (4)$$

Now, consider the design of the mathematical model of the MF generated by compensating windings of active shielding. We set the vector $\boldsymbol{X_a}$ of initial geometric values of the dimensions of the compensating windings of active shielding, as well as the currents amplitude $\boldsymbol{A_{ai}}$ and phases $\boldsymbol{\varphi_{ai}}$ in the compensating windings [29–33]. We set the currents in the compensating windings wires in a complex form

$$\boldsymbol{I_{ai}}(t) = \boldsymbol{A_{ai}} \exp j(\omega t + \varphi_{\boldsymbol{wi}}). \quad (5)$$

Then the vector $\boldsymbol{B_a}(Q_i,\boldsymbol{X_a},t)$ of the MF generated by all compensating windings wires of active shielding $\boldsymbol{B_{ai}}(Q_i,\boldsymbol{X_a},t)$ in point Q_i of the shielding space can also calculated based Biot-Savart's law [6]

$$\boldsymbol{B_a}(Q_i,\boldsymbol{X_a},t) = \sum \boldsymbol{B_{ai}}(Q_i,\boldsymbol{X_a},t) \quad (6)$$

Then the vector $\boldsymbol{B_{Ra}}(Q_i,\boldsymbol{X_a},\boldsymbol{\delta},t)$ of the resulting MF generated by power lines and only windings of the active shielding system calculated as sum

$$\boldsymbol{B_{Ra}}(Q_i,\boldsymbol{X_a},\boldsymbol{\delta},t) = \boldsymbol{B_L}(Q_i,\boldsymbol{\delta},t) + \boldsymbol{B_a}(Q_i,\boldsymbol{X_a},t) \quad (7)$$

Now, consider the design of the mathematical model of the MF generated by multy-circuit passive shield [35–37]. Let us set the vector $\boldsymbol{X_p}$ of initial values of the geometric dimensions, thickness and material of the multy-circuit passive loop shield. Then, for the given vector $\boldsymbol{B_{Ra}}(Q_i,\boldsymbol{X_a},\boldsymbol{\delta},t)$ of the resulting MF generated by power lines and only windings of the active shielding system and for values of the vector $\boldsymbol{X_p}$ of geometric dimensions of the passive loop shield, the magnetic flux $\boldsymbol{\Phi_l}(\boldsymbol{X_a},\boldsymbol{X_p},\boldsymbol{\delta},t)$ calculated

$$\boldsymbol{\Phi_l}(\boldsymbol{X_a},\boldsymbol{X_p},\boldsymbol{\delta},t) = \int_S \boldsymbol{B_{Ra}}(\boldsymbol{X_a},\boldsymbol{\delta},t)\mathrm{d}S. \quad (8)$$

The current $\boldsymbol{I_{Pl}}(\boldsymbol{X_a},\boldsymbol{X_p},\boldsymbol{\delta},t)$ in a complex form induced in the passive loop shield determined from Ohm law in integral form and Faraday law [6]:

$$\boldsymbol{I_{Pl}}(\boldsymbol{X_a},\boldsymbol{X_p},\boldsymbol{\delta},t) = -j\omega\boldsymbol{\Phi}(\boldsymbol{X_a},\boldsymbol{X_p},\boldsymbol{\delta},t)/\ldots \\ \ldots/(\boldsymbol{R_l}(\boldsymbol{X_p}) + j\omega\boldsymbol{L_l}(\boldsymbol{X_p})). \quad (9)$$

The active resistance $\boldsymbol{R_l}(\boldsymbol{X_p})$ and the self-inductance coefficient $\boldsymbol{L_l}(\boldsymbol{X_p})$ of the passive loop shield.

Then for the calculated currents $\boldsymbol{I_{Pl}}(\boldsymbol{X_a},\boldsymbol{X_p},\boldsymbol{\delta},t)$ in the passive loop screen [36–38] and their geometric dimensions given by the vector $\boldsymbol{X_p}$, on the basis of Biot-Savart's law, the vector $\boldsymbol{B_R}(Q_i,\boldsymbol{X_a},\boldsymbol{\delta},t)$ of the resulting MF calculated as sum the vector $\boldsymbol{B_L}(Q_i,\boldsymbol{\delta},t)$ generated by overhead power transmission lines, the vector $\boldsymbol{B_a}(Q_i,\boldsymbol{X_a},t)$ generated by all compensating windings wires of active shielding and the vector $\boldsymbol{B_p}(Q_i,\boldsymbol{X_a},\boldsymbol{X_p},\boldsymbol{\delta},t)$ generated by all loops of the passive shield at the point Q_i, similarly (7)

$$\boldsymbol{B_R}(Q_i,\boldsymbol{X_a},\boldsymbol{X_p},\boldsymbol{\delta},t) = \boldsymbol{B_L}(Q_i,\boldsymbol{\delta},t) + \ldots \\ \ldots + \boldsymbol{B_a}(Q_i,\boldsymbol{X_a},t) + \boldsymbol{B_p}(Q_i,\boldsymbol{X_a},\boldsymbol{X_p},\boldsymbol{\delta},t). \quad (10)$$

Solution method. We introduce the vector $\boldsymbol{X}$ of the desired parameters of the problem of designing a combined shield, the components of which are the vector $\boldsymbol{X_a}$ values of the geometric dimensions of the compensation windings, as well as the currents $\boldsymbol{A_{wi}}$ and phases $\boldsymbol{\varphi_{wi}}$ in the compensation windings, as well as the vector $\boldsymbol{X_p}$ of geometric dimensions, thickness and material of the passive loop shield [39, 40].

Then for the given initial values of the vector $\boldsymbol{X}$ of the desired parameters and the vector $\boldsymbol{\delta}$ of the uncertainty parameters of the combined screen design problem, the value $\boldsymbol{B_R}(\boldsymbol{X},\boldsymbol{\delta},P_i)$ effective value of induction of the resulting MF $\boldsymbol{B_R}(Q_i,\boldsymbol{X_a},\boldsymbol{X_p},\boldsymbol{\delta},t)$ at the point Q_i of the shielding space calculated based on the finite element calculations system COMSOL Multiphysics. Then the problem of designing a passive screen is reduced to computing the solution of the vector game

$$\boldsymbol{B_R}(\boldsymbol{X},\boldsymbol{\delta}) = \langle \boldsymbol{B_R}(\boldsymbol{X},\boldsymbol{\delta},P_1)\rangle. \quad (11)$$

The components of the game payoff vector $\boldsymbol{B_R}(\boldsymbol{X},\boldsymbol{\delta},P_i)$ are the effective values of the induction of the resulting MF at all considered points Q_i in the shielding space.

In this vector game it is necessary to find the minimum of the game payoff vector (11) by the vector $\boldsymbol{X}$, but the maximum of the same game payoff vector by the vector $\boldsymbol{\delta}$.

At the same time, naturally, it is necessary to take into account constraints [41] on the vector $\boldsymbol{X}$ desired parameters of a combined shield in the form of vector inequality and, possibly, vector equality

$$\boldsymbol{G}(\boldsymbol{X}) \le \boldsymbol{G}_{max}, \quad \boldsymbol{H}(\boldsymbol{X}) = 0. \qquad (12)$$

Note that the components of the vector game (11) and vector constraints (12) are the nonlinear functions of the vector of the required parameters [42–45] and calculated based on the calculations system COMSOL Multiphysics.

Solution algorithm. Let us consider an algorithm for solving on a computer the formulated multyobjective optimization problem (11) with constraints (12). To find a unique solution to the problem of multycriteria optimization from the Pareto set of optimal solutions, in addition to the vector optimization criterion (11) and constraints (12), it is also necessary to have information about the binary preference relations of local solutions relative to each other [46–48].

To find such a single optimal solution, it is first necessary to develop an algorithm for constructing the entire area of Pareto-optimal solutions. Then, based on the analysis of the entire set of possible optimal solutions to the original problem of multycriteria optimization, narrow the range of solutions under consideration and, consequently, reduce the complexity of the decision maker in choosing the only option for the optimal solution.

A feature of the considered problem of finding a local minimum at one point in the space under consideration is multy-extremality, so that the considered area of possible solutions contains local minima and maxima. This is due to the fact that when minimizing the level of induction of the resulting MF in one current of the search space, the induction at another point increases due to undercompensation or overcompensation of the initial MF. Therefore, to solve the considered multycriteria problem, it is advisable to use the algorithms of stochastic multy-agent optimization [48–50].

Consider an algorithm for finding a set of Pareto-optimal solutions to multyobjective non-linear programming problems based on stochastic multy-agent optimization – PSO algorithms based on the idea of a collective mind of a swarm of particles, based on algorithms for finding the globally optimal value $y_j^*(t)$ – gbest PSO found by all particles swarm, and the locally optimal value $y_{ij}(t)$ – lbest PSO found by one swarm particle [48–50].

At present, the use of stochastic multy-agent optimization methods for solving multycriteria optimization problems causes certain difficulties, but this direction continues to be intensively developed using various heuristic techniques. Consider a stochastic multy-agent optimization algorithm for solving the original multycriteria problem of nonlinear programming (11) with constraints (12) based on a set of swarms j of particles i, the number of which is equal to the number of components of the vector optimization criterion (11).

In the simplest algorithm for calculating the optimal position $x_{ij}(t)$ and speed $\upsilon_{ij}(t)$ of the movement of particle i swarm j, the movement speeds $\upsilon_{ij}(t)$change according to linear laws. However, recently, to increase the speed of finding a global solution, special non-linear algorithms of stochastic multy-agent optimization have become widespread. One of such algorithms is an algorithm in which the Heaviside function H is used to switch the motion of a particle, respectively, from the local $y_{ij}(t)$ to the global $y_j^*(t)$ optimum. Parameters of switching the cognitive p_{1j} and social p_{2j} components of the speed of particle movement in accordance with the local and global optimum; random numbers $\varepsilon_{1j}(t)$ and $\varepsilon_{2j}(t)$ determine the parameters of switching the movement of the particle according to the local and global optimum. If $p_{1j} < \varepsilon_{1j}(t)$ and $p_{2j} < \varepsilon_{2j}(t)$, then the speed of movement of particle i swarm j does not change at the step t and the particle moves in the same direction as in the previous optimization step. In this algorithm, the motion of particle i swarm j described by the following expressions

$$\begin{aligned} v_{ij}(t+1) = w_j v_{ij}(t) + c_{1j} r_{1j}(t) H\left(p_{1j} - \varepsilon_{1j}(t)\right) \times \dots \\ \dots \times \left[y_{ij}(t) - x_{ij}(t)\right] + c_{2j} r_{2j}(t) H\left(p_{2j} - \varepsilon_{2j}(t)\right) \times \dots \\ \dots \times \left[y_j^*(t) - x_{ij}(t)\right], \end{aligned} \qquad (13)$$

$$x_{ij}(t+1) = x_{ij}(t) + v_{ij}(t+1), \qquad (14)$$

where c_1, c_2 are positive constants that determine the weights of the cognitive and social components of the speed of particle movement; $r_{1j}(t)$, $r_{2j}(t)$ are random numbers from the range [0, 1], which determine the stochastic component of the particle's speed.

With the multycriteria optimization of the vector criterion (11), with the help of separate swarms, the optimization problems of scalar criteria, which are components, are solved. In order to find a global solution to the original multycriteria problem.

In the process of searching for a global solution to the original multycriteria problem (11), individual swarms exchange information with each other in the course of searching for optimal solutions to local criteria. Information about the global optimum obtained by the particles of another swarm is used to calculate the speed of movement of the particles of the other swarm, which makes it possible to calculate all potential Pareto-optimal solutions.

At each step t of the movement of particle i swarm j, the advantages functions $y_{ij}(t)$ of local solutions obtained by all swarms y_j^* are used. The solution $X_j^*(t)$ obtained during the optimization of the objective function $B(X(t),P_j)$ using the swarm j is better than the solution $X_k^*(t)$ obtained during the optimization of the objective function $B(X(t),P_k)$ using the swarm k, i.e. $X_j^*(t) \succ X_k^*(t)$, if the condition is fulfilled

$$\max_{i=1,m} B\left(P_i, X_j^*(t)\right) < \max_{i=1,m} B\left(P_i, X_k^*(t)\right). \qquad (15)$$

The global solution $X_k^*(t)$ obtained by the swarm k used as the global optimal solution $X_j^*(t)$ of the swarm j, which is better in relation to the global solution $X_k^*(t)$ of the swarm k on the basis of the preference relationship (15).

The main idea of successively narrowing of Pareto-optimal solutions area of trade-offs – all that cannot be chosen according to the available information about the preference are sequentially removed from the initial set of

possible solutions based on information about the relative importance of local solutions. The deletion is carried out until a globally optimal solution is obtained [51].

Simulation results. Let us consider the results of the design of electromagnetic hybrid active-passive shielding by overhead power lines MF generated by a double-circuit power line in a residential building. During the design of the electromagnetic hybrid active-passive shield, the coordinates of the spatial arrangement of 11 circuits passive screens were calculated. In addition, the coordinates of the spatial location of one compensation winding, as well as the current and phase in this winding of the active shielding system, were calculated.

Note that, unlike the works [21, 22], in this work the coordinates of the spatial arrangement of the contours of the multyloop passive screen calculated in the course of solving the multy-criteria two-player antagonistic game (10) with restrictions (11) and electromagnetic hybrid active-passive shield used to screen the initial MF.

The layout of the power transmission line, the winding of the active screen and 11 circuits passive screen shown in Fig. 1.

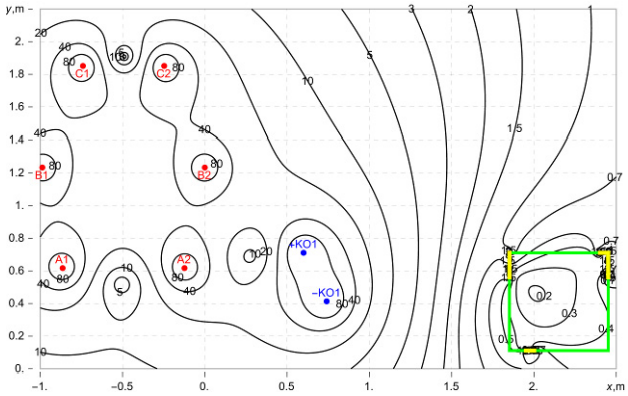

Fig. 1. The layout of the power transmission line, the winding of the active screen and 11 circuits of the passive screen

Figure 2 shows the distribution of the calculated initial MF induction. Initial MF induction changes from 2.2 μT to 1.4 μT. MF induction level in the central part of the shielding space is 1.75 μT.

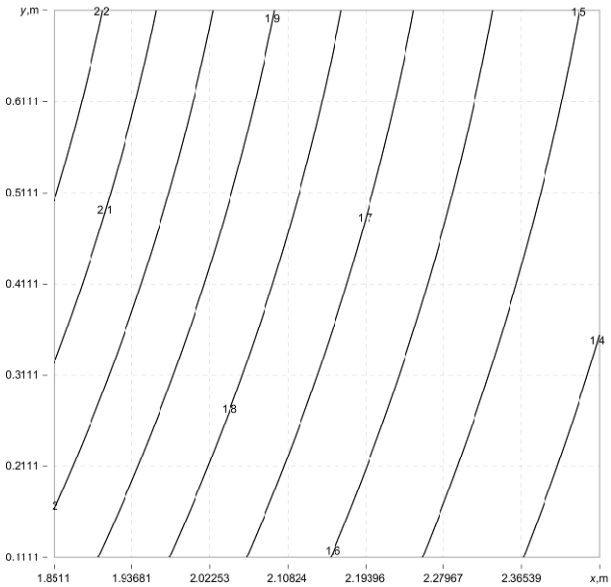

Fig. 2. The distribution of the calculated initial MF induction

Figure 3 shows the distribution of the calculated resulting MF induction with only multy-circuit passive shield. The coordinates of the spatial arrangement of 11 multy-circuit passive screens were calculated during the design of the hybrid multy-circuits passive and active shielding.

The resulting MF induction with only multy-circuit passive screen changes from 2 μT to 1.35 μT. The MF level in the central part of the shielding space is 1.35 μT.

The calculated shielding factor maximum value of resulting MF whith only multy-circuit passive shield in the central part of the screening space is more 1.29 units.

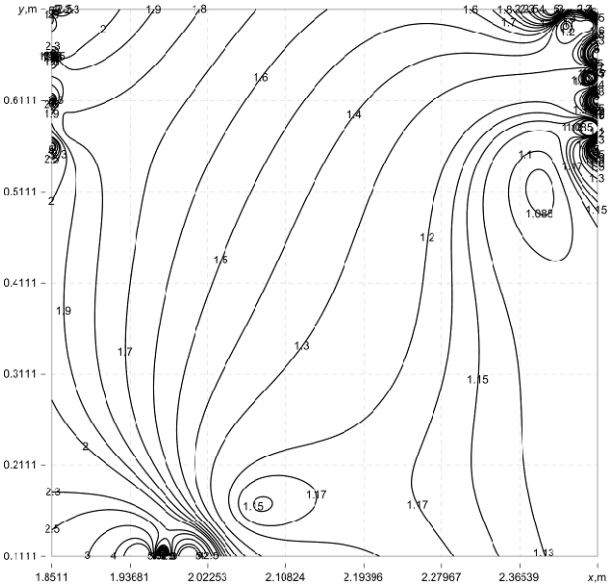

Fig. 3. The distribution of the calculated resulting MF induction with only multy-circuit passive shield

Figure 4 shows the distribution of the calculated resulting MF induction with only active shield.

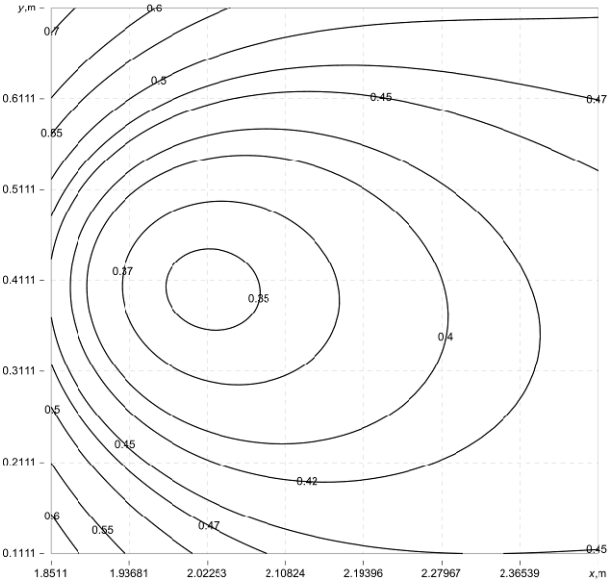

Fig. 4. The distribution of the calculated resulting MF induction with only active shield

The resulting MF induction with only active screen changes from 0.7 μT to 0.35 μT. The MF level in the central part of the shielding space is 0.35 μT.

The calculated shielding factor maximum value of resulting MF with only active shield in the central part of the screening space is more then 5 units.

Figure 5 shows the distribution of the calculated resulting MF induction with electromagnetic hybrid active-passive shield.

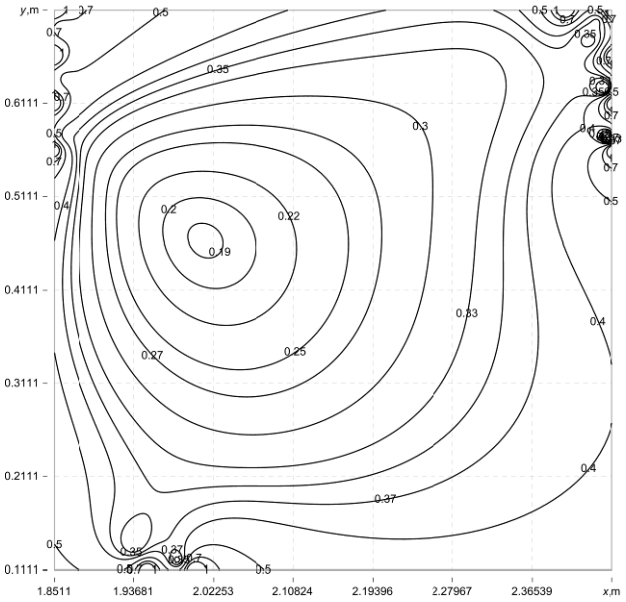

Fig. 5. The distribution of the calculated resulting MF induction with electromagnetic hybrid active-passive shield

The resulting MF induction with electromagnetic hybrid active-passive shield changes from 0.7 μT to 0.19 μT. The MF level in the central part of the shielding space is 0.19 μT.

The calculated shielding factor maximum value of resulting MF with only active shield in the central part of the screening space is more then 9.21 units.

Thus, the use of electromagnetic hybrid active-passive shield makes it possible to increase the screening factor of the active screen by 1.84 times.

Note that the product of shielding factors with only a multy-circuit passive screen of 1.29 and a shielding factor with only an active screen of 5 gives a value of 6.45, while the shielding factor with a electromagnetic hybrid active-passive shield is 9.21. Thus, the simultaneous use of active and multy-circuit passive screens leads to an increase in the screening factor by 1.42 times.

In addition, the use of electromagnetic hybrid active-passive shield makes it possible to reduce the level of the initial MF in a much larger area of the screening space compared to using only the active screen.

Results of experimental studies. Let us now consider the results of experimental studies of the electromagnetic hybrid active-passive shield.

Figure 6 shows the compensation winding and multy-circuit passive shield of the experimental setup.

Figure 7 shows multy-circuit passive shield and the control system of the experimental setup of multy-circuit passive and active shielding.

Figure 8 shows the experimental distribution of the initial and resulting MF induction with only multy-circuit passive shield.

Figure 9 shows the experimental shielding factor of resulting MF whith only multy-circuit passive shield.

The experimental shielding factor maximum value of resulting MF whith only multy-circuit passive shield is more then 1.2 units.

Fig. 6. The compensation winding and multy-circuit passive shield of the experimental setup

Fig. 7. The multy-circuit passive shield and the control system of the experimental setup of multy-circuit passive and active shielding

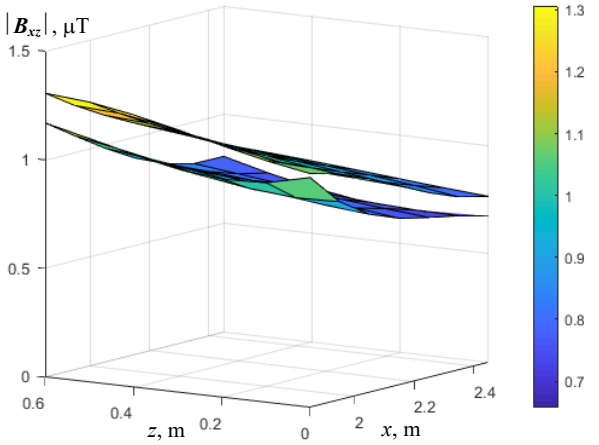

Fig. 8. The experimental distribution of the initial and resulting MF induction with only multy-circuit passive shield

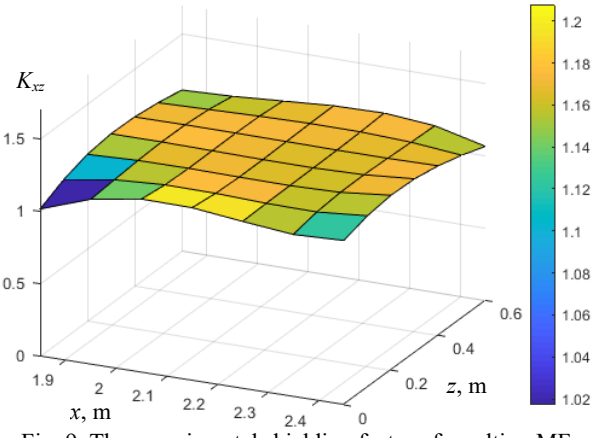

Fig. 9. The experimental shielding factor of resulting MF whith only multy-circuit passive shield

Figure 10 shows the experimental spatio-temporal characteristic of the resulting MF with only multy-circuit passive shield.

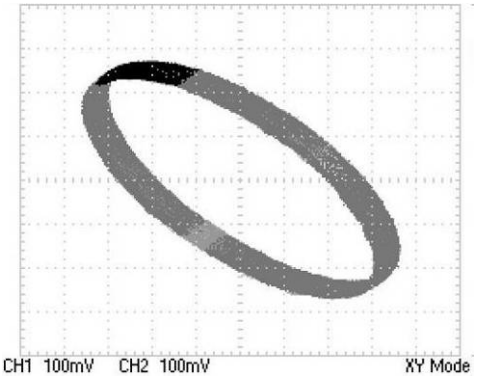

Fig. 10. The experimental spatio-temporal characteristic of the resulting MF with only multy-circuit passive shield

The experimental spatio-temporal characteristic of the resulting MF with only multy-circuit passive shield is about 1.2 times less than the spatio-temporal characteristic of the initial MF.

Figure 11 shows the experimental distribution of the initial and resulting MF induction with only active shield.

Figure 12 shows the experimental shielding factor of resulting MF whith only active shield.

The experimental shielding factor maximum value of resulting MF whith only active shield is more then 5 units.

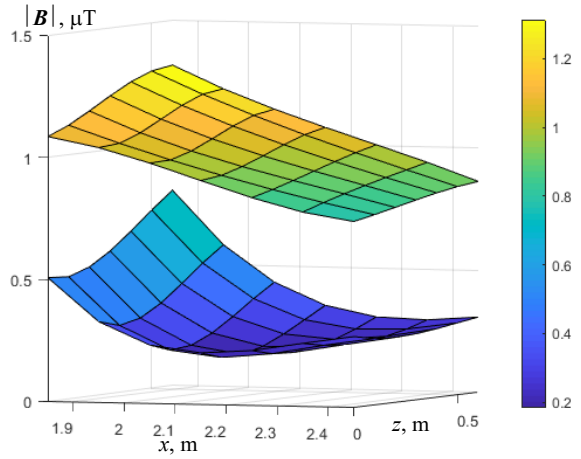

Fig. 11. The experimental distribution of the initial and resulting MF induction with only active shield

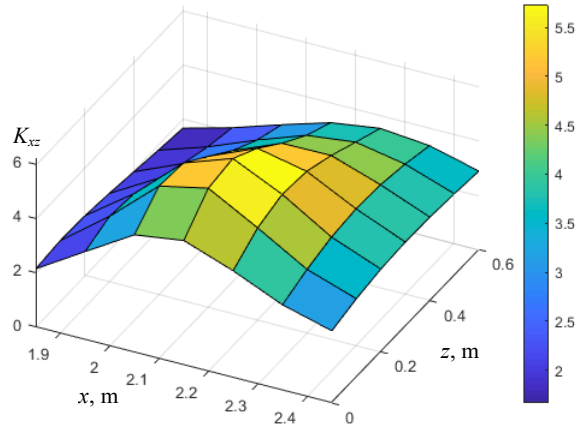

Fig. 12. The experimental shielding factor of resulting MF whith only active shield

Figure 13 shows the experimentally measured spatio-temporal characteristic of the MF generated by only one compensating winding of the active shielding system.

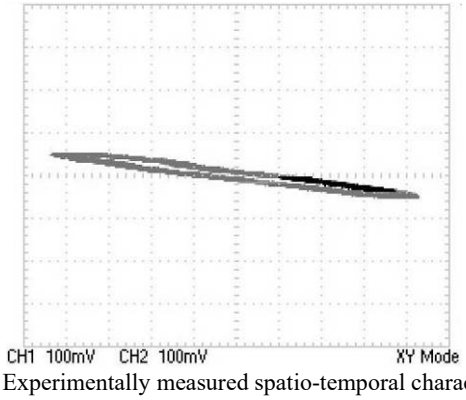

Fig. 13 Experimentally measured spatio-temporal characteristic of the MF generated by only one compensating winding of the active shielding system

This characteristic is practically a straight line parallel to the major axis of the ellipse of the experimentally measured spatiotemporal characteristic of the initial MF. Note that with the help of such an active screening system, the large axis of the spatiotemporal characteristic of the initial MF compensated, which determines the high value of the screening factor. In this case, the experimentally measured spatio-temporal characteristic of the resulting MF is a small cloud due to the noise of measurements of the MF components.

Figure 14 shows the experimental distribution of the initial and resulting MF induction with electromagnetic hybrid active-passive shield.

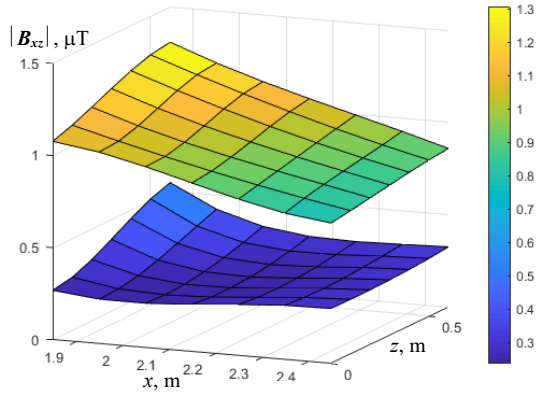

Fig. 14. The experimental distribution of the initial and resulting MF induction with electromagnetic hybrid active-passive shield

When using electromagnetic hybrid active-passive shield the level of the resulting MF is significantly lower in the entire shielding space than when using only the active shield.

Figure 15 shows the experimental shielding factor of resulting MF with electromagnetic hybrid active-passive shield.

The maximum value of the experimental shielding factor of the MF when using electromagnetic hybrid active-passive shield is more than 4.2 units. The main advantage of the hybrid multy-circuit passive and active shield is the significantly lower level of the resulting MF induction over the entire shielding space by a factor of two or more compared to the active shield.

Consider one more setting of the active screening system when using a hybrid screen. Figure 16 shows the experimental distribution of the initial and resulting MF induction with electromagnetic hybrid active-passive shield for another setting of the active shielding system.

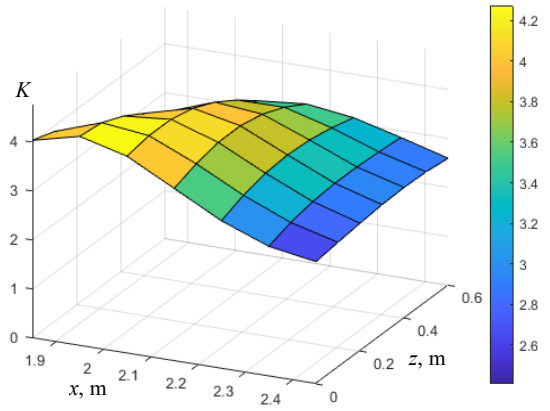

Fig. 15. The experimental shielding factor of resulting MF with electromagnetic hybrid active-passive shield

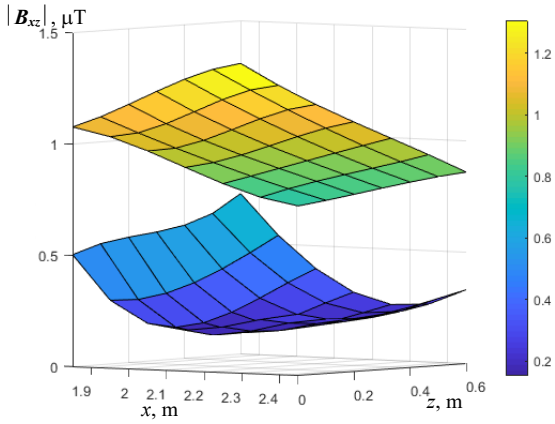

Fig. 16. The experimental distribution of the initial and resulting MF induction with electromagnetic hybrid active-passive shield for another setting of the active shielding system

Figure 17 shows the experimental shielding factor of resulting MF with electromagnetic hybrid active-passive shield for another setting of the active shielding system.

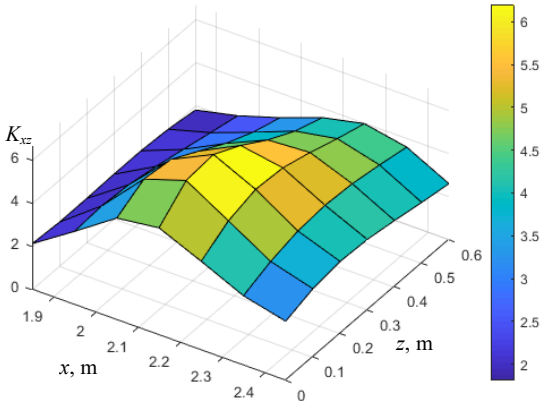

Fig. 17. The experimental shielding factor of resulting MF with electromagnetic hybrid active-passive shield for another setting of the active shielding system

For sush another setting of the active shielding system the maximum value of the experimental shielding factor of the MF when using electromagnetic hybrid active-passive shield is more 6.2 units, wich is more 1.47 times more than with the previously considered setting of the active shielding system. However, at the same time, at the edges of the shielding space, a significantly lower shielding efficiency is realized – more 1.7 times compared to the previously considered setting of the active shielding system.

Conclusions.

1. For the first time the method for designing electromagnetic hybrid active-passive shield, consisting from active and multy-circuit passive parts, which is characterized by increased effectiveness of reducing the industrial frequency magnetic field created by two-circuit overhead power lines in residential buildings was developed.

2. The problem of design of electromagnetic hybrid active-passive shield solved based on the multy-criteria two-player antagonistic game. The game payoff vector calculated based on the calculations system COMSOL Muliphysics. The solution of this game calculated based on algorithms of multy-swarm multy-agent optimization from sat of Pareto-optimal solutions based on binary preferences relationship.

3. The main advantage of using a electromagnetic hybrid active-passive shield, including an active and a multy-circuit passive part, is the possibility of reducing the level of the initial magnetic field induction in a significantly larger part of the shielding space compared to using only the active shield.

4. During the design of electromagnetic hybrid active-passive shield, the coordinates of the spatial arrangement of 11 circuit passive screens and the coordinates of the spatial location of one compensation winding, as well as the current and phase in this winding of the active shielding system were calculated.

5. The results of the performed theoretical studies what is confirmed byexperimental studies have shown that the shielding factor for only multy-circuit passive shield consisting of 11 aluminum contours with a diameter of 8 mm is about 1.2 units, for only active shield made in the form of a winding consisting of 20 turns is about 4 units and for electromagnetic hybrid active-passive shield, the shielding factor is more 6.2 units, what is confirmed by theoretical and experimental studies.

6. The practical use of the developed electromagnetic hybrid active-passive shield will allow to reduce the level of the magnetic field in a residential building from a double-circuit power transmission line with a «barrel» type arrangement of wires to a safe level for the population of 0.5 μT.

Acknowledgments. The authors express their gratitude to the engineers Sokol A.V. and Shevchenko A.P. of the Department of Magnetism of Technical Objects of Anatolii Pidhornyi Institute of Mechanical Engineering Problems of the National Academy of Sciences of Ukraine for the creative approach and courage shown during the creation under fire, under martial law, of an experimental installation and successful testing of a laboratory model of the system of active silencing.

Conflict of interest. The authors declare that they have no conflicts of interest.

REFERENCES

1. Sung H., Ferlay J., Siegel R.L., Laversanne M., Soerjomataram I., Jemal A., Bray, F. Global Cancer Statistics 2020: GLOBOCAN Estimates of Incidence and Mortality Worldwide for 36 Cancers in 185 Countries. *CA: A Cancer Journal for Clinicians*, 2021, vol. 71, no. 3, pp. 209-249. doi: https://doi.org/10.3322/caac.21660.

2. Directive 2013/35/EU of the European Parliament and of the Council of 26 June 2013 on the minimum health and safety requirements regarding the exposure of workers to the risks arising from physical agents (electromagnetic fields). Available at: http://data.europa.eu/eli/dir/2013/35/oj (Accessed 25.04.2024).

3. *The International EMF Project. Radiation & Environmental Health Protection of the Human Environment World Health Organization*. Geneva, Switzerland, 1996. 2 p. Available at: https://www.who.int/initiatives/the-international-emf-project (Accessed 25.04.2024).
4. Rozov V., Grinchenko V., Tkachenko O., Yerisov A. Analytical Calculation of Magnetic Field Shielding Factor for Cable Line with Two-Point Bonded Shields. *2018 IEEE 17th International Conference on Mathematical Methods in Electromagnetic Theory (MMET)*, 2018, pp. 358-361. doi: https://doi.org/10.1109/MMET.2018.8460425.
5. Rozov V.Yu., Reutskyi S.Yu., Pelevin D.Ye., Kundius K.D. Approximate method for calculating the magnetic field of 330-750 kV high-voltage power line in maintenance area under voltage. *Electrical Engineering & Electromechanics*, 2022, no. 5, pp. 71-77. doi: https://doi.org/10.20998/2074-272X.2022.5.12.
6. Rozov V.Y., Pelevin D.Y., Levina S.V. Experimental research into indoor static geomagnetic field weakening phenomenon. *Electrical Engineering & Electromechanics*, 2013, no. 6, pp. 72-76. (Rus).
7. Rozov V.Y., Kvytsynskyi A.A., Dobrodeyev P.N., Grinchenko V.S., Erisov A.V., Tkachenko A.O. Study of the magnetic field of three phase lines of single core power cables with two-end bonding of their shields. *Electrical Engineering & Electromechanics*, 2015, no. 4, pp. 56-61. (Rus). doi: https://doi.org/10.20998/2074-272X.2015.4.11.
8. Salceanu A., Paulet M., Alistar B.D., Asiminicesei O. Upon the contribution of image currents on the magnetic fields generated by overhead power lines. *2019 International Conference on Electromechanical and Energy Systems (SIELMEN).* 2019. doi: https://doi.org/10.1109/sielmen.2019.8905880.
9. Del Pino Lopez J.C., Romero P.C. Influence of different types of magnetic shields on the thermal behavior and ampacity of underground power cables. *IEEE Transactions on Power Delivery*, Oct. 2011, vol. 26, no. 4, pp. 2659-2667. doi: https://doi.org/10.1109/tpwrd.2011.2158593.
10. Hasan G.T., Mutlaq A.H., Ali K.J. The Influence of the Mixed Electric Line Poles on the Distribution of Magnetic Field. *Indonesian Journal of Electrical Engineering and Informatics (IJEEI)*, 2022, vol. 10, no. 2, pp. 292-301. doi: https://doi.org/10.52549/ijeei.v10i2.3572.
11. Victoria Mary S., Pugazhendhi Sugumaran C. Investigation on magneto-thermal-structural coupled field effect of nano coated 230 kV busbar. *Physica Scripta*, 2020, vol. 95, no. 4, art. no. 045703. doi: https://doi.org/10.1088/1402-4896/ab6524.
12. Ippolito L., Siano P. Using multi-objective optimal power flow for reducing magnetic fields from power lines. *Electric Power Systems Research*, 2004, vol. 68, no. 2, pp. 93-101. doi: https://doi.org/10.1016/S0378-7796(03)00151-2.
13. Barsali S., Giglioli R., Poli D. Active shielding of overhead line magnetic field: Design and applications. *Electric Power Systems Research*, May 2014, vol. 110, pp. 55-63. doi: https://doi.org/10.1016/j.epsr.2014.01.005.
14. Bavastro D., Canova A., Freschi F., Giaccone L., Manca M. Magnetic field mitigation at power frequency: design principles and case studies. *IEEE Transactions on Industry Applications*, May 2015, vol. 51, no. 3, pp. 2009-2016. doi: https://doi.org/10.1109/tia.2014.2369813.
15. Beltran H., Fuster V., García M. Magnetic field reduction screening system for a magnetic field source used in industrial applications. *9 Congreso Hispano Luso de Ingeniería Eléctrica (9 CHLIE)*, Marbella (Málaga, Spain), 2005, pp. 84-99.
16. Bravo-Rodríguez J., Del-Pino-López J., Cruz-Romero P. A Survey on Optimization Techniques Applied to Magnetic Field Mitigation in Power Systems. *Energies*, 2019, vol. 12, no. 7, p. 1332. doi: https://doi.org/10.3390/en12071332.
17. Canova A., del-Pino-López J.C., Giaccone L., Manca M. Active Shielding System for ELF Magnetic Fields. *IEEE Transactions on Magnetics*, March 2015, vol. 51, no. 3, pp. 1-4. doi: https://doi.org/10.1109/tmag.2014.2354515.
18. Canova A., Giaccone L. Real-time optimization of active loops for the magnetic field minimization. *International Journal of Applied Electromagnetics and Mechanics*, Feb. 2018, vol. 56, pp. 97-106. doi: https://doi.org/10.3233/jae-172286.
19. Canova A., Giaccone L., Cirimele V. Active and passive shield for aerial power lines. *Proc. of the 25th International Conference on Electricity Distribution (CIRED 2019)*, 3-6 June 2019, Madrid, Spain. Paper no. 1096.
20. Canova A., Giaccone L. High-performance magnetic shielding solution for extremely low frequency (ELF) sources. *CIRED - Open Access Proceedings Journal*, Oct. 2017, vol. 2017, no. 1, pp. 686-690. doi: https://doi.org/10.1049/oap-cired.2017.1029.
21. Grinchenko V.S., Chunikhin K.V. Magnetic field normalization in residential building located near overhead line by grid shield. *Electrical Engineering & Electromechanics*, 2020, no. 5, pp. 38-43. doi: https://doi.org/10.20998/2074-272X.2020.5.06.
22. Chunikhin K.V., Grinchenko V.S. Normalization of double-circuit overhead line magnetic field inside Khrushchev building. *Electrical Engineering & Electromechanics*, 2021, no. 3, pp. 38-41. doi: https://doi.org/10.20998/2074-272X.2021.3.06.
23. Celozzi S. Active compensation and partial shields for the power-frequency magnetic field reduction. *2002 IEEE International Symposium on Electromagnetic Compatibility*, Minneapolis, MN, USA, 2002, vol. 1, pp. 222-226. doi: https://doi.org/10.1109/isemc.2002.1032478.
24. Celozzi S., Garzia F. Active shielding for power-frequency magnetic field reduction using genetic algorithms optimization. *IEE Proceedings - Science, Measurement and Technology*, 2004, vol. 151, no. 1, pp. 2-7. doi: https://doi.org/10.1049/ip-smt:20040002.
25. Celozzi S., Garzia F. Magnetic field reduction by means of active shielding techniques. *WIT Transactions on Biomedicine and Health*, 2003, vol. 7, pp. 79-89. doi: https://doi.org/10.2495/ehr030091.
26. Popov A., Tserne E., Volosyuk V., Zhyla S., Pavlikov V., Ruzhentsev N., Dergachov K., Havrylenko O., Shmatko O., Averyanova Y., Ostroumov I., Kuzmenko N., Sushchenko O., Zaliskyi M., Solomentsev O., Kuznetsov B., Nikitina T. Invariant Polarization Signatures for Recognition of Hydrometeors by Airborne Weather Radars. *Computational Science and Its Applications – ICCSA 2023. Lecture Notes in Computer Science*, 2023, vol. 13956, pp. 201-217. doi: https://doi.org/10.1007/978-3-031-36805-9_14.
27. Sushchenko O., Averyanova Y., Ostroumov I., Kuzmenko N., Zaliskyi M., Solomentsev O., Kuznetsov B., Nikitina T., Havrylenko O., Popov A., Volosyuk V., Shmatko O., Ruzhentsev N., Zhyla S., Pavlikov V., Dergachov K., Tserne E. Algorithms for Design of Robust Stabilization Systems. *Computational Science and Its Applications – ICCSA 2022. ICCSA 2022. Lecture Notes in Computer Science*, 2022, vol. 13375, pp. 198-213. doi: https://doi.org/10.1007/978-3-031-10522-7_15.
28. Ostroverkhov M., Chumack V., Monakhov E., Ponomarev A. Hybrid Excited Synchronous Generator for Microhydropower Unit. *2019 IEEE 6th International Conference on Energy Smart Systems (ESS)*, Kyiv, Ukraine, 2019, pp. 219-222. doi: https://doi.org/10.1109/ess.2019.8764202.
29. Ostroverkhov M., Chumack V., Monakhov E. Ouput Voltage Stabilization Process Simulation in Generator with Hybrid Excitation at Variable Drive Speed. *2019 IEEE 2nd Ukraine Conference on Electrical and Computer Engineering (UKRCON)*, Lviv, Ukraine, 2019, pp. 310-313. doi: https://doi.org/10.1109/ukrcon.2019.8879781.
30. Tytiuk V., Chornyi O., Baranovskaya M., Serhiienko S., Zachepa I., Tsvirkun L., Kuznetsov V., Tryputen N. Synthesis of a fractional-order $PI^{\lambda}D^{\mu}$-controller for a closed system of switched reluctance motor control. *Eastern-European Journal of Enterprise Technologies*, 2019, no. 2 (98), pp. 35-42. doi: https://doi.org/10.15587/1729-4061.2019.160946.
31. Zagirnyak M., Chornyi O., Zachepa I. The autonomous sources of energy supply for the liquidation of technogenic accidents. *Przeglad Elektrotechniczny*, 2019, no. 5, pp. 47-50. doi: https://doi.org/10.15199/48.2019.05.12.
32. Chornyi O., Serhiienko S. A virtual complex with the parametric adjustment to electromechanical system parameters. *Technical Electrodynamics*, 2019, no. 1, pp. 38-41. doi: https://doi.org/10.15407/techned2019.01.038.
33. Shchur I., Kasha L., Bukavyn M. Efficiency Evaluation of Single and Modular Cascade Machines Operation in Electric Vehicle. *2020 IEEE 15th International Conference on Advanced Trends in Radioelectronics, Telecommunications and Computer Engineering (TCSET)*, Lviv-Slavske, Ukraine, 2020, pp. 156-161. doi: https://doi.org/10.1109/tcset49122.2020.235413.
34. Zhyla S., Volosyuk V., Pavlikov V., Ruzhentsev N., Tserne E., Popov A., Shmatko O., Havrylenko O., Kuzmenko N., Dergachov K., Averyanova Y., Sushchenko O., Zaliskyi M., Solomentsev O., Ostroumov I., Kuznetsov B., Nikitina T. Practical imaging algorithms in ultra-wideband radar systems using active aperture synthesis and

stochastic probing signals. *Radioelectronic and Computer Systems*, 2023, no. 1, pp. 55-76. doi: https://doi.org/10.32620/reks.2023.1.05.
35. Havrylenko O., Dergachov K., Pavlikov V., Zhyla S., Shmatko O., Ruzhentsev N., Popov A., Volosyuk V., Tserne E., Zaliskyi M., Solomentsev O., Ostroumov I., Sushchenko O., Averyanova Y., Kuzmenko N., Nikitina T., Kuznetsov B. Decision Support System Based on the ELECTRE Method. *Data Science and Security. Lecture Notes in Networks and Systems*, 2022, vol. 462, pp. 295-304. doi: https://doi.org/10.1007/978-981-19-2211-4_26.
36. Solomentsev O., Zaliskyi M., Averyanova Y., Ostroumov I., Kuzmenko N., Sushchenko O., Kuznetsov B., Nikitina T., Tserne E., Pavlikov V., Zhyla S., Dergachov K., Havrylenko O., Popov A., Volosyuk V., Ruzhentsev N., Shmatko O. Method of Optimal Threshold Calculation in Case of Radio Equipment Maintenance. *Data Science and Security. Lecture Notes in Networks and Systems*, 2022, vol. 462, pp. 69-79. doi: https://doi.org/10.1007/978-981-19-2211-4_6.
37. Shmatko O., Volosyuk V., Zhyla S., Pavlikov V., Ruzhentsev N., Tserne E., Popov A., Ostroumov I., Kuzmenko N., Dergachov K., Sushchenko O., Averyanova Y., Zaliskyi M., Solomentsev O., Havrylenko O., Kuznetsov B., Nikitina T. Synthesis of the optimal algorithm and structure of contactless optical device for estimating the parameters of statistically uneven surfaces. *Radioelectronic and Computer Systems*, 2021, no. 4, pp. 199-213. doi: https://doi.org/10.32620/reks.2021.4.16.
38. Volosyuk V., Zhyla S., Pavlikov V., Ruzhentsev N., Tserne E., Popov A., Shmatko O., Dergachov K., Havrylenko O., Ostroumov I., Kuzmenko N., Sushchenko O., Averyanova Yu., Zaliskyi M., Solomentsev O., Kuznetsov B., Nikitina T. Optimal Method for Polarization Selection of Stationary Objects Against the Background of the Earth's Surface. *International Journal of Electronics and Telecommunications*, 2022, vol. 68, no. 1, pp. 83-89. doi: https://doi.org/10.24425/ijet.2022.139852.
39. Halchenko V., Trembovetska R., Bazilo C., Tychkova N. Computer Simulation of the Process of Profiles Measuring of Objects Electrophysical Parameters by Surface Eddy Current Probes. *Lecture Notes on Data Engineering and Communications Technologies*, 2023, vol. 178, pp. 411-424. doi https://doi.org/10.1007/978-3-031-35467-0_25.
40. Halchenko V., Bacherikov D., Filimonov S., Filimonova N. Improvement of a Linear Screw Piezo Motor Design for Use in Accurate Liquid Dosing Assembly. *Smart Technologies in Urban Engineering. STUE 2022. Lecture Notes in Networks and Systems*, 2023, vol. 536, pp. 237-247. doi: https://doi.org/10.1007/978-3-031-20141-7_22.
41. Ruzhentsev N., Zhyla S., Pavlikov V., Volosyuk V., Tserne E., Popov A., Shmatko O., Ostroumov I., Kuzmenko N., Dergachov K., Sushchenko O., Averyanova Y., Zaliskyi M., Solomentsev O., Havrylenko O., Kuznetsov B., Nikitina T. Radio-Heat Contrasts of UAVs and Their Weather Variability at 12 GHz, 20 GHz, 34 GHz, and 94 GHz Frequencies. *ECTI Transactions on Electrical Engineering, Electronics, and Communications*, 2022, vol. 20, no. 2, pp. 163-173. doi: https://doi.org/10.37936/ecti-eec.2022202.246878.
42. Maksymenko-Sheiko K.V., Sheiko T.I., Lisin D.O., Petrenko N.D. Mathematical and Computer Modeling of the Forms of Multi-Zone Fuel Elements with Plates. *Journal of Mechanical Engineering*, 2022, vol. 25, no. 4, pp. 32-38. doi: https://doi.org/10.15407/pmach2022.04.032.
43. Hontarovskyi P.P., Smetankina N.V., Ugrimov S.V., Garmash N.H., Melezhyk I.I. Computational Studies of the Thermal Stress State of Multilayer Glazing with Electric Heating. *Journal of Mechanical Engineering*, 2022, vol. 25, no. 1, pp. 14-21. doi: https://doi.org/10.15407/pmach2022.02.014.
44. Kostikov A.O., Zevin L.I., Krol H.H., Vorontsova A.L. The Optimal Correcting the Power Value of a Nuclear Power Plant Power Unit Reactor in the Event of Equipment Failures. *Journal of Mechanical Engineering*, 2022, vol. 25, no. 3, pp. 40-45. doi: https://doi.org/10.15407/pmach2022.03.040.
45. Rusanov A.V., Subotin V.H., Khoryev O.M., Bykov Y.A., Korotaiev P.O., Ahibalov Y.S. Effect of 3D Shape of Pump-Turbine Runner Blade on Flow Characteristics in Turbine Mode. *Journal of Mechanical Engineering*, 2022, vol. 25, no. 4, pp. 6-14. doi: https://doi.org/10.15407/pmach2022.04.006.
46. Ummels M. *Stochastic Multiplayer Games Theory and Algorithms*. Amsterdam University Press, 2010. 174 p.
47. Ray T., Liew K.M. A Swarm Metaphor for Multiobjective Design Optimization. *Engineering Optimization*, 2002, vol. 34, no. 2, pp. 141-153. doi: https://doi.org/10.1080/03052150210915.
48. Xiaohui Hu, Eberhart R.C., Yuhui Shi. Particle swarm with extended memory for multiobjective optimization. *Proceedings of the 2003 IEEE Swarm Intelligence Symposium*. SIS'03 (Cat. No.03EX706), Indianapolis, IN, USA, 2003, pp. 193-197. doi: https://doi.org/10.1109/sis.2003.1202267.
49. Dergachov K., Havrylenko O., Pavlikov V., Zhyla S., Tserne E., Volosyuk V., Ruzhentsev N., Ostroumov I., Averyanova Y., Sushchenko O., Popov A., Shmatko O., Solomentsev O., Zaliskyi M., Kuzmenko N., Kuznetsov B., Nikitina T. GPS Usage Analysis for Angular Orientation Practical Tasks Solving. *2022 IEEE 9th International Conference on Problems of Infocommunications, Science and Technology (PIC S&T)*, 2022, pp. 187-192. doi: https://doi.org/10.1109/PICST57299.2022.10238629.
50. Zhyla S., Volosyuk V., Pavlikov V., Ruzhentsev N., Tserne E., Popov A., Shmatko O., Havrylenko O., Kuzmenko N., Dergachov K., Averyanova Y., Sushchenko O., Zaliskyi M., Solomentsev O., Ostroumov I., Kuznetsov B., Nikitina T. Statistical synthesis of aerospace radars structure with optimal spatio-temporal signal processing, extended observation area and high spatial resolution. *Radioelectronic and Computer Systems*, 2022, no. 1, pp. 178-194. doi: https://doi.org/10.32620/reks.2022.1.14.
51. Hashim F.A., Hussain K., Houssein E.H., Mabrouk M.S., Al-Atabany W. Archimedes optimization algorithm: a new metaheuristic algorithm for solving optimization problems. *Applied Intelligence*, 2021, vol. 51, no. 3, pp. 1531-1551. doi: https://doi.org/10.1007/s10489-020-01893-z.

Received 14.01.2024
Accepted 13.03.2024
Published 20.06.2024

B.I. Kuznetsov[1], *Doctor of Technical Science, Professor,*
T.B. Nikitina[2], *Doctor of Technical Science, Professor,*
I.V. Bovdui[1], *PhD, Senior Research Scientist,*
K.V. Chunikhin[1], *PhD, Senior Research Scientist,*
V.V. Kolomiets[2], *PhD, Assistant Professor,*
B.B. Kobylianskyi[2], *PhD, Assistant Professor,*
[1] Anatolii Pidhornyi Institute of Mechanical Engineering Problems of the National Academy of Sciences of Ukraine,
2/10, Pozharskogo Str., Kharkiv, 61046, Ukraine,
e-mail: kuznetsov.boris.i@gmail.com (Corresponding Author)
[2] Educational Scientific Professional Pedagogical Institute V.N. Karazin Kharkiv National Univesity,
9a, Nosakov Str., Bakhmut, Donetsk Region, 84511, Ukraine,
e-mail: nnppiuipa@ukr.net

How to cite this article:
Kuznetsov B.I., Nikitina T.B., Bovdui I.V., Chunikhin K.V., Kolomiets V.V., Kobylianskyi B.B. The method for design of electromagnetic hybrid active-passive shielding by overhead power lines magnetic field. *Electrical Engineering & Electromechanics*, 2024, no. 4, pp. 22-30. doi: https://doi.org/10.20998/2074-272X.2024.4.03

UDC 621.3 https://doi.org/10.20998/2074-272X.2024.4.04

Ch. Sajan, P. Satish Kumar, P. Virtic

Enhancing grid stability and low voltage ride through capability using type 2 fuzzy controlled dynamic voltage restorer

Introduction. *The integration of Renewable Energy Sources (RESs), particularly Wind Energy Conversion Systems (WECS), is vital for reducing reliance on fossil fuels and addressing climate change. However, this transition poses challenges, including ensuring grid stability in the face of intermittent RESs. Compliance with grid codes is crucial, with a focus on Low Voltage Ride Through (LVRT) capability.* ***Problem.*** *The intermittent nature of RESs, specifically in Permanent Magnet Synchronous Generator (PMSG) based WECS, presents challenges to grid stability during voltage dips.* ***Goal.*** *To enhance voltage stability and LVRT capability in PMSG-based WECS by integrating a Dynamic Voltage Restorer (DVR) with an energy storage device. This involves regulating the input DC voltage to the DVR using a type 2 fuzzy controller, adapting intelligently to changing conditions.* ***Methodology.*** *DVR, powered by an energy storage device, is strategically integrated with WECS. A type 2 fuzzy controller regulates the DC voltage to DVR. The rectified WECS output undergoes processing through an isolated flyback converter. A 31-level Cascaded H-Bridge Multilevel Inverter (CHBMLI) with PI control ensures high-quality AC output.* ***Results.*** *The validation of developed system is executed using MATLAB/Simulink revealing a reduced Total Harmonic Distortion (THD) value of 1.8 %, ensuring significance in LVRT capability.* ***Originality.*** *The strategic integration of DVR with PMSG-based WECS, addresses the LVRT challenges. The use of type 2 fuzzy controller for intelligent voltage regulation and a sophisticated multilevel inverter contributes to the uniqueness of proposed solution.* ***Practical value.*** *The developed system provides benefits by ensuring reliable LVRT capability in PMSG-based WECS with reduced THD of 1.8 % indicating improved grid compatibility.* References 26, tables 5, figures 20.

Key words: **permanent magnet synchronous generator, wind energy conversion systems, low voltage ride through, type 2 fuzzy controller, isolated flyback converter, 31-level cascaded H-bridge multilevel inverter, PI controller.**

Вступ. *Інтеграція відновлюваних джерел енергії (RESs), особливо систем перетворення енергії вітру (WECS), має життєво важливе значення для зниження залежності від викопного палива та вирішення проблеми зміни клімату. Однак цей перехід створює проблеми, у тому числі забезпечення стабільності мережі в умовах уривчастої роботи RESs. Дотримання мережевих норм має вирішальне значення, при цьому особлива увага приділяється можливості роботи при низькій напрузі (LVRT).* ***Проблема***. *Уривчастий характер RESs, особливо в WECS на основі синхронного генератора з постійними магнітами (PMSG), створює проблеми для стабільності мережі під час провалів напруги.* ***Мета***. *Підвищити стабільність напруги та можливості LVRT у WECS на базі PMSG за рахунок інтеграції динамічного відновника напруги (DVR) із пристроєм зберігання енергії. Це передбачає регулювання вхідної постійної напруги на DVR за допомогою нечіткого контролера типу 2, що інтелектуально адаптується до умов, що змінюються.* ***Методологія***. *DVR, який працює від накопичувача енергії, стратегічно інтегрований із WECS. Нечіткий контролер типу 2 регулює напругу постійного струму, що подається на DVR. Випрямлений вихідний сигнал WECS проходить обробку через ізольований зворотноходовий перетворювач. 31-рівневий каскадний багаторівневий інвертор H-Bridge (CHBMLI) із ПІ-регулюванням забезпечує високоякісний вихід змінного струму.* ***Результати***. *Валідація розробленої системи виконується з використанням MATLAB/Simulink, демонструючи зменшене значення загального гармонічного спотворення (THD) 1,8 %, що забезпечує важливість можливостей LVRT.* ***Оригінальність***. *Стратегічна інтеграція DVR із WECS на базі PMSG вирішує проблеми LVRT. Використання нечіткого контролера 2-го типу для інтелектуального регулювання напруги та складного багаторівневого інвертора сприяє унікальності запропонованого рішення.* ***Практична цінність***. *Розроблена система забезпечує переваги, забезпечуючи надійну роботу LVRT у WECS на базі PMSG зі зниженим THD на 1,8 %, що вказує на покращену сумісність із мережею.* Бібл. 26, табл. 5, рис. 20.

Ключові слова: **синхронний генератор з постійними магнітами, системи перетворення енергії вітру, прохідність низької напруги, нечіткий контролер типу 2, ізольований зворотноходовий перетворювач, 31-рівневий каскадний багаторівневий інвертор Н-мосту, ПІ-регулятор.**

Abbreviations

CHBMLI	Cascaded H-Bridge Multilevel Inverter	STATCOM	Static Synchronous Compensator
DVR	Dynamic Voltage Restorer	SVC	Static Var Compensator
ESD	Energy Storage Device	THD	Total Harmonic Distortion
LVRT	Low Voltage Ride Through	T2-FLC	Type 2 Fuzzy Logic Controller
PMSG	Permanent Magnet Synchronous Generator	VSI	Voltage Source Inverter
PCC	Point of Common Coupling	VUF	Voltage Unbalance Factor
PWM	Pulse Width Modulator	WECS	Wind Energy Conversion Systems
RES	Renewable Energy Source	WT	Wind Turbines

Introduction. The adoption of wind power has experienced rapid growth, evident from the surge in wind farm installations. In 2018 alone, 51.3 GW of wind energy capacity was added, contributing to a significant total installed capacity of 591 GW by that year. Wind power stands out as a sustainable and eco-friendly energy source, offering the advantage of offshore installations to conserve land resources [1]. Despite these benefits, the expanding presence of wind power raises concerns about the stability of the power grid. Consequently, there is a pressing need for more stringent grid regulations to ensure the incorporation of wind power systems without compromising the existing grid's reliability and stability [2].

As wind power integration expands, grid stability becomes crucial. PMSG WTs offer superior control. Unlike doubly fed induction generator [3] turbines, PMSG turbines have a broader operational range using advanced converters. The key advantage of PMSG WTs lies in their wide operational range, leveraging power converters like machine-side converters and grid-side converters to their fullest extent [4]. To regulate power

© Ch. Sajan, P. Satish Kumar, P. Virtic

flow in PMSG-WECS during unbalanced conditions, back-to-back converters are essential [5]. These converters help maintain stable voltages, particularly during asymmetrical faults. Due to the nonlinear nature of wind farms, automated control strategies are crucial [6].

Numerous techniques have been suggested to mitigate fluctuations in wind power. In prior studies, researchers [7] focused on pitch angle control, aiming to achieve stable output power levels and minimize flicker. Another approach explored the utilization of indirect field oriented control for power smoothing [8]. However, these methods have limitations in terms of control range due to reduced wind power acquisition. PMSG is highly susceptible to grid voltage disturbances, leading to issues such as rotor over-current, excessive DC-link voltage, and torque oscillations during grid faults. These problems impact the drive's lifespan. To enhance LVRT capability of PMSG-WECS, various solutions have been suggested that are broadly categorized as software-based and hardware-based [9]. Table 1 summarizes some of the hardware and software based solution with their challenges.

Table 1

Summary of existing solution

Solution	Advantages	Challenges	Solutions proposed
Software based solution			
Demagnetizing control [10]	Suitable for Moderate faults	Limited effectiveness during severe grid faults	DVR with type 2 fuzzy overcomes limited effectiveness during severe grid faults
Flux linkage tracking control [11]	Enhanced stability and better fault detection	Increased computational load and limited to specific grid conditions	Fuzzy logic controllers are known for their ability to handle uncertainties and variations without requiring precise mathematical models, potentially leading to a more computationally efficient solution
Partial feedback linearization control [12]	Improved response time with enhanced grid integration	Complexity in implementation and requires precise modeling of system dynamics	Type 2 fuzzy logic, are known for their ability to handle uncertainties and variations in a flexible manner thereby facilitating reduced computational complexity
Hardware based solution			
Fault current limiter [13]	High fault tolerance	Expensive technology and maintenance challenges	Reduces the need for constant fine-tuning and adjustment which is beneficial for maintenance
Crowbar and chopper scheme [14]	Quick response to faults	Disruptive to grid during activation and limited effectiveness for prolonged faults	In the context of prolonged faults, the type 2 fuzzy controller could intelligently adjust the control parameters to maintain optimal performance, ensuring sustained effectiveness
Series grid-side converter [15]	Provides grid support and effective for unbalanced faults	Requires precise control	Type 2 fuzzy controller intelligently regulates the input DC voltage to the DVR, adapting to the dynamic and changing conditions that may occur during grid faults which is crucial in scenarios where precise control would be difficult

Flexible AC transmission system technology, utilizing power electronics, addresses power industry challenges. Devices like STATCOM [16] and SVC [17] come in series, shunt, and hybrid connections. STATCOM supplies reactive power to regulate voltage at PCC, while SVC enhances system stability. However, drawbacks include high cost, complexity, and grid-specific effectiveness, making implementation challenging for some utilities. As a consequence, DVR [18] is implemented in the proposed work, to compensate for LVRT and maintain a stable voltage supply to sensitive loads. When voltage sags occur due to faults or disturbances in the grid, the DVR detects sag and injects compensating voltage, restoring power quality to connected equipment.

These protective methods enhance LVRT performance to some extent. However, without an ESD, WTs are unable to regulate output power fluctuations effectively. Alternatively, ESDs have been widely considered [19, 20], for smooth active power fluctuations but also regulate reactive power. In such a way, DVRs are connected in series with the load and coupled with ESD, transformer, and inverter. These components compensate for active and reactive power needs during voltage fluctuations [21]. DVRs stabilize voltages by injecting compensating voltage into the distribution system via a transformer. In [22] optimized PI control with a gradient adaptive variable learning rate Least Mean Square algorithm is developed to ensure adaptability by adjusting step sizes, making it robust in dynamic system conditions. Still, optimizing and implementing adaptive algorithms, require significant computational resources and could add complexity to system. Levenberg Marquardt back-propagation algorithm, and Adaptive Neuro-Fuzzy Inference System model in [23] shows improved accuracy and power quality responses. However, potential challenges include the complexity of implementing advanced artificial intelligence techniques, requiring expertise, and the computational resources. Addressing these research gaps would provide a more exact understanding of the challenges and opportunities in enhancing LVRT capabilities in PMSG-wind energy systems, leading to more effective and reliable grid integration solutions. Therefore, the main purpose of this work is to address the challenges associated with the integration of RESs, specifically focusing on the intermittent nature of PMSG based WECS. The primary goal is to enhance grid stability and LVRT capability by proposing a solution that strategically integrates a DVR with an ESD. The innovative use of a type 2 fuzzy controller for intelligent regulation of the DVR's input DC voltage, coupled with a sophisticated 31-Level CHBMLI, aims to ensure high-quality AC output and reduced THD, ultimately providing a practical and reliable system for improved grid compatibility and stability in PMSG based WECS. The key contributions of the work include:

- Integrates DVR with supercapacitor to enhance LVRT capability of WECS.

• Implements type 2 fuzzy controller for precise and adaptive control of DVR, ensuring stable responses to voltage fluctuations and grid disturbances.

• Incorporates DVR, isolated flyback converter, and reduced switch 31-Level CHBMLI controlled by PI controller for seamless power flow and high-quality AC output.

Description of proposed work. The goal of this research is to address the challenges associated with integrating RESs, particularly WECS, into the modern power grid (Fig. 1). The focus lies on enhancing LVRT capability, crucial for maintaining grid stability in the presence of intermittent and variable RESs. This has been achieved through the strategic integration of key components.

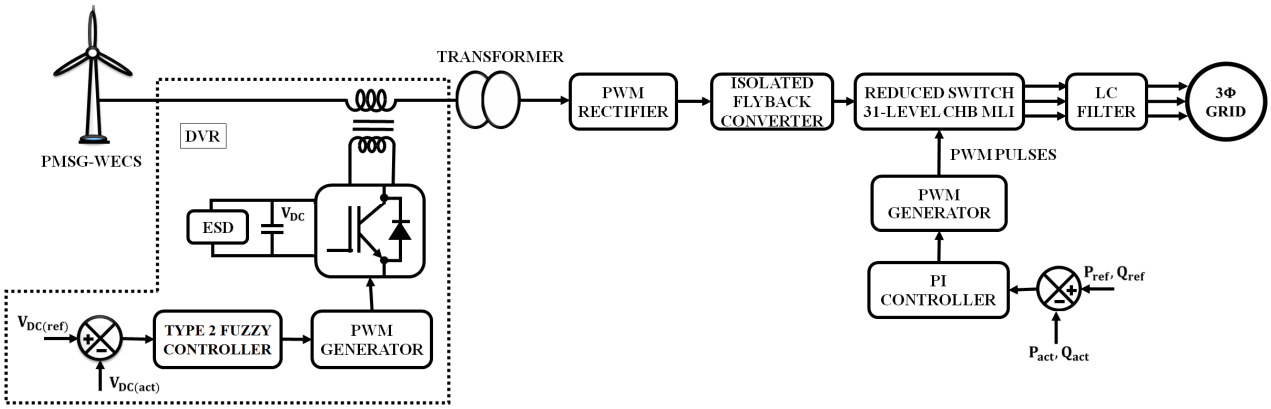

Fig. 1. Proposed PMSG-WECS with DVR

The proposed system is an intricate and efficient solution for integrating wind energy into power grid, ensuring grid stability, even during voltage dips and disturbances. It begins with a WECS equipped with a PMSG that captures wind energy and transforms it into electrical power. To tackle situations of LVRT, the system seamlessly activates DVR linked to a supercapacitor acting as an ESD. This combination ensures a continuous supply of stable AC power to the grid, mitigating voltage fluctuations. Crucially, a type 2 fuzzy controller regulates the input voltage to DVR, adapting to dynamic grid conditions. To refine the power output, the system utilizes a transformer to step up the voltage and PWM rectifier to convert the AC supply into DC, which is directed to an isolated flyback converter. This converter adjusts voltage levels and ensures electrical isolation. The regulated output from flyback converter is then fed into 31 CHBMLI. This advanced inverter converts DC into AC power by creating multiple voltage levels, minimizing harmonics and voltage variations in output. To ensure precision control, the PI controller at the grid side continuously monitors real and reactive power, generating control signals for 31-level CHBMLI. These signals adjust the inverter's operation, maintaining the required voltage and frequency, facilitating efficient and reliable grid synchronization. The proposed LVRT solution with DVR surpasses existing systems by offering a combination of fast response times, continuous supply stability, adaptability, reduced voltage fluctuations, improved grid resilience, and a unified system integration approach.

Modelling of system components. PMSG-WT modelling. Modelling a PMSG-based WT is essential for understanding its dynamic behavior and optimizing performance. Figure 2 depicts the schematic representation of PMSG wind system.

Aerodynamic modelling. The PMSG based WT harnesses wind energy to produce mechanical power through the following mechanism:

$$P_W = \frac{1}{2}\rho A V_W^3 C_p(\lambda,\beta). \quad (1)$$

Here, the captured wind power P_W in the PMSG-WT is determined by power coefficient C_p, air density ρ, swept area A and wind velocity without rotor interference V_W^3. As shown in (1), the power coefficient of a WT is determined by the ratio of pitch angle β to tip speed λ:

$$C_p(\lambda,\beta) = c_1\left(\frac{c_2}{\lambda_i} - c_3\beta - c_4\right)e^{-c_5/\lambda_i} + c_6\lambda, \quad (2)$$

where

$$\frac{1}{\lambda_i} = \frac{1}{\lambda - 0.08\beta} - \frac{0.035}{\beta^3 + 1}, \quad (3)$$

and characteristics of wind are represented as c_1 – c_6, respectively.

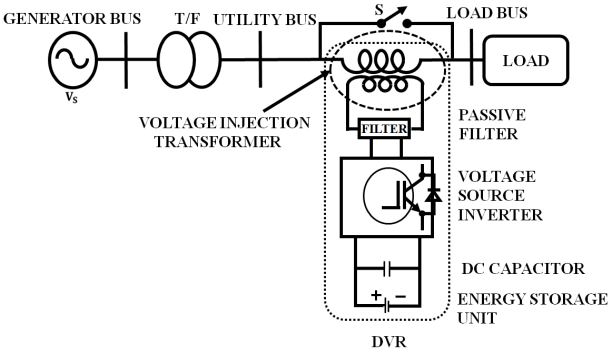

Fig. 2. DVR based scheme for LVRT improvement of PMSG

PMSG modelling. The dynamic model of PMSG WT employs *dq* reference rotating frame, expressed as:

$$\frac{d\psi_{sd}}{dt} = -V_{sd} - R_s I_{sd} - \omega_e \psi_{sq}; \quad (4)$$

$$\frac{d\psi_{sq}}{dt} = -V_{sq} - R_s I_{sq} - \omega_e \psi_{sd}. \quad (5)$$

From (4) and (5):

$$\psi_{sd} = (L_{sd} + L_{md})I_{sd} + \psi_m; \quad (6)$$

$$\psi_{sq} = (L_{sq} + L_{mq})I_{sq}, \quad (7)$$

where ψ_{sq}, ψ_{sd} are the stator flux linkages; L_{sq}, L_{sd} are the stator leakage inductances; L_{md}, L_{mq} refer to magnetizing

inductances; ψ_m is the linkage flux of the permanent magnet in the motor.

On solving the differential expression becomes

$$L_d \frac{\mathrm{d}I_{sd}}{\mathrm{d}t} = -V_{sd} - R_s I_{sd} - \omega_e L_q I_{sq}\,; \tag{8}$$

$$L_q \frac{\mathrm{d}I_{sq}}{\mathrm{d}t} = -V_{sq} - R_s I_{sq} - \omega_e L_d I_{sd} + \omega_e \psi_m\,; \tag{9}$$

$$P_s = V_{sd} I_{sd} + V_{sq} I_{sq}\,; \tag{10}$$

$$Q_s = V_{sq} I_{sd} - V_{sd} I_{sq}\,; \tag{11}$$

Enhancing LVRT by DVR technology. The DVR is essential for mitigating LVRT issues in renewable energy systems, especially PMSG-WECS. During grid faults, it swiftly detects voltage deviations and injects compensating voltage into the system. Continuous monitoring at the PCC allows the DVR to calculate and counteract voltage errors, ensuring rapid correction within milliseconds. Key elements like ESD, VSI and passive filters work together to manage voltage sags and harmonics, enhancing the resilience of power networks and minimizing disruptions to sensitive loads.

Energy storage device. ESD within a DVR incorporates various storage devices, in the proposed work it is supercapacitor. Its primary function is to provide essential real power during instances of voltage sags. DVR's compensating ability depends on ESD's quick charging and draining response times, where the rate of discharge determines how much internal space is set aside for energy storage.

Voltage source inverter. The pulse-width modulated VSI is responsible for converting DC voltage sourced from the ESD into AC voltage. This converted AC voltage is then supplied to the series transformer, which acts as a step-up voltage injection transformer. The series transformer elevates the voltage to effectively counteract conditions of voltage sag. Notably, the VSI operates with minimal voltage output, and for DVR protection, a bypass switch is commonly integrated.

Passive filters. To address the high-frequency harmonic in output of VSI, DVRs are equipped with passive filters. When positioned on inverter side, passive filters notably reduce stress on injection transformer. Simultaneously, when placed on the load side, they minimize harmonic content originating from transformer's secondary side. This integration of passive filters contributes to enhanced system performance and stability by mitigating the impact of harmonic distortions in DVR's output.

The DVR integrated in the line between PMSG and grid, enhances PMSG's LVRT capability. Capable of mitigating voltage fluctuations, including swells, sags, and harmonics, the DVR is particularly effective in compensating for voltage sag incidents in LVRT applications of PMSG. Figure 2 illustrates the installation of DVR at PCC, where it injects series voltage to compensate for active and reactive power in grid, aiding recovery from faults.

The injected series voltage by the DVR is expressed as:

$$V_{DVR} = V_L + Z_{TH} I_L - V_{TH}\,, \tag{12}$$

where I_L is the load current; V_L is the load voltage; Z_{TH} is the load impedance; V_{TH} is the system voltage during fault. The expression for load current is:

$$I_l = \frac{P_L + jQ_L}{V}\,. \tag{13}$$

On considering V_L as a reference, the equation is reformulated as:

$$V^*_{DVR} = V_L^{\angle 0} + Z_{TH}^{\angle(\beta-\theta)} - V_{TH}^{\angle\delta}\,, \tag{14}$$

where

$$\theta = \tanh^{-1}\left(\frac{\theta_L}{P_L}\right). \tag{15}$$

The expression for DVR's complex power output is:

$$S_{DVR} = V_{DVR} \cdot I^*_{DVR}\,. \tag{16}$$

The DVR's power rating is determined by magnitude of fault voltage to be compensated, and relationship provided calculates required active power of the DVR (P_{DVR}) for voltage sags and swells, considering a zero-phase angle jump:

$$P_{DVR} = \left(\frac{V_{pcc} - V_f}{V_{pcc}}\right) \cdot P_{load}\,, \tag{17}$$

where V_f is the voltage at terminals of voltage source converter in DVR; P_{load} is the active power consumed by load; V_{pcc} is the voltage at PCC.

Additionally, the Voltage Unbalance Factor (VUF) is assessed according to the standards set by the National Electrical Manufacturers Association is expressed as:

$$VUF(\%) = \frac{V_2}{V_1} \cdot 100\%\,, \tag{18}$$

where the positive sequence voltage V_1 and negative sequence voltage V_2 are considered, with phase angle δ between grid voltage V_g and terminal voltage of PMSG V_t needing to be kept below a specified maximum value to prevent overloading of DVR.

The given equation establishes the maximum allowable phase angle:

$$\delta_{\max} = \cos^{-1}\left(\frac{V_t^2 + V_g^2 - V_{c(\max)}^2}{2 \cdot V_d \cdot V_t}\right), \tag{19}$$

where $V_{c\max}$ is the maximum compensating voltage provided by DVR.

For enhancing performance of DVR the proposed work implements type 2 fuzzy controller, which ensures precise and adaptive regulation of voltage fluctuations and grid disturbances for seamless operation.

Type 2 fuzzy logic controller. T2-FLC is an advanced fuzzy logic system that handles uncertainties more effectively than traditional fuzzy controllers. In the context of DVR control, where power grid disturbances and uncertainties are prevalent, T2-FLC offers enhanced capabilities. The architecture of proposed T2-FLC is illustrated in Fig. 3.

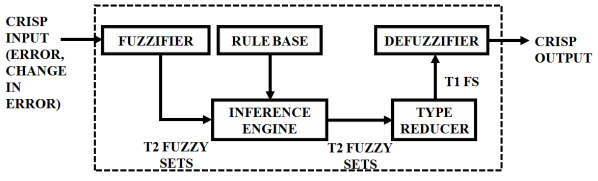

Fig. 3. Proposed structure of T2-FLC

Here's how type 2 fuzzy logic can be specifically applied for DVR control.

Fuzzification. Crisp input signals are generated by comparing the reference DC link voltage (expected stable voltage level) and the actual DC link voltage (measured voltage level during grid disturbances). These crisp inputs are fuzzified by T2-FLC into fuzzy variables using appropriate membership functions. The use of type 2 fuzzy sets allows the controller to handle uncertainties and variations effectively.

Rule base. The T2-FLC utilizes a set of fuzzy IF-THEN rules stored in the rule base. These rules capture the relationships between the fuzzy input variables. For instance, «IF Deviation is Negative Large AND Change in Deviation is Positive Small, THEN Control Signal is X». These rules encode the expert knowledge or system behavior and guide the inference process.

Inference engine. The inference engine applies FLC operations (such as AND, OR) on fuzzy input variables based on the fuzzy rules. This process results in fuzzy output sets that represent the intermediate control actions inferred from the inputs. In T2-FLC, additional operations are performed to handle uncertainties in the inference process, ensuring robust control decisions.

Table 2 illustrates generic example of fuzzy rules for a simplified scenario involving the control of DVR based on 2 input variables: «Error» (deviation between reference and actual DC link voltage) and «Change in Error» (rate of change of error).

Table 2

Fuzzy rule

Error	Change in error	Control signal
NL	*NL*	*NL*
NL	*NS*	*NM*
NL	*Z*	*NS*
NL	*PS*	*Z*
NL	*PL*	*PS*
NS	*NL*	*NM*
NS	*NS*	*NS*
NS	*Z*	*Z*
NS	*PS*	*PS*
NS	*PL*	*PM*

In Table 2 *NL*, *NS*, *NM* are negative large, negative small and negative medium, while *PL*, *PS*, *PM* are positive large, positive small and positive medium. Also *Z* indicates zero.

Type reducer. The output from the inference stage is a T2-fuzzy set, which contains more uncertainty than type-1 fuzzy sets. Type reduction is the process of converting the T2 fuzzy set into a more manageable T1-fuzzy set. It reduces the uncertainty associated with the control decisions, making them more reliable.

Defuzzification. Fuzzy output sets back into crisp control signals using defuzzification methods. This algorithm calculates the crisp control signals using the centroids and spreads of fuzzy output sets, ensuring precise and effective control actions.

Crisp output. The crisp control signals obtained after defuzzification represent the necessary actions the DVR system must take to restore voltage stability. These actions typically involve injecting compensating voltage into the distribution system through the transformer, effectively mitigating voltage sags or swells and ensuring that sensitive loads connected to the grid remain operational.

Thereby, the T2-FLC ensures precise and adaptive control actions, enabling DVR to effectively compensate for voltage fluctuations and maintain stable power supply.

Isolated flyback converter. The isolated flyback converter is shown in Fig. 4, it is a crucial component in the proposed system, designed to adjust voltage levels, ensure electrical isolation, and facilitate stable power transfer.

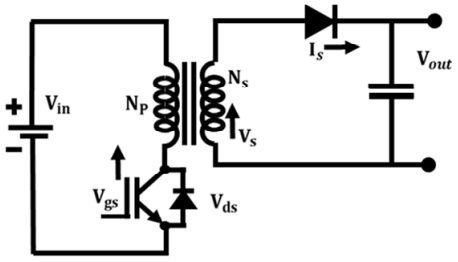

Fig. 4. Configuration of isolated flyback converter

In this intricate process, the converter receives regulated DC power from the PWM rectifier, which has previously converted unstable AC supply into a stable form. Operating in distinct switch-on and switch-off periods, the flyback converter employs a transformer to achieve electrical isolation. By precisely controlling the switch-on and switch-off periods, the flyback converter regulates output voltage, a crucial aspect for stable power transfer. The regulated DC output, now free from ripples, is subsequently rectified and filtered, ensuring a smooth waveform. Prominently, the flyback converter provides electrical isolation, safeguarding components from voltage spikes and disturbances in grid. Its efficient energy transfer, minimal power losses, and precise control, guided by signals from the PI controller at the grid side.

Reduced switch 31 level CHBMLI. The rectified output from WECS is processed through an isolated flyback converter before reaching the reduced switch 31-level CHBMLI. This converter ensures the adjustment of voltage levels and provides electrical isolation. The primary function of the 31-level CHBMLI is to convert the DC power from the isolated flyback converter into high-quality AC power.

The proposed configuration streamlines the design by reducing the number of DC source into single source, facilitated by the implementation of isolated flyback converter. The design of MLI is founded on H-bridge inverter, featuring a total 8 switches (Fig. 5). This design comprises a level generation unity and a polarity generation unit (H-bridge inverter). The switches associated with polarity generation (T_1 – T_4) and level generation (S_1 – S_4) collectively contribute to the generation of 31 voltage levels. The activation of switches T_1 and T_2 occur during positive half cycle, while T_3 and T_4 are engaged during the negative half cycle. Notably, the deactivation of all level generation switches yields the zero voltage level. This configuration allows for effective control and modulation of the output voltage levels, ensuring the desired multilevel characteristics of the inverter.

In positive half cycle, conduction occurs through D_2, D_3 and D_4 with switch S_1 turned ON. Table 3 presents the switching operations and corresponding output voltage levels during the operation of proposed system.

Transitioning to mode 2 in the positive half cycle, conduction shifts to D_1, D_3 and D_4 with switch S_2 turned ON, and yielding an output.

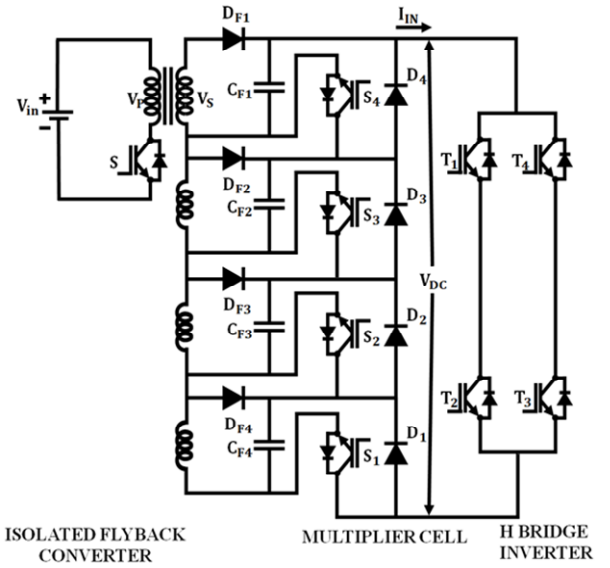

Fig. 5. Reduced switch 31-level MLI

Table 3

Switching operations and output voltage levels of reduced switch 31-level MLI

S_1	S_2	S_3	S_4	Output voltage
1	1	1	1	$V_{S1} + V_{S2} + V_{S3} + V_{S4}$
0	1	1	1	$V_{S2} + V_{S3} + V_{S4}$
1	0	1	1	$V_{S1} + V_{S3} + V_{S4}$
0	0	1	1	$V_{S3} + V_{S4}$
1	1	0	1	$V_{S1} + V_{S2} + V_{S4}$
0	1	0	1	$V_{S2} + V_{S4}$
1	0	0	1	$V_{S1} + V_{S4}$
0	0	0	1	V_{S4}
1	1	1	0	$V_{S1} + V_{S2} + V_{S3}$
0	1	1	0	$V_{S2} + V_{S3}$
1	0	1	0	$V_{S1} + V_{S3}$
0	0	1	0	V_{S3}
1	1	0	0	$V_{S1} + V_{S2}$
0	1	0	0	V_{S2}
1	0	0	0	V_{S1}
0	0	0	0	0
1	0	0	0	$-V_{S1}$
0	1	0	0	$-V_{S2}$
1	1	0	0	$-(V_{S1} + V_{S2})$
0	0	1	0	$-V_{S3}$
1	0	1	0	$-(V_{S1} + V_{S3})$
0	1	1	0	$-(V_{S2} + V_{S3})$
1	1	1	0	$-(V_{S1} + V_{S2} + V_{S3})$
0	0	0	1	$-V_{S4}$
1	0	0	1	$-(V_{S1} + V_{S4})$
0	1	0	1	$-(V_{S2} + V_{S4})$
1	1	0	1	$-(V_{S1} + V_{S2} + V_{S4})$
0	0	1	1	$-(V_{S3} + V_{S4})$
1	0	1	1	$-(V_{S1} + V_{S3} + V_{S4})$
0	1	1	1	$-(V_{S2} + V_{S3} + V_{S4})$
1	1	1	1	$-(V_{S1} + V_{S2} + V_{S3} + V_{S4})$

This sequential switching pattern continues through the 15 modes, with switches being activated in sequence. The same switching sequence is then repeated for negative half cycle. In addition, a PI controller is implemented for controlling the operation of 31-level CHBMLI. The PI controller continuously monitors real and reactive power, generating control signals for the inverter. This ensures precise control over the output voltage and current. This guarantees that the wind farm can seamlessly integrate with the grid without causing disruptions.

Table 3 enumerates the switching operations and associated output voltage levels for reduced switch 31-level MLI. Each row in the table corresponds to a specific switch configuration, where «1» indicates the switch is turned ON, and «0» denotes it is OFF. The switches are denoted as (S_1 – S_4). The output voltage column shows the cumulative voltage produced by the active switches according to the specified configuration. Columns (S_1 – S_4) represent the ON/OFF status of each switch in the inverter. Columns (V_{S1} – V_{S4}) specifies the resulting output voltage based on active switches. The notation (V_{S1} – V_{S4}) represents the voltage levels associated with each switch. The cumulative output voltage is calculated by adding the voltages of active switches. For example, the row «1 1 1 1» indicates that all 4 switches (S_1 – S_4) are turned ON, contributing their respective voltage levels to the total output voltage. In contrast, the row «0 0 0 0» signifies that none of the switches are active, resulting in zero output voltage. This table serves as a reference for understanding the relationship between switch configurations and the generated output voltage levels in the reduced switch 31-level MLI.

Result and discussion. The validation of proposed system has been precisely carried out using MATLAB simulation. Through rigorous analysis and simulation, the performance and effectiveness of each component within the system have been assessed. Table 4 presents a detailed breakdown of the specification parameters crucial to the design of the proposed system.

Table 4

Specification of design parameters

Parameters	Value
PMSG-wind system	
No. of turbines	1
Power, kW	10
Voltage, V	575
Stator resistance, Ω	0.975
Flux linkage, Wb	0.91
PMSG inductance, H	0.01
Pole pairs	3
Air density, kg/m^3	1.218
Pitch angle beta, degree	2
Base wind speed, m/s	12
DC link capacitor, μF	1500
DVR	
Switching frequency, kHz	10
Series voltage injection, V	100
Grid voltage, V	415
Filter inductance, mH	2.7
Filter capacitance, μF	50
Line resistance, Ω	0.1
Line inductance, mH	0.5

The following sections delve into the comprehensive results and discussions, shedding light on the system's response to grid disturbances, the role of DVR, and the overall enhancement of LVRT capability in PMSG based WECS.

Scenario 1. Voltage sag. The response of a PMSG during a voltage sag condition is illustrated in Fig. 6. Subfigures (*a*) and (*b*) respectively showcase the voltage and current waveforms of PMSG system under the influence of voltage sag. The occurrence is notable

between 0.2 s and 0.3 s, attributed to the uneven nature of the wind affecting the generator. The inphase waveform under voltage sag condition is depicted in Fig. 6,*c*. This visual representation enables a detailed observation of how PMSG system responds to voltage sag, offering valuable information about its dynamic characteristics in the presence of such adverse electrical conditions. The implementation of DVR plays a crucial role in mitigating voltage sag scenario.

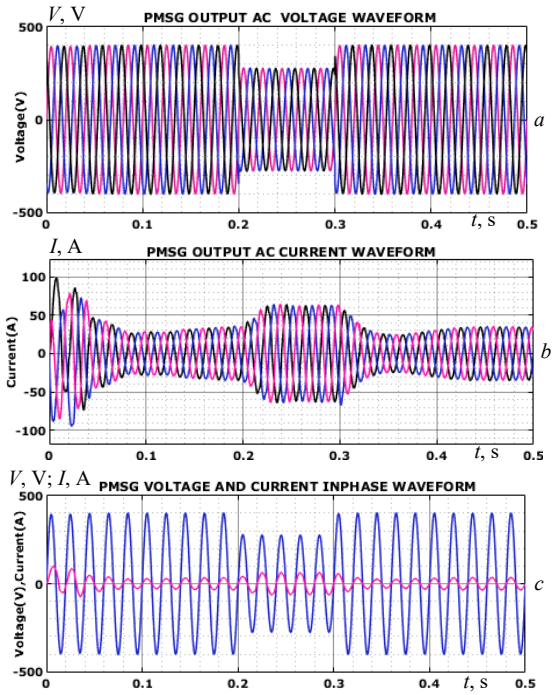

Fig. 6. PMSG behavior in voltage sag:
a – voltage; *b* – current; *c* – inphase waveforms

In Fig. 7, two key aspects of the system are depicted. Figure 7,*a* illustrates the output from the rectifier, displaying a gradual voltage increase with minor oscillations, indicating successful conversion of wind system power. Figure 7,*b* shows the stabilized DC link voltage at 800 V, highlighting a successful conversion and regulation process. This stable DC link voltage is essential for ensuring overall system performance and efficiency in subsequent stages.

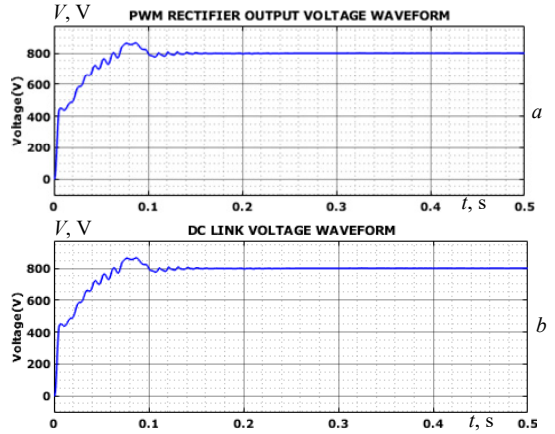

Fig. 7. *a* – output voltage from rectifier; *b* – voltage across DC link

In Fig. 8 the output characteristics of the 31-level MLI is shown. Figure 8,*a* illustrates the output voltage, showcasing a stabilized and consistent voltage profile. Concurrently, Fig. 8,*b* demonstrates the corresponding output current profile, which also maintains a stable and steady behavior. This stability in both voltage and current outputs highlights the efficacy of the 31-level MLI in providing a reliable and consistent power supply. The achieved output stability is crucial for ensuring the proper functioning of the connected load and contributes to the overall performance and efficiency of the system.

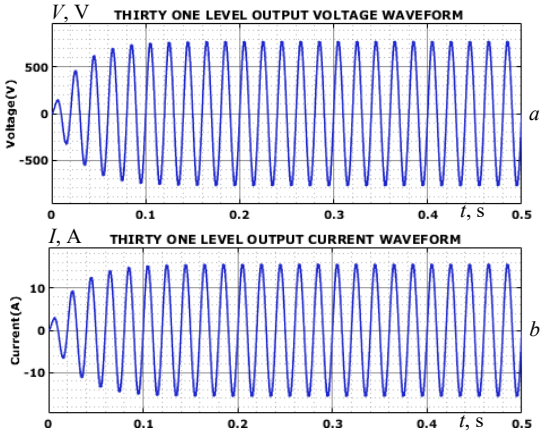

Fig. 8. Output voltage (*a*) and current (*b*) profile of 31 level MLI

Figure 9 provides a visual representation of the voltage and current characteristics in 3 phase grid load under the influence of proposed system. Figure 9,*a* displays the load voltage waveform, showcasing the stabilized nature of voltage. This stabilization is a result of proposed system's effective mitigation of voltage sag issues, ensuring a consistent and reliable voltage supply to the grid load. Simultaneously, Fig. 9,*b* illustrates the load current waveform, indicating a stabilized current value. The ability to maintain stable voltage and current levels is crucial for the overall performance and reliability of the grid load, emphasizing positive impact of proposed system on mitigating voltage sag and ensuring the steady operation of grid load.

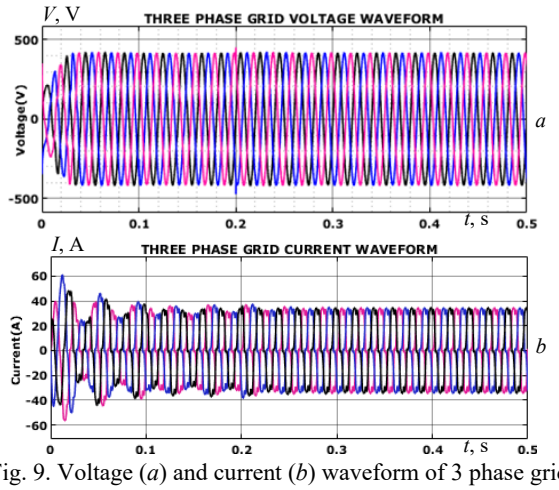

Fig. 9. Voltage (*a*) and current (*b*) waveform of 3 phase grid

Figure 10 illustrates the dynamics of both real and reactive power waveforms, providing insights into the power characteristics of proposed system under operating conditions. The real power waveform represents the actual power consumed by the system, while the reactive power waveform indicates system's ability to maintain voltage levels. Together, these waveforms offer a

comprehensive view of the power behavior of the system, aiding in the evaluation of its performance and efficiency.

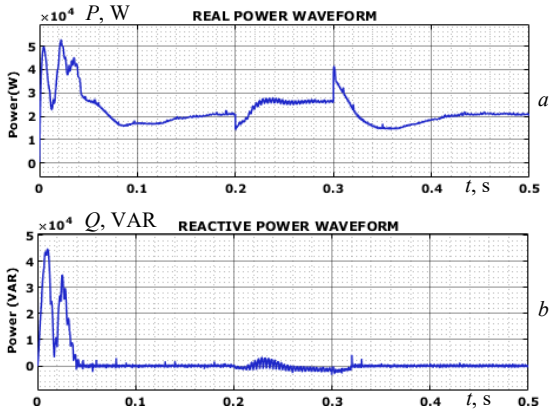

Fig. 10. Real (*a*) and reactive (*b*) power waveform

Scenario 2. Voltage swell. The response of PMSG system under voltage swell conditions is shown in Fig. 11. Figure 11,*a* illustrates the voltage waveform, showcasing how the system's voltage output is affected by voltage swell condition between 0.2 – 0.3 s. In parallel, Fig. 11,*b* details the corresponding current waveform, providing insights into the system's electrical behavior in response to the voltage swell. Additionally, the inphase representation of current and voltage is also revealed in Fig. 11,*c*.

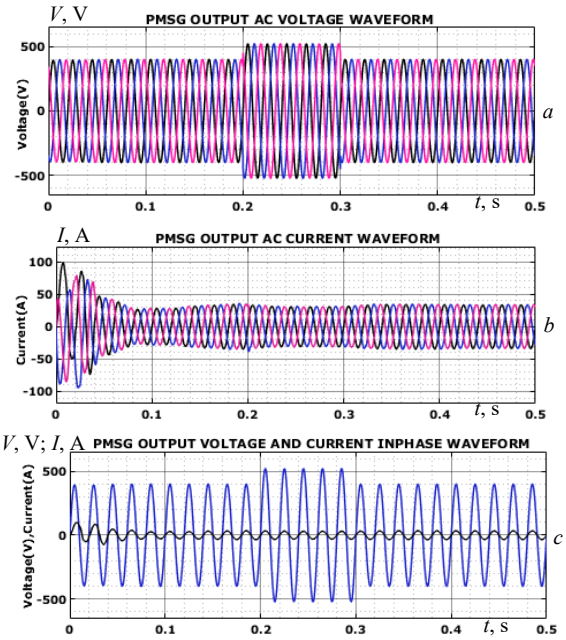

Fig. 11. PMSG system response to voltage swell: *a* – voltage; *b* – current; *c* – inphase waveform

In Fig. 12, two essential elements of the system are depicted: output from rectifier and the resulting DC link voltage. Figure 12,*a* illustrates the rectifier's output, displaying a gradual voltage increase with minor oscillations. This highlights the rectifier's role in converting wind system input power into a usable form. Figure 12,*b* shows the DC link voltage, indicating a stabilized output at 800 V. This successful conversion and regulation process ensures a consistent and reliable DC supply for the subsequent stages of the system, contributing to overall performance and efficiency.

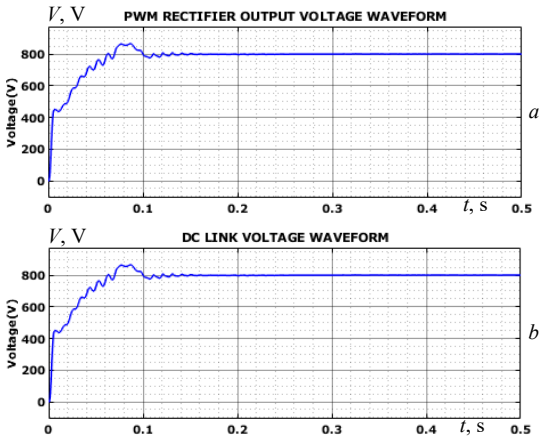

Fig. 12. Rectifier output voltage (*a*) and DC link voltage (*b*)

In Fig. 13, the output voltage and current profiles of 31-level MLI under voltage swell conditions are depicted. Figure 13,*a* illustrates the stabilized output voltage, emphasizing system's ability to mitigate the effects of voltage swell and maintain a consistent voltage supply. Simultaneously, Fig. 13,*b* presents the corresponding output current profile, showcasing the system's capability to deliver stable current despite the voltage variations. This analysis underscores the effectiveness of the proposed system in adapting to both voltage sag and swell conditions and ensuring reliable power delivery to connected load.

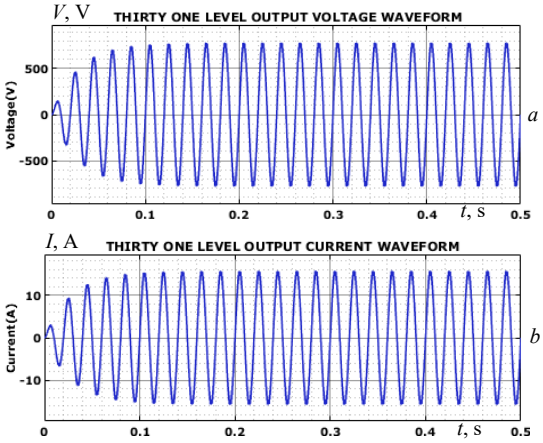

Fig. 13. *a* – stabilized output voltage; *b* – consistent output current profile of 31-level MLI under voltage swell condition

The voltage and current dynamics within 3 phase grid load influenced by the proposed system is depicted in Fig. 14. Figure 14,*a* depicts the load voltage waveform, demonstrating the system's proficiency in stabilizing voltage by effectively addressing voltage swell issues. Concurrently, Fig. 14,*b* portrays the load current waveform, showcasing a steady and controlled current level. The system's capability to maintain stability in both voltage and current is instrumental for the reliable performance of grid load, underscoring the positive impact of the proposed solution in mitigating voltage swell and ensuring uninterrupted operation of grid load.

The concise view of power dynamics, encompassing both real and reactive power waveforms is illustrated in Fig. 15. Figure 15,*a* represents the real power waveform, reflecting the actual power consumed. Simultaneously, Fig. 15,*b* depicts the reactive power waveform, indicating

the non-working power component that oscillates between source and load. This comprehensive representation of real and reactive power dynamics is crucial for assessing the system's performance and efficiency in delivering power to the connected load.

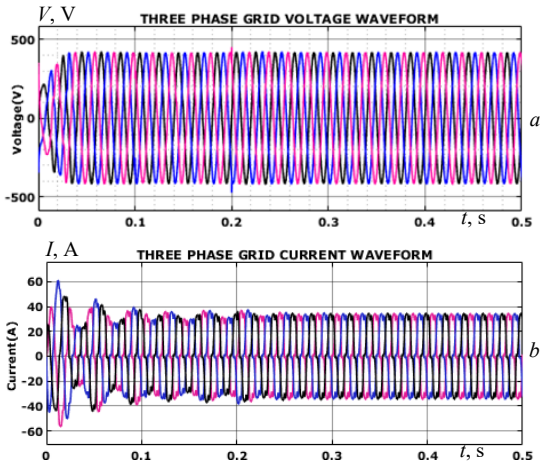

Fig. 14. Voltage (*a*) and current (*b*) waveform of 3 phase grid

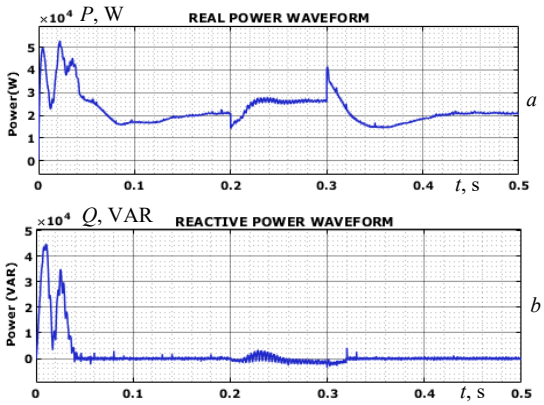

Fig. 15. Real (*a*) and reactive (*b*) power waveform

The power factor waveform accomplished by the proposed system is illustrated in Fig. 16. The achieved unity power factor signifies optimal utilization and balance between real and reactive power, showcasing the efficiency and stability of the system under voltage swell conditions. The consistent power factor dynamics affirm the system's capability to maintain a balanced and reliable operation even in challenging scenarios.

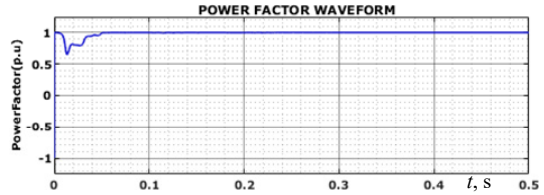

Fig. 16. Power factor dynamics

Figure 17 presents the THD value, which is recorded at 1.8 %. This low THD value indicates a minimal level of harmonic distortion in the system's output, highlighting the efficiency and quality of the power signal generated by the proposed configuration.

A comprehensive comparison of THD analysis among various techniques is listed in Table 5. The table serves as a valuable reference for evaluating and contrasting the harmonic distortion levels achieved by different approaches, with the lower THD values indicating better performance in terms of generating a cleaner and more stable power output.

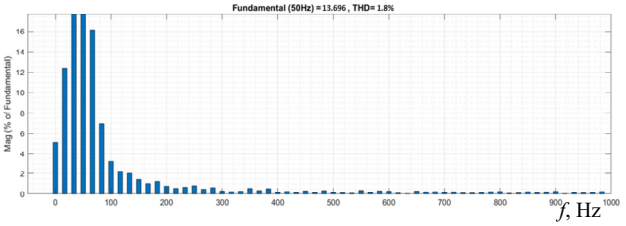

Fig. 17. THD waveform

From Table 5, the first three rows represent the THD percentages reported by different authors, specifically Pal R. [24], Moghassemi A. [25], and Ibrahim N.F. [26], revealing THD value of 7.85 %, 4.89 % and 2.3 % respectively. While, the proposed technique included in the comparison, shows a reduced THD value of 1.8 %, with optimal performance.

Table 5

Comparison of THD analysis

Techniques	THD (%)
Pal R. [24]	7.85
Moghassemi A. [25]	4.89
Ibrahim N.F. [26]	2.3
Proposed	1.8

The comparison of cost function between a fuzzy controller and a T2-FLC for optimal DVR control is illustrated in Fig. 18. The analysis reveals that T2-FLC outperforms traditional fuzzy controller, achieving a minimized cost. Figure 18 provides valuable insights into the effectiveness of T2-FLC controller in optimizing DVR control and reducing associated costs, showcasing its superiority over conventional fuzzy control strategies.

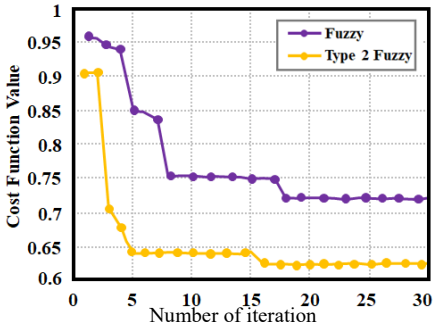

Fig. 18. Comparison of cost function

A comparative analysis of convergence speed between fuzzy controller and T2-FLC controller is represented in Fig. 19. The comparison highlights the enhanced convergence speed achieved by type 2 fuzzy controller, showcasing its greater performance in optimizing convergence dynamics compared to conventional fuzzy. Figure 19 provides valuable insights into the efficiency and effectiveness of type 2 fuzzy controller in ensuring faster convergence for improved control outcomes.

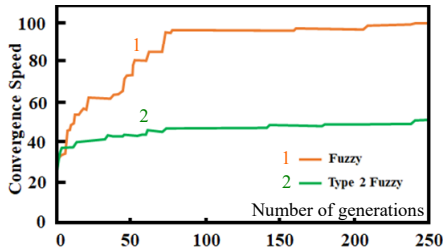

Fig. 19. Comparison of convergence speed

Figure 20 illustrates a comprehensive comparison of DVR controller errors. This analysis examines and contrasts the errors associated with different control strategies employed for the DVR system. It observed that the proposed type 2 fuzzy shed light on accuracy and efficacy of each control approach in minimizing errors within the DVR system in contrast to fuzzy approach.

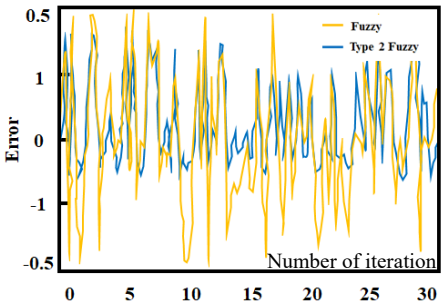

Fig. 20. DVR controller error comparison

Conclusions. In conclusion, the proposed integration of PMSG-WECS with an advanced power conditioning system, including a DVR represents a significant advancement in enhancing grid stability and LVRT capability. The type 2 fuzzy controller intelligently regulates the input DC voltage to DVR, adapting dynamically to changing conditions and tackling voltage fluctuations and grid disturbances. The subsequent processing of rectified WECS output through an isolated flyback converter and a 31-level CHBMLI with PI control ensures the delivery of high-quality AC output to grid, minimizing harmonics and voltage deviations. This holistic approach significantly improves the WECS's LVRT capability with reduced THD value of 1.8 %, providing a cleaner and more stable power output compared to existing techniques. The comprehensive comparison of THD analysis with other techniques and the examination of controller errors affirm the scientific novelty and effectiveness of the proposed system. In conclusion, the research not only addresses the stated research problem but also contributes novel insights into the integration of RES into the power grid, emphasizing the significance of advanced control strategies, such as type 2 fuzzy control, in improving the system's consistency. To raise the overall resilience and efficiency of the system, future work will concentrate on modified controllers for even more adaptability, scaling up and optimizing the suggested PMSG-WECS integration, and investigating new developments in energy storage technologies.

Conflict of interest. The authors declare that they have no conflicts of interest.

REFERENCES

1. Zhou A., Li Y.W., Mohamed Y. Mechanical Stress Comparison of PMSG Wind Turbine LVRT Methods. *IEEE Transactions on Energy Conversion*, 2021, vol. 36, no. 2, pp. 682-692. doi: https://doi.org/10.1109/TEC.2020.3018093.

2. Chojaa H., Derouich A., Zamzoum O., Watil A., Taoussi M., Abdelaziz A.Y., Elbarbary Z.M.S., Mossa M.A. Robust Control of DFIG-Based WECS Integrating an Energy Storage System With Intelligent MPPT Under a Real Wind Profile. *IEEE Access*, 2023, vol. 11, pp. 90065-90083. doi: https://doi.org/10.1109/ACCESS.2023.3306722.

3. Bouraghda S., Sebaa K., Bechouat M., Sedraoui M. An improved sliding mode control for reduction of harmonic currents in grid system connected with a wind turbine equipped by a doubly-fed induction generator. *Electrical Engineering & Electromechanics*, 2022, no. 2, pp. 47-55. doi: https://doi.org/10.20998/2074-272X.2022.2.08.

4. Kim C., Kim W. Low-Voltage Ride-Through Coordinated Control for PMSG Wind Turbines Using De-Loaded Operation. *IEEE Access*, 2021, vol. 9, pp. 66599-66606. doi: https://doi.org/10.1109/ACCESS.2021.3076787.

5. Khan A., Ahmad H., Ahsan S.M., Gulzar M.M., Murawwat S. Coordinated LVRT Support for a PMSG-Based Wind Energy Conversion System Integrated into a Weak AC-Grid. *Energies*, 2021, vol. 14, no. 20, art. no. 6588. doi: https://doi.org/10.3390/en14206588.

6. Yuan L., Meng K., Huang J., Dong Z.Y., Zhang W., Xie X. Development of HVRT and LVRT Control Strategy for PMSG-Based Wind Turbine Generators. *Energies*, 2020, vol. 13, no. 20, art. no. 5442. https://doi.org/10.3390/en13205442.

7. Kim C., Kim W. Enhanced Low-Voltage Ride-Through Coordinated Control for PMSG Wind Turbines and Energy Storage Systems Considering Pitch and Inertia Response. *IEEE Access*, 2020, vol. 8, pp. 212557-212567. doi: https://doi.org/10.1109/ACCESS.2020.3040905.

8. Desalegn B., Gebeyehu D., Tamrat B. Smoothing electric power production with DFIG-based wind energy conversion technology by employing hybrid controller model. *Energy Reports*, 2023, vol. 10, pp. 38-60. doi: https://doi.org/10.1016/j.egyr.2023.06.004.

9. Ghanem S., Fandi G., Kyncl J., Müller Z. A novel scheme for control by active and reactive power utilized in gearless variable speed wind turbine system with PMSG connected to the grid. *Electrical Engineering & Electromechanics*, 2022, no. 2, pp. 56-68. doi: https://doi.org/10.20998/2074-272X.2022.2.09.

10. Döşoğlu M.K., Güvenç U., Sönmez Y., Yılmaz C. Enhancement of demagnetization control for low-voltage ride-through capability in DFIG-based wind farm. *Electrical Engineering*, 2018, vol. 100, no. 2, pp. 491-498. doi: https://doi.org/10.1007/s00202-017-0522-6.

11. Zhang A., Chen Z., Gao R., Wang J., Ma Z., Wang S., Wang Y. Crowbarless Symmetrical Low-Voltage Ride Through Based on Flux Linkage Tracking For Brushless Doubly Fed Induction Generators. *IEEE Transactions on Industrial Electronics*, 2020, vol. 67, no. 9, pp. 7606-7616. doi: https://doi.org/10.1109/TIE.2019.2944096.

12. Chowdhury M.A., Shafiullah G.M., Ferdous S.M. Low voltage ride-through augmentation of DFIG wind turbines by simultaneous control of back-to-back converter using partial feedback linearization technique. *International Journal of Electrical Power & Energy Systems*, 2023, vol. 153, art. no. 109394. doi: https://doi.org/10.1016/j.ijepes.2023.109394.

13. Liu J., Zhao C., Xie Z. Power and Current Limiting Control of Wind Turbines Based on PMSG Under Unbalanced Grid Voltage. *IEEE Access*, 2021, vol. 9, pp. 9873-9883. doi: https://doi.org/10.1109/ACCESS.2021.3049839.

14. Jayasawal K., Thapa K. An Enhanced Low Voltage Ride-Through Control Scheme of a DIFG based WTG Using Crowbar and Braking Chopper. *Journal of the Institute of Engineering*, 2021, vol. 16, no. 1, pp. 61-67. doi: https://doi.org/10.3126/jie.v16i1.36537.

15. Gontijo G.F., Tricarico T.C., da Silva L.F., Krejci D., Franca B.W., Aredes M., Guerrero J.M. Modeling, Control, and Experimental Verification of a DFIG With a Series-Grid-Side Converter With Voltage Sag, Unbalance, and Distortion Compensation Capabilities. *IEEE Transactions on Industry Applications*, 2020, vol. 56, no. 1, pp. 584-600. doi: https://doi.org/10.1109/TIA.2019.2946950.

16. Labed M.A., Zellagui M., Benidir M., Sekhane H., Tebbakh N. Optimal hybrid photovoltaic distributed generation and distribution static synchronous compensators planning to minimize active power losses using adaptive acceleration

coefficients particle swarm optimization algorithms. *Electrical Engineering & Electromechanics*, 2023, no. 6, pp. 84-90. doi: https://doi.org/10.20998/2074-272X.2023.6.15.
17. Rezaie H., Kazemi-Rahbar M.H. Enhancing voltage stability and LVRT capability of a wind-integrated power system using a fuzzy-based SVC. *Engineering Science and Technology, an International Journal*, 2019, vol. 22, no. 3, pp. 827-839. doi: https://doi.org/10.1016/j.jestch.2018.12.018.
18. Zahra S.T., Khan R.U., Ullah M.F., Begum B., Anwar N. Simulation-based analysis of dynamic voltage restorer with sliding mode controller at optimal voltage for power quality enhancement in distribution system. *Electrical Engineering & Electromechanics*, 2022, no. 1, pp. 64-69. doi: https://doi.org/10.20998/2074-272X.2022.1.09.
19. Zhu Y., Wang Z., Guo X., Wei Z. An improved kinetic energy control strategy for power smoothing of PMSG-WECS based on low pass filter and fuzzy logic controller. *Electric Power Systems Research*, 2023, vol. 214, art. no. 108816. doi: https://doi.org/10.1016/j.epsr.2022.108816.
20. Nguyen Huy T., Le Hanh D., Takano H., Nguyen Duc T. Cooperative LVRT control for protecting PMSG-based WTGs using battery energy storage system. *Energy Reports*, 2023, vol. 9, pp. 590-598. doi: https://doi.org/10.1016/j.egyr.2023.05.112.
21. Abas N., Dilshad S., Khalid A., Saleem M.S., Khan N. Power Quality Improvement Using Dynamic Voltage Restorer. *IEEE Access*, 2020, vol. 8, pp. 164325-164339. https://doi.org/10.1109/ACCESS.2020.3022477.
22. Appala Naidu T., Arya S.R., Maurya R., Padmanaban S. Performance of DVR Using Optimized PI Controller Based Gradient Adaptive Variable Step LMS Control Algorithm. *IEEE Journal of Emerging and Selected Topics in Industrial Electronics*, 2021, vol. 2, no. 2, pp. 155-163. doi: https://doi.org/10.1109/JESTIE.2021.3051553.
23. Kumar P., Arya S.R., Mistry K.D., Yadav S. A self-tuning ANFIS DC link and ANN-LM controller based DVR for power quality enhancement. *CPSS Transactions on Power Electronics and Applications*, 2023, vol. 8, no. 4, pp. 424-436. doi: https://doi.org/10.24295/CPSSTPEA.2023.00032.
24. Pal R., Gupta S. Topologies and Control Strategies Implicated in Dynamic Voltage Restorer (DVR) for Power Quality Improvement. *Iranian Journal of Science and Technology, Transactions of Electrical Engineering*, 2020, vol. 44, no. 2, pp. 581-603. doi: https://doi.org/10.1007/s40998-019-00287-3.
25. Moghassemi A., Ebrahimi S., Ferdowsi F. A Novel Control Scheme for TransZSI-DVR to Enhance Power Quality in Solar Integrated Networks. *2021 North American Power Symposium (NAPS)*, 2021, pp. 1-6. doi: https://doi.org/10.1109/NAPS52732.2021.9654507.
26. Ibrahim N.F., Alkuhayli A., Beroual A., Khaled U., Mahmoud M.M. Enhancing the Functionality of a Grid-Connected Photovoltaic System in a Distant Egyptian Region Using an Optimized Dynamic Voltage Restorer: Application of Artificial Rabbits Optimization. *Sensors*, 2023, vol. 23, no. 16, art. no. 7146. doi: https://doi.org/10.3390/s23167146.

Received 07.01.2024
Accepted 14.03.2024
Published 20.06.2024

Ch. Sajan[1], *Research Scholar*,
P. Satish Kumar[1], *Professor*,
P. Virtic[2], *Professor*,
[1] Department of Electrical Engineering,
University College of Engineering, Osmania University,
Hyderabad, Telangana 500007, India,
e-mail: sajan4315@gmail.com (Corresponding Author);
satish_8020@yahoo.co.in
[2] Faculty of Energy Technology,
University of Maribor, Krško, Slovenia,
e-mail: peter.virtic@um.si

How to cite this article:
Sajan Ch., Satish Kumar P., Virtic P. Enhancing grid stability and low voltage ride through capability using type 2 fuzzy controlled dynamic voltage restorer. *Electrical Engineering & Electromechanics*, 2024, no. 4, pp. 31-41. doi: https://doi.org/10.20998/2074-272X.2024.4.04

UDC 621.314 https://doi.org/10.20998/2074-272X.2024.4.05

C. Bousnoubra, Y. Djeghader, H. Belila

Contribution of using a photovoltaic unified power quality conditioner in power quality improvement

Introduction. *With the increasing complexity of power systems and the integration of diverse energy sources, issues such as voltage sags, swells, and signal distortions have emerged as critical challenges. These power quality problems can result in equipment malfunction, production downtime, and financial losses for industries, as well as inconvenience and potential damage to electrical appliances in households. There is an urgent need for enhanced system efficiency.* ***Methods.*** *This objective is effectively achieved through the utilization of the newly proposed power theory, which is rooted in solar photovoltaic (PV) control, in conjunction with the Unified Power Quality Conditioner (UPQC).* ***Purpose.*** *The proposed method incorporates a modified synchronous reference frame scheme, coupled with a phase-locked loop mechanism. This control strategy enables the UPQC to effectively mitigate power quality issues.* ***Novelty.*** *PV-UPQC is utilized to uphold power integrity in the presence of diverse current and voltage distortions. This device, known as a multi-objective power conditioning apparatus, serves the purpose of maintaining power quality. PV-UPQC incorporates both a shunt and series voltage source converter, which are interconnected through a shared DC-link. Additionally, the PV system is interconnected at the DC-link of the UPQC in order to supply power to the load.* ***Results****. In this study, a novel approach is presented for controlling the UPQC, aiming to address power quality concerns such as unbalanced grid voltage and harmonic distortions and enabling us to control active and reactive power.* References 16, tables 2, figures 15.
Key words: **unified power quality conditioner, photovoltaic system, phase lock loop, reactive power, harmonics.**

Вступ*. Зі зростанням складності енергетичних систем та інтеграцією різних джерел енергії такі проблеми, як провали напруги, стрибки напруги та спотворення сигналу, стали критичними проблемами. Ці проблеми з якістю електроенергії можуть призвести до збоїв у роботі обладнання, простоїв виробництва та фінансових втрат для промисловості, а також до незручностей та потенційного пошкодження електроприладів у домашніх господарствах. Існує гостра необхідність підвищення ефективності системи.* ***Методи****. Ця мета ефективно досягається за рахунок використання нещодавно запропонованої теорії енергетики, що базується на управлінні сонячними фотоелектричними (PV) системами, у поєднанні з єдиним перетворювачем якості електроенергії (UPQC).* ***Мета****. Пропонований метод включає модифіковану схему синхронної системи координат у поєднанні з механізмом фазового автопідстроювання частоти. Ця стратегія керування дозволяє UPQC ефективно усувати проблеми з якістю електроенергії.* ***Новизна****. PV-UPQC використовується для підтримки цілісності електроживлення за наявності різних спотворень струму та напруги. Цей пристрій, відомий як багатоцільовий пристрій стабілізації потужності, служить підтримці якості електроенергії. PV-UPQC включає як шунтуючий, так і послідовний перетворювач напруги, які з'єднані між собою через загальне коло постійного струму. Крім того, фотоелектричну систему підключено до ланки постійного струму UPQC для подачі живлення на навантаження.* ***Результати****. У цьому дослідженні представлений новий підхід до управління UPQC, спрямований на вирішення проблем якості електроенергії, таких як незбалансована напруга мережі та гармонічні спотворення, що дозволяє контролювати активну та реактивну потужність.* Бібл. 16, табл. 2, рис. 15.
Ключові слова: **єдиний стабілізатор якості електроенергії, фотоелектрична система, фазове автопідстроювання частоти, реактивна потужність, гармоніки.**

Introduction. Power electronic-based loads play a crucial and influential role in the propagation of harmonic currents within the electrical grid at the point of common coupling (PCC), serving as substantial contributors to this phenomenon [1, 2]. Voltage Source Converters (VSCs) are extensively utilized in various power quality (PQ) enhancement applications owing to their exceptional capacity to absorb or deliver reactive power, thereby providing enhanced versatility [1, 3]. Enhancing PQ is paramount for ensuring the dependability and efficiency of electrical systems, guaranteeing a stable and uninterrupted supply of electricity to meet the varied requirements of consumers [1, 2]. In the context of solar PV integration for PQ improvement, a combined utilization of photovoltaic (PV) systems and Unified Power Quality Conditioners (UPQC) has been implemented [3, 4]. This paper presents comprehensive research into the design and performance analysis of a three-phase Photovoltaic-Unified Power Quality Conditioner (PV-UPQC). To enhance dynamic performance during active current extraction an advanced Phase-Locked Loop (PLL) based Direct Current Control (DCC) theory approach is employed [5-7]. The proposed system offers numerous notable advantages, including seamless integration of clean energy generation and PQ enhancement. It achieves simultaneous improvements in both voltage and current quality, while significantly enhancing load current compensation through the utilization of DCC control of PV-UPQC [7-9]. Furthermore, the PV-UPQC operates to stabilize the system amidst a plethora of dynamic scenarios, encompassing voltage sags/swells, load unbalance, and variations in irradiation [10, 11]. To thoroughly evaluate the performance of the proposed system, extensive analysis is conducted under both dynamic and steady-state conditions, employing the MATLAB/Simulink, simulating real-world distribution system scenarios such as voltage sags/swells, load unbalances, and variations in irradiation.

System configuration of PV-UPQC and control strategy. The system is shown in Fig. 1 showcases the configuration block diagram of the considered setup. It comprises a shunt VSC and a series VSC, which are interconnected through a shared DC link capacitor. The shunt VSC is connected to the load side through interfacing inductors, while the series VSC is linked in series with the grid via coupling inductors, in order to facilitate the integration of the PV-UPQC system [4].

To facilitate the injection of the voltage signal generated by the series VSC, the PV-UPQC system uses a series transformer. The shunt VSC is connected at the

© C. Bousnoubra, Y. Djeghader, H. Belila

PCC on the load side, serving a dual role of compensating for load current harmonics and delivering PV power to the load [8, 12].

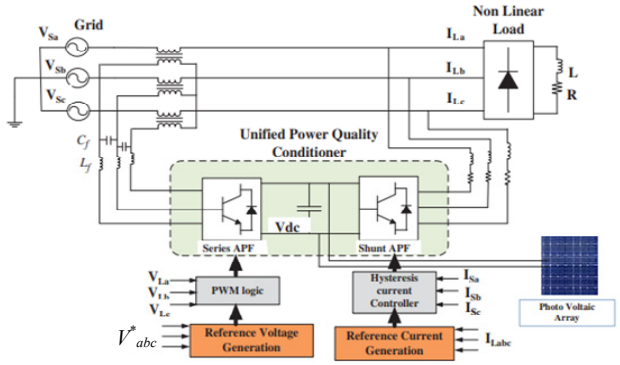

Fig. 1. General structure of PV-UPQC in grid

Series active power filter control. The series active power filter (APF) plays a crucial role in voltage compensation by determining the required voltage injection into the grid to achieve a sinusoidal voltage waveform with the correct magnitude and frequency [10]. The reference voltage V^*_{abc} is subtracted from the supply voltage, and the resulting voltage error is calculated and compared to the system's internal error voltage. The hysteresis voltage controller governs the switching pattern of the inverter, ensuring precise regulation of the output voltage of the series APF [11]. Figure 2 illustrates the fundamental schematic of a fixed hysteresis band (HB) voltage control. Whenever the sensed output signal deviates from the reference by a predetermined margin, a comparison is made between the instantaneous value of the output voltage and the reference voltage V^*_{abc}. Subsequently, the inverter is activated to minimize the discrepancy. Consequently, switching occurs each time the output voltage crosses the HB threshold. The output voltage signal of the series APF is provided by this control mechanism:

$$V_c = V_c^* + HB \ - \text{in rising case;}$$

$$V_c = V_c^* - HB \ - \text{in decreasing case.}$$

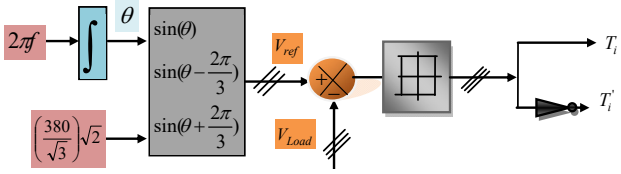

Fig. 2. Simplified model for fixed HB voltage control

Shunt APF control. Figure 3,*a* illustrates the fundamental principle of compensation of an APF controlled by DCC. The control architecture for the APF is designed to supply harmonic currents and compensate for reactive power in non-linear loads, alleviating the burden of supplying anything beyond the fundamental active current [9]. The objective of this identification strategy is to generate high-quality reference currents using a simplified algorithm. After calculating the 3 sinusoidal signals through the application of the PLL technique, as illustrated in Fig. 3,*b*, the output of the PI controller in the DC voltage regulation stage is utilized as the peak current (I_{sp}) [5-7]. This peak current can be multiplied by the sinusoidal signals to obtain the reference source currents, expressed in:

$$\begin{cases} i_{sa}^*(t) = I_{sp}\sin(\omega t); \\ i_{sb}^*(t) = I_{sp}\sin(\omega t - 120); \\ i_{sc}^*(t) = I_{sp}\sin(\omega t - 240). \end{cases} \quad (1)$$

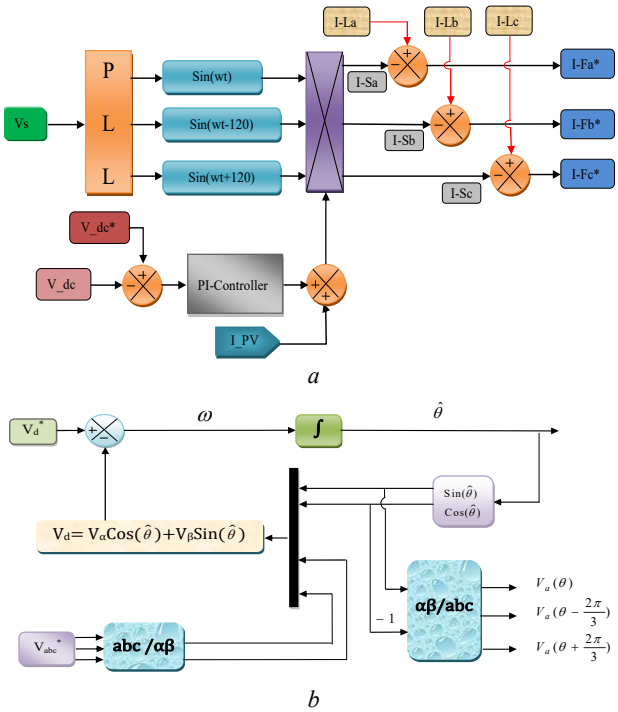

Fig. 3. Model of DCC (*a*) and PLL mechanism (*b*)

In accordance with the diagram presented in Fig. 3, the source current at the PCC is represented as:

$$i_s(t) = i_L(t) - i_f(t), \quad (2)$$

where $i_s(t)$, $i_L(t)$, $i_f(t)$ denote, in sequence, the instantaneous magnitudes of the source current, load current and filter current.

In the presence of a nonlinear load, the load current can be disintegrated into a fundamental component and harmonic components, which can be expressed through a Fourier series expansion in the following manner:

$$\begin{aligned} i_L(t) &= \sum_{n=1}^{\infty} I_n \sin(n\omega t + \phi_n); \\ i_L(t) &= I_1 \sin(\omega t + \phi_1) + \sum_{n=2}^{\infty} I_n \sin(n\omega t + \phi_n), \end{aligned} \quad (3)$$

where I_n and ϕ_n denote the magnitude and phase angle of the n^{th} harmonic current, while I_1 and ϕ_1 represent the magnitude and phase angle of the fundamental current. Moreover, the instantaneous load power $P_L(t)$ can be determined by the following:

$$P_L(t) = V_s(t) \cdot i_L(t). \quad (4)$$

By utilizing (3) and (4), the load power can be rewritten as follows:

$$\begin{aligned} P_L(t) &= V_m I_1 \sin^2(\omega t)\cos(\phi_1) + \\ &+ V_m I_1 \sin(\omega t)\cos(\omega t)\sin(\phi_1) + \\ &+ V_m \sin(\omega t)\sum_{n=2}^{\infty} I_m \sin(n\omega t + \phi_n). \end{aligned} \quad (5)$$

Furthermore, the load power can be represented as:

$$P_L(t) = P_{fun}(t) + P_r(t) + P_h(t)\,, \qquad (6)$$

where $P_{fun}(t)$, $P_r(t)$, $P_h(t)$ correspond, respectively, to the fundamental power (real power), reactive power and harmonic power consumed by the nonlinear load.

In an ideal compensation scenario, only the fundamental power needs to be provided by the source. The reactive and harmonic components are supplied by the active filter. By examining (5) and (6), it can be inferred that the absorbed fundamental power by the nonlinear load can be expressed as:

$$P_{fun}(t) = V_m I_1 \sin^2(\omega t)\cos(\phi_1) = V_s(t) i_s(t)\,. \qquad (7)$$

Based on (7) after compensation the current supplied by the source is:

$$i_s(t) = \frac{P_{fun}(t)}{v_s(t)} = I_1 \cos(\phi_1)\sin(\omega t) = I_{sm}\sin(\omega t)\,. \qquad (8)$$

Taking into account certain losses in the inverter, the total peak current I_{sp} shown in Fig. 3 can be defined as:

$$I_{sp} = I_{sm} + I_{sl}\,, \qquad (9)$$

where I_{sp}, I_{sm}, I_{sl} denote, respectively, the total peak current, the maximum source current and the inverter loss component.

In the DCC algorithm, the estimation of the peak current relies on the DC current at the output of the DC bus controller, and it can be expressed as:

$$I_{sp} = I_{dc}. \qquad (10)$$

The three-phase reference currents of the filter can now be expressed as:

$$\begin{cases} i^*_{sa}(t) = I^*_{sp}\sin(\omega t); \\ i^*_{sb}(t) = I^*_{sp}\sin(\omega t - 120); \\ i^*_{sc}(t) = I^*_{sp}\sin(\omega t - 240). \end{cases} \qquad (11)$$

PV system control. There are several maximum power point tracking (MPPT) control methods and techniques available in the literature. However, the most commonly used is Perturb and Observe (P&O) control [13] used in this work. This algorithm maximizes power output in solar energy systems through system perturbations and monitoring the effects on output power. It compares current and previous power values to determine the optimal perturbation direction for maximum power. It is a widely used and renowned algorithm in MPPT [13-16] (Fig. 4).

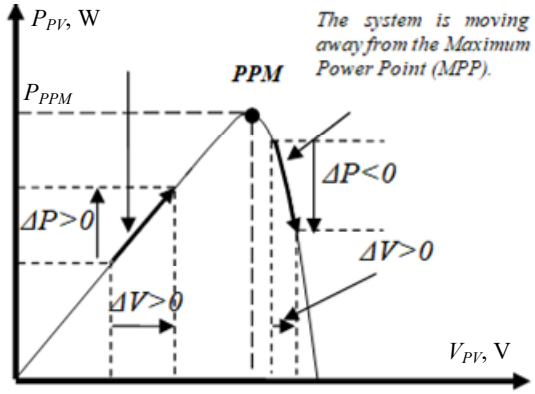

Fig. 4. Characteristic $P_{PV} = f(V_{PV})$ of a solar panel

Figure 5 shows the flowchart of P&O algorithm.

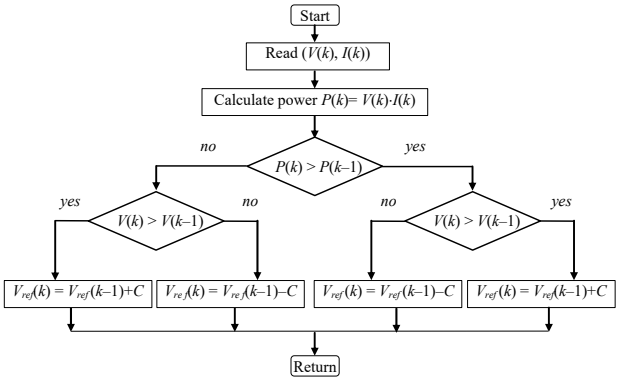

Fig. 5. P&O algorithm

Simulation results. The simulation parameters are detailed in Table 1.

Table 1

Parameters of simulation

Parameter	Value
Source voltage	380 V
Line frequency	50 Hz
Line impedance	R_s = 0.01 Ω, L_s = 0.1 H
DC voltage	700 V
DC capacitor	2.35 mF
Load impedance 1	R = 90 Ω, L = 1 mH
Load impedance 2	R = 55 Ω, L = 50 mH

After deciding which perturbations to apply to the grids such as: voltage sag, swell and variation load to test the response of our active filter, simulations were performed using MATLAB/Simulink. The disruptions follow the timeline shown below:

From 0 s to 0.2 s – UPQC.

From 0.2 s to 1.3 s – PV-UPQC is commissioned with 700 W/m^2.

From 0.4 s to 0.6 s – sag voltage (with 70 % of normal voltage).

From 0.6 s to 1 s – normal operation.

From 1 s to 1.2 s – swell voltage (with 120 % of normal voltage).

From 1.2 s to 2.3 s – normal operation.

From 1.3 s to 2 s – PV-UPQC commissioned with 1000 W/m^2.

1.65 s – another load is applied.

From 2 s to 2.3 s – UPQC.

All details are summarized in Table 2. These simulations were performed to analyze the behavior of the active filter under different operating conditions and disturbances.

Table2

Variations of voltage and load

Time, s	0–0.2	0.2–0.4	0.4–0.6	0.6–1	1–1.2	1.2–2.3	1.65–2.3
Voltage, pu	1	1	0.7	1	1.2	1	1
Load	Load 1						Load 2

Simulation results before using the PV-UPQC. Active and reactive powers transit from the green source to the load. This study encompasses 2 comprehensive tests to evaluate the performance of our system. In the first test, we conducted a simulation of the system involving a source and a non-linear load. Our observations revealed that the source dynamically provides active and reactive power in response to load variations, including voltage sag and swell. We

meticulously explain the correlation between active and reactive power variations and changes in voltage and current, aligning them with the specific requirements of the load (Fig. 6). The Total Harmonic Distortion (THD) values are notably elevated in this case due to the presence of a non-linear load (Fig. 7).

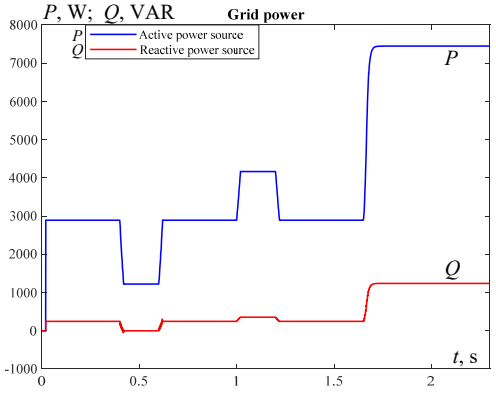

Fig. 6. Active and reactive power source

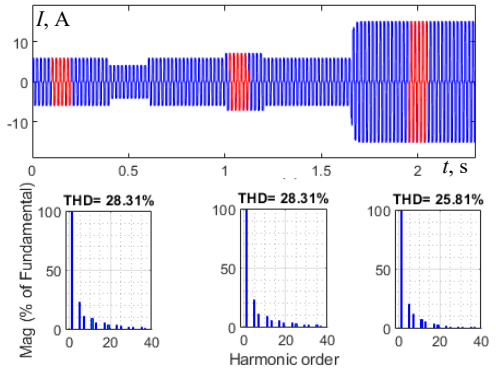

Fig. 7. Source current and its spectral analysis

Simulation results after using the PV-UPQC. The study is divided into 2 modes: the first mode is the exclusive use of an UPQC in the intervals [0–0.2] s and [2.1–2.3] s. The second mode involves using an UPQC in conjunction with a PV (PV-UPQC) generator between 0.2 s and 2.1 s, with a non-linear load variation at 1.65 s.

Figure 8 represents the variation of the irradiance on the PV system.

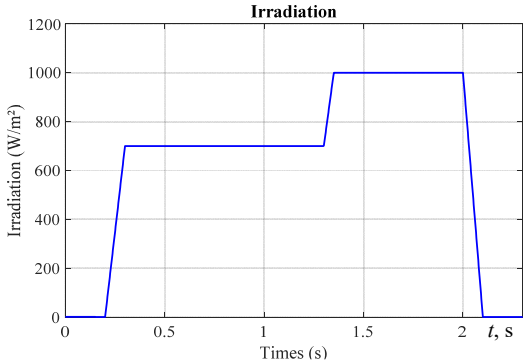

Fig. 8. Variation of irradiation

When the irradiance is zero, the source only provides active power equal to the power consumed by the load. The reactive power consumed by the load is handled by the UPQC (Fig. 9). This mode of operation is reflected in the voltage and current of the grid being in phase (Fig. 10).

The increase in irradiance is accompanied by a decrease in source current with reversed phases, signifying the grid's initiation of absorbing active power from the PV-UPQC (see Fig. 9, 10). Between 0.4 s and 0.6 s a deliberate voltage sag is applied, causing the voltage to drop to 0.7 times the nominal voltage. Source current flow intensifies to meet the load demand, as evidenced by Fig. 9, 10, highlighting the substantial contribution of the PV-UPQC in compensating for active power instead of relying solely on the source.

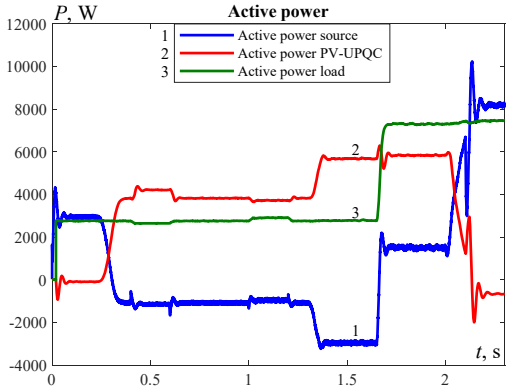

Fig. 9. Active power variation

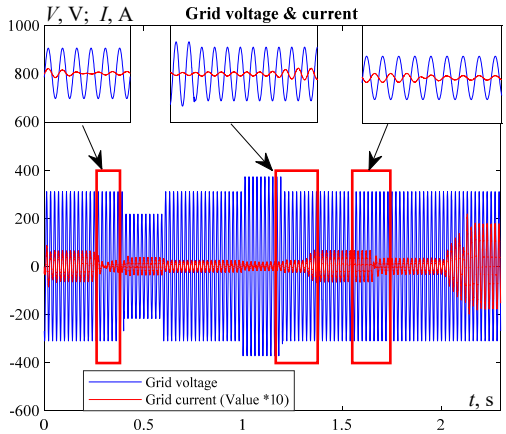

Fig. 10. Delay phase between grid voltage and current

The integration of PV-UPQC ensures optimized source current flow, effectively meeting load demand while minimizing losses and enhancing overall system efficiency. In contrast, during the time interval from 1 to 1.2 s, a voltage swell is introduced, resulting in the voltage rising to 1.2 times the nominal voltage, consequently, source current decreases.

Figures 9 – 11 illustrate the significant contribution of PV-UPQC in compensating for active power instead of relying solely on the source. At the instant 1.3 s, an increase in irradiation to 1000 W/m^2 leads to a subsequent rise in current value and, consequently, an increase in the active power of the PV-UPQC. However, the introduction of a new load at 1.65 s exceeds the capacity of the PV-UPQC to fully meet the load's power requirements, resulting in a portion of the source's power being utilized.

Figure 12 represents the evolution of the current injected by the PV-UPQC, which follows its reference accurately identified directly by the DCC method. We can see that in the absence of irradiance, the PV Fast Active Power (FAP) injects only harmonic currents. However, in the presence of irradiance, the PV-FAP injects both the PV current and the harmonic currents.

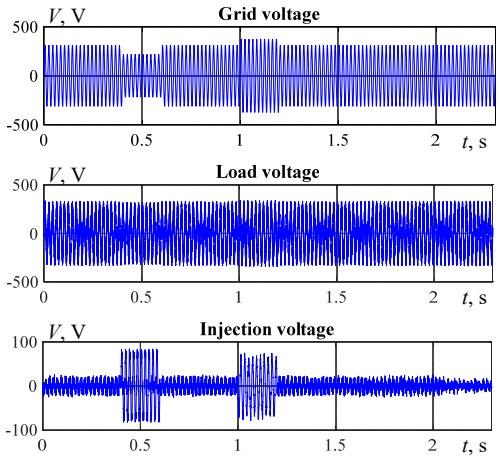

Fig. 11. Grid, load and injection voltage

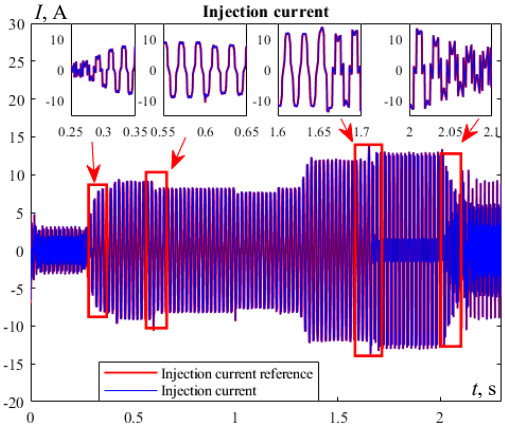

Fig. 12. Injection current of PV-UPQC and its reference

UPQC compensates reactive power through one of its main components, the shunt active power filter (SAPF). To compensate for reactive power, the SAPF injects a current into the system that is 180° out of phase with the reactive component of the load's current. This injected current interacts with the reactive power, effectively canceling it out and reducing the system's overall reactive power demand, as shown in Fig. 13. Thus reducing the system's reactive power demand and improving PQ.

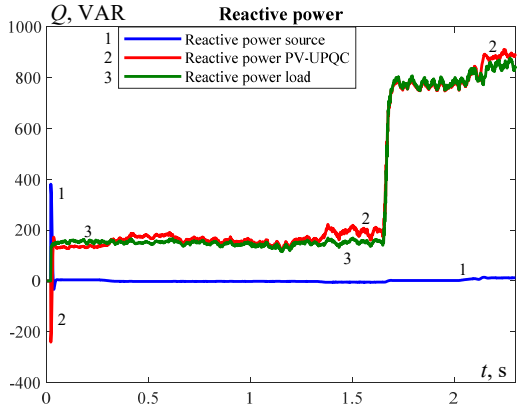

Fig. 13. Reactive power variation

UPQC-PV effectively reduces the THD of the current (Fig. 14).

Figure 15 demonstrates that DC bus voltage follows its reference after each interruption, which shows the effectiveness of the proposed controller.

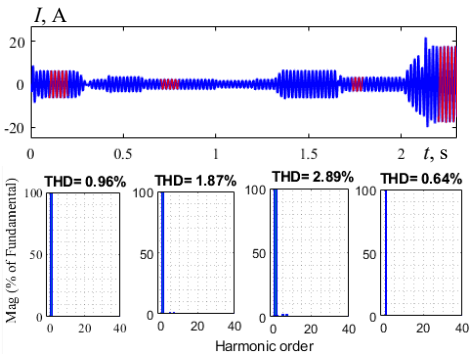

Fig. 14. Source current and its spectral analysis after using PV-UPQC

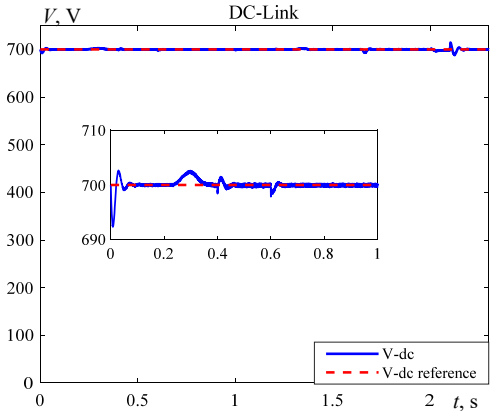

Fig. 15. DC bus V_{dc} and its reference

Conclusions. Photovoltaic-Unified Power Quality Conditioner (PV-UPQC) assumes a pivotal role in enhancing power quality. This paper underscores its valuable features, including its ability to improve instantaneous waveforms (both currents and voltages), mitigate voltage sags and swells, save active power, and compensate reactive power. These attributes are crucial for optimizing the utilization of electrical energy and reducing energy wastage.

Our proposed method involves employing the direct current control method for the parallel active power filter. This method enables real-time injection of harmonic currents equal in magnitude and opposite in phase to those absorbed by the nonlinear load. Additionally, for series active power filters, we utilize hysteresis control, which acts as a controllable voltage source and counters troublesome voltage variations such as sags and swells. This comprehensive control approach addresses multiple issues simultaneously, including the mitigation of voltage disturbances, improvement of current waveforms, compensation for reactive power, and utilization of solar energy when available (irradiation-based).

Finally, the positive results outlined in this paper affirm the effectiveness of the PV-UPQC device in enhancing the reliability and flexibility of energy systems. These benefits extend across a wide range of industrial and residential applications, thereby providing tangible advantages to users.

Conflict of interest. The authors declare that they have no conflicts of interest.

REFERENCES

1. Song Y., Nian H. Sinusoidal Output Current Implementation of DFIG Using Repetitive Control Under a Generalized Harmonic Power Grid With Frequency Deviation. *IEEE*

Transactions on Power Electronics, 2015, vol. 30, no. 12, pp. 6751-6762. doi: https://doi.org/10.1109/TPEL.2015.2390213.

2. Azeredo L.F.S., Yahyaoui I., Fiorotti R., Fardin J.F., Garcia-Pereira H., Rocha H.R.O. Study of reducing losses, short-circuit currents and harmonics by allocation of distributed generation, capacitor banks and fault current limiters in distribution grids. *Applied Energy*, 2023, vol. 350, art. no. 121760. doi: https://doi.org/10.1016/j.apenergy.2023.121760.

3. Wang G., Wu Z., Liu Z. Predictive direct control strategy of unified power quality conditioner based on power angle control. *International Journal of Electrical Power & Energy Systems*, 2024, vol. 156, art. no. 109718. doi: https://doi.org/10.1016/j.ijepes.2023.109718.

4. Reisi A.R., Moradi M.H., Showkati H. Combined photovoltaic and unified power quality controller to improve power quality. *Solar Energy*, 2013, vol. 88, pp. 154-162. doi: https://doi.org/10.1016/j.solener.2012.11.024.

5. Chemidi A., Benhabib M.C., Bourouis M.A. Performance improvement of shunt active power filter based on indirect control with a new robust phase-locked loop. *Electrical Engineering & Electromechanics*, 2022, no. 4, pp. 51-56. doi: https://doi.org/10.20998/2074-272X.2022.4.07.

6. Chen D., Xu Z., Xiao L., Yan W., Guo Y. A direct current control strategy based on vector resonance controller for shunt active power filter. *Energy Reports*, 2022, vol. 8, pp. 122-130. doi: https://doi.org/10.1016/j.egyr.2022.01.158.

7. Patjoshi R.K., Mahapatra K.K. Performance comparison of direct and indirect current control techniques applied to a sliding mode based shunt active power filter. *2013 Annual IEEE India Conference (INDICON)*, 2013, pp. 1-5. doi: https://doi.org/10.1109/INDCON.2013.6725854.

8. Djeghader Y., Zellouma L., Lakehal A., Chelli Z. Harmonic Mitigation in Electrical Radial Distribution System Using Photovoltaic Unified Power Quality Conditioner (PV-UPQC). *2019 8th International Conference on Systems and Control (ICSC)*, 2019, pp. 94-99. doi: https://doi.org/10.1109/ICSC47195.2019.8950507.

9. Nedeljkovic D., Nemec M., Drobnic K., Ambrozic V. Direct Current Control of Active Power Filter without Filter Current Measurement. *2008 International Symposium on Power Electronics, Electrical Drives, Automation and Motion*, 2008, pp. 72-76. doi: https://doi.org/10.1109/SPEEDHAM.2008.4581257.

10. Javadi A., Woodward L., Al-Haddad K. Real-Time Implementation of a Three-Phase THSeAF Based on a VSC and a P+R Controller to Improve the Power Quality of Weak Distribution Systems. *IEEE Transactions on Power Electronics*, 2018, vol. 33, no. 3, pp. 2073-2082. doi: https://doi.org/10.1109/TPEL.2017.2697821.

11. Gopal Reddy S., Ganapathy S., Manikandan M. Power quality improvement in distribution system based on dynamic voltage restorer using PI tuned fuzzy logic controller. *Electrical Engineering & Electromechanics*, 2022, no. 1, pp. 44-50. doi: https://doi.org/10.20998/2074-272X.2022.1.06.

12. Sai Thrinath B.V., Prabhu S., Meghya Nayak B. Power quality improvement by using photovoltaic based shunt active harmonic filter with Z-source inverter converter. *Electrical Engineering & Electromechanics*, 2022, no. 6, pp. 35-41. doi: https://doi.org/10.20998/2074-272X.2022.6.06.

13. Belila H., Boudjerda N., Bahri I., Boubakir A. Robust Hybrid Control Strategy PI-Sliding Mode Control of a STATCOM in the Presence of a Decentralized PV Source. *Przeglad Elektrotechniczny*, 2022, vol. 98, no. 10, pp. 292-298. doi: https://doi.org/10.15199/48.2022.10.66.

14. Djazia K., Sarra M. Improving the quality of energy using an active power filter with zero direct power command control related to a photovoltaic system connected to a network. *Electrical Engineering & Electromechanics*, 2023, no. 5, pp. 20-25. doi: https://doi.org/10.20998/2074-272X.2023.5.03.

15. Djeghader Y., Boumous Z., Boumous S. Investigation and Filtering of Harmonic Currents in Hybrids Renewable Energy System. *Przeglad Elektrotechniczny*, 2023, vol. 99, no. 1, pp. 124-128. doi: https://doi.org/10.15199/48.2023.01.24.

16. Mansor M.A., Hasan K., Othman M.M., Noor S.Z.B.M., Musirin I. Construction and Performance Investigation of Three-Phase Solar PV and Battery Energy Storage System Integrated UPQC. *IEEE Access*, 2020, vol. 8, no. 103511-103538. doi: https://doi.org/10.1109/ACCESS.2020.2997056.

Received 06.01.2024
Accepted 26.03.2024
Published 20.06.2024

Choayb Bousnoubra[1], *PhD Student,*
Yacine Djeghader[1], *Associate Professor,*
Hassen Belila[2], *Associate Professor,*
[1] University of Souk-Ahras, LEER Laboratory,
41000, Souk-Ahras, Algeria,
e-mail: c.bousnoubra@univ-soukahras.dz (Corresponding Author);
yacine.djeghader@univ-soukahras.dz
[2] University of Oum El Bouaghi, Science and Applied Sciences Faculty, LENT Laboratory, 04000, Oum El Bouaghi, Algeria,
e-mail: hassen.belila@univ-oeb.dz

How to cite this article:
Bousnoubra C., Djeghader Y., Belila H. Contribution of using a photovoltaic unified power quality conditioner in power quality improvement. *Electrical Engineering & Electromechanics*, 2024, no. 4, pp. 42-47. doi: https://doi.org/10.20998/2074-272X.2024.4.05

UDC 621.314 https://doi.org/10.20998/2074-272X.2024.4.06

A. Lanani, D. Djamai, A. Beddiaf, A. Saidi, A. Abboudi

Photovoltaic system faults detection using fractional multiresolution signal decomposition

Introduction. *In this paper, we present an innovative methodology based on fractional wavelets for detecting defects in photovoltaic systems. Photovoltaic solar systems play a key role in the transition to a low-carbon economy, but they are susceptible to various defects such as microcracks, wiring faults, and hotspots. Early detection of these anomalies is crucial to prevent energy losses and extend the lifespan of installations.* ***Novelty*** *of the proposed work resides in its pioneering nature, leveraging a family of fractional wavelets, with a specific emphasis on fractional Haar wavelets. This approach enhances sensitivity in anomaly detection, introducing a fresh and promising perspective to enhance the reliability of photovoltaic installations.* ***Purpose*** *of this study is to develop a defect detection methodology in photovoltaic systems using fractional wavelets. We aim to improve detection sensitivity with a specific focus on low-amplitude defects such as microcracks.* ***Method****. Our innovative methodology is structured around two phases. Firstly, we undertake a crucial step of filtering photovoltaic signals using fractional Haar wavelets. This preliminary phase is of paramount importance, aiming to rid signals of unwanted noise and prepare the ground for more precise defect detection. The second phase of our approach focuses on the effective detection of anomalies. We leverage the multiresolution properties of fractional wavelets, particularly emphasizing fractional Haar wavelets. This step achieves increased sensitivity, especially in the detection of low-amplitude defects.* ***Results.*** *By evaluating the performance of our method and comparing it with techniques based on classical wavelets, our results highlight significant superiority in the accurate detection of microcracks, wiring faults, and hotspots. These substantial advances position our approach as a promising solution to enhance the reliability and efficiency of photovoltaic installations.* ***Practical value****. These advancements open new perspectives for preventive maintenance of photovoltaic installations, contributing to strengthening the sustainability and energy efficiency of solar systems. This methodology offers a promising solution to optimize the performance of photovoltaic installations and ensure their long-term reliability.* References 21, tables 3, figures 10.

Keywords: **fault detection, photovoltaic systems, microcracks, wiring defects, hot spots, preventive maintenance, multiresolution analysis, fractional wavelets.**

Вступ*. У статті ми представляємо інноваційну методологію, засновану на дробових вейвлетах для виявлення дефектів у фотоелектричних системах. Фотоелектричні сонячні системи відіграють ключову роль у переході до низьковуглецевої економіки, але вони схильні до різних дефектів, таких як мікротріщини, несправності проводки та гарячі точки. Раннє виявлення цих аномалій має вирішальне значення для запобігання втратам енергії та продовження терміну служби установок.* ***Новизна*** *запропонованої роботи полягає у її новаторському характері, в якій використовується сімейство дробових вейвлетів з особливим упором на дробові вейвлети Хаара. Цей підхід підвищує чутливість виявлення аномалій, відкриваючи нову суттєву перспективу для підвищення надійності фотоелектричних установок.* ***Метою*** *дослідження є розробка методології виявлення дефектів у фотоелектричних системах з використанням дробових вейвлетів. Ми прагнемо покращити чутливість виявлення, приділяючи особливу увагу дефектам малої амплітуди, таким як мікротріщини.* ***Метод****. Наша інноваційна методологія складається із двох етапів. По-перше, ми робимо вирішальний крок щодо фільтрації фотоелектричних сигналів з використанням дробових вейвлетів Хаара. Цей попередній етап має першорядне значення, оскільки його мета - позбавити сигнали від небажаного шуму та підготувати ґрунт для більш точного виявлення дефектів. Другий етап нашого підходу спрямовано на ефективне виявлення аномалій. Ми використовуємо властивості множини роздільної здатності дробових вейвлетів, приділяючи особливу увагу дробовим вейвлетам Хаара. На цьому етапі досягається підвищена чутливість, особливо у разі виявлення дефектів малої амплітуди.* ***Результати****. Оцінюючи ефективність нашого методу та порівнюючи його з методами, заснованими на класичних вейвлетах, наші результати підкреслюють значну перевагу у точному виявленні мікротріщин, несправностей проводки та гарячих точок. Ці суттєві досягнення роблять наш підхід багатообіцяючим рішенням для підвищення надійності та ефективності фотоелектричних установок.* ***Практична цінність****. Ці досягнення відкривають нові перспективи для профілактичного обслуговування фотоелектричних установок, сприяючи підвищенню стійкості та енергоефективності сонячних систем. Ця методологія пропонує багатообіцяюче рішення для оптимізації продуктивності фотоелектричних установок та забезпечення їхньої довгострокової надійності.* Бібл. 21, табл. 3, рис. 10.

Ключові слова: **виявлення несправностей, фотоелектричні системи, мікротріщини, дефекти проводки, гарячі точки, профілактика, множинний аналіз, дробові вейвлети.**

Introduction. Photovoltaic (PV) solar energy plays a crucial role in the transition to a low-carbon economy. However, the efficiency and reliability of PV systems are susceptible to various defects, such as microcracks, hot spots, and wiring faults. Early detection of these anomalies is essential to prevent energy losses and extend the useful life of PV installations.

In response to this complex challenge, the scientific community has developed a range of sophisticated methodologies. Among these highly relevant and frequently utilized approaches in this field, the method based on Independent Component Analysis stands out [1, 2]. The latter distinguishes itself by its ability to provide remarkable spatial resolution in detecting microcracks. Significantly, defect detection based on Support Vector Machines offers another valuable perspective for identifying various anomalies in PV installations [3, 4]. In parallel, artificial intelligence plays a crucial role in the field of defect diagnosis, where the utilization of Convolutional Neural Networks has yielded promising results for defect detection in PV systems [5, 6]. The approach based on Deep Neural Networks has also garnered increasing interest for its potential in defect detection in PV modules [7]. Furthermore, methods based on wavelet transforms have proven effective in detecting defects by analyzing the frequency variations of PV signals, offering a robust and sensitive approach to anomaly detection [8, 9]. Finally, recent studies [10-13] have successfully combined neural networks with Discrete Wavelet Transform (DWT) for defect diagnosis in PV systems. This innovative approach has demonstrated great effectiveness in defect detection and precise localization.

© A. Lanani, D. Djamai, A. Beddiaf, A. Saidi, A. Abboudi

However, despite the undeniable advantages of these methods, limitations persist, especially in terms of sensitivity to the subtlest signal variations. It is precisely at this stage that fractional wavelets come into play, offering an alternative approach capable of overcoming these challenges.

The purpose of the paper is to present an innovative approach based on fractional wavelets aimed at enhancing fault detection in PV systems. Fractional wavelets provide a multiresolution representation and can be adapted to capture features at different scales in signals with remarkable precision. This capability stems from the flexibility, selectivity, and high accuracy of the filters comprising fractional wavelets. En incorporating these properties into fault diagnosis, our aim is to enhance the level of sensitivity and precision in detecting anomalies, be they microcracks in solar cells, wiring defects, or hot spots. Moreover, this approach allows for a more accurate localization of faults, thereby facilitating their intervention and repair. This promising methodology paves the way for a new generation of diagnostic techniques for PV installations, offering significant advantages in terms of reliability and operational efficiency.

Fractional wavelets. Fractional wavelets represent a powerful extension of the well-established tool of wavelets, providing increased flexibility in the multiresolution decomposition of signals. Unlike classical wavelets, fractional wavelets enable the capture of features at different scales with unparalleled precision. This capability stems from the fractional nature of the wavelet filters, which can be tailored to extract crucial information from PV signals, be it microcracks in solar cells, wiring defects, or hot spots.

Over the past few decades, the emergence of fractional wavelets in both continuous and discrete forms has marked a significant conceptual advance. This development has merged the power of classical wavelet transform with the properties of fractional Fourier transform [14]. This synergy has led to a new formulation, simplifying the construction significantly while ensuring increased accuracy. Particularly in the continuous domain, the integration of fractional derivative concepts within mathematical functions has greatly facilitated operations. Examples include generating wavelets from the Gaussian function and its fractional derivatives, as well as using the spline function with fractional degrees [15]. Quincunx wavelets have also been generalized to non-integer orders with a construction based on fractional Quincunx filters, which are generated through the diamond McClellan transform [16].

However, the definition of the discrete fractional wavelet transform has been a gap in scientific literature. To address this deficiency, a robust definition has been developed by discretizing the continuous version. Furthermore, the creation of discrete fractional wavelet bases has materialized through the generalization of the composing filters, leveraging fractional delay [17]. Indeed, from an architectural standpoint, the DWT manifests as a set of iterative filters, conferring upon it a multiresolution characteristic. This paves the way for the utilization of fractional-order filters in the realization of fractional wavelets, thus providing an innovative and accurate approach [18, 19].

The construction typically begins with the selection of a low-pass digital filter, enjoying the property of orthogonality; it is then generalized using fractional operators, ensuring the preservation of required orthogonality, compactness, and regularity properties. The high-pass filter can be derived from the low-pass filter through a simple modulation, thereby allowing, through the cascade algorithm [20], the deduction of the associated scaling function and wavelet function.

Our study focuses on the application of fractional Haar wavelets [18]. These types of wavelets stand out for their intriguing characteristics and properties. Thanks to the flexibility of the associated filters and their exceptional selectivity, they demonstrate an extraordinary ability to optimize a multitude of data processing tasks.

Fractional Haar wavelet. Its principle is based on the generalization of the low-pass filter associated with the ordinary Haar basis through fractional delay [17], where the integer delay Z^{-n}, $n \in Z$, is replaced by a fractional delay Z^{-D}, $D \in \Re$:

$$\tilde{H}_f(Z) = A + B \cdot Z^{-D}, \qquad (1)$$

where D is the filter order, A and B are its coefficients.

The orthogonality and regularity of the scaling and wavelet functions are ensured by the proper choice of coefficients A and B [18].

To ensure the feasibility of implementing fractional delays, an approximation method based on Lagrange interpolation has been chosen [17]. This approach was favored due to its simplicity in calculating filter coefficients and its ability to generate frequency responses with a flat magnitude at low frequencies.

The fractional high-pass filter will be constructed through a simple modulation of the fractional low-pass filter and deducing, through the cascade algorithm, the associated scaling and wavelet functions [18].

The frequency responses of the designed fractional filters are adjusted by varying the parameter D, as shown in Fig. 1. It appears that the generalization of ordinary filters via the fractional delay Z^{-D} leads to more flexible filters with better accuracy, where key filter parameters are continuously adjusted.

Methodology for fault detection in PV systems via fractional wavelets. In our study, we explored the practical application of the fractional wavelets that we specifically developed. To do so, we selected a widely adopted PV system, comprising solar panels, a DC-DC converter, and a battery for storage (Fig. 2), where we utilized measurements from a system described in [21]. Fault detection was carried out twice, at two different levels of the system, under various meteorological conditions.

Initially, we focused on faults that may occur at the level of the solar panels, such as microcracks and hot spots. We analyzed a signal captured at the output of the solar panel (V_{pv}), presented in Fig. 3. This initial phase was conducted under stable meteorological conditions, characterized by constant solar irradiance. Subsequently, we performed detection after the chopper, aiming to identify connection or wiring faults, using a signal captured after the chopper (V_0), as illustrated in Fig. 3.

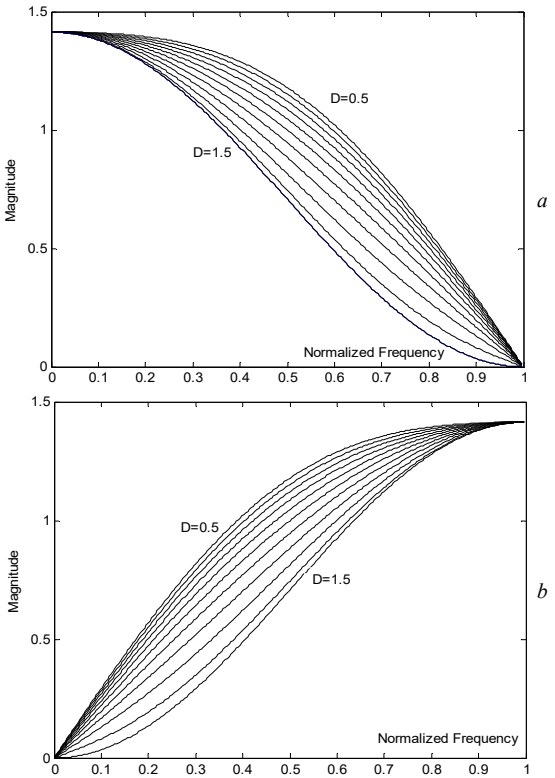

Fig. 1. Frequency responses of the fractional filters: *a* – low-pass filter; *b* – high-pass filter

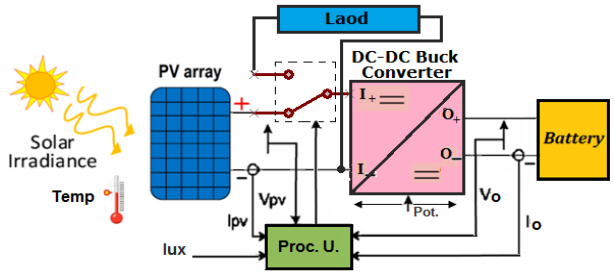

Fig. 2. PV system with a DC-DC buck converter, battery load and processing unit [21]

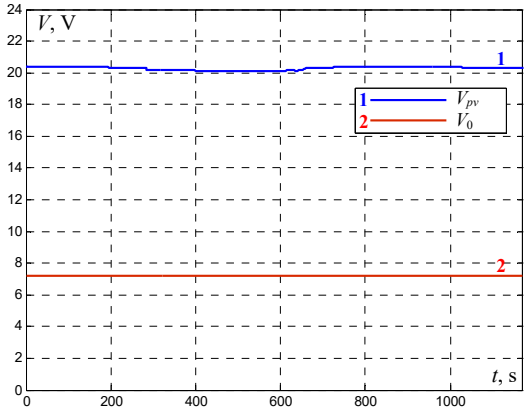

Fig. 3. Signals captured at the output of the solar panel (V_{pv}) and after the chopper (V_0) under stable meteorological conditions [21]

In a second phase, we proceeded with the detection of faults in the same previous system but under unstable meteorological conditions, characterized by the presence of clouds affecting solar radiation. The signals of the system under these conditions are presented in Fig. 4.

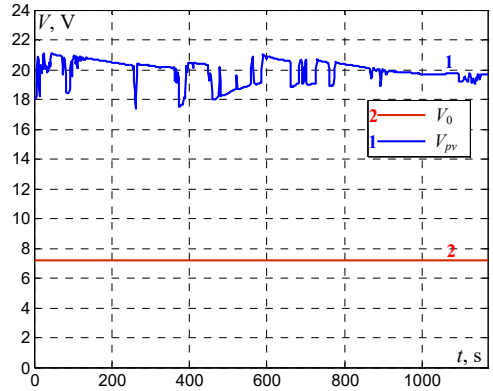

Fig. 4. Signals captured at the output of the solar panel (V_{pv}) and after the chopper (V_0) under unstable meteorological conditions [21]

Defects and noise were added to the signals to reflect various fault scenarios encountered in PV systems (Fig. 5). These anomalies were incorporated precisely and controlled to replicate realistic conditions. Simulated faults included microcracks modeled by pulses, wiring faults represented by voltage drops, and simulated hot spots represented by voltage spikes.

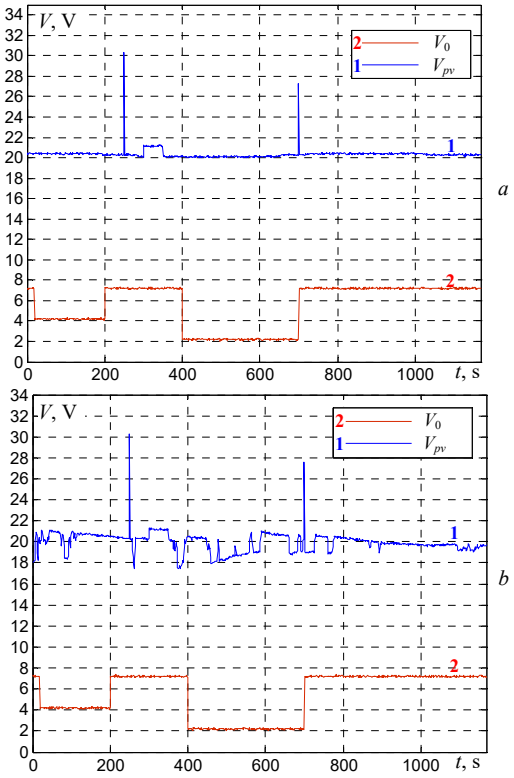

Fig. 5. Solar panel and chopper signals (V_{pv}, V_0) with simulated faults: *a* – stable meteorological conditions; *b* – unstable meteorological conditions

Our approach comprises several steps, as shown in Fig. 6.

Signal denoising using the designed fractional wavelets (pre-processing signal phase). Before proceeding with the fault detection, we denoised the signals using fractional wavelets. This phase is crucial as it aims to accurately detect and isolate various components of noise, thereby preparing the ground for subsequent anomaly detection. These filtered and isolated data were then utilized in our detection approach, contributing to a more precise identification and a better understanding of faults in the studied systems.

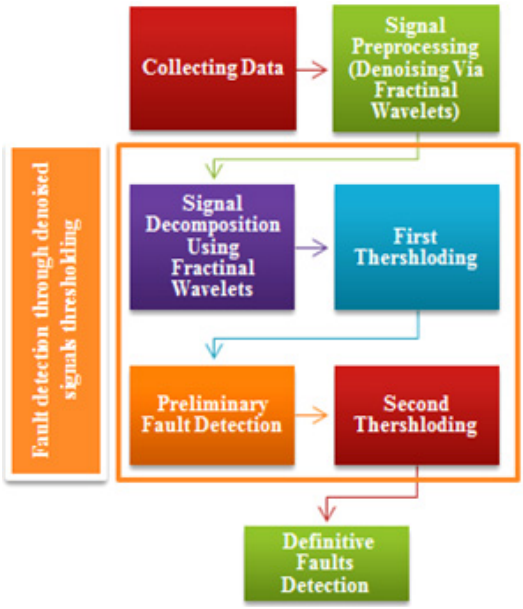

Fig. 6. Proposed method steps

Fault detection through denoised signals thresholding. After an appropriate decomposition of the denoised signals using the fractional wavelets we developed, thresholding was employed as a crucial step in our methodology. The choice of threshold is a delicate process, as it must be precisely calibrated to ensure reliable fault detection. This step is essential for isolating relevant signal details and thereby highlighting anomalies.

The thresholded signal details are carefully examined. Components with amplitudes exceeding the threshold are identified as potential fault points. These points are then located in the original signal, enabling us to accurately determine their temporal location.

In order to enhance detection precision and eliminate any points identified as faults erroneously, a second thresholding process was conducted on all initially identified suspect points.

Once the second thresholding is completed and the suspect fault points are detected, we compare their locations with the actual locations of anomalies previously introduced into the signals. This allowed us to quantify the performance of our method. We defined the following terms to evaluate these performances:

- True Positive (TP): The number of actual faults correctly detected.
- True Negative (TN): The number of points correctly identified as non-faulty.
- False Positive (FP): The number of points identified as faulty when they are not.
- False Negative (FN): The number of actual faults not detected.

$$Sensitivity = \frac{TP}{TP + FN}; \quad (2)$$

$$Specificity = \frac{TN}{TN + FP}; \quad (3)$$

$$Precision = \frac{TP}{TP + FP}. \quad (4)$$

This quantitative evaluation of performance has allowed us to validate the effectiveness of our fractional wavelet-based approach in the accurate and reliable detection of faults in PV systems.

Results and discussion. After applying our fractional wavelet-based methodology to simulated signals from various levels of the PV system and under different meteorological conditions, we conducted a detailed analysis to assess the effectiveness of our approach.

Firstly, concerning the detection of faults at the solar panel level, we analyzed the signals under different meteorological conditions. The use of fractional wavelets allowed for a precise decomposition of the signals, providing a fine separation between their various components, which was crucial for improved fault detection, notably for microcracks and hot spots as illustrated in Fig. 7. The detailed thresholded components revealed salient points corresponding to abnormal voltage variations. These points serve as potential indicators of faults in the PV system.

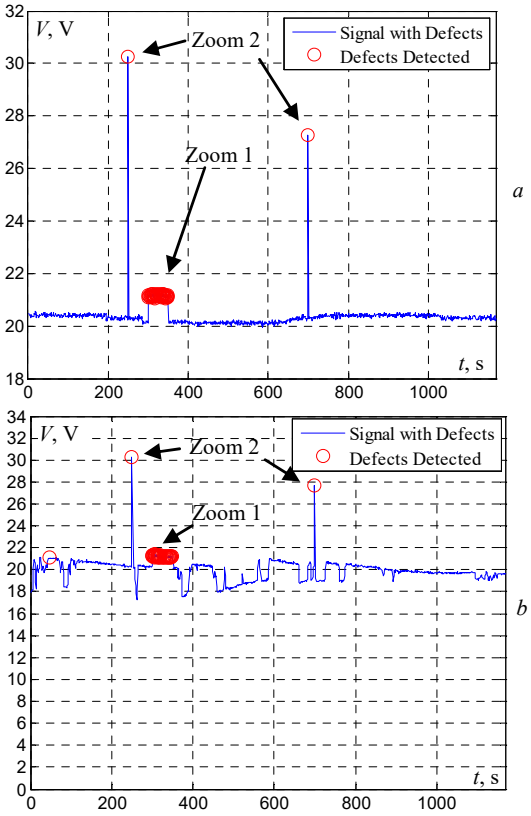

Fig. 7. Fault detection using the proposed method at the solar panels level: *a* – stable meteorological conditions; *b* – unstable meteorological conditions

Microcracks are subtle yet critical anomalies in solar cells. Through our methodology, we were able to accurately detect these micro-cracks, even when they were of low amplitude and under unstable meteorological conditions (Fig. 8). This demonstrates the heightened sensitivity of our approach.

Hot spots. Our methodology proved particularly effective in detecting hot spots, which can cause serious damage if not detected in time. By analyzing the signals using our fractional wavelets, we accurately and reliably identified the voltage peaks caused by hot spots (Fig. 9). This ability to spot these critical anomalies demonstrates the effectiveness of our approach in detecting the most serious defects in all meteorological conditions.

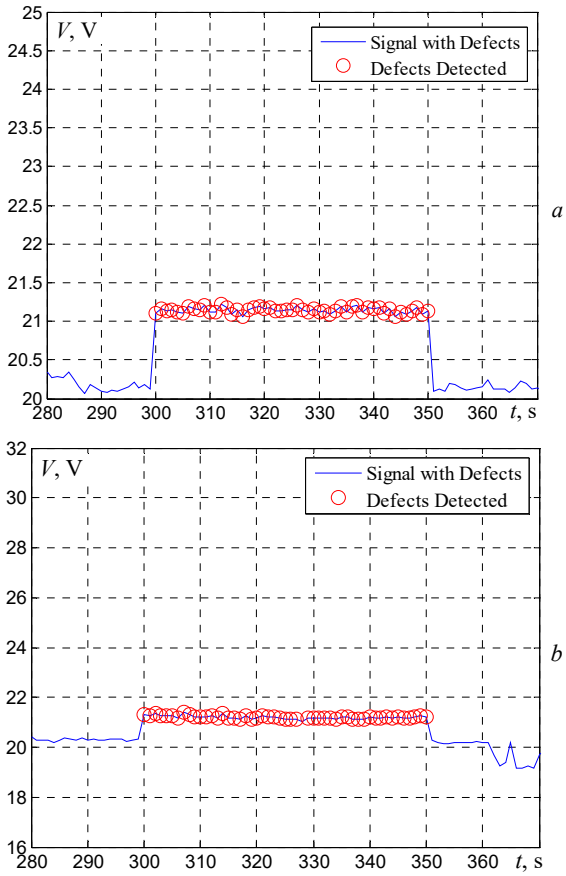

Fig. 8. Zoom 1: detection of micro-cracks: *a* – stable meteorological conditions; *b* – unstable meteorological conditions

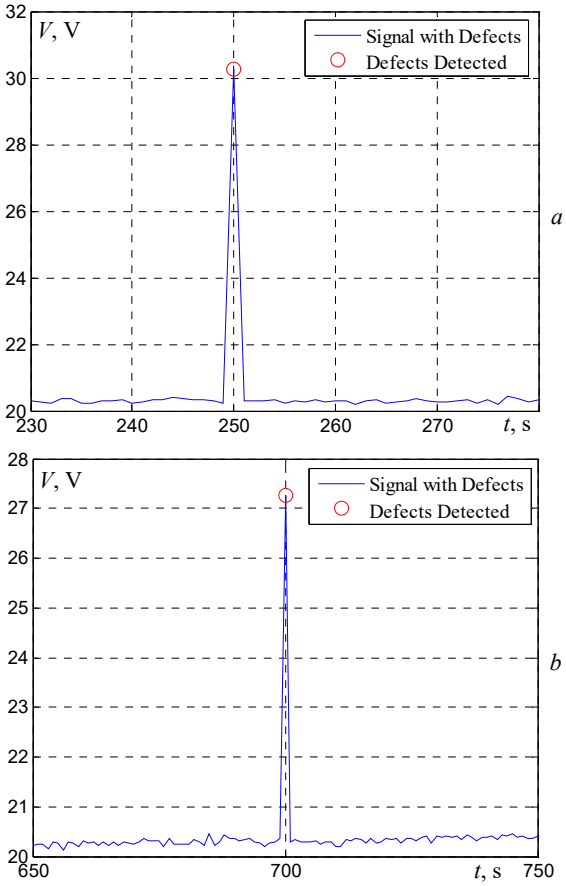

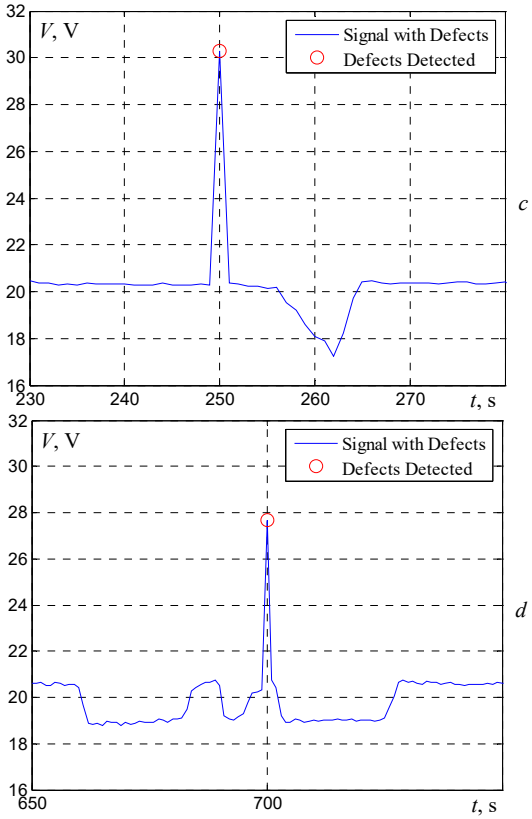

Fig. 9. Zoom 2: detection of hot spots: *a*, *b* – stable meteorological conditions; *c*, *d* – unstable meteorological conditions

Wiring defects. During the detection of wiring faults after the chopper, our method demonstrated remarkable effectiveness. By decomposing the captured signals using our fractional wavelets, we were able to precisely isolate abnormal voltage variations associated with wiring faults. This ability to detect wiring faults, even in scenarios where voltage fluctuations are subtle, underscores the robustness and accuracy of our approach in identifying critical system anomalies, as clearly illustrated in Fig. 10.

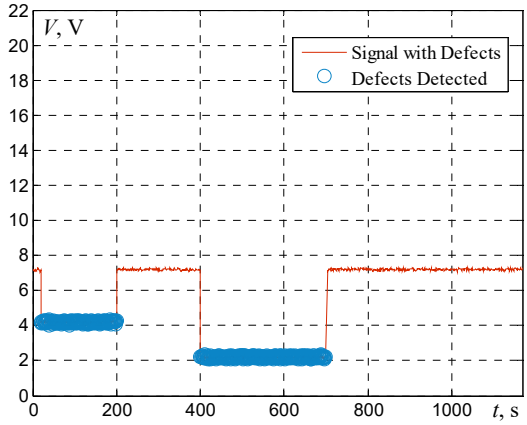

Fig. 10. Fault detection using the proposed method at the chopper level (detection of wiring faults)

In order to quantify the performance of our methodology, we calculated various metrics, including True Positives (TP), True Negatives (TN), False Positives (FP), and False Negatives (FN), as well as sensitivity, precision, and specificity. These calculations were conducted for each signal and under different meteorological conditions to capture the variability of our approach's performance in realistic scenarios.

Subsequently we compared the results obtained with those of classical wavelets commonly used in fault detection in PV systems. Specifically, we examined Haar, Daubechies, Coiflets, Symlets, Meyer wavelets, and bi-orthogonal wavelets. The performance evaluation results are presented in Tables 1 – 3.

Table 1

Results of fault detection at the chopper level using different wavelet families

Wavelet type	Number of detected faults	TP	TN	FP	FN	Sensitivity, %	Specificity, %	Precision, %
Fractional wavelet (developed model)	**482**	**482**	**687**	**0**	**0**	**100**	**100**	**100**
Haar	424	410	673	14	72	85.06	97.96	96.7
db6	444	438	681	6	44	90.87	99.13	98.65
coif5	440	431	678	9	51	89.42	89.69	97.95
sym5	429	417	675	12	65	86.51	98.25	97.20
dmey	446	444	685	2	38	92.11	99.71	99.55
bior3.3	439	429	677	10	53	89.00	98.54	97.72
rbio4.4	430	407	664	23	75	84.44	96.65	94.65

Table 2

Results of fault detection at the solar panel level using different wavelet families (stable meteorological condition)

Wavelet type	Number of detected faults	TP	TN	FP	FN	Sensitivity, %	Specificity, %	Precision, %
Fractional wavelet (developed model)	**53**	**53**	**1116**	**0**	**0**	**100**	**100**	**100**
Haar	48	27	1095	21	26	50.94	98.12	56.25
db6	51	34	1099	17	19	64.15	98.48	66.67
coif5	50	37	1103	13	16	69.81	98.83	74.00
sym5	52	35	1099	17	18	66.04	98.48	67.31
dmey	51	48	1113	3	5	90.57	99.73	94.12
bior3.3	52	40	1104	12	13	75.47	98.93	76.92
rbio4.4	51	36	1101	15	17	67.93	98.66	70.59

Table 3

Results of fault detection at the solar panel level using different wavelet families (unstable meteorological condition)

Wavelet type	Number of detected faults	TP	TN	FP	FN	Sensitivity, %	Specificity, %	Precision, %
Fractional wavelet (developed model)	**53**	**52**	**1115**	**1**	**1**	**98.11**	**99.91**	**98.11**
Haar	29	0	1087	29	53	00	97.40	00
Db6	49	37	1104	12	16	69.81	98.92	75.51
coif5	45	32	1103	13	21	60.38	98.84	71.11
sym5	48	29	1097	19	24	54.71	98.30	60.42
dmey	49	45	1112	4	8	84.91	99.64	91.84
bior3.3	42	18	1092	24	35	33.96	97.85	42.86
rbio4.4	47	35	1104	12	18	66.04	98.93	74.47

The results revealed an exceptional sensitivity of our approach, reaching 100 % for both the chopper signal (Table 1) and the solar panel signal under stable meteorological conditions (Table 2), demonstrating a robust capability to accurately detect real faults. Furthermore, the high specificity and precision indicate correct identification of non-faulty points. In contrast, under unstable meteorological conditions, our method's performance remained satisfactory, as evidenced by a low number of false positives (Table 3), highlighting its capability to mitigate false detections.

These results demonstrate the power and precision of our methodology based on fractional wavelets for fault detection in PV systems. The advantages of this approach are particularly evident in detecting low-amplitude faults and subtle anomalies, reinforcing its relevance in the context of solar installation inspection.

In comparison with classical wavelets, our methodology has demonstrated a superior ability to isolate relevant signal details. This is attributed to the significant flexibility and selectivity of the filters comprising the fractional wavelet, leading to a more precise detection of anomalies. This quantitative evaluation confirms the effectiveness of our fractional wavelet-based approach in accurately and reliably detecting faults in PV systems. These promising results pave the way for practical applications in the field of solar installation maintenance and optimization.

Conclusions. Our study has highlighted the remarkable effectiveness of fractional wavelets in the accurate detection of faults in photovoltaic systems. Through this innovative approach, we achieved significant selectivity and precision, enabling reliable detection of anomalies such as microcracks, wiring faults, and hot spots.

The implementation of our methodology yielded extremely promising results. We also conducted a comprehensive comparison with other commonly used wavelet types. This comparative study demonstrated that our fractional wavelet-based approach significantly outperforms methods based on classical wavelets.

These advancements open new perspectives for preventive maintenance of eco-friendly energy

installations, contributing significantly to the sustainability and overall efficiency of solar energy. A major innovation lies in the ability of our approach to synergistically combine with other cutting-edge methods, notably convolutional neural networks. This synergy expands possibilities for even more precise fault detection, solidifying our fractional model as a benchmark in the analysis of photovoltaic systems.

Conflict of interest. The authors declare that they have no conflicts of interest.

REFERENCES

1. Tsai D.-M., Wu S.-C., Chiu W.-Y. Defect Detection in Solar Modules Using ICA Basis Images. *IEEE Transactions on Industrial Informatics*, 2013, vol. 9, no. 1, pp. 122-131. doi: https://doi.org/10.1109/TII.2012.2209663.

2. Qureshi F.A., Uddin Z., Satti M.B., Ali, M. ICA-based solar photovoltaic fault diagnosis. *International Transactions on Electrical Energy Systems*, 2020, vol. 30, no. 8, art. no. e12456. doi: https://doi.org/10.1002/2050-7038.12456.

3. Badr M.M., Hamad M.S., Abdel-Khalik A.S., Hamdy R.A. Fault Detection and Diagnosis for Photovoltaic Array Under Grid Connected Using Support Vector Machine. *2019 IEEE Conference on Power Electronics and Renewable Energy (CPERE)*, 2019, pp. 546-553. doi: https://doi.org/10.1109/CPERE45374.2019.8980103.

4. Wang J., Gao D., Zhu S., Wang S., Liu H. Fault diagnosis method of photovoltaic array based on support vector machine. *Energy Sources, Part A: Recovery, Utilization, and Environmental Effects*, 2023, vol. 45, no. 2, pp. 5380-5395. doi: https://doi.org/10.1080/15567036.2019.1671557.

5. Saraswathi Devi K.V.B., Srivenkatesh M. Convolutional Neural Networks for Fault Detection in Grid-Connected Photovoltaic Panels. *Ingenierie des Systemes d'Information*, 2023, vol. 28, no. 6, pp. 1619-1625. doi: https://doi.org/10.18280/isi.280619.

6. Lu S.-D., Wang M.-H., Wei S.-E., Liu H.-D., Wu C.-C. Photovoltaic Module Fault Detection Based on a Convolutional Neural Network. *Processes*, 2021, vol. 9, no. 9, art. no. 1635. doi: https://doi.org/10.3390/pr9091635.

7. Kellil N., Aissat A., Mellit A. Fault diagnosis of photovoltaic modules using deep neural networks and infrared images under Algerian climatic conditions. *Energy*, 2023, vol. 263, part C, art. no. 125902. doi: https://doi.org/10.1016/j.energy.2022.125902.

8. Haque A., Bharath K.V.S., Khan M.A., Khan I., Jaffery Z.A. Fault diagnosis of Photovoltaic Modules. *Energy Science & Engineering*, 2019, vol. 7, no. 3, pp. 622-644. doi: https://doi.org/10.1002/ese3.255.

9. Suman T., Mahela O.P., Ola S.R. Detection of transmission line faults in the presence of solar PV generation using discrete wavelet. *2016 IEEE 7th Power India International Conference (PIICON)*, 2016, pp. 1-6. doi: https://doi.org/10.1109/POWERI.2016.8077203.

10. Jayamaha D.K.J.S., Lidula N.W.A., Rajapakse A.D. Wavelet-Multi Resolution Analysis Based ANN Architecture for Fault Detection and Localization in DC Microgrids. *IEEE Access*, 2019, vol. 7, pp. 145371-145384. doi: https://doi.org/10.1109/ACCESS.2019.2945397.

11. Jayamaha D.K.J.S., Lidula N.W.A., Rajapakse A.D. Wavelet Based Artificial Neural Networks for Detection and Classification of DC Microgrid Faults. *2019 IEEE Power & Energy Society General Meeting (PESGM)*, 2019, pp. 1-5. doi: https://doi.org/10.1109/PESGM40551.2019.8974108.

12. Bengharbi A.A., Laribi S., Allaoui T., Mimouni A. Photovoltaic system faults diagnosis using discrete wavelet transform based artificial neural networks. *Electrical Engineering & Electromechanics*, 2022, no. 6, pp. 42-47. doi: https://doi.org/10.20998/2074-272X.2022.6.07.

13. Sakhara S., Brahimi M., Nacib L., Layadi T.M. Application of a wavelet neural network approach to detect stator winding short circuits in asynchronous machines. *Electrical Engineering & Electromechanics*, 2023, no. 3, pp. 21-27. doi: https://doi.org/10.20998/2074-272X.2023.3.03.

14. Tao R., Deng B., Wang Y. Research progress of the fractional Fourier transform in signal processing. *Science in China Series F*, 2006, vol. 49, no. 1, pp. 1-25. doi: https://doi.org/10.1007/s11432-005-0240-y.

15. Unser M., Blu T. Fractional Splines and Wavelets. *SIAM Review*, 2000, vol. 42, no. 1, pp. 43-67. doi: https://doi.org/10.1137/S0036144598349435.

16. Feilner M., Jacob M., Unser M. Orthogonal quincunx wavelets with fractional orders. Proceedings *2001 International Conference on Image Processing (Cat. No.01CH37205)*, 2001, vol. 1, pp. 606-609. doi: https://doi.org/10.1109/ICIP.2001.959118.

17. Laakso T.I., Valimaki V., Karjalainen M., Laine U.K. Splitting the unit delay [FIR/all pass filters design]. *IEEE Signal Processing Magazine*, 1996, vol. 13, no. 1, pp. 30-60. doi: https://doi.org/10.1109/79.482137.

18. Abderrahim L., Salama M., Abdelbaki D. Novel design of a fractional wavelet and its application to image denoising. *Bulletin of Electrical Engineering and Informatics*, 2020, vol. 9, no. 1, pp. 129-140. doi: https://doi.org/10.11591/eei.v9i1.1548.

19. Lanani A., Abboudi A. New Fractional Wavelet with Compact Support and Its Application to Signal Denoising. *Journal of Nano- and Electronic Physics*, 2023, vol. 15, no. 2, art. no. 02023. doi: https://doi.org/10.21272/jnep.15(2).02023.

20. Daubechies I. Orthonormal bases of compactly supported wavelets. *Communications on Pure and Applied Mathematics*, 1988, vol. 41, no. 7, pp. 909-996. doi: https://doi.org/10.1002/cpa.3160410705.

21. Saidi A., Azoui B., Ghenai C., Lekmine F. Design and Conception of Platform that Allows to Connect Different Solar Panels and Loads through a DC-DC Buck Converter. *Journal of Nano- and Electronic Physics*, 2022, vol. 14, no. 6, art. no. 06004. doi: https://doi.org/10.21272/jnep.14(6).06004.

Received 30.01.2024
Accepted 26.03.2024
Published 20.06.2024

Abderrahim Lanani [1,2]*, Doctor of Technical Science, Associate Professor,*
Djemouai Djamai [1]*, Doctor of Technical Science, Associate Professor,*
Abdelaziz Beddiaf [1,2]*, Doctor of Technical Science, Associate Professor,*
Abdelkader Saidi [1]*, PhD Student,*
Abdelaziz Abboudi [1]*, PhD, Professor,*
[1] Abbes Laghrour University, Khenchela, 40000, Algeria,
[2] SATIT Laboratory,
Abbes Laghrour University, Khenchela, 40000, Algeria,
e-mail: lanani_arahim@univ-khenchela.dz (Corresponding Author);
ddjamai@yahoo.fr; beddiafaziz@yahoo.fr;
saidi.abdelkader@univ-khenchela.dz;
aboudiabdelaziz23@gmail.com

How to cite this article:
Lanani A., Djamai D., Beddiaf A., Saidi A., Abboudi A. Photovoltaic system faults detection using fractional multiresolution signal decomposition. *Electrical Engineering & Electromechanics*, 2024, no. 4, pp. 48-54. doi: https://doi.org/10.20998/2074-272X.2024.4.06

UDC 621.316 https://doi.org/10.20998/2074-272X.2024.4.07

S. Bedoui, A. Bayadi

Statistical approach for insulation coordination of high voltage substation exposed to lightning strikes

Introduction. *Insulation coordination requires accurate prediction of overvoltages at various points within a substation. Computer simulations of electromagnetic transients in real structures of substations become more precise due to the improvements of used models.* ***Goal.*** *This paper discusses in a first step the use of the modified ZnO arrester dynamic model alongside other substation equipment models, considering electrical phenomena like the corona model for reproducing the stresses that lightning can cause in an air-insulated substation and (**method**) then conducting a statistical approach based on the Monte Carlo method. The implemented MATLAB/ATP procedure estimates not only the substation Mean Time between Failures (MTBF), but also is used to select surge arresters or substation basic insulation levels (BILs). In this procedure ATP transients program is used to calculate lightning overvoltages and multicore environment for the calculations.* ***Results.*** *The obtained MTBF curves offer guidance for selecting appropriate insulation levels based on specific system requirements and conditions. The obtained results comply well with existing international insulation standards. This valuable approach significantly contributes to the field of lightning protection.* References 31, tables 3, figures 10.

Key words: **insulation coordination, substation, arrester, lightning overvoltages, basic insulation level, mean time between failures, Monte Carlo method.**

Вступ. *Координація ізоляції вимагає точного прогнозування перенапруг у різних точках підстанції. Комп'ютерне моделювання електромагнітних перехідних процесів у реальних конструкціях підстанцій стає більш точним за рахунок удосконалення моделей, що використовуються.* ***Мета***. *У цій статті на першому етапі обговорюється використання модифікованої динамічної моделі обмежувача перенапруги ZnO поряд з іншими моделями обладнання підстанції, розглядаються електричні явища, такі як модель коронного розряду, для відтворення напруг, які блискавка може викликати на підстанції з повітряною ізоляцією, та (**метод**) подальшого використання статистичного підходу, що базується на методі Монте-Карло. Впроваджена процедура MATLAB/ATP оцінює не лише середній час напрацювання на відмову підстанції (MTBF), але й використовується для вибору обмежувачів перенапруги або основних рівнів ізоляції підстанції. У цій процедурі використовується програма перехідних процесів ATP для розрахунку грозових перенапруг та багатоядерне середовище для розрахунків.* ***Результати***. *Отримані MTBF криві дають рекомендації щодо вибору відповідних рівнів ізоляції на основі вимог та умов конкретної системи. Отримані результати добре відповідають міжнародним стандартам ізоляції. Цей цінний підхід робить значний внесок у сферу блискавкозахисту.* Бібл. 31, табл. 3, рис. 10.

Ключові слова: **координація ізоляції, підстанція, обмежувач перенапруги, грозові перенапруги, базовий рівень ізоляції, середній час напрацювання на відмову, метод Монте-Карло.**

Introduction. The electrical system parts involved in lightning calculations must be represented taking into account the associated frequency margins [1]. In addition, the procedures must be developed keeping in mind the random nature of lightning phenomena [2]. It is well known that the substation is properly shielded [3, 4]; then, the actual work will only be concerned by lightning hitting the lines that are connected to it [5]. To ensure effective insulation coordination, it is crucial to accurately predict surges at different locations within the substation [6]. This requires consideration the presence of ZnO surge arresters at key points within the substation, which should provide some protective benefits [7, 8]. The analysis of atmospheric overvoltage in electrical substations or transmission lines has always posed a problem in determining the lightning current amplitude which falls on the protected object [9, 10].

This work details the analysis of the insulation coordination of a complete three-phase operational air-insulation substation considering the incoming surges through one of the transmission lines. The overvoltages at the critical points in the substation are measured and compared to the equipments insulation strength. For this purpose 3 scenarios were identified.

In the first one, the substation Mean Time between Failures (MTBF) has been determined knowing the equipment Basic Insulation Level (BIL) and the arrester. In the second one, the adequate BIL has been determined requiring both the MTBF and the arrester. Finally, the suitable arrester has been selected once both BIL and MTBF are required. In this case, it is necessary to simulate the system for each arrester.

Briefly speaking, this paper discusses the selection of insulation levels, specifically the BIL and the MTBF, which are crucial factors in the reliability of electrical systems, particularly in gas-insulated and air-insulated stations. Gas-insulated stations typically require higher MTBFs, ranging from 300 to 1000 years, while air-insulated stations may still maintain acceptable reliability with MTBFs around 100 years [1].

In such a study, a precise calculation is highly recommended. For that reason, the Monte Carlo statistical analysis technique was chosen [11]. Although it is extremely long due to the extensive number of simulations and the complexity of the system model, it provides exact results [12]. In this paper, this method has been implemented in MATLAB and integrated with the ATP-EMTP program for conducting system simulations. To speed up the overall solution process, MATLAB's parallel calculation feature was employed by using several cores to reduce the computing time in proportion to the number of cores [13, 14]. The dynamic model [15], of which the parameters were optimised using genetic algorithm technique, was used to account for the characteristics of ZnO arresters under lightning overvoltages.

This suggests that the paper provides guidelines for determining appropriate insulation levels based on the type of station and desired level of reliability.

© S. Bedoui, A. Bayadi

Studied system modelling. The studied system (Fig. 1) is a 400 kV, 50 Hz air-insulated substation in Oued El-Athmania (Algeria) [16]. The substation has 4 input lines, 2 busbars and 2 power autotransformers with 500 MVA. For protection purposes, ZnO surge arresters are installed at a distance of 3 m from the autotransformers. The connected transmission lines are three-phase lines with 2 conductors per phase and an optical fiber ground wire.

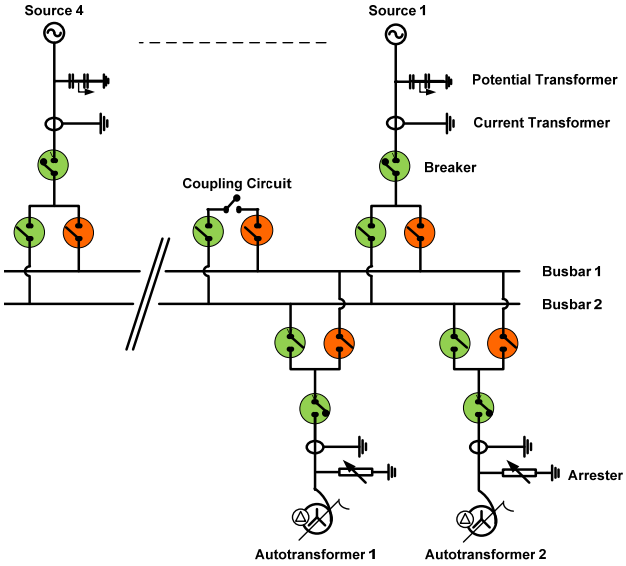

Fig. 1. Single line diagram of the studied substation

The following points summarize the modelling part:

• HV transmission line (Fig. 2,*a*) is represented by several spans (6 to 7 (390 m each), values within parenthesis are mid-span heights) with a long line termination to avoid reflection [14]. These blocks are represented using frequency-dependent distributed-parameter models. Note that the concatenation of phases and shield wire is also taken into consideration in the modeling of the transmission line.

• towers are represented by the multistory model (Fig. 2,*b*) proposed in [17-19]. It is composed of 3 sections; each one contains a lossless line with a parallel R-L circuit. The parameters of this model are calculated as:

$$R_i = \frac{-2Z_{ti}\ln\sqrt{\gamma}}{h_1+h_2}h_i, \quad i=1,2; \tag{1}$$

$$R_3 = -2Z_{t3}\ln\sqrt{\gamma}; \tag{2}$$

$$L_i = \frac{\alpha R_i 2H}{V_t}, \quad i=1,3, \tag{3}$$

where Z_{ti} is the tower surge impedance; γ is the attenuation coefficient; V_t is the surge propagation velocity; α is the damping coefficient; R is the damping resistance; L is the damping inductance; H is the tower height; h_i is the tower section height.

• Air-gap model (Fig. 2,*c*) is based on the leader propagation representation [20, 21]. The leader velocity $v(t)$ is calculated as:

$$v(t) = \frac{\mathrm{d}L}{\mathrm{d}t} = k_1\frac{U^2}{(D-L)} + k_2 C U^2 v\frac{L}{[D(D-L)]}, \tag{4}$$

where $k_1 = 2\cdot10^{-7}$ m^2/V^2·s; $k_2 = 3\cdot10^{-3}$ m^2/V^2·A·s; $C = 5\cdot10^{-10}$ F/m; D is the insulator length (5 m); L is the leader length; U is the actual voltage in the gap.

If leader velocity v is obtained at time t, leader length L at $(t + \Delta t)$ is calculated as:

$$L(t+\Delta t) = L(t) + v\cdot\Delta t. \tag{5}$$

The process of calculating the leader length continues until it reaches or exceeds the gap length ($L \geq D$) to sustain the discharge.

• The grounding impedance model of each tower (Fig. 2,*d*) is approximated by a nonlinear controlled resistance R_t [22, 23] given by:

$$R_t = R_0 \Big/ \sqrt{1 + I/I_g}, \tag{6}$$

where R_0 is the grounding resistance (20 Ω); I is the stroke current; I_g is the limiting current to initiate soil ionization, calculated as:

$$I_g = \frac{E_0\rho}{2\pi R_0^2}, \tag{7}$$

where ρ is the soil resistivity (Ω·m); E_0 is the soil ionization gradient (400 kV/m).

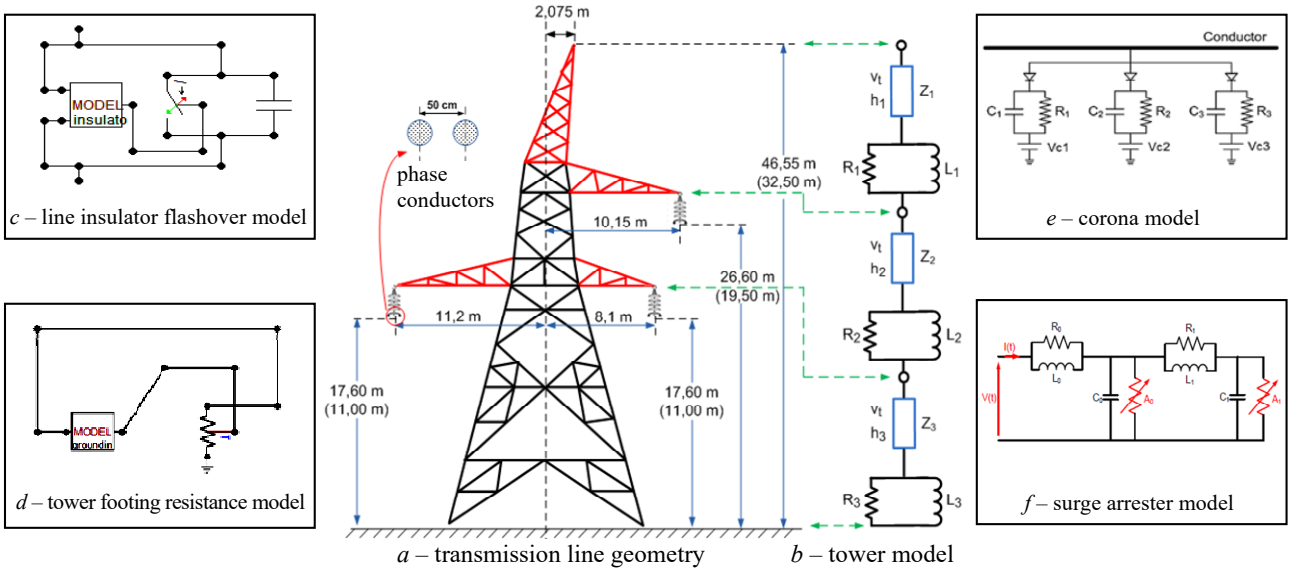

Fig. 2. Modelling of the system elements

• Corona effect (Fig. 2,*e*) is included into the line model using the circuit proposed in [24] in which:

$$V_{cr} = 23.8r\left(1+\frac{0.67}{r^{0.4}}\right)\ln\left(\frac{2h}{r}\right); \quad (8)$$

$$C_i = k_c \frac{1}{18\ln(2h/r)}, \quad (9)$$

where k_c must be adjusted to obtain a propagation model as close as possible to that recommended by standards; r, h are respectively the radius and height of the conductor; V_{cr} is the corona inception voltage; C_i is the corona capacitance.

• A sophisticated model of arrester (Fig. 2,*f*) based on genetic algorithm optimisation techniques is used [15, 25, 26].

Monte Carlo procedure. The article [14] provides a concise overview of essential steps in the MATLAB/ATP procedure designed for calculating lightning overvoltages in an outdoor substation. This procedure was first implemented in ATP using the models already presented.

Lightning stroke parameters (current magnitude, rise time and tail time) follow a statistical variation assumed to conform to a log-normal distribution, as described in [27-29]. The probability density function then takes the following form:

$$p(x) = \frac{1}{\sqrt{2\pi}\cdot x\cdot\sigma_{inx}}\exp\left[-\frac{1}{2}\left(\frac{\ln x - \ln x_m}{\sigma_{inx}}\right)^2\right], \quad (10)$$

where σ_{inx} is the standard deviation of ln$x$; x_m is the median value of x.

A correlation coefficient between the generated parameters such as the current magnitude and the rise time is considered [30] (more details in [14]).

The electro-geometric model, which is a set of probabilistic decisions (Fig. 3), is used to determine the lightning impact point on the transmission line [1, 12] (more details in [14]).

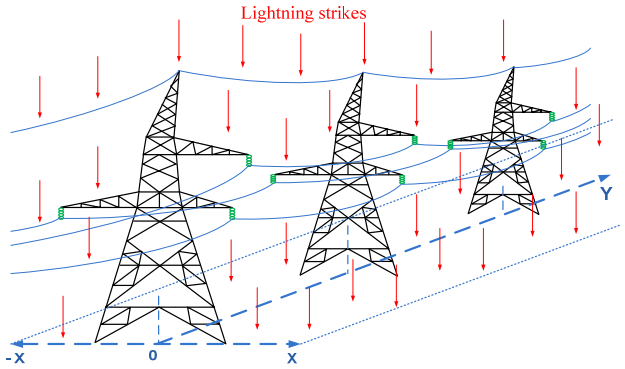

Fig. 3. Area of lightning strikes distribution

MTBF calculation is determined using the faults number (n_f) recorded at the substation equipment (overvoltages number that exceeds the equipments BIL value) and the number of years being simulated (Y_s):

$$MTBF = Y_s / n_f. \quad (11)$$

Once the system model has been implemented in ATP, the main steps of the lightning performance analysis procedure for the statistical study are summarized in Fig. 4.

Simulation results. In the present work, a statistical approach is proposed to evaluate the lightning performance of the substation. The incoming surges are analyzed to study the substation insulation strength based on the MTBF, BIL and arrester.

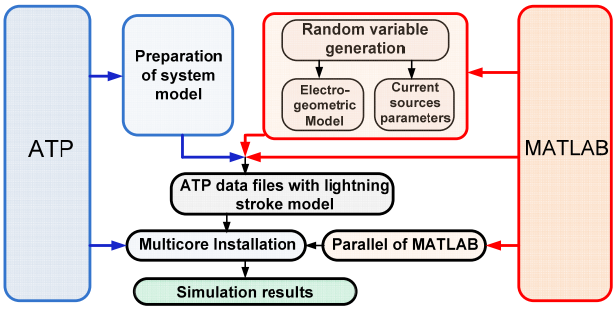

Fig. 4. Lightning performance analysis diagram for the statistical study

With the help of the parallel computing technique, the processing time was significantly reduced from several hours, which was necessary when using a single core, to just a few minutes, with a specific duration depending on the number of cores in use. A set of 60000 random number combinations was generated to evaluate the test system's lightning performance. These combinations equate to an analysis spanning 30769 years, taking into consideration a ground lightning strike density (N_g) of one strike per square kilometer per year.

The work involved analysing incoming surges to a substation through line 1. The surges were filtered using an electro-geometric model, specifically selecting 4690 cases out of a total of 60000 generated cases. This suggests a rigorous process of selection and analysis to focus on relevant surge scenarios, likely aiming to understand the impact of these surges on the substation's operation and/or to optimize its design for lightning protection.

Initially, the overvoltages at critical points in the substation are measured and compared to the equipments insulation strength (BIL). Simulations are repeated for the total number of generated cases, the considered scenarios are presented in Table 1.

Table 1

Studied scenarios

	MTBF	BIL	Arresters
Scenario A	to be determined	+	+
Scenario B	+	to be determined	+
Scenario C	+	+	to be determined

In the 1st scenario, a standard value of BIL is chosen together with an arrester and the corresponding MTBF will determine.

For the 2nd scenario the desired MTBF is fixed with an arrester, then the corresponding BIL will determine.

The 3rd scenario is proposed to determine a suitable arrester for a desired MTBF and required BIL.

In Table 2, the used ZnO arresters data from ABB are presented corresponding to the 400 kV network system [31].

Table 2

Main data of ZnO arresters

Arresters	Rated voltage, kV	Maximum service voltage, kV	Temporal overvoltages capacity, kV		Maximum residual voltage, kV_{max}						
					30/60 μs			8/20 μs			
	U_r	U_c	1 s	10 s	1 kA	2 kA	3 kA	5 kA	10 kA	20 kA	40 kA
Arrester 1	330	267	382	363	644	667	684	714	751	823	901
Arrester 2	336	272	389	369	656	679	696	727	765	838	918
Arrester 3	360	291	417	396	702	728	746	779	819	897	983
Arrester 4	372	301	431	409	726	752	771	804	847	927	1021
Arrester 5	378	306	438	415	737	764	783	817	860	942	1037
Arrester 6	390	315	452	429	761	788	808	843	888	972	1070
Arrester 7	420	336	487	462	819	849	870	908	956	1051	1152

Scenario A. As mentioned in Table 1, the 1st scenario aims to determine the substation MTBF knowing the equipments BIL and the arrester. As an example, Fig. 5 presents the simulation results for the case where the arrester №2 is used for two normalized BIL values (1050 and 1175 kV). As observed, for the operating zone recommended by international standards which require a safety margin between 80 and 85 % of BIL, the obtained MTBF for the BIL = 1050 kV ranges between 8 and 53 years. However, for 1175 kV, the MTBF is higher than 263 years. This means that enhancing insulation could be a viable solution.

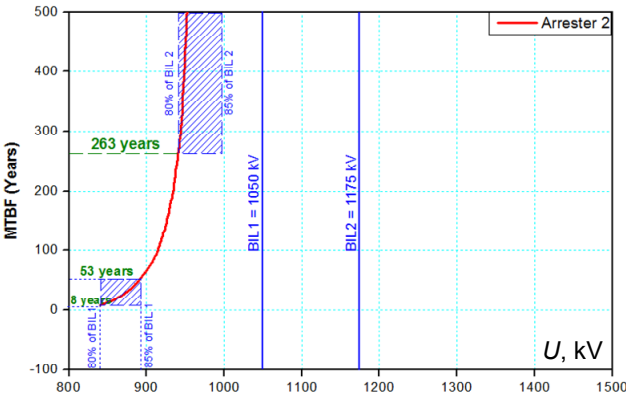

Fig. 5. Selection of the MTBF corresponding to BIL of 1050 kV and 1175 kV (case of arrester 2)

2nd example is chosen for the case where arrester №7 is installed. The BIL value now is taken equal to 1300 kV and the obtained results are shown in Fig. 6. By examining Fig. 6, it is clear that the MTBF ranges between 35 and 264 years, taking into account the safety margins required by international standards.

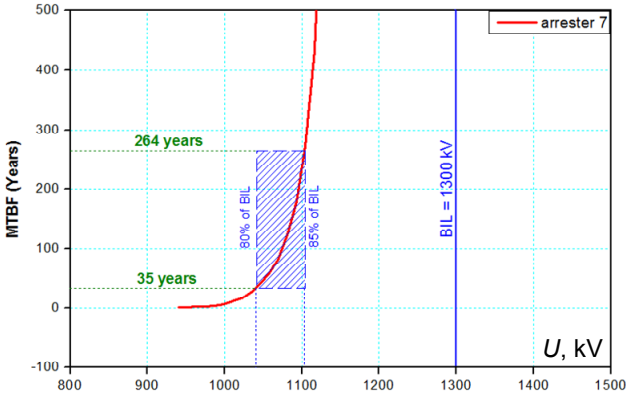

Fig. 6. Selection of the MTBF corresponding to the BIL of 1300 kV (case of arrester 7)

Scenario B. This scenario concerns the case where the desired MTBF is required with a chosen arrester in order to evaluate the adequate BIL value.

In such a situation, the point giving the necessary BIL is the intersection point between the horizontal straight line representing the desired MTBF value and the curve giving the variation of the MTBF as a function of the voltage value. As shown in Fig. 7, where the arrester №5 and the MTBF of 150 years are chosen, the obtained point has a value of 985 kV, which corresponds to 84 % of the BIL 1175 kV, so this BIL was selected for this case. When the operating point is not situated within the safety zone, in this case the highest value of the standard BIL was selected.

As shown in Fig. 8, the obtained operating point which guarantees the use of arrester №3 with an MTBF of 100 years is equal to 928 kV which corresponds to the point situated between 2 safety margin of the BIL 1050 kV and 1175 kV respectively, the largest one is selected in this case for safety reasons. On the other hand, the BIL 1050 kV can be chosen, when the system was protected using the arrester №1.

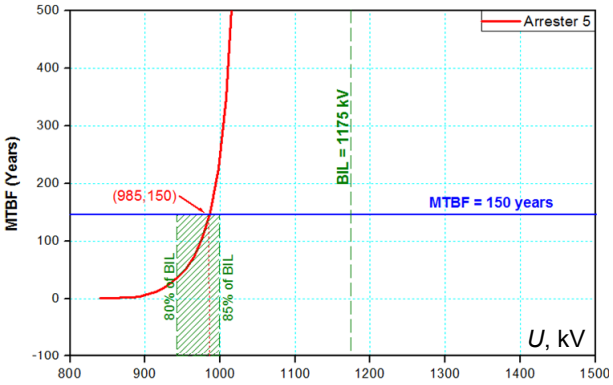

Fig. 7. Selection of the BIL corresponding to a MTBF = 150 years (case of arrester №5)

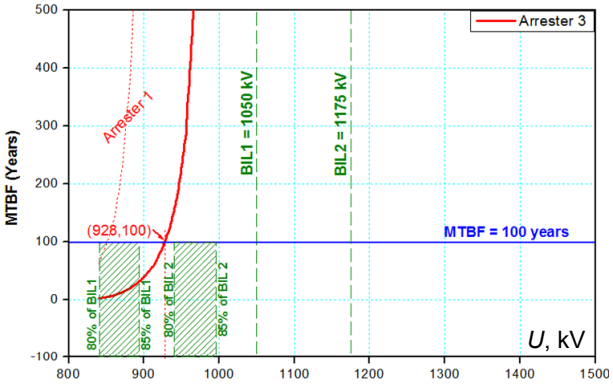

Fig. 8. Selection of the BIL corresponding to a MTBF = 100 years (case of arrester №3)

Scenario C. In this scenario, the aim is to determine the appropriate arrester, when both BIL and MTBF are required. In this case, it is necessary to simulate the system for each arrester. Consequently, a family of curves was obtained giving the variation of the MTBF as a function of the voltage value corresponding to the used arresters. The obtained curves will allow the selection of the appropriate arrester to be used according to the desired BIL and MTBF. In this scenario, only two cases are chosen as shown in Table 3.

Table 3

Studied cases for Scenario C

Studied case	MTBF, years	BIL, kV
Case 1	100	1050
Case 2	125	1300

The obtained results for the 1st case where the BIL is 1050 kV and the MTBF is 100 years are shown in Fig. 9. As can be seen, arrester №1 has to be selected since it meets the international standards.

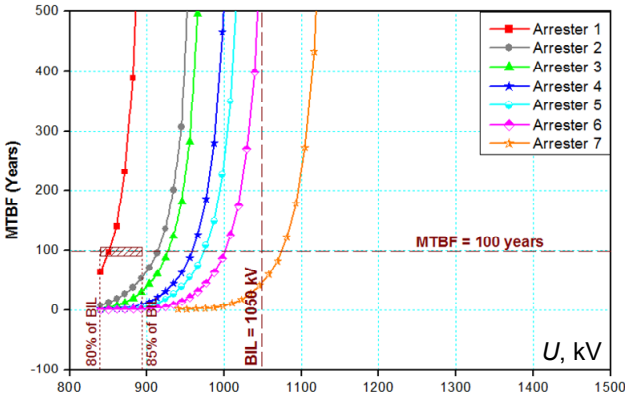

Fig. 9. Selection of the arrester corresponding to a BIL = 1050 kV and MTBF = 100 years

Another example, where the BIL and the MTBF are respectively 1300 kV and 125 years, is presented in Fig. 10. In this case, the arrester №7 has to be selected. The selection of this arrester is closely related to the desired MTBF and BIL.

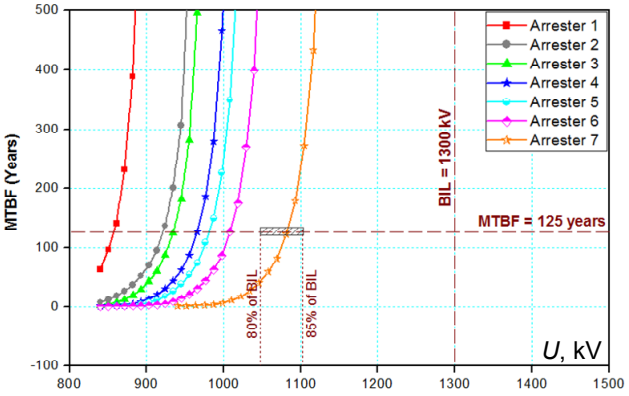

Fig. 10. Selection of the arrester corresponding to a BIL = 1300 kV and MTBF = 125 years

Conclusions. This paper discusses the key aspects of insulation coordination studies. Firstly it focuses on the use of modified ZnO arrester dynamic model alongside other substation equipment models, considering electrical phenomena like the corona model then conducting a statistical study based on the Monte Carlo method.

By incorporating a 20 % safety margin, a series of MTBF curves were generated as a function of voltages, depending on the selected arrester. These curves offer guidance for selecting appropriate insulation levels based on specific system requirements and conditions.

The results obtained can be summarized as follows:

- In the 1st scenario, the substation MTBF was determined (ranging from 8 to 53 years) by selecting BIL = 1050 kV and arrester №2. With BIL = 1175 kV for the same case, the MTBF obtained exceeds 263 years.
- In the 2nd scenario, using arrester №3 with an MTBF of 100 years is illustrated. The operating point, ensuring the intersection between the required values, is 928 kV, leading to select a BIL of 1175 kV for safety reasons.
- In the 3rd scenario, the adequate arrester was arrester №1 for a BIL of 1050 kV and an MTBF of 100 years. However, when a BIL of 1300 kV and an MTBF of 125 years were selected, arrester №7 was found the most appropriate choice.

These results demonstrate good alignment with international insulation standards. It is also important to mention that the implemented MATLAB/ATP procedure uses a statistical approach based on the Monte Carlo method in which ATP is used to estimate lightning overvoltages and the calculations are carried out with a multicore installation.

Moreover, the adopted methodology, focusing on air-insulated substations, can be extended to other substation technologies, such as GIS substations, by adjusting the specified models. This valuable approach significantly contributes to the field of lightning protection.

Conflict of interest. The authors declare that they have no conflicts of interest.

REFERENCES

1. Hileman A.R. *Insulation Coordination for Power Systems*. CRC Press, 2018, 767 p. doi: https://doi.org/10.1201/9781420052015.

2. Alto P. *Transmission Line Reference Book – 345 kV and Above. 2nd Edition*. Electric Power Research Institute, California, 1982. 625 p.

3. *BS EN 60071-2. Insulation Coordination Part 2. Application Guide*. 1997. 378 p.

4. *IEEE Std 1313.2-1999. IEEE Guide for the Application of Insulation Coordination*. 1999. 68 p. doi: https://doi.org/10.1109/IEEESTD.1999.90576.

5. Savic M.S., Savic A.M. Substation Lightning Performance Estimation Due to Strikes Into Connected Overhead Lines. *IEEE Transactions on Power Delivery*, 2015, vol. 30, no. 4, pp. 1752-1760. doi: https://doi.org/10.1109/TPWRD.2015.2404771.

6. *IEC TR 60071-4. Insulation co-ordination – Part 4: Computational guide to insulation co-ordination and modelling of electrical networks*. 2004. 118 p.

7. *IEC 60099-4:2014. Surge arresters – Part 4: Metal-oxide surge arresters without gaps for a.c. systems*, 2014, 353 p.

8. Bedoui S., Bayadi A., Haddad A.M. Analysis of lightning protection with transmission line arrester using ATP/EMTP: Case of an HV 220 kV double circuit line. *45th International Universities Power Engineering Conference UPEC2010*, Cardiff, UK, 2010, pp. 1-6.

9. Takami J., Okabe S., Zaima E. Study of Lightning Surge Overvoltages at Substations Due to Direct Lightning Strokes to Phase Conductors. *IEEE Transactions on Power Delivery*, 2010, vol. 25, no. 1, pp. 425-433. doi: https://doi.org/10.1109/TPWRD.2009.2033975.

10. Nowak W., Tarko R. Computer Modelling and Analysis of Lightning Surges in HV Substations due to Shielding Failure. *IEEE Transactions on Power Delivery*, 2010, vol. 25, no. 2, pp. 1138-1145. doi: https://doi.org/10.1109/TPWRD.2009.2033077.
11. Zio E. *The Monte Carlo Simulation Method for System Reliability and Risk Analysis*. Springer Publ., 2013. 198 p. doi: https://doi.org/10.1007/978-1-4471-4588-2.
12. Martinez J.A., Castro-Aranda F. Lightning Performance Analysis of Overhead Transmission Lines Using the EMTP. *IEEE Transactions on Power Delivery*, 2005, vol. 20, no. 3, pp. 2200-2210. doi: https://doi.org/10.1109/TPWRD.2005.848454.
13. Martínez-Velasco J.A., Corea-Araujo J.A., Bedoui S. Lightning Performance Analysis of Transmission Lines Using Parallel Computing. *European EMTP-ATP Conference - EEUG Meeting 2016*, Birmingham, England, 2016.
14. Bedoui S., Bayadi A. Probabilistic evaluation of the substation performance under incoming lightning surges. *Electric Power Systems Research*, 2018, vol. 162, pp. 125-133. doi: https://doi.org/10.1016/j.epsr.2018.05.011.
15. Bayadi A. Parameter identification of ZnO surge arrester models based on genetic algorithms. *Electric Power Systems Research*, 2008, vol. 78, no. 7, pp. 1204-1209. doi: https://doi.org/10.1016/j.epsr.2007.10.001.
16. *Sonelgaz Engineering Subcommittee. Specifications for the Construction of HV Electrical Substations*. 2004.
17. Dommel H.W. *Electromagnetic Transients Program Theory Book.* BPA, Portland, USA, 1986. 631p.
18. Ishii M., Kawamura T., Kouno T., Ohsaki E., Shiokawa K., Murotani K., Higuchi T. Multistory transmission tower model for lightning surge analysis. *IEEE Transactions on Power Delivery*, 1991, vol. 6, no. 3, pp. 1327-1335. doi: https://doi.org/10.1109/61.85882.
19. Baha Y., Ishii M. Numerical electromagnetic field analysis on lightning surge response of tower with shield wire. *IEEE Transactions on Power Delivery*, 2000, vol. 15, no. 3, pp. 1010-1015. doi: https://doi.org/10.1109/61.871367.
20. Shindo T., Suzuki T. A New Calculation Method of Breakdown Voltage-Time Characteristics of Long Air Gaps. *IEEE Transactions on Power Apparatus and Systems*, 1985, vol. PAS-104, no. 6, pp. 1556-1563. doi: https://doi.org/10.1109/TPAS.1985.319172.
21. Harada T. V-t Characteristics of Air Gaps for Steep Front Impulse Voltage. *Proceedings of 3rd ISH Milan*, 1979, vol. 52, no. 6, pp. 372-376.
22. *CIGRE WG 33-01. Guide to Procedures for Estimating the Lightning Performance of Transmission Lines*. CIGRE Brochure 63, 1991.
23. Boumous S., Boumous Z., Anane Z., Nouri H. Comparative study of 220 kV overhead transmission lines models subjected to lightning strike simulation by using electromagnetic and alternative transients program. *Electrical Engineering & Electromechanics*, 2022, no. 4, pp. 68-74. doi: https://doi.org/10.20998/2074-272X.2022.4.10.
24. Gallagher T.J., Dudurych I.M. Model of corona for an EMTP study of surge propagation along HV transmission lines. *IEE Proceedings - Generation, Transmission and Distribution*, 2004, vol. 151, no. 1, pp. 61-66. doi: https://doi.org/10.1049/ip-gtd:20030927.
25. Modeling guidelines for fast front transients. *IEEE Transactions on Power Delivery*, 1996, vol. 11, no. 1, pp. 493-506. doi: https://doi.org/10.1109/61.484134.
26. Modeling of metal oxide surge arresters. *IEEE Transactions on Power Delivery*, 1992, vol. 7, no. 1, pp. 302-309. doi: https://doi.org/10.1109/61.108922.
27. Martínez Velasco J.A., Corea Araujo J., Bedoui S. Lightning performance analysis of transmission lines using the Monte Carlo method and parallel computing. *Ingeniare. Revista Chilena de Ingeniería*, 2018, vol. 26, no. 3, pp. 398-409. doi: https://doi.org/10.4067/S0718-33052018000300398.
28. Chowdhuri P., Anderson J.G., Chisholm W.A., Field T.E., Ishii M., Martinez J.A., Marz M.B., McDaniel J., McDermott T.E., Mousa A.M., Narita T., Nichols D.K., Short T.A. Parameters of lightning strokes: a review. *IEEE Transactions on Power Delivery*, 2005, vol. 20, no. 1, pp. 346-358. https://doi.org/10.1109/TPWRD.2004.835039.
29. Kniaziev V.V. Determination of the probability of a lightning strike in the elements of the object taking into account the statistical distribution of the current value. *Electrical Engineering & Electromechanics*, 2023, no. 5, pp. 57-62. doi: https://doi.org/10.20998/2074-272X.2023.5.08.
30. Borghetti A., Nucci C.A., Paolone M. An Improved Procedure for the Assessment of Overhead Line Indirect Lightning Performance and Its Comparison with the IEEE Std. 1410 Method. *IEEE Transactions on Power Delivery*, 2007, vol. 22, no. 1, pp. 684-692. doi: https://doi.org/10.1109/TPWRD.2006.881463.
31. ABB High Voltage Products. *Surge Arresters – Buyer's Guide*. Edition 6, 2008, Catalog Publ. 1HSM 9543.

Received 28.02.2024
Accepted 26.04.2024
Published 20.06.2024

S. Bedoui[1], *Doctor of Science*,
A. Bayadi[2], *Professor*,
[1] Laboratory of Electrical Engineering and Automatic (LGEA),
University of Oum El Bouaghi, Algeria,
e-mail: bs_1182@yahoo.fr (Corresponding Author)
[2] Automatic Laboratory of Setif (LAS),
University of Setif-1, Algeria,
e-mail: a_bayadi@univ-setif.dz

How to cite this article:
Bedoui S., Bayadi A. Statistical approach for insulation coordination of high voltage substation exposed to lightning strikes. *Electrical Engineering & Electromechanics*, 2024, no. 4, pp. 55-60. doi: https://doi.org/10.20998/2074-272X.2024.4.07

UDC 621.3.022:621.396.6:533.93 https://doi.org/10.20998/2074-272X.2024.4.08

K.V. Korytchenko, V.F. Bolyukh, S.G. Buriakovskyi, Y.V. Kashansky, O.I. Kocherga

Plasma acceleration in the atmosphere by pulsed inductive thruster

Introduction. *One of the directions of development of plasma technologies consists in the formation of gas-metal plasma formations and throwing them to a certain distance. Known thrusters of plasma formation either have an electrode system that is prone to erosion, or a discharge system in a solid dielectric substance in which ablation occurs, or a complex gas-dynamic system with fuel supply. They do not provide acceleration of plasma formation in the atmosphere for a significant distance.* ***Purpose.*** *A theoretical and experimental study of electromechanical and thermophysical processes in a plasma thruster, which ensures the formation of a plasma formation due to thermal ionization by an induced current in a thin conductor layer during a high-voltage discharge on an inductor and the accelerating of a plasma formation in the atmosphere for a significant distance.* ***Methodology.*** *The proposed concept of a plasma thruster, in which the inductor inductively interacts with a combined armature, which includes an aluminum armature in the form of a thin (0.5-1 μm) foil, a copper armature made of a thicker foil (35-50 μm).On the basis of a mathematical model that takes into account the uneven distribution of currents in the inductor and conductive armatures, the features of the process of acceleration the combined armature in the atmosphere were established and experimental studies were carried out.* ***Results****. The electromechanical and thermal characteristics of the plasma thruster were calculated. It was established that the choice of the thickness of the dielectric layer of the armature, to which the aluminum and copper armatures are attached, is determined by the energy balance between the heating temperature of the aluminum armature and the electromechanical indicators of the thrower.* ***Scientific novelty.*** *It was experimentally established that the greatest density and homogeneity is observed in the middle of the plasma formation, which has the shape of a torus, moving away from the dielectric sheet on which the aluminum armature was located. As the voltage of the capacitive energy storage increases, the induced current density in the armature increases and the plasma formation becomes more uniform.* ***Practical value.*** *In comparison with the experimental results, the calculated current in the inductor coincides both in shape and in magnitude with an accuracy of 7 %. The biggest difference between the calculated and experimental currents of the inductor occurs when the aluminum armature is thermally destroyed. The transition of an aluminum armature into a plasma formation depends significantly on the voltage of the capacitive energy storage.* References 26, figures 16.

Key words: **plasma formation pulsed inductive thruster, acceleration in the atmosphere, electromechanical and thermal processes, experimental research.**

Вступ. *Один з напрямків розвитку плазмових технологій полягає у формування газо-металевих плазмових утворень та метанні їх на певну відстань. Відомі метальники плазмового утворення або мають електродну систему, яка схильна до ерозії, або розрядну систему в твердій діелектричній речовині, в якій відбувається абляція, або складну газодинамічну систему з подачею палива. Вони не забезпечують метання плазмового утворення в повітряному середовищі на значну відстань.* ***Мета.*** *Теоретичне та експериментальне дослідження електромеханічних та теплофізичних процесів в метальнику плазми, який забезпечує формування плазмового утворення за рахунок термічної іонізації індукованим струмом в тонкому провідникового шару при високовольтному розряді на індуктор та метання плазмового утворення у повітряному середовищі на значну відстань.* ***Методика.*** *Запропонована концепція метальника плазмового утворення, у якого індуктор індукційно взаємодіє з комбінованим якорем, що включає алюмінієвий якір у вигляді тонкої (0,5-1 мкм) фольги, мідний якір, який виконаний з більш товстої фольги (35-50 мкм). На базі математичної моделі, яка враховує нерівномірний розподіл струмів в індукторі і електропровідних якорях, встановлені особливості процесу метання комбінованого якоря в повітряному середовищі та проведені експериментальні дослідження.* ***Результати.*** *Розраховані електромеханічні і теплові характеристики плазмового метальника. Встановлено, що, вибір товщини діелектричного шару якоря, до якого прикріплені алюмінієвий і мідний якоря, обумовлений енергетичним балансом між температурою нагріву алюмінієвого якоря і електромеханічними показниками метальника.* ***Наукова новизна.*** *Експериментально встановлено, що найбільша густина і однорідність спостерігається в середині плазмового утворення, яке має форму тора, що віддаляється від діелектричного листа, на якому розташовувався алюмінієвий якір. З підвищенням напруги ємнісного накопичувача енергії збільшується густина індукованого струму в якорі і плазмове утворення стає більш однорідним.* ***Практична цінність.*** *У порівнянні з експериментальними результатами розрахований струм в індукторі співпадає як за формою, так і за значенням з точністю до 7 %. Найбільша відмінність між розрахунковим і експериментальним струмами індуктора виникає при термічному руйнуванні алюмінієвого якоря. Перехід алюмінієвого якоря в плазмове утворення суттєво залежить від напруги ємнісного накопичувача енергії.* Бібл. 26, рис. 16.

Ключові слова: **плазмове утворення, імпульсний індуктивний метальник, прискорення в атмосфері, електромеханічні та теплові процеси, експериментальні дослідження.**

Introduction. Plasma technologies are used in various industrial technologies, in scientific research, in defense systems, etc. One of the directions of development of such technologies consists in the formation of plasma formations and accelerating them to a certain distance. Work on the creation of plasma throwers is being carried out in many scientific centers of the world [1-4].

At the University of Missouri, USA, the accelerating of a plasma formation in the air environment is being studied [5]. But the duration of the existence of a plasma formation is short (several ms), and it moves in the atmosphere for an insignificant distance of 0.5-0.6 m.

In [6], the application and development of plasma thrusters are considered. Electrode designs, discharge patterns, fuel supply and ignition methods are analyzed. The authors consider various methods of modeling the discharge circuit, as well as the processes of ablation, ionization, and acceleration of plasma formation.

Pulsed plasma thrusters, in which high-frequency accelerating of plasma formation occurs, are considered for use in small satellites, because they provide a long operating time, high specific thrust impulse and significant power [7]. Such plasma thrusters are relatively easily adapted to the specific requirements of the satellite mission.

A promising direction in the development of thrusters for space vehicles is the development of plasma thrusters without electrodes, which are prone to plasma erosion [8, 9]. Such thrusters are more durable, have a reduced mass of

© K.V. Korytchenko, V.F. Bolyukh, S.G. Buriakovskyi, Y.V. Kashansky, O.I. Kocherga

fuel compared to chemical ones, which create the same thrust. Electrodeless plasma thrusters include devices that provide a rotating magnetic or electric field, pulsed inductive devices that use the Lorentz force acting on induction currents in the plasma. According to the indicators of specific impulse and traction efficiency, the most promising designs are those that use the Lorentz force, which directly ensures the acceleration and throwing of plasma through magnetic nozzles.

Plasma technologies are actively developing and play an important role in many developing fields, such as medicine, agriculture, processing of materials and surfaces, catalysis, aerospace engineering, etc. [10].

Plasma thruster analysis. Let's consider the state of work on the creation of plasma thrusters that work in pulse mode and plasma thrusters that work for a long time in cyclic high-frequency mode.

In [11], the method of formation of plasma formations under the conditions of a high-voltage discharge in the atmosphere using a needle electrode is investigated. It was established that the presence of hemispherical aluminum foil can increase the electric field at the tip of the needle electrode. During a discharge under the action of a gas flow, an arc tip is formed in the electric field on the electrode. It forms a plasma jet that extends into the outer space of the gas nozzle. The pulsed discharge, which is formed by the interelectrode arc, forms a plasma jet of high density.

In [12], a plasma thruster with electrodes is considered, one of which is made in the form of a copper rod, and the other in the form of a plate. Under the action of an electric discharge between the electrodes in a solid dielectric substance, ablation occurs, that is, the substance evaporates from the surface. The plasma thruster works under low gas pressure in the accelerator channel. This thruster of plasma formation has a low efficiency and specific power, which is due to the use of only the energy stored by the electric field. The effectiveness of this thruster is limited by the long process of recovery of the working substance and the unevenness of its evaporation.

A well-known plasma thruster, which contains electrodes connected through an ohmic and inductive load to capacitive energy storage (CES), an end ceramic insulator that separates the electrodes and dielectric checkers installed between the electrodes, made of the material in which the ablation takes place [13]. When a high-voltage pulse is applied to the electrodes, as a result of a surface breakdown, a plasma formation is formed, which short-circuits the electrodes. The working substance that evaporates from the surface of the dielectric checkers is ionized and moved under the influence of electromagnetic forces and gas-dynamic pressure. This thruster has increased efficiency due to the use of both electromagnetic forces and gas-dynamic pressure. However, it has a low specific power due to the use of electrical energy to create electromagnetic and gas-dynamic forces.

A well-known plasma thruster, which consists of a guide tube covered by a magnet made in the form of sections, and a system of thermal ionization of matter to the plasma state [14]. One end of the pipe is in the atmosphere, and on the other end there is a gas flow formation system using a gas turbine engine. The system of thermal ionization of matter consists of discharge electrodes located inside the guide tube and an induction plasma heater. The electromagnetic coil of the heater, which covers the guide tube, ensures the formation of plasma inside the guide tube. Due to the gas turbine engine, a heated gas flow is formed, which is directed into the guide pipe. Gas heated above 1000 °C is sent to the thermal ionization system, where it is heated by arc discharges to a high temperature (5000-10000 °C). The gas enters the region of the induction heater, where plasma formation occurs. Under the action of pulsed magnetic fields alternately created by sections of the magnet along the guide tube, a plasma formation is thrown.

In [15], the pulsed inductive thruster of plasma formation is considered, in which a high specific power is achieved due to the combined use of the chemical energy of fuel combustion and the energy of the electromagnetic field. This electrodeless thruster works by passing a large pulsed current through an inductor, creating an electromagnetic field that induces a current in the plasma and accelerates it to a high speed. The authors have proposed and tested different configurations of the thruster, which provide plasma throwing and use a magnetic field to hold it during acceleration. But this thruster has too complicated a design.

In [16], the pulsed inductive plasma thruster designed for a spacecraft is investigated. Spatial distributions of various physical fields are considered, which describe the evolution of the structure of the plasma current layer, the relationship between the traction force and the excitation current, the efficiency of the magnetic connection between the plasma and the excitation circuit, and the energy conversion process. The positive contribution of the secondary current layer to the maximum thrust of the thruster is shown. Oppression the initial gas to the inductor surface and improving its radial homogeneity can help strengthen the coupling between the plasma and the inductor. But the grounded metal plate on which the CES is attached can impair the process of plasma acceleration if the CES is in the zone of magnetic connection with the inductor.

Work [17] analyzes the circuits of the pulsed inductive plasma thruster with conical inductor coils, which can have cone angles from 0° (straight theta-pinch coil) to 90° (flat coil). The plasma is considered as a deformed projectile that moves radially and axially under the action of the electrodynamic force from the side of the inductor. A local maximum of the efficiency and specific impulse is found for angles less than 90°, but the absolute maximum for both of these values is observed at an angle of 90°.

In [18], a high-voltage pulsed power source for the formation of plasma in the atmosphere is considered. This photovoltaic-driven source provides voltage pulse widths from 1 μs to 10 μs and amplitudes in excess of 10 kV with frequencies from 0.5 kHz to 5 kHz.

In [19], the physical process of a planar induction-pulse plasma thruster was studied. When the environment was filled with argon as a fuel, the shape of the current in the inductor, the CES voltage, the intensity of the plasma radiation were measured, and photographs of the plasma structure were taken. Processes at different values of CES voltage and gas pressure were studied. Based on the results of the experiments, the physical mechanisms of the

initial phase of ionization and the subsequent phase of plasma formation acceleration were analyzed.

Based on the analysis, it can be concluded that known thrusters for the plasma formation of either have an electrode system that is prone to erosion, or a discharge system in a solid dielectric substance in which ablation occurs, or a complex gas-dynamic system with the supply of appropriate fuel. In addition, known thrusters, forming the plasma, do not ensure its accelerating in the atmosphere for a significant distance.

The purpose of the article is a theoretical and experimental study of electromechanical and thermophysical processes in a plasma thruster, which ensures the formation of a gas-metal plasma due to thermal ionization by an induced current in a thin conductor layer during a high-voltage discharge on an inductor and the accelerating of a plasma formation in the atmosphere for a considerable distance.

The concept of a pulsed inductive plasma thruster. As it was shown in [20], when using CES with a relatively low voltage (U_0 = 20 kV, capacity C_0 = 360 μF), an aluminum armature with a thickness of 18 μm is only partially transformed into a plasma formation. A large part of this armature is moved vertically upwards to a considerable height (more than 5 m) and after testing the armature is a crumpled and compressed aluminum foil with a bunch of small particles. It is these elements of the armature, which have not passed into the plasma state, under the action of electrodynamic forces from the side of the inductor, are moved to a considerable distance. It was established that at the same CES voltage, only a part of the aluminum armature went into the plasma state, while the copper armature did not go at all. This can be explained by the fact that the melting point of aluminum (660 °C) is significantly lower than that of copper (1083 °C).

On the basis of these experimental studies, a pulsed inductive plasma thruster is proposed, in which a combined armature is located opposite the disc-shaped inductor, which includes an aluminum armature adjacent to the inductor and made in the form of a thin (0.5-1 μm) foil, a copper armature that is directed in the direction of throwing and made of a thicker foil (35-50 μm). These armatures are attached to the dielectric layer located between them (Fig. 1). This layer can be made of aerogel, which has a low density (1 kg/m^3), is resistant to high temperature (1000 °C), has a low thermal conductivity (λ = 0.013~0.019 W/(m·K)), a low Young's modulus, does not compress and is resistant to deformation [21].

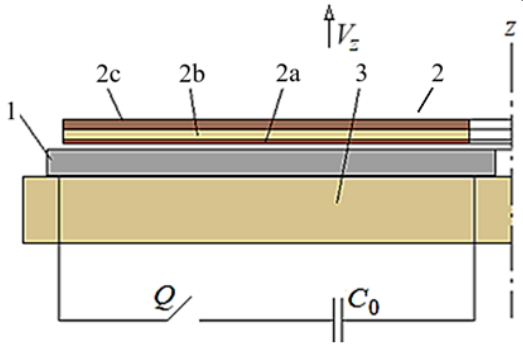

Fig. 1. Design scheme of a pulsed inductive plasma thruster: 1 – inductor; 2 – combined armature; 2a – aluminum armature; 2b – dielectric layer; 2c – copper armature; 3 – insulating support

When the inductor is excited by the high-voltage CES C_0, induced currents flow in the conductive armatures. In a thinner aluminum armature, due to a higher density of the induced current and a lower melting temperature, thermal ionization and the transition to plasma formation occur. The thickness of the aluminum armature is significantly less than the depth of the skin layer. In a thicker copper armature, thermal ionization does not occur due to the reduced magnetic field of the inductor, lower induced current density and higher melting temperature. Under the action of electrodynamic forces, the plasma formation from the aluminum armature is pressed against the dielectric layer, and the copper armature connected to this layer is moved to a considerable distance from the inductor under the action of electrodynamic forces. The copper armature, taking on the aerodynamic resistance of the atmosphere, moves the dielectric layer attached to it with plasma formation, protecting the latter from intense cooling. The dielectric layer of the armature keeps the plasma formation in the form of a ring from being «ruptured» by radially directed electrodynamic forces.

Combined armatures formed from two electrically conductive armatures located in parallel, one of which can be stationary, are used in electromechanical pulse accelerators [22, 23]. These armatures do not go into a plasma formation due to high temperature, but move to a considerable distance.

A mathematical model that describes electromechanical and thermophysical processes during the accelerating of a plasma formation is presented in [20]. The thruster has a coaxial design and the combined armature moves along the z-axis at a speed of V_z. Since plasma formation is characterized by the uncertainty of dynamically changing parameters, in order to establish the general characteristics of the process, we consider that electrically conductive armatures do not change their shape and aggregate state during operation. This approach is widely used when calculating the electromechanical processes of a plasma thruster [24]. To implement a mathematical model that describes time-varying processes with spatially distributed parameters, a system of partial differential equations with respect to spatial and temporal variables was used [22]. The mathematical model describes the stress of the electrical support of the inductor and the combined armature as a function of temperature.

The mathematical model of the process of accelerating a combined armature in the atmosphere takes into account the uneven distribution of currents in the inductor and conductive armatures. It is implemented in the COMSOL Multiphysics software package using the finite element method when accounting for all relationships between physical processes. At the same time, data is exchanged between processes, calculation areas are allocated for each physical problem, provided that the grid division is consistent for all problems.

The calculation area of the model is a cylinder with a radius whose value is more than 5 times greater than the radius of the furthest element of the thrower in the radial direction from the z axis. The height of the calculated cylinder is more than 10 times greater than the highest height of the thruster elements. This makes it possible to

achieve the required accuracy with an acceptable calculation time, considering the calculation limit to be conditionally infinite.

Electromechanical and thermal processes in pulsed inductive plasma thruster with combined armature. Consider a plasma thruster with the following parameters: CES: voltage U_0=35 kV, capacity C_0=18.5 μF; **inductor**: shape – Archimedes disk spiral, material – steel, number of turns N_1=5, outer diameter D_{ex1}=280 mm, inner diameter D_{in1}=70 mm, width of turn Δr_1=10 mm, high turn h_1=5 mm, distance between turns 10 mm; **combined armature**: outer diameter D_{ex2}=280 mm, inner diameter D_{in2}=0 mm, thickness of aluminum armature h_{2a}=0.7 μm; distance from the inductor z_0=1 mm; **excitation circuit**: L_0= 1.5 μH, R_0= 105 mΩ.

The current density in the turns of the steel inductor is distributed significantly unevenly. In Fig. 2 shows the distribution of the current density in the turns of the inductor j_1 at maximum current and the absence of an armature.

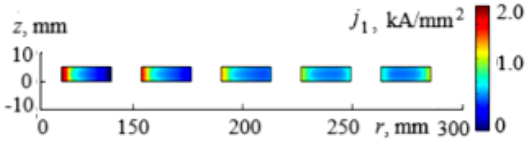

Fig. 2. Distribution of the current density in the turns of the inductor j_1 at the maximum current

The highest current density is observed on the inner coil, namely on the side facing the center, and the lowest current density is observed on the outer side of the inner coil. When calculating processes over time, we will use the current density averaged over the cross section of the turn.

Let us consider the mentioned processes in the plasma thruster with small (h_{2b}=1 mm) and large (h_{2b}=15 mm) thickness of the dielectric layer and with the thickness of the copper armature h_{2c}=0.05 mm. The currents in the inductor have an oscillating and decaying character over time (Fig. 3). With a small thickness of the h_{2b} dielectric layer, the amplitude of the first half-period is 17 % larger, and the oscillation period is reduced compared to the variant with a large h_{2b} thickness. This is due to the inductive effect of the copper armature, which strengthens the magnetic connection with the inductor.

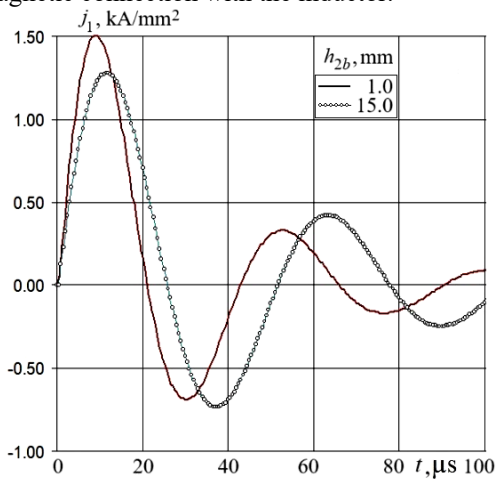

Fig. 3. Time dependences of the current density in the inductor

The amplitude of the density of the induced current in the copper armature j_{2c} increases by 53 % with a smaller thickness (h_{2b}=1 mm) of the dielectric layer of the armature compared to the version with a greater thickness (h_{2b}=15 mm) (Fig. 4).

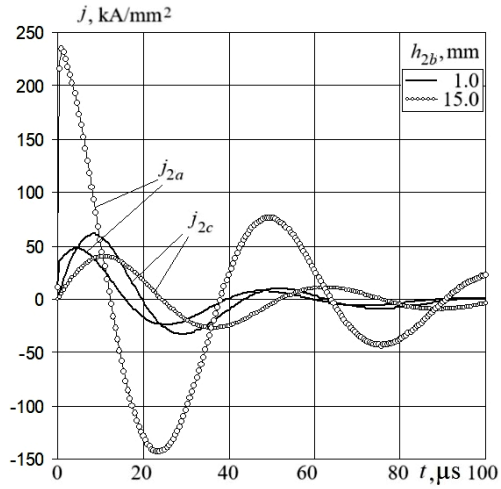

Fig. 4. Time dependences of current density in aluminum j_{2a} and copper j_{2c} armatures

But the amplitude of the current density in the aluminum armature j_{2a} decreases by almost 5 times, which does not lead to its thermal ionization. Such a change in the currents in the armatures is caused primarily by the influence of a thicker copper armature due to the induction connection with the inductor. When the copper armature moves away from the inductor, its demagnetizing effect on the aluminum armature weakens, which leads to a significant increase of induced current in the aluminum armature.

In Fig. 5 shows temperature extremes of aluminum $\theta_{2a}=T_0-T_{2a}$ and copper $\theta_{2c}=T_0-T_{2c}$ armatures, where T_0 is the temperature of the air medium, T_{2a}, T_{2c} are the temperature of the aluminum and copper armature, respectively.

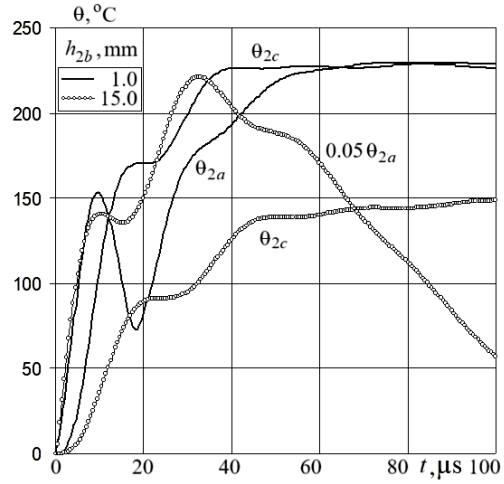

Fig. 5. Time dependences of temperature rise in aluminum θ_{2a} and copper θ_{2c} armatures

At a significant distance (h_{2b}=15 mm) of a thicker copper armature (h_{2c}=50 μm) from a thinner aluminum armature (h_{21}=0.7 μm), the aluminum armature is heated to a temperature whose maximum excess θ_{2a}=4420 °C is many times higher than the temperature aluminum smelting. With a small distance between the armatures (h_{2b}=1 mm), the maximum heating of the aluminum armature reaches only θ_{2a}=229 °C and does not lead to its

thermal damage. Note that both at large and at small distances between the h_{2b} armatures, the heating of the copper armature does not exceed its melting point.

But when the copper armature is moved away from the aluminum one, the electromechanical indicators of the thrower significantly deteriorate. As calculations show, the resulting electrodynamic force f_z acting on the combined armature consists of more than 97 % of the force acting on the thicker copper armature. When the thickness of the dielectric layer h_{2b} increases from 1 mm to 15 mm, the maximum magnitude of the electrodynamic force decreases by 2.48 times, which leads to a decrease in the maximum speed of the armature V_z by 1.75 times (Fig. 6).

Thus, the choice of the thickness of the dielectric layer h_{2b} of the armature is due to a compromise between the high heating temperature of the aluminum armature and low electromechanical indicators of the thruster at a significant value of h_{2b}=15 mm and high electromechanical indicators and low heating temperature of the aluminum armature at a small value of h_{2b}=1 mm.

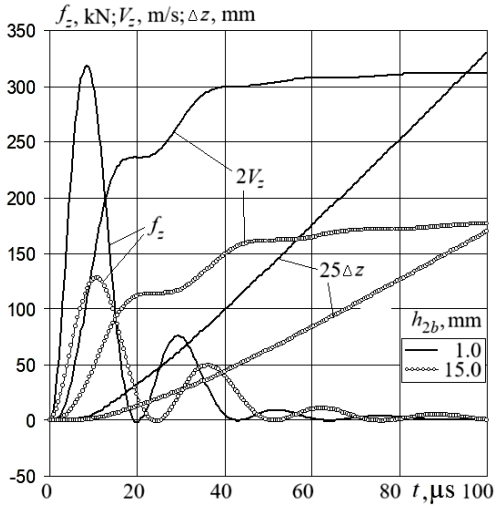

Fig. 6. Time dependences of electromechanical parameters of the thruster

Let's consider the effect of the thickness of the dielectric layer h_{2b} on the indicators of a thruster whose copper armature has a small (0.01 mm), medium (0.05 mm) and significant (0.5 mm) thickness h_{2c}. In Fig. 7 shows the dependence of the maximum current density jm, the maximum electrodynamic force f_{zm} and speed V_{zm}, the maximum temperature rise θ_m of the armatures on the thickness of the dielectric layer h_{2b} between them.

When the thickness of the dielectric layer h_{2b} of the armature increases, the maximum current density in the aluminum armature j_{2a} increases, and in the copper armature j_{2c} it decreases (Fig. 7,*a*).

If in a copper armature, the smaller its thickness, the greater the maximum current density, then in an aluminum armature there is no such unequivocal relationship. Since the main electromechanical characteristics of the thruster are determined by the copper armature, when the thickness of the dielectric layer h_{2b} increases, that is, when the copper armature is moved away from the inductor, the maximum value of the electrodynamic force f_{zm} and the maximum speed V_{zm} decrease (Fig. 7,*b*). When the thickness of the h_{2c} copper armature increases, the total weight of the armature increases significantly, almost proportionally. At the same time, the maximum force f_{zm} increases, and the maximum speed V_{zm} decreases.

When the thickness of the dielectric layer h_{2b} increases, the maximum temperature rise θ_{2c} of the copper armature decreases due to a decrease in the induced current (Fig. 7,*c*).

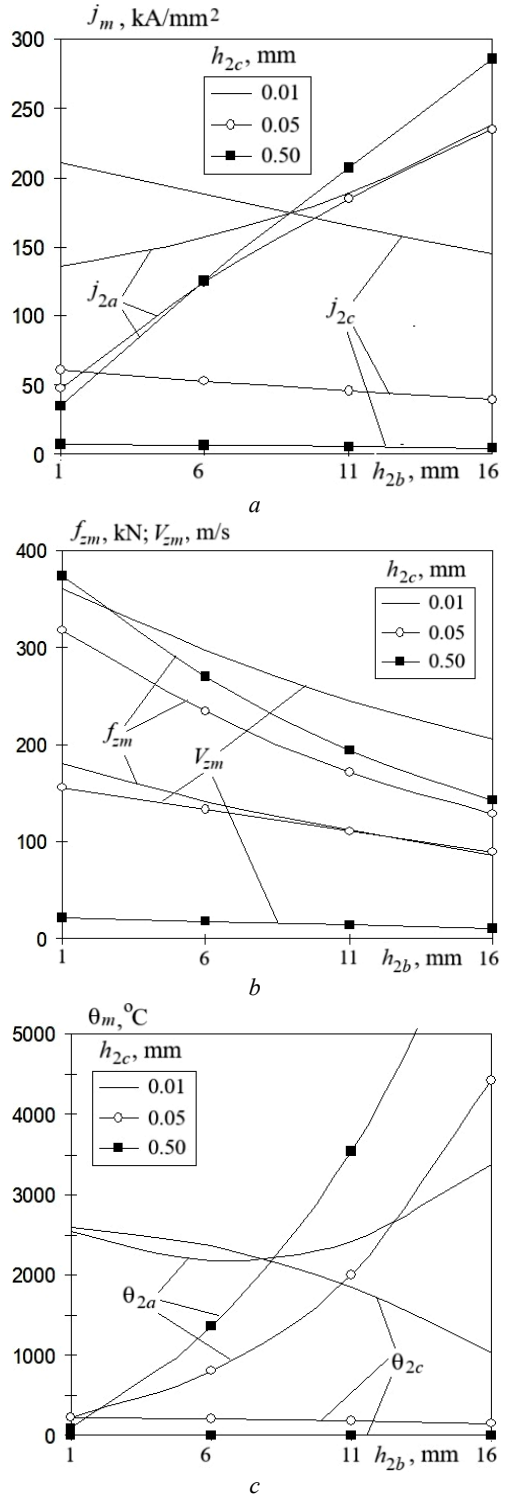

Fig. 7. Dependence of the maximum current density (*a*), the maximum electrodynamic force and speed (*b*), and the maximum temperature rise of the armatures (*c*) on the thickness of the dielectric layer h_{2b}

And an increase in the thickness of the copper armature h_{2c} reduces the density of the induced current, and

accordingly, the maximum value of the temperature rise θ_{2c}. But with the maximum excess temperature of the aluminum armature θ_{2a}, there is no such unequivocal dependence.

When the copper armature with a thickness of h_{2c}=0.05 mm or 0.5 mm is moved away, the temperature rise of the aluminum armature increases, and more at h_{2c}=0.5 mm. And when the copper armature has a small thickness h_{2c}=0.01 mm, when the thickness of the dielectric layer h_{2b} increases from 1 mm to 6 mm, the maximum excess temperature of the aluminum armature θ_{2a} decreases with a further relatively insignificant increase.

The conducted studies took into account the invariance of the mechanical state of the aluminum armature. But, as shown by calculations using a mathematical model that takes into account the thermal destruction of an aluminum armature at a temperature above 660 °C, the results practically do not differ from the results described above. This is explained by the fact that the thicker (71.5 times) copper armature than the aluminum one mainly determines the electromechanical processes of the thrower. The confirmation of this statement is the results of the calculations of the thruster, which includes only one aluminum armature, which causes a certain distortion of the current shape of the inductor until the moment of thermal damage of the armature.

Experimental studies. To test the proposed concept of plasma acceleration by pulsed inductive thruster in the atmosphere on the basis of the high-voltage electrophysical stand of the Research and Design Institute «Molniya» of National Technical University «Kharkiv Polytechnic Institute» using the methodology [25], experimental studies of a plasma formation thruster with one or a copper or aluminum armature in the form of a flat foil were conducted (Fig. 8).

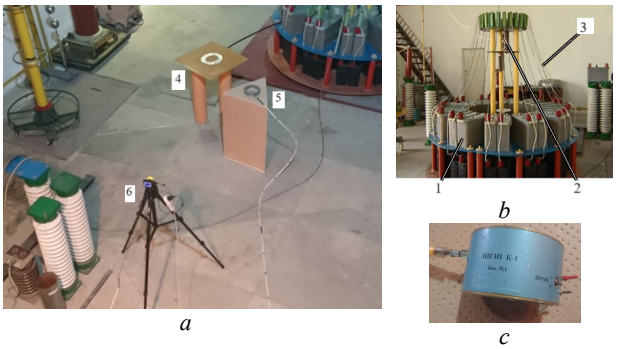

a *b* *c*

Fig. 8. Photo of the experimental setup (*a*), pulse source (*b*), electric field sensor (*c*): 1 – battery of pulse capacitors; 2 – high-voltage arrester; 3 – system of prefabricated tires; 4 – thruster of plasma formation; 5 – electric field sensor; 6 – high-speed camera

Experimental studies were carried out with two disc inductors, which are made in the form of an Archimedes disk spiral made of steel (Fig. 9). They have an outer diameter D_{ex1}=280 mm, an inner diameter D_{in1}=70 mm and a height h_1=5 mm. Inductor No. 1 has 7 turns with a width of 9.4 mm with a distance between turns of 5 mm. Inductor no. 2 has 5 turns with a width of 10 mm with a distance between turns of 10 mm. The inductor was placed horizontally on the dielectric base, and the conductive anchor through the dielectric sheet was installed on top of it.

The INEP K-1 sensor was used to measure the electric field strength, which is connected to a digital oscilloscope through a fiber optic cable (Fig. 8,*c*). It is located at a distance of 1 m from the center of the inductor. The measurement was carried out in the position of the maximum sensitivity of the sensor. A high-speed camera was located at a distance of 2.8 m from the center of the inductor to record the process of throwing the plasma formation (Fig. 8,*a*).

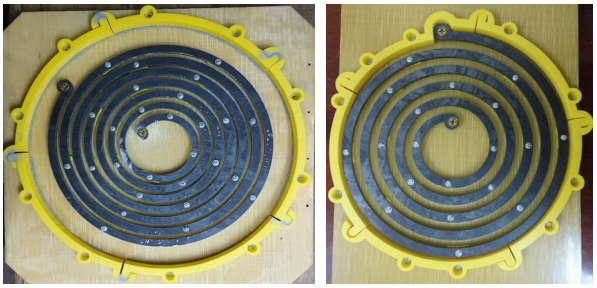

a *b*

Fig. 9. Photo of inductor no. 1 (*a*) and inductor no. 2 (*b*)

In order to experimentally confirm the calculated results about the circular shape of the induced current in the conductive armature, the following experiment was conducted. A 900×900×1 mm^3 glass-textolite sheet, on the outside of which a copper foil with a thickness of 35 μm was fixed, was placed above the horizontally located inductor no. 1. When a CES discharge with a voltage of U_0=20 kV was applied to the inductor in the fiberglass foil, which functions as a copper armature, a circular circuit of thermal heating was formed without significant mechanical damage. At the same time, the radial temperature distribution was in good agreement with the calculated results (Fig. 10). It should be noted that under similar conditions, thermal ionization took place in the aluminum armature with a transition to the plasma state and significant mechanical damage [20]. Based on this experiment, an aluminum armature was made in the form of a ring from foil 18 μm thick (Fig. 10,*c*).

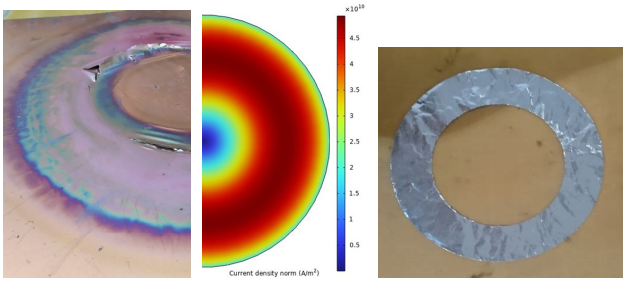

a *b* *c*

Fig. 10. Photo of the glass-textolite copper foil after the discharge of the inductor (*a*), calculated induced current (*b*) and photo of the aluminum armature (*c*)

In Fig. 11, with the CES voltage U_0=40 kV and the presence of an aluminum armature, the forms of the current in the inductor no. 2 and the electric field strength measured by the INEP K-1 sensor at the oscillograph sweep of 25 ms/div are shown on a digital oscilloscope.

The forms of the inductor current and the electric field have an oscillatory-damping character with a frequency of f = 12.15 kHz. The amplitude of the first half-cycle of the current is I_{1m}=49.2 kA, and the amplitude of the electric field intensity E_m=430 V/m.

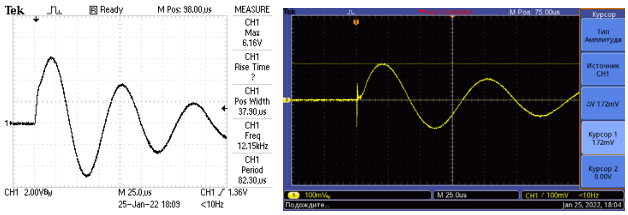

a *b*

Fig. 11. Registered forms of current in inductor no. 2 (*a*) and electric field strength (*b*) in the presence of an aluminum armature and voltage U_0=40 kV

In the course of 5 μs, in the form of the current of the inductor in the presence of an aluminum armature, there is a distortion from the similar form of the current in the absence of the armature. This is more pronounced when the sweep of the oscilloscope is reduced by 5 times (Fig. 12).

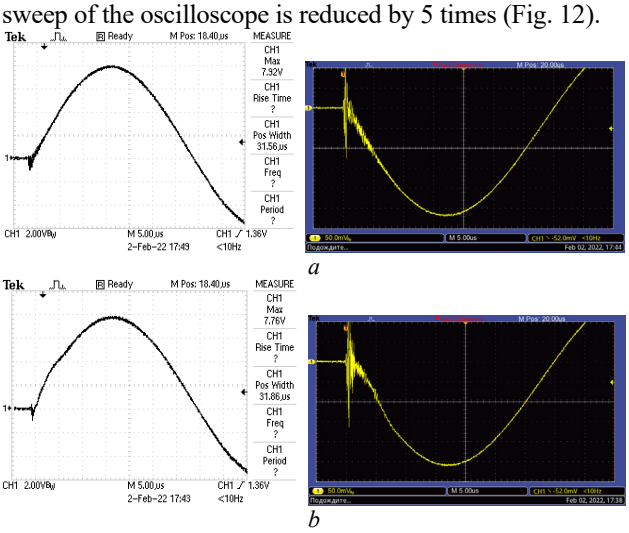

a

b

Fig. 12. Oscillograms of inductor current (left) and electric field strength (right) in the absence (*a*) and presence (*b*) of an aluminum armature

This distortion is explained by the inductive effect of the conductive armature and shows that for 5 μs there is an inductive interaction between the inductor and the armature. After this time, the induced current of the armature ceases to interact with the inductor both due to its movement and due to the fact that the aluminum armature is destroyed due to thermal ionization. The lack of interaction of the induced current in the armature with the inductor leads to the return of the inductor current curve to the state observed in the absence of the armature.

There is no specified distortion on the electric field intensity curve. This is explained by the fact that the sensor measures the combined electric field from the inductor and the armature, and the induced current in the armature is directed opposite to the inductor current, compensating for this distortion.

In Fig. 13 shows the calculated shape of the current density of the inductor j_1 and the aluminum armature j_{2a}, which is destroyed at a temperature higher than 660 °C. It is the induction current in the armature that causes distortion in the inductor current curve. In comparison with the experimental dependence, the calculated current in the inductor coincides both in shape and in magnitude with an accuracy of 7 %.

The greatest difference between the expansion and experimental struts of the inductor arises in the process of thermal destruction of the aluminum armature.

At the stage of transition of the aluminum armature into the plasma mill, its support rapidly grows, which leads to a change in the shape of the pulse from oscillating and decaying character (Fig. 4) to "cut" with a short trailing edge (Fig. 13). When calculating the process of the transition to the plasma state, the resistance of the aluminum armature is described by a polynomial, which increases from a certain value up to the melting temperature (~550 °C) to infinity when this temperature is exceeded (~700 °C).

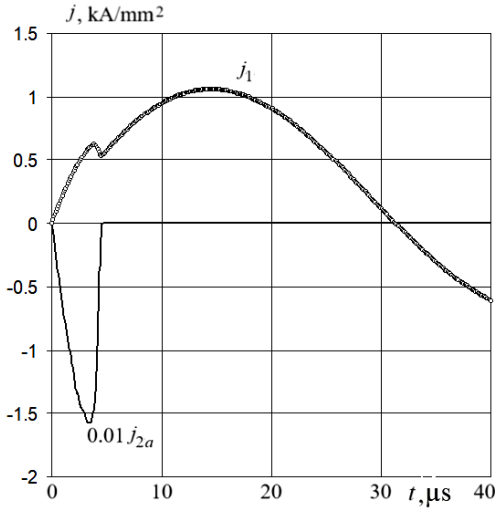

Fig. 13. Calculated form of current density of inductor j_1 and aluminum armature j_{2a}

As experimental studies show, the process of destruction of an aluminum armature occurs more slowly than it is laid down in the mathematical model.

The transition of the aluminum armature into a plasma formation depends significantly on the CES voltage U_0. This is illustrated by Fig. 14, where photos taken without a light filter are shown of the plasma formation into which the aluminum armature has turned, at a voltage of U_0=20 kV, 30 kV and 40 kV.

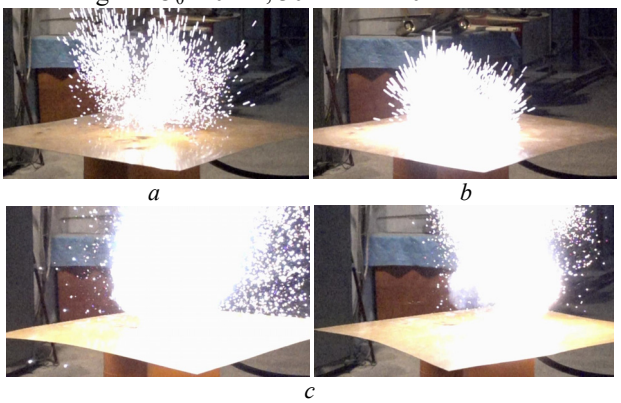

a *b*

c

Fig. 14. Photos of plasma formation obtained at voltage U_0: 20 kV (*a*), 30 kV (*b*), 40 kV (*c*), taken without a light filter

The measured inductor current amplitudes of the first half-cycle I_{1m} are 30.6 kA, 47 kA and 64.5 kA, respectively. The higher the density of the induced current in the armature, the more homogeneous the plasma formation. In this case, the duration of the induced current flow in the plasma formation increases. And due to the electrodynamic interaction of this current with the magnetic field of the inductor, the plasma formation is accelerating over a greater distance.

When using inductor no. 1, the amplitude of the first half-cycle of the inductor current, and therefore the density of this current, decreases. Thus, at a voltage of U_0=40 kV, the current amplitude is I_{1m}=53 kA (Fig. 15). At the same time, the greater part of the aluminum armature, in comparison with the similar voltage in the inductor no. 2, flies into the air environment in the form of a pile of small high-temperature particles.

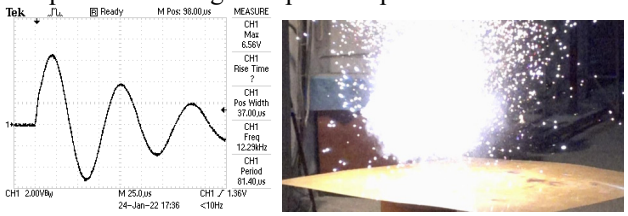

a *b*

Fig. 15. Recorded form of current in inductor no. 1 (*a*) and photo plasma formation (*b*) at voltage U_0=40 kV

In order to investigate the processes in the plasma formation in more detail, experiments were conducted with photographing them accelerating a light filter from welding glasses with 12 DIN dimming. In Fig. 16 shows a photo of a plasma formation with the use of a light filter and an oscillogram of the inductor current and electric field strength during an CES discharge with a voltage of U_0=40 kV on inductor no. 1.

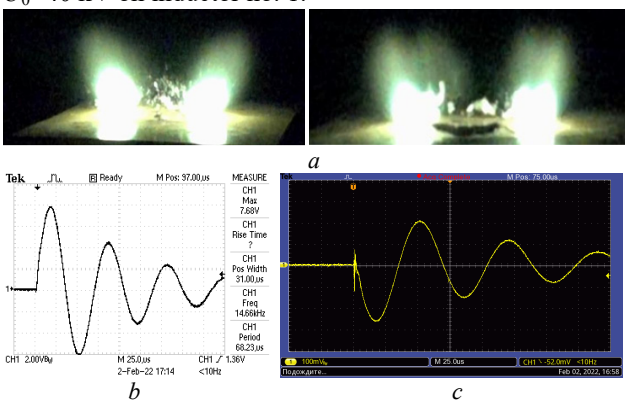

a *b* *c*

Fig. 16. Photo of plasma formation using a light filter (*a*), inductor current oscillogram (*b*) and electric field strength (*c*)

The amplitude of the first half-cycle of the inductor current is I_{1m}=51.6 kA, and the corresponding amplitude of the electric field strength is E_m=450 V/m. A photo using a light filter shows that the greatest density and uniformity is observed in the middle of the plasma formation. Moreover, it has the shape of a torus, which is separated from the dielectric sheet on which the aluminum armature was located.

Thus, the formation of gas-metal plasma formations and accelerating them to a certain distance contributes to the development of plasma technologies for promising areas of industry and scientific research. Among the directions of practical applications of throwing plasma formations formed during an induction discharge, one can note the possibility of their use in coating technologies, which are an alternative to vacuum electron beam methods for obtaining aluminum-copper compounds, as described, for example, in [26].

Conclusions.

1. The proposed concept of the plasma acceleration by pulsed inductive thruster in the atmosphere, in which a combined armature is located opposite the inductor, which includes an aluminum armature made in the form of a thin foil, adjacent to the inductor, and a copper armature made of thicker foil, which is directed in the direction of accelerating. These armatures are attached to the dielectric layer of aerogel placed between them.

2. When using a mathematical model in the COMSOL Multiphysics software package, which takes into account interrelated electromechanical and thermal processes and uneven distribution of currents in the inductor and conductive armatures, it was established that under the action of electrodynamic forces from the inductor side, the copper armature moves a considerable distance, moving the attached to it is a dielectric layer with a plasma formation, into which the aluminum armature has turned.

3. It was established that the choice of the thickness of the dielectric layer of the armature is due to a compromise between the heating temperature of the aluminum armature and the electromechanical indicators of the thruster.

4. It was experimentally established that the greatest density and homogeneity is observed in the middle of the plasma formation, which has the shape of a torus, moving away from the dielectric sheet on which the aluminum armature was located.

5. As the voltage of the capacitive energy storage increases, the induced current density in the armature increases and the plasma formation becomes more uniform.

Conflict of interest. The authors declare that they have no conflicts of interest.

REFERENCES

1. Kirchen M., Jalas S., Messner P., Winkler P., Eichner T., Hübner L., Hülsenbusch T., Jeppe L., Parikh T., Schnepp M., Maier A.R. Optimal Beam Loading in a Laser-Plasma Accelerator. *Physical Review Letters*, 2021, vol. 126, no. 17, art. no. 174801. doi: https://doi.org/10.1103/PhysRevLett.126.174801.

2. Albert F., Couprie M.E., Debus A., et al. 2020 roadmap on plasma accelerators. *New Journal of Physics*, 2021, vol. 23, no. 3, art. no. 031101. doi: https://doi.org/10.1088/1367-2630/abcc62.

3. Ji H., Daughton W. Phase diagram for magnetic reconnection in heliophysical, astrophysical, and laboratory plasmas. *Physics of Plasmas*, 2011, vol. 18, no. 11, pp. 111207-111217. doi: https://doi.org/10.1063/1.3647505.

4. Korytchenko K.V., Bolyukh V.F., Rezinkin O.L., Burjakovskij S.G., Mesenko O.P. Axial coil accelerator of plasma ring in the atmospheric pressure air. *Problems of Atomic Science and Technology*, 2019, vol. 119, no. 1, pp. 120-123.

5. Anthony S. *Open-air plasma device could revolutionize energy generation, US Navy's weaponry*. Available at: https://www.extremetech.com/defense/153630-open-air-plasma-device-could-revolutionize-energy-generation-us-navys-weaponry (accessed 08.01.2024).

6. Wu Z., Huang T., Liu X., Ling W.Y.L., Wang N., Ji L. Application and development of the pulsed plasma thruster. *Plasma Science and Technology*, 2020, vol. 22, no. 9, art. no. 094014. doi: https://doi.org/10.1088/2058-6272/aba7ac.

7. Ling W.Y.L., Zhang S., Fu H., Huang M., Quansah J., Liu X., Wang N. A brief review of alternative propellants and requirements for pulsed plasma thrusters in micropropulsion applications. *Chinese Journal of Aeronautics*, 2020, vol. 33, no. 12, pp. 2999-3010. doi: https://doi.org/10.1016/j.cja.2020.03.024.

8. Bathgate S.N., Bilek M.M.M., Mckenzie D.R. Electrodeless plasma thrusters for spacecraft: a review. *Plasma Science and Technology*, 2017, vol. 19, no. 8, art. no. 083001. doi: https://doi.org/10.1088/2058-6272/aa71fe.

9. Zhang Z., Ling W.Y.L., Tang H., Cao J., Liu X., Wang N. A review of the characterization and optimization of ablative pulsed plasma thrusters. *Reviews of Modern Plasma Physics*, 2019, vol. 3, no. 1, art. no. 5. doi: https://doi.org/10.1007/s41614-019-0027-z.
10. Keidar M., Weltmann K.-D., Macheret S. Fundamentals and Applications of Atmospheric Pressure Plasmas. *Journal of Applied Physics*, 2021, vol. 130, no. 8, art. no. 080401. doi: https://doi.org/10.1063/5.0065750.
11. Li Z., Liu W. Erratum to: The Formation of Atmospheric Pressure Air Low Temperature Plasma Jet. *Plasma Physics Reports*, 2022, vol. 48, no. 12, pp. 1422-1422. doi: https://doi.org/10.1134/S1063780X22330017.
12. Spanjers G.G., McFall K.A., Gulczinski F.S., Spores R.A. Investigation of propellant inefficiencies in a pulsed plasma thruster. *32nd Joint Propulsion Conference and Exhibit*, 1996, doi: https://doi.org/10.2514/6.1996-2723.
13. Takahashi K. Magnetic nozzle radiofrequency plasma thruster approaching twenty percent thruster efficiency. *Scientific Reports*, 2021, vol. 11, no. 1, art. no. 2768. doi: https://doi.org/10.1038/s41598-021-82471-2.
14. Di Canto G. *Plasma propulsion system and method*. Patent US WO2016151609. 2016. Available at: https://patentscope.wipo.int/search/en/detail.jsf?docId=WO2016151609&_cid=P10-LL70BV-97870-1 (accessed 08.01.2024).
15. Polzin K., Martin A., Little J., Promislow C., Jorns B., Woods J. State-of-the-Art and Advancement Paths for Inductive Pulsed Plasma Thrusters. *Aerospace*, 2020, vol. 7, no. 8, art. no. 105. doi: https://doi.org/10.3390/aerospace7080105.
16. Che B., Cheng M., Li X., Guo D. Physical mechanisms and factors influencing inductive pulsed plasma thruster performance: a numerical study using an extended magnetohydrodynamic model. *Journal of Physics D: Applied Physics*, 2018, vol. 51, no. 36, art. no. 365202. doi: https://doi.org/10.1088/1361-6463/aad47f.
17. Martin A.K. Performance scaling of inductive pulsed plasma thrusters with coil angle and pulse rate. *Journal of Physics D: Applied Physics*, 2016, vol. 49, no. 2, art. no. 025201. doi: https://doi.org/10.1088/0022-3727/49/2/025201.
18. Li M., Luo K., Xiong Z. Design of Adjustable High Voltage Pulse Power Supply Driven by Photovoltaic Cells for Cold Plasma Generation. *2021 IEEE 4th International Electrical and Energy Conference (CIEEC)*, 2021, pp. 1-6. doi: https://doi.org/10.1109/CIEEC50170.2021.9510416.
19. Li X.-K., Che B.-X., Cheng M.-S., Guo D.-W., Wang M.-G., Yang Y.-T. Investigation on plasma structure evolution and discharge characteristics of a single-stage planar-pulsed-inductive accelerator under ambient fill condition. *Chinese Physics B*, 2020, vol. 29, no. 11, art. no. 115201. doi: https://doi.org/10.1088/1674-1056/ab9f2a.
20. Korytchenko K.V., Bolyukh V.F., Buriakovskyi S.G., Kashansky Y.V., Kocherga O.I. Electromechanical and thermophysical processes in the pulse induction accelerator of plasma formation. *Electrical Engineering & Electromechanics*, 2023, no. 5, pp. 69-76. doi: https://doi.org/10.20998/2074-272X.2023.5.10.
21. *Aerogel*. Available at: https://en.wikipedia.org/wiki/Aerogel (accessed 08.01.2024).
22. Bolyukh V.F., Kocherga A.I. Efficiency and Practical Implementation of the Double Armature Linear Pulse Electromechanical Accelerator. *2021 IEEE 2nd KhPI Week on Advanced Technology (KhPIWeek)*, 2021, pp. 153-158. doi: https://doi.org/10.1109/KhPIWeek53812.2021.9570065.
23. Bolyukh V.F. Effect of electric conducting element on indicators of linear pulse electromechanical converter induction type. *Technical Electrodynamics*, 2020, no. 3, pp. 22-29. doi: https://doi.org/10.15407/techned2020.03.022.
24. Polzin K.A., Sankaran K., Ritchie A.G., Reneau J.P. Inductive pulsed plasma thruster model with time-evolution of energy and state properties. *Journal of Physics D: Applied Physics*, 2013, vol. 46, no. 47, art. no. 475201. doi: https://doi.org/10.1088/0022-3727/46/47/475201.
25. Janda M., Korytchenko K., Shypul O., Krivosheev S., Yeresko O., Kasimov A. Optical and electrical investigation of plasma generated by high-energy self-stabilized spark ignition system. *Physics of Plasmas*, 2023, vol. 30, no. 5, art. no. 053501. doi: https://doi.org/10.1063/5.0141261.
26. Donets S.E., Klepikov V.F., Lytvynenko V.V., et al. Aluminum surface coating of copper using high-current electron beam. *Problems of Atomic Science and Technology*, 2015, vol. 98, no. 4, pp. 302-305.

Received 09.01.2024
Accepted 26.02.2024
Published 20.06.2024

K.V. Korytchenko[1], *Doctor of Technical Science, Professor,*
V.F. Bolyukh[1], *Doctor of Technical Science, Professor,*
S.G. Buriakovskyi[2], *Doctor of Technical Science, Professor,*
Y.V. Kashansky[1], *Postgraduate Student,*
O.I. Kocherga[1], *PhD*, *Assistant Professor*,
[1] National Technical University «Kharkiv Polytechnic Institute»,
2, Kyrpychova Str., Kharkiv, 61002, Ukraine,
e-mail: vfbolyukh@gmail.com (Corresponding Author);
[2] Research and Design Institute «Molniya»
of National Technical University «Kharkiv Polytechnic Institute»,
47, Shevchenko Str., Kharkiv, 61013, Ukraine.

How to cite this article:
Korytchenko K.V., Bolyukh V.F., Buriakovskyi S.G., Kashansky Y.V., Kocherga O.I. Plasma acceleration in the atmosphere by pulsed inductive thruster. *Electrical Engineering & Electromechanics*, 2024, no. 4, pp. 61-69. doi: https://doi.org/10.20998/2074-272X.2024.4.08

UDC 621.3.013 https://doi.org/10.20998/2074-272X.2024.4.09

V.Yu. Rozov, S.Yu. Reutskiy, K.D. Kundius

Protection of workers against the magnetic field of 330-750 kV overhead power lines when performing work without removing the voltage under load

Problem. *One of the acute problems that needs to be solved when performing repair work under voltage on power transmission lines (PTLs) is the protection of workers' health from high-intensity electromagnetic fields.* ***Goal****. The purpose of the work is to develop the methodological foundations for the protection of workers from the magnetic field (MF) of the 330-750 kV PTL during repairing work without removing the voltage and under loading.* ***Methodology.*** *A methodology for calculating the maximum allowable PTL loading factor has been developed. It limits the flux density of the MF in the working area of the power transmission line to the maximum permissible level of sanitary standards for the given period of work at the potential and the minimum thickness of the protective layer between the wires and the worker's body.* ***Originality****. Methodological principles for protecting workers from magnetic fields have been created. They are based on the joint use of the developed method of mode load minimization and the method of increasing the working distance, and the developed method of calculating the maximum allowable loading factor of PTLs.* ***Practical value****. The graphic dependence of the maximum allowable loading factor of the PTL is proposed as a function of the required working time and the thickness of the introduced additional protective layer between the wires and the body of the worker. It allows one quickly determines the maximum allowable loading factors to conform the accepted limit-allowable normative level of flux density of MF for various types of PTLs 330-750 kV.* References 45, tables 1, figures 10.

Key words: **high-voltage power line, work on wires without removing the voltage, reducing the magnetic field.**

Проблема. *Однією із гострих проблем, що потребує вирішення при виконанні ремонтних робіт під напругою на лініях електропередачі (ЛЕП), є захист здоров'я працівників від електромагнітного поля високої інтенсивності.* ***Мета.*** *Метою роботи є розроблення методологічних основ захисту працівників від магнітного поля (МП) ЛЕП 330-750 кВ при виконанні ремонтних робіт без зняття напруги і під навантаженням.* ***Методика****. Розроблено методику розрахунку гранично допустимого коефіцієнту навантаження ЛЕП, який обмежує індукцію МП в робочій зоні ЛЕП до гранично допустимого рівня санітарних норм при заданих терміні робіт на потенціалі і мінімальній товщині захисного слою між проводами та тілом працівника.* ***Наукова новизна****. Створені методологічні засади захисту працівників від МП, що ґрунтуються на сумісному використанні розроблених методу режимної мінімізації навантаження і методу збільшення робочої дистанції, та розробленої методики розрахунку гранично допустимого коефіцієнту навантаження ЛЕП.* ***Практична значимість*** *Запропоновані графічні залежності гранично допустимого коефіцієнту навантаження ЛЕП в функції від необхідного часу роботи та товщини введеного додаткового захисного слою між проводами та тілом працівника, що при прийнятому гранично допустимому нормативному рівні індукції МП дозволяє оперативно визначати гранично допустимі коефіцієнти навантаження для різних типів ЛЕП 330-750 кВ.* Бібл. 45, табл. 1, рис. 10.

Ключові слова: **високовольтна лінія електропередачі, роботи без зняття напруги, зменшення магнітного поля.**

Introduction. Carrying out repair work on high-voltage overhead power transmission lines (PTLs) without de-energizing is a common method of increasing their profitability [1-4]. One of the acute problems that needs to be solved when performing such works is the protection of workers' health from the electromagnetic field (EMF) of power frequency PTLs with increased intensity [5-8]. Such EMF can be characterized by independent components – electric field (EF) and magnetic field (MF) [9, 10], each of which negatively affects human health [11, 12]. Therefore, in the leading countries of the world, methods of replacing workers with robotic devices when performing work on the potential of PTLs are currently developing rapidly [13-15].

In Ukraine, workers have been working on the potential of high-voltage PTLs for more than 40 years, and their technology is constantly being improved [1-4]. To date, the problem of protecting the health of working personnel from the negative effects of PTLs' EF, based on the use of special protective suits made of electrically conductive material, has been solved [4]. But the solution of the problem of protecting workers from the action of the MF is in a significantly worse state. This problem remains insufficiently developed both theoretically and practically. Therefore, a certain step in its solution was the development by the authors of a mathematical model of the MF in the area of work without removing the voltage under the load [16], and the methodology for its calculation, which are based on the results of previously performed studies of the MF of various technical objects [17-31]. The latest research by the authors [16] confirms the relevance of solving the problem of protecting workers from the effects of the MF in Ukraine when performing work on PTLs without de-energizing. For example, in [16] it is shown that for typical 330-750 kV PTLs, in the nominal mode of their operation, it is possible to significantly exceed the upper limit level of MF flux density by 1.5-1.9 times over the norms adopted in Ukraine and the European Union [12, 32-34]. Therefore, the task of creating scientific principles for the protection of working personnel from the action of the MF by reducing it to a safe level in the PTL wires execution zone is urgent.

The goal of the work is to develop methodological principles for the protection of workers from the magnetic field of the 330-750 kV PTLs when carrying out repair work without removing the voltage and under load.

© V.Yu. Rozov, S.Yu. Reutskiy, K.D. Kundius

Normalization of the limit level of the MF action with frequency of 50 Hz. In Ukraine, the limit level of action (LLA) of the MF flux density on PTL workers is regulated in [33] and summarized in item 1 of Table 1. For example, for the body of a worker, the LLA is no more than 7.5 mT when working for up to 1 hour and no more than 1.8 mT when working for 8 hours. In the interval between one and eight hours, the MF LLA B_{PD} in [33, 34] is determined as a function of time according to the methodology developed on the basis of sanitary-hygienic and biological research carried out in the institutes of the National Academy of Medical Sciences of Ukraine [35-37]. For the limbs of the worker, the MF LLA is much larger and amounts to 15 mT (item 1, Table 1).

In Europe, in accordance with the Directives of the European Union [12], the MF LLA for workers is stricter. Thus, the upper level of LLA for the body is 6 mT (with short-term exposure), and the lower one is 1 mT (with long-term exposure). To date, this standard [12] has been approved in Ukraine [32] and it is expected to be put into effect after the termination or abolition of martial law in Ukraine. Therefore, we will consider this European Standard to be promising.

Taking into account the above, in the further analysis we will use the «State sanitary rules and regulations for the performance of work in non-switched-off electrical installations with voltage of up to 750 kV inclusive» (item 1, Table 1) in force in Ukraine as the standard for the 50 Hz MF LLA in the further analysis, and for comparison – the Directives of the European Union [32], which are promising for Ukraine, approved by the order of the Ministry of Health No. 81 dated 13.01.2023.

Table 1

LLA of the flux density B_{PD} of the sinusoidal MF with frequency of 50 Hz per worker

No.	Normative document	Work time of the worker (t_r) at the PTL potential (hours)							
		≤1	2	3	4	5	6	7	≥8
		LLA of the flux density B_{PD} when affecting the body/limbs, mT							
1	**Current regulatory document:** Order of the Ministry of Health of Ukraine dated 09.07.1997 No. 198 «State sanitary rules and regulations for the performance of work in non-switched-off electrical installations with voltage up to and including 750 kV»	7,5/ 15,0	6,1/ 15,0	5,0/ 15,0	4,0/ 15,0	3,1/ 15,0	2,5/ 15,0	2,0/ 15,0	1,8/ 15,0
2	**Prospective maximum permissible levels of MF action** based on Directives 89/391/EEC and Order of the Ministry of Health dated 13.01.2023 No. 81 «Minimum requirements for health and safety of workers exposed to electromagnetic fields», supplemented by marked with * B_{PD} values, according to the method used in Ukraine	6,00/ 18,00	4,65*/ 18,00	3,60*/ 18,00	2,78*/ 18,00	2,15*/ 18,00	1,67*/ 18,00	1,29*/ 18,00	1,00/ 18,00

The working distance between the wires and the worker's body and the working MF flux density. When performing work on the PTL potential, the worker is in a precarious position, at a height of tens of meters [4], and as a support he is forced to use PTL wires (Fig. 1), which leads to direct contact through the protective suit of various parts of his body with the wires. Here, without taking special measures, almost all the time the worker is on the PTL potential and under load, the distance between his body and the surface of the wires is minimal and is determined only by the thickness of the protective suit (≈ 2 mm). This fact forces during the further analysis to take into account the value of the working flux density of MF, which corresponds to the minimum distance (2 mm) between the worker's body and the PTL wire during exposure for the entire time the worker performs work at the potential.

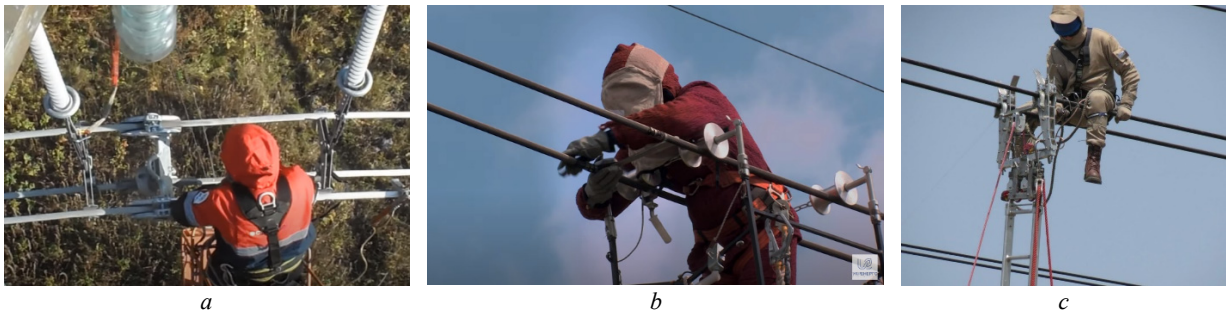

a *b* *c*

Fig. 1. The typical position of the worker's body when performing work on the PTL potential, where he uses as a support wires under load

The flux density of the MF acting on the worker when performing work at the potential of PTLs and under load was studied by the authors in [16], and their main results are presented in Fig. 2, 3. For example, in Fig. 2, the results of the verified calculation of the maximum value of the flux density of the MF of various PTLs during the performance of works according to the technology adopted by NEC «UkrEnergo» are given. They confirm the need to significantly reduce the iflux density of their MF [16]. Thus, in accordance with the current sanitary standards of Ukraine [33] (item 1 of Table 1), the flux density of the 330 kV PL at the nominal current of its load must be reduced from 11.5 to 7.5 mT when working at a potential of up to 1 hour (Fig. 2). According to the norms of the European Union [12, 32], when working up to 1 hour, a reduction of B_{PD} is required not only for 330 kV PTLs, but also for PTLs 750 kV, N=4. Reduction of flux density of MF for all PTLs is also necessary when t_r is more than two hours.

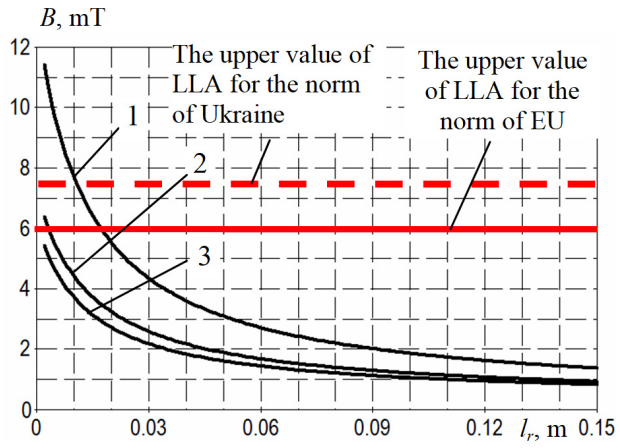

Fig. 2. Dependence of the maximum values of the effective MF flux density of the 330-750 kV PTL in its working zone at the nominal current as a function of the distance l_r from the wire surface to the worker's body (1 – PTL 330, N = 2; 2 – PTL 750, N = 4; 3 – PTL 750, N = 5)

As for the LLA of the MF for the limbs of the worker, which according to Table 1 is 15-18 mT, then there are no special problems with its provision for all PTLs under consideration.

The choice of methods for reducing the flux density of MF when performing work on the potential of PTLs under load. In order to reduce the PTLs' MF when performing work on the potential of PTLs, it is possible to use such well-known methods [38, 39] as shielding and distance protection.

Shielding is widely used when working on the potential PTLs to reduce EF using shielding suits made of electrically conductive material [2-4]. Their use is mandatory. But, as shown in [40-43], such suits do not shield MF of power frequency. This conclusion was also experimentally confirmed by the authors on a laboratory setup (Fig. 4), which consists of an adjustable MF 50 Hz source with flux density of 0-0.6 mT and a magnetometer with a remote sensor fixed in the working area. Measurements of MF flux density were carried out in the absence and presence of a protective suit of the EK-1 shielding kit [4] with material thickness of 2 mm, which covered the sensor. The results of the experiment confirmed the absence of any effect of MF shielding by a protective suit. However, this result was quite expected, since according to [44], only for the implementation of small (1.2-1.5 times) shielding of MF with frequency of 50 Hz, it is necessary to use massive metal conductive (magnetostatic) screens that are at the potential of the wires of PTLs is practically impossible. Therefore, the use of shielding methods to reduce the MF on the potential of the PTL is not considered below.

Distance shielding is widely used to reduce the potential electromagnetic field [10, 45], which decreases with distance from the source. The PTL MF is also potential, which intensively decreases near its wires when moving away from the wire with gradient of about 0.4 mT/mm (Fig. 3).

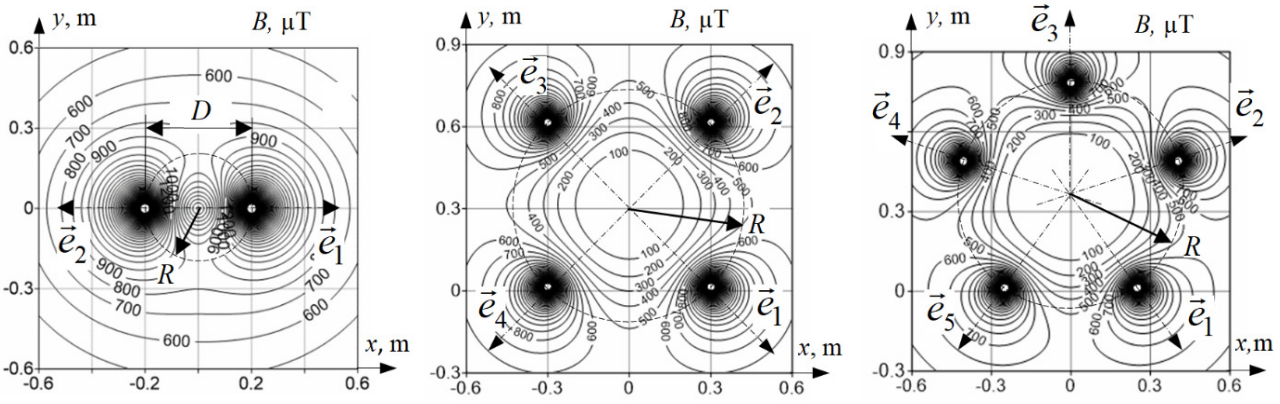

a *b* *c*

Fig. 3. The nature of the distribution of MF flux density in the working zones of the 330-750 kV PTLs near the split wires of their phases

Fig. 4. Experimental studies of the effect of shielding of MF of powerfrequency with a protective suit of a set of individual shielding EK-1

Therefore, increasing the minimum working distance between the worker's body and the surface of the PTL wires is an effective method of reducing the impact of MF on the worker. In practice, this can be achieved by introducing additional material of the required thickness (2-15 mm) between the wires and the worker's body, which does not deform under the worker's weight. Such a material can be, for example, a special protective suit with increased thickness (10-15 mm), or special capes for PTL wires of the appropriate thickness. For example, with an increase in the working distance from the worker's body to the wires of the 330 kV PTL from 2 mm to 15 mm, and a corresponding increase in l_r, the flux density of MF (Fig. 2) is reduced by almost half – from 11.5 mT to the normative level of 6 mT. Thus, distance protection, based on increasing the working distance to PTL wires, is an effective method of protecting personnel from MF when performing work at potential. But for its practical implementation, it is necessary to introduce new technological operations and special protective means.

The reduction of PTL MF by reducing the operating current I_r of the PTL [16] is called the method of mode load minimization of the PTL. It can be implemented during the repair of PTLs with a corresponding reduction of both the operating current and the flux density of the MF proportional to it. This method is preferable, since its implementation requires only organizational measures agreed with consumers, which provide for planned disconnection of individual consumers during repairs. The effectiveness of using the method of mode load minimization of PTLs to reduce their MF can be expressed through the load factor (k_r) of the PTL, which is defined as the ratio between the operating (I_r) and nominal (I_n) currents of the PTL:

$$k_r = I_r / I_n\,,\ 0 \le k_r \le 1\,. \qquad (1)$$

Therefore, the method of mode load minimization of the PTL, which is implemented by reducing the load factor (1) of the PTL for the period of repair, can be recommended as the main method of protecting the working personnel from the PTL MF when performing repair work at their potential. In the event when the use of the main method of protection does not achieve the set goal, together with it, it is recommended to use an additional method of increasing the working distance to the PTL wires based on the use of special protective means – a protective suit with increased thickness of its material (5-15 mm), or protective capes with thickness of 3-13 mm for a guaranteed increase in the distance between the worker's body and the PTL wires.

Definition of conditions for ensuring protection working personnel from PTLs' MF. In order to protect the health of personnel from the effect of MF, it is necessary to guarantee the level of the MF flux density B_R on the body (extremities) of the worker to the limit level of B_{PD}, which is a function of time t_r. Then the conditions of worker's protection can be defined as:

$$B_R(I_r) \le B_{PD}(t_r)\,, \qquad (2)$$

where t_r is working time of the worker at the PTL potential.

As shown by the authors in [16], the maximum iflux density values of MF B_R in the working area of the PTL are concentrated along the axes of symmetry $\vec{e}$ of N suspension of the split wires of its phases (Fig. 3). The MF flux density at the observation point P (Fig. 5) depends on the distance l from the surface of the worker's body (on which the observation point P is located) to the axis of the nearest power line wire, when the x axis coincides with the direction $\vec{e}$.

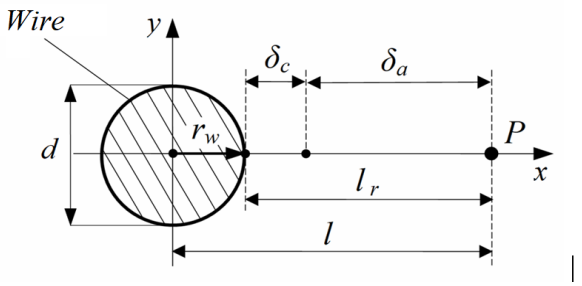

Fig. 5. On the determination of the distance l from the axis of the PTL wire to the observation point P

The MFfluxdensity also depends on such parameters of the transmission line as the number N of split phase wires, their radius r_w, and the distance D between the split phase wires. Here, according to Fig. 5:

$$l = r_w + l_r = r_w + \delta_c + \delta_a\,, \qquad (3)$$

where l_r is the distance from the wire surface to the worker's body; δ_c is the fabric thickness of the standard protective suit of the EK-1 shielding kit (2 mm); δ_a is the thickness of the additional protective layer when using special protective means.

Let us determine the conditions for the implementation of relation (2) when using the method of

mode load minimization and the method of increasing the working distance for 3 different types of PTL (Fig. 3), the parameters of which correspond to real (PTL 330 kV, I_n = 1733 A, N = 2, r_w = 14 mm, D = 400 mm; PTL2 750 kV, I_n = 2000 A, N = 4; r_w = 15.4 mm, D = 600 mm; PTL3 750 kV, I_n = 2000 A, N = 5, r_w = 14 mm, D = 500 mm).

To do this, we find the maximum permissible load factors (k_{rD}) of PTLs, which allow limiting the flux density of MF in their working zone to the maximum permissible level of sanitary standards B_{PD}. The value of k_{rD} can be found by using the mathematical model of MF in the working area of the PTL proposed by the authors in [16], taking into account condition (2) and the requirements of sanitary standards from the maximum permissible level of flux density action B_{PD}. As a result, we will get the following calculation ratios that allow us to determine the maximum permissible load factors k_{rD} for different (Fig. 3) PTLs:

$$k_{rD(N=2)} \le \frac{B_{PD}}{I_n}\left[\frac{\mu_0}{2\pi}\frac{(l+R)}{l(l+2R)}\right]^{-1}; \quad (4)$$

$$k_{rD(N=4)} \le \frac{B_{PD}}{I_n}\left(\frac{\mu_0}{2\pi}\left[\frac{(l+R)^3}{(l+R)^4-R^4}\right]\right)^{-1}; \quad (5)$$

$$k_{rD(N=5)} \le \frac{B_{PD}}{I_n}\left[\frac{\mu_0}{10\pi}\left(\frac{1}{l}+\right.\right.$$
$$+\frac{2\left(l+R-R\cos\left(2\pi/5\right)\right)}{\left(l+R-R\cos\left(2\pi/5\right)\right)^2+\left(R\sin\left(2\pi/5\right)\right)^2}+ \quad (6)$$
$$\left.\left.+\frac{2\left(l+R-R\cos\left(4\pi/5\right)\right)}{\left(l+R-R\cos\left(4\pi/5\right)\right)^2+\left(R\sin\left(4\pi/5\right)\right)^2}\right)\right]^{-1};$$

$$R=\frac{D}{2\sin\left(\pi/N\right)}. \quad (7)$$

Based on rationships (1) – (7) and item 1 of Table 1, in Fig. 6 graphic dependenceis of k_{rD} for the case are plotted δ_a = 0.

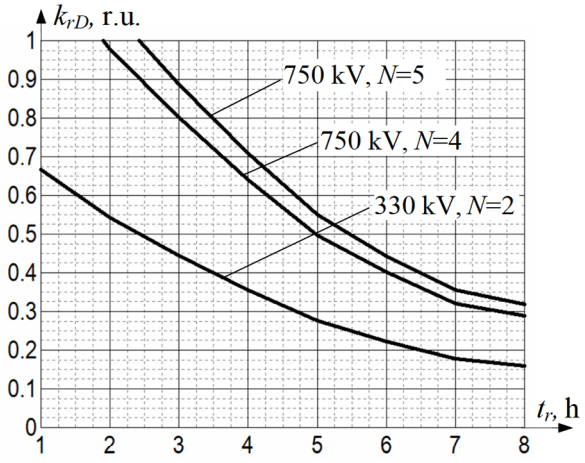

Fig. 6. The maximum allowable load factor k_{rD} of different transmission PTLs at δ_a = 0 depending on the term t_r of works on the potential of PTLs 330-750 kV according to the current standards of Ukraine

From Fig. 6 it follows that the worst situation occurs for the 330 kV PTL. Its maximum permissible load factor k_{rD} already at t_r = 1 h should be less than 0.67, at t_r = 4 h – 0.36, and at t_r = 8 h – 0.16. But the practical achievement of low load factors (k_r < 0.5) can be problematic, and especially, with a large amount of repair work on PTLs, the execution of which requires a significant amount of time.

For 750 kV PTLs with a large number of split wires (N = 4; 5) and at t_r = 1 h, k_{rD} of the PTL (Fig. 6) is close to 1, at t_r = 4 h – 0.65-0.7, and at 8 hours – about 0.29-0.32. For these PTLs, the use of the mode load minimization method may be sufficient when $k_{rD} \ge 0.5$ and t_r < 5 hours.

The joint use of the mode load minimization method and the method of increasing the working distance may be appropriate for 330 kV PTLs with t_r > 1 h, and is illustrated by the curves in Fig. 7, constructed in accordance with relationships (1)-(7) and item 1 of Table 1.

Thus, when an additional distance δ_a = 5 mm is introduced, the coefficient k_{rD} for this PTL can be increased in the entire range of t_r by up to 30%, at δ_a = 10 mm – up to 60%, and at δ_a = 15 mm – almost twice. This confirms the high efficiency of the method of increasing the working distance. The joint use of the proposed methods may also be appropriate in case of high labor intensity of works on the PTL potential, or in the case of the impossibility of significantly reducing the coefficient k_{rD} by the mode load minimization method.

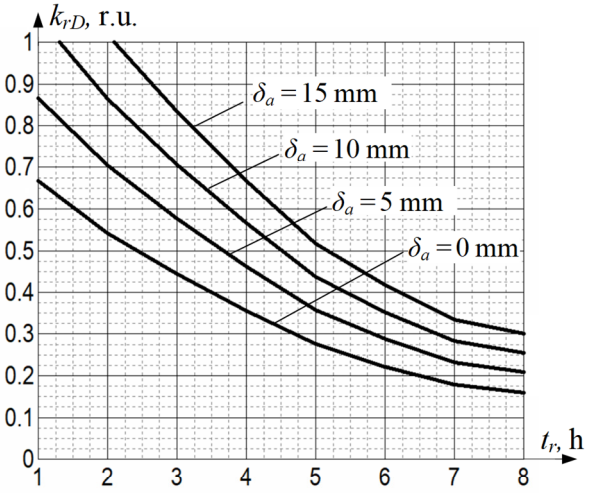

Fig. 7. The maximum allowable load factor k_{rD} of the 330 kV PTL (N = 2) in case of introducing an additional working distances δ_a according to current standards of Ukraine

The set of methods proposed above for reducing the MF acting on the worker, and the developed methodology for calculating the maximum allowable load factor k_{rD} of the PTLs, as well as the fulfillment of the formulated condition (2), constitutes the methodology for protecting workers from the magnetic field of the PTLs.

Now let's evaluate the effectiveness of using the considered methodology of worker's protection to reduce the flux of the PTL MF to the stricter Standards of the

European Union [12]. But in [12] normalization of only the upper (6 mT) and lower (1 mT) LLA of the MF flux density is provided, and there is no normalization for different working hours of employees (between 1 and 8 hours), as it is done in [33, 34]. In order to perform the specified assessment, we will supplement the standard [12] with the values of the LLA of the MF flux density as a function of the staff's working time t_r according to the methodology of the National Academy of Medical Sciences of Ukraine used in [33, 34].

Thus, as follows from the analysis of the current regulations in Ukraine [33, 34] developed by the Institutes of the National Academy of Medical Sciences of Ukraine, the dependence $B_{PD} = f(t_r)$ on them is expressed by an exponential function:

$$B_{PD} = be^{-at_r}, \quad (8)$$

which, according to the data of item 1 of Table 1, presented in the form of curve 1 in Fg. 8.

Let's use (8) to determine the possible dependence $B_{PD} = f(t_r)$ for the implementation of European Union Standards. Such a dependence at $a = 0.2560$, $b = 7.7503$ is presented in the form of curve 2 in Fig. 8, and the B_{PD} values calculated on its basis, marked with asterisks, are summarized in item 2 of Table 1. It is obvious that when implementing European Union Standards [12, 33] in Ukraine, the dependence $B_{PD} = f(t_r)$ needs clarification based on the latest research of the National Academy of Medical Sciences of Ukraine.

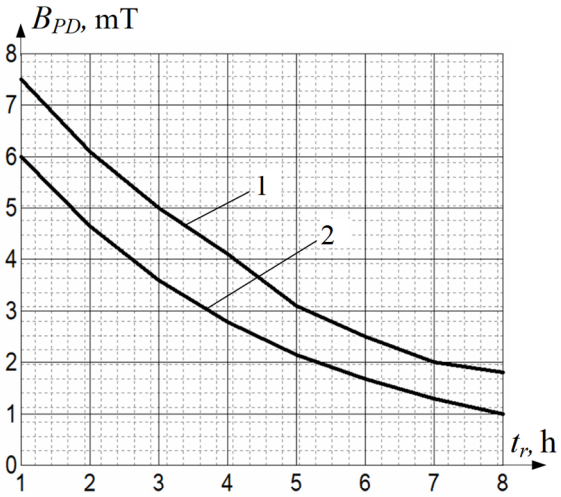

Fig. 8. Dependence of the limit level of MF flux density B_{PD} for the body of the worker on time t_r in accordance with current 1 [33] and promising 2 [12, 32] sanitary standards

Built in accordance with the data of item 2 of Table 1 dependencies $k_{rD} = f(t_r)$ at $\delta_a = 0$ for European Union standards are presented in Fig. 9. Their analysis shows that for the worst case (330 kV PTL), already at $t_r = 1$ h, the coefficient k_{rD} of the PTL should be no more than 0.53, at $t_r = 4$ h – 0.25, and at $t_r = 8$ h – 0.09. Therefore, the implementation of European Union Standards (item 2 of Table 1) without using additional methods of increasing the working distance can be problematic.

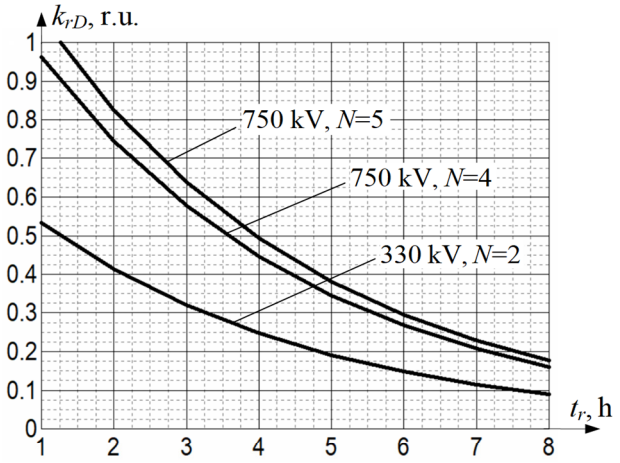

Fig. 9. The maximum allowable load factor k_{rD} according to prospective Standards of the European Union (item 2 of Table 1) of various PTLs depending on the term of performance t_r of works on the potential of 330-750 kV PTLs at $\delta_a = 0$

The results of ensuring the standards of the European Union [12, 32] when using an additional distance protection method are presented in Fig. 10.

Here, the maximum allowable load coefficients k_{rD} are determined in accordance with (1)-)8) and item 2 of Table 1 at δ_a from 0 to 15 mm. Their analysis shows that for the worst case (330 kV PTL) it is possible to reach the regulatory value of B_{PD} already at $k_{rD} = 0.5$ for $t_r < 4$ h, and $\delta_a = 15$ mm. The obtained results confirm the possibility of compliance with the European Union norms (item 2 of Table 1) when using the developed methods of protecting workers from the PYLs MF.

Presented in Fig. 6, 7, 9, 10 graphical dependencies allow to quickly, in working conditions, implement the developed methodology of protection of workers from MF of 330-750 kV PTLs with the implementation of both the current sanitary standards of Ukraine and the Directives of the European Union.

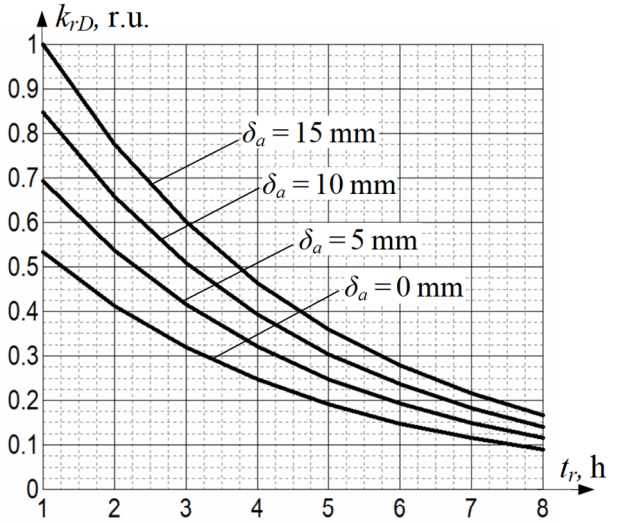

Fig. 10. The maximum permissible load factor k_{rD} according to the perspective Standards of the European Union (item 2 of Table 1) for 330 kV PTLs, depending on the term of completion of works t_r on the potential in case of introducing an additional working distance δ_a

Conclusions.

1. It is shown that practically during the entire time the worker is working on the potential of the wires of the power transmission lines using the technology of NEC «UkrEnergo», a minimum distance (≈ 2 mm) is maintained between the worker's body and the surface of the wires, which is determined by the thickness of the EK-1 protective suit. This circumstance should be taken into account when determining the flux density of the magnetic field acting on the worker during work on the potential of power transmission lines.

2. The methods of reducing the magnetic field in the working area of power transmission lines are proposed, such as the method of mode minimization of its load factor for the duration of the repair, and the method of increasing the working distance by introducing additional material of certain thickness (2-15 mm) between the wires and the worker's body, the use of which allows to reduce the flux density of the magnetic field when performing work on the potential of power transmission lines to a safe level.

3. A methodology for calculating the maximum permissible load factor of power transmission lines 330-750 kV has been developed, the use of which allows limiting the flux density of the magnetic field in their working zones to the maximum permissible level of sanitary standards for a given period of work on the potential and a given thickness of the additional protective layer between the wires and the worker's body.

4. Methodological principles for the protection of workers from the magnetic field during repair work without removing the voltage under load on 330-750 kV power transmission lines have been created, based on the combined use of the developed method of mode minimization of the load factor and the method of increasing the working distance, and a method has been developed of calculating the maximum allowable of the load factor under the condition of limiting the level of the magnetic field to the normative one. Their implementation makes it possible to reduce the flux density of the magnetic field in the working area of power transmission lines to the maximum permissible value in accordance with both current and future sanitary standards.

5. The obtained results can form a scientific basis for the development of normative documents of the Ministry of Energy, which regulate the rules of safe work of personnel in the magnetic field during repair work on 330-750 kV power transmission lines without voltage removal and under load.

Conflict of interest. The authors declare no conflict of interest.

REFERENCES

1. *Electrical installation regulations*. Kharkiv, Fort Publ., 2017. 760 p. (Ukr).

2. *SOU-N EE 20.666:2007. Instructions for performing live work on 110-750 kV power lines*. Kyiv, OEP GRIFRE Publ., 2007. (Ukr).

3. Sobchuk V.S., Sobchuk N.V. *Technologies of works under tension*. Vinnytsia, VNTU Publ., 2006. 101 p. (Ukr).

4. Kazanskij S.V. *Operation of electrical systems. Maintenance of electrical networks under working voltage*. Kyiv, NTUU «KPI» Publ., 2016. 237 p. (Ukr).

5. *The International EMF Project. Radiation & Environmental Health Protection of the Human Environment World Health Organization*. Geneva, Switzerland. 1996. 2 p. Режим доступу: www.who.int/initiatives/the-international-emf-project (Дата звернення: 04.01.2024).

6. *IEEE Guide for Maintenance Methods on Energized Power Lines, in IEEE Std 516-2021*. 2022, pp. 1-159. doi: https://doi.org/10.1109/ieeestd.2022.9678146.

7. Stam R. *Comparison of international policies on electromagnetic fields (power frequency and radiofrequency fields).* National Institute for Public Health and the Environment Ministry of Health, Welfare and Sport, 2018. 18 p. doi: https://doi.org/10.21945/rivm-document-electromagnetic-fields.

8. Göcsei G., Németh B., Tarcsa D. Extra low frequency electric and magnetic fields during live-line maintenance. *2013 IEEE Electrical Insulation Conference (EIC)*, 2013, pp. 100-104. doi: https://doi.org/10.1109/eic.2013.6554212.

9. Nesterenko A.D. *Introduction to Theoretical Electrical Engineering*. Kyiv, Naukova Dumka Publ., 1969. 351 p. (Rus).

10. Shimoni K. *Theoretical Electrical Engineering* (Translation from German). Moscow, Mir Publ., 1964. 774 p. (Rus).

11. ICNIRP. Guidelines for limiting exposure to time varying electric and magnetic fields (1 Hz – 100 kHz). *Health Physics*, 2010, vol. 99 no. 6, pp. 818-836. Available at: https://www.icnirp.org/cms/upload/publications/ICNIRPLFgdl.pdf (accessed 04 January 2024).

12. Directive 2013/35/EU of the European Parliament and of the Council of 26 June 2013 on the minimum health and safety requirements regarding the exposure of workers to the risks arising from physical agents (electromagnetic fields). *Official Journal of the European Union*, 2013, L 179, pp. 1-21. (Table B2) Available at: https://eurlex.europa.eu/LexUriServ/LexUriServ.do?uri=OJ:L:2013:179:0001:0021:EN:PDF (accessed 04 January 2024).

13. Alhassan A.B., Zhang X., Shen H., Xu H. Power transmission line inspection robots: A review, trends and challenges for future research. *International Journal of Electrical Power & Energy Systems*, 2020, vol. 118, art. no. 105862. doi: https://doi.org/10.1016/j.ijepes.2020.105862.

14. Wu G., Cao H., Xu X., Xiao H., Li S., Xu Q., Liu B., Wang Q., Wang Z., Ma Y. Design and Application of Inspection System in a Self-Governing Mobile Robot System for High Voltage Transmission Line Inspection. *2009 Asia-Pacific Power and Energy Engineering Conference*, 2009, pp. 1-4. doi: https://doi.org/10.1109/APPEEC.2009.4918256.

15. Nguyen V.N., Jenssen R., Roverso D. Automatic autonomous vision-based power line inspection: A review of current status and the potential role of deep learning. *International Journal of Electrical Power & Energy Systems*, 2018, vol. 99, pp. 107-120. doi: https://doi.org/10.1016/j.ijepes.2017.12.016.

16. Rozov V.Y., Reutskyi S.Y., Pelevin D.Y., Kundius K.D. Approximate method for calculating the magnetic field of

330-750 kV high-voltage power line in maintenance area under voltage. *Electrical Engineering & Electromechanics*, 2022, no. 5, pp. 71-77. doi: https://doi.org/10.20998/2074-272X.2022.5.12.
17. Chunikhin K.V., Grinchenko V.S. Normalization of double-circuit overhead line magnetic field inside Khrushchev building. *Electrical Engineering & Electromechanics*, 2021, no. 3, pp. 38-41. doi: https://doi.org/10.20998/2074-272X.2021.3.06.
18. Grinchenko V.S. Mitigation of three-phase power line magnetic field by grid electromagnetic shield. *Technical Electrodynamics*, 2018, no. 4, pp. 29-32. (Ukr). doi: https://doi.org/10.15407/techned2018.04.029.
19. Tkachenko A. O. Determination of analytical calculation error of magnetic field of high-voltage cable lines with two-point bonded cable shields caused by non-uniform current distribution in the shields. *Electrical Engineering & Electromechanics*, 2017, no. 3, pp. 27-31. doi: https://doi.org/10.20998/2074-272X.2017.3.04.
20. Rozov V.Y., Reutskyi S.Y., Pelevin D.Y., Yakovenko V.N. The research of magnetic field of high-voltage AC transmissions lines. *Technical Electrodynamics*, 2012, no. 1, pp. 3-9. (Rus).
21. Pelevin D.Y. The methods of reducing of the magnetic fields of overhead power lines outside security zones. *Technical Electrodynamics*, 2014, no. 5, pp. 14-16. (Rus).
22. Kuznetsov B.I., Nikitina T.B., Bovdui I.V., Voloshko O.V., Kolomiets V.V., Kobylianskiy B.B. Method of adjustment of three circuit system of active shielding of magnetic field in multi-storey buildings from overhead power lines with wires triangular arrangement. *Electrical Engineering & Electromechanics*, 2022, no. 1, pp. 21-28. doi: https://doi.org/10.20998/2074-272X.2022.1.03.
23. Kuznetsov B.I., Nikitina T.B., Bovdui I.V., Voloshko O.V., Kolomiets V.V., Kobylianskyi B.B. Synthesis of an effective system of active shielding of the magnetic field of a power transmission line with a horizontal arrangement of wires using a single compensation winding. *Electrical Engineering & Electromechanics*, 2022, no. 6, pp. 15-21. doi: https://doi.org/10.20998/2074-272X.2022.6.03.
24. Kuznetsov B.I., Nikitina T.B., Bovdui I.V., Kolomiets V.V., Kobylianskiy B.B. Overhead power lines magnetic field reducing in multi-story building by active shielding means. *Electrical Engineering & Electromechanics*, 2021, no. 2, pp. 23-29. doi: https://doi.org/10.20998/2074-272X.2021.2.04.
25. Rozov V., Grinchenko V., Tkachenko O., Yerisov A. Analytical Calculation of Magnetic Field Shielding Factor for Cable Line with Two-Point Bonded Shields. *2018 IEEE 17th International Conference on Mathematical Methods in Electromagnetic Theory (MMET)*, 2018, pp. 358-361. doi: https://doi.org/10.1109/MMET.2018.8460425.
26. Rozov V.Y., Kvytsynskyi A.A., Dobrodeyev P.N., Grinchenko V.S., Erisov A.V., Tkachenko A.O. Study of the magnetic field of three phase lines of single core power cables with two-end bonding of their shields. *Electrical Engineering & Electromechanics*, 2015, no. 4, pp. 56-61. (Rus). doi: https://doi.org/10.20998/2074-272X.2015.4.11.
27. Rozov V.Y., Pelevin D.Y., Levina S.V. Experimental research into indoor static geomagnetic field weakening phenomenon. *Electrical Engineering & Electromechanics*, 2013, no. 6, pp. 72-76. (Rus).
28. Rozov V.Y., Pelevin D.Y., Kundius K.D. Simulation of the magnetic field in residential buildings with built-in substations based on a two-phase multi-dipole model of a three-phase current conductor. *Electrical Engineering & Electromechanics*, 2023, no. 5, pp. 87-93. doi: https://doi.org/10.20998/2074-272X.2023.5.13.
29. Krasnozhon A.V., Buinyi R.O., Dihtyaruk I.V., Kvytsynskyi A.O. The investigation of distribution of the magnetic flux density of operating two-circuit power line 110 kV «ChTPP-Chernihiv-330» in the residential area and methods of its decreasing to a safe level. *Electrical Engineering & Electromechanics*, 2020, no. 6, pp. 55-62. doi: https://doi.org/10.20998/2074-272X.2020.6.08.
30. Reutskiy S., Zhang Y., Lu J., Pubu C. A Novel Method for Linear Systems of Fractional Ordinary Differential Equations with Applications to Time-Fractional PDEs. *Computer Modeling in Engineering & Sciences*, 2024, vol. 139, no. 2, pp. 1583-1612. doi: https://doi.org/10.32604/cmes.2023.044878.
31. Reutskiy S., Zhang Y., Lin J., Lu J., Xu H., He Y. A novel B-spline method to analyze convection-diffusion-reaction problems in anisotropic inhomogeneous medium. *Engineering Analysis with Boundary Elements*, 2020, vol. 118, pp. 216-224. doi: https://doi.org/10.1016/j.enganabound.2020.06.013.
32. *On the approval of Minimum requirements for health and safety of workers exposed to electromagnetic fields*. Ministry of Health of Ukraine. Order on January 13, 2023 no. 81. Available at: https://zakon.rada.gov.ua/laws/show/z0184-23#Text (accessed 04 January 2024).
33. *On the approval of State sanitary rules and norms for the performance of work in non-switched off electrical installations with a voltage of up to and including 750 kV*. Ministry of Health of Ukraine. Order on July 09, 1997. no. 198. Available at: https://zakon.rada.gov.ua/rada/show/v0198282-97#Text (accessed 04 January 2024).
34. *On approval of State sanitary norms and rules for working with sources of electromagnetic fields (DSNiP 3.3.6.096-2002)*. Ministry of Health of Ukraine. Order on December 18, 2002. no. 476. Available at: https://zakon.rada.gov.ua/laws/show/z0203-03#Text (accessed 04 January 2024).
35. Serdyuk A.M. *Interaction organism with electromagnetic fields as the environmental factors*. Kyiv, Naukova Dumka Publ., 1977. 228 p. (Rus).
36. Dumanskyi V.Y., Koziarin I.P., Ivakhno O.P. Electromagnetic fields as an eco-hygienic problem of our time. *Environment & Health*, 2021, vol. 100(3), pp. 44-48. doi: https://doi.org/10.32402/dovkil2021.03.044.
37. Nazarenko V.I. Magnetic field induction of industrial frequency as a factor of professional hazard a tthermal power stations. *Ukrainian journal of Occupational Health*, 2007, no. 4, pp. 18-26. (Ukr). doi: https://doi.org/10.33573/ujoh2007.04.018.
38. Conti R., Giorgi A., Rendina R., Sartore L., Sena E.A. Technical solutions to reduce 50 Hz magnetic fields from power lines. *2003 IEEE Bologna Power Tech Conference Proceedings*, 2003, vol. 2, pp. 1016-1021. doi: https://doi.org/10.1109/PTC.2003.1304685.
39. Bravo-Rodríguez J., Del-Pino-López J., Cruz-Romero P. A Survey on Optimization Techniques Applied to Magnetic

Field Mitigation in Power Systems. *Energies*, 2019, vol. 12, no. 7, art. no. 1332. doi: https://doi.org/10.3390/en12071332.
40. Gocsei G., Nemeth B., Tamus Z.A., Kiss I. Face protection investigation against electric field on live line workers. *2012 IEEE International Symposium on Electrical Insulation*, 2012, pp. 535-539. doi: https://doi.org/10.1109/ELINSL.2012.6251527.
41. Malgesini R., Valagussa C., Villa A., Carraro R., De Dona G., Milanello C.D., Parizia A.A. Conductive clothing for live line working. *2014 11th International Conference on Live Maintenance (ICOLIM)*, 2014, pp. 1-4. doi: https://doi.org/10.1109/ICOLIM.2014.6934340.
42. Göcsei G., Németh B., Kiss I., Berta I. Shielding efficiency of conductive clothing in magnetic field. *Journal of Electrostatics*, 2013, vol. 71, no. 3, pp. 392-395. doi: https://doi.org/10.1016/j.elstat.2013.01.001.
43. Gocsei G., Nemeth B., Kiss I., Berta I. Health effects of magnetic fields during live-line maintenance. *2014 11th International Conference on Live Maintenance (ICOLIM)*, 2014, pp. 1-6. doi: https://doi.org/10.1109/ICOLIM.2014.6934329.
44. Bavastro D., Canova A., Freschi F., Giaccone L., Manca M. Magnetic Field Mitigation at Power Frequency: Design Principles and Case Studies. *IEEE Transactions on Industry Applications*, 2015, vol. 51, no. 3, pp. 2009-2016. doi: https://doi.org/10.1109/TIA.2014.2369813.
45. Rozov V.Y., Pelevin D.Y., Pielievina K.D. External magnetic field of urban transformer substations and methods of its normalization. *Electrical Engineering & Electromechanics*, 2017, no. 5, pp. 60-66. doi: https://doi.org/10.20998/2074-272X.2017.5.10.

Надійшла (Received) 26.01.2024
Прийнята (Accepted) 19.03.2024
Опублікована (Published) 20.06.2024

V.Yu. Rozov[1]*, Doctor of Technical Science, Professor, Corresponding member of NAS of Ukraine,*
S.Yu. Reutskiy[1]*, PhD, Senior Researcher,*
K.D. Kundius[1]*, PhD,*
[1] Anatolii Pidhornyi Institute of Mechanical Engineering Problems of the National Academy of Sciences of Ukraine, 2/10, Pozharskogo Str., Kharkiv, 61046, Ukraine,
e-mail: vyurozov@gmail.com (Corresponding Author); sergiyreutskiy@gmail.com; kundiuckateryna@ukr.net

How to cite this article:
Rozov V.Yu., Reutskiy S.Yu, Kundius K.D. Protection of workers against the magnetic field of 330-750 kV overhead power lines when performing work without removing the voltage under load. *Electrical Engineering & Electromechanics*, 2024, no. 4, pp. 70-78. doi: https://doi.org/10.20998/2074-272X.2024.4.09

Матеріали приймаються за адресою:
Кафедра "Електричні апарати", НТУ "ХПІ", вул. Кирпичева, 2, м. Харків, 61002, Україна
Електронні варіанти матеріалів по e-mail: a.m.grechko@gmail.com

Довідки за телефонами: +38 067 359 46 96 Гречко Олександр Михайлович

Передплатний індекс: 01216